UNIVERSITY OF LONDON THESIS

Degree PhD Year 2008 Name of Author NICOLAN, Nick

Single and Two-Photon Fluorescence Studies of Linear and Non-Linear Optical Chromophores

Nick Nicolaou

Submitted for the degree of
Doctor of Philosophy

University of London
2008

Department of Physics and Astronomy

University College London

ProQuest LLC
789 East Eisenhower Parkway
P.O. Box 1346
Ann Arbor, MI 48106-1346

I Nick Nicolaou declare that the work presented in this thesis is my own. Where information has been derived from other sources, I confirm that this has been indicated in the thesis appropriately.

Signed

To my niece, Poppy

"In that book which is
My memory...
On the first page
That is the chapter when
I first met you
Appear the words...
Here begins a new life"

Abstract

The subject matter presented in this thesis concerns the structural and dynamic studies of new fluorescent probe molecules and the application of polarised fluorescence techniques and analysis to molecular motion, order and solvation in a highly ordered environment.

Chapter 1 reviews recent group research providing a context to the work in this thesis, whilst Chapters 2 and 3 concern the study of fluorescent probe dynamics. Time resolved photoselection techniques were used to probe the order and full angular motion of Coumarin 6 and Coumarin 153 in the nematic and isotropic phases of the liquid crystal 5CB. The uptake of coumarin molecules into this host differs from previously studied (Xanthene) probes - in particular, Coumarin 6 is seen to adopt a disruptive position within the alkyl tails due to its size and hydrophobic nature; this is discussed in Chapter 2.

Furthermore, Coumarin 153 undergoes a substantial increase in dipole moment upon electronic excitation; this led to a unique study of time dependent solvation dynamics in both a globally and locally structured environment. The presence of strong solvent–solute interactions necessitated the development of a new approach to the analysis of time resolved polarised fluorescence in ordered systems. This approach and the study of time dependent solvation dynamics in the isotropic and nematic phases of 5CB is presented in Chapter 3.

Structural studies of new two-photon fluorescent probes in collaboration with CNRS Rennes and Los Alamos are described in the final two chapters. Large two-photon resonances in the green-visible were observed together with a fuller characterisation of those in the near IR. Polarised two-photon absorption and anisotropy measurements were used to examine the structure of the two-photon resonances. Finally, the stimulated emission depletion dynamics of a branched two-photon fluorophore were investigated and found to differ markedly from conventional (non-degenerate) fluorophores.

Acknowledgments

It is unlikely that I will be in this position again so I would like to take this very rare opportunity to express my gratitude to a number of people. Heartfelt thanks to my supervisor Dr Angus Bain for his excellent guidance and support. To Dr Richard Marsh, for omniscient guidance and Dr Daven Armoogum for an understanding way beyond the call of duty, I am deeply indebted to you both. To Tom good luck with the final run-in, Ricky V, keep on producing and Nick, good luck in finishing. Finally to Dr Stan Zochowski "chief", thanks for showing genuine interest during my apprenticeship.

My family have stood beside me throughout this time and I would like to thank-you for your love, patience and understanding Ma, Pa, Sis, Andy and Chris. To my dear friends who have supported throughout, you know who you are so no need for name checks. Yes indeed, it is done, so crack open the Macallan. Mum-Raa!!

And finally, to my beloved Marcie, who has devoted much in my pursuit of self-fulfilment, thank-you so much for the love, understanding and tolerance you have shown. Your role in the completion of my work cannot be overstated.

Table of Contents

List of Figures

CHAPTER 4

CHAPTER 5

List of Tables

List of Collaborators

Experiment: Two-Photon Absorption Cross-Section Measurements of Quadrupolar and Branched Chromophores.
Collaborators: Dr Richard Marsh, Dr Martinus Werts, Mr Nick Leonczek.

Experiment: Two-Photon Transition Tensor Measurements of Quadrupolar and Branched Chromophores.
Collaborators: Dr Richard Marsh.

Experiment: Two-Photon Excited Stimulated Emission Depletion Measurements of a Branched Chromophore.
Collaborators: Dr Daven Armoogum, Dr Richard Marsh.

Chapter 1

Photophysics of Molecular Probes

1.1 Introduction

The work in this thesis describes the development and application of polarised single and two-photon time resolved photoselection techniques to investigate the electronic structure, order and dynamical properties of fluorescent probes.

The past twenty years has seen great change in the application of fluorescence techniques primarily reserved for use as research tools in the physical sciences. Fluorescence is now an interdisciplinary methodology not only applied in the fields of physics and chemistry, but also in the life sciences. As a result the application of fluorescent probes has become widespread and varied.

1.2 Molecular Fluorescence

Various physical and chemical parameters such as viscosity, pH, temperature, polarity, electric potential, quenchers, pressure and hydrogen bonds [1] have a profound influence on the fluorescence of a probe molecule. These effects are manifest for example by the time dependent and steady state fluorescence spectra, the fluorescence lifetime and the fluorescence polarisation. Thus the assimilation of a probe can provide specific information on the local environment of a host such as the orientational order and rotational dynamics in a liquid crystal [2, 3], the structural changes and conformational transitions and dynamics in biological membranes, in proteins and in living cells [4].

The absorption and emission processes which take place when a probe molecule absorbs electromagnetic radiation can be depicted by means of a Perrin-Jablonski energy level diagram as shown in figure 1.1. In single photon excitation a molecule absorbs a photon of appropriate energy such that it is raised from its lowest ground state vibrational level to one of several vibrational levels of the first excited singlet state

($S_0 \rightarrow S_1$) In a condensed medium such as a liquid or solid a molecule in a high vibrational state collides repeatedly with neighbouring molecules rapidly losing its excess vibrational energy (vibrational relaxation occurs in $\approx 10^{-12}$s). Providing the competing rate constants are small compared with radiative relaxation to the ground state then there is a high probability for emission of fluorescence [5]. For isolated molecules the subsequent emission spectrum can be sub-divided into three types of transition between the molecular quantum states. For any given molecular electronic state, the level is sub-divided into groups separated by approximately equal energy levels. These levels correspond to successive states of vibration of the nuclei. The vibrational level is further sub-divided into a fine structure of levels ascribed to the different states of rotation of the molecule. The energy separation between adjacent rotational levels ($\approx$ 0.001ev-0.0001ev), and vibrational levels ($\approx$ 0.1ev) is small [6]. At ambient temperatures these levels become populated according to Boltzmann statistics so at any given wavelength it is possible to excite a multitude of ro-vibronic ground to excited state transitions. The characteristic shape of the emission spectra for different fluorescent compounds is dependant upon the individual vibrational levels in the ground and excited states. Compounds which possess vibrational structure will have emission spectra characterised by patterns of maxima (peaks) and minima (troughs). In the condensed phases the emission spectrum of a molecular probe is devoid of detailed structure due to the density of the vibrational states, the numerous solvent-solute collisions and ultrafast relaxation dynamics [7].

The absorption and emission spectra can be considered as depicting the vibrational state density of the first excited state and the vibrational state density of the ground state respectively. For absorption and emission spectra which possess similarly structured intensity patterns the spectra are deemed to possess mirror symmetry. Due to fast relaxation in the excited state, emission energy is less than that of absorption. Therefore emission resulting from single photon excitation is at longer wavelengths than absorption. This is known as the Stokes shift.

Not all transitions are equally probable when considering the possible transitions from the vibrational levels of one electronic state to vibrational levels of another electronic state (e.g. $S_0 \rightarrow S_1$). Selection rules govern the possible transitions and the transition

probabilities are dependent upon the overlap between the vibrational wavefunctions of the two states (Franck-Condon factor).

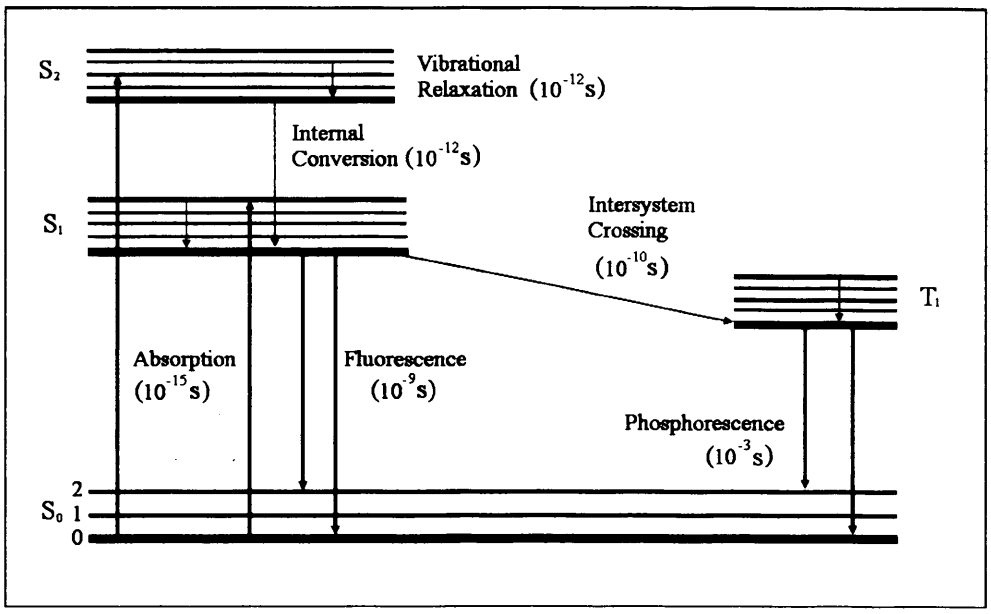

Figure 1.1: A Perrin-Jablonski diagram in which S_0, S_1, S_2... denote singlet states and T_1 a triplet state. Singlet states possess net spin angular momentum 0 whilst triplet states possess net spin angular momentum 1. Radiative relaxation to the ground state is highly improbable from states of different electron spin multiplicity. Arrows pointing upwards represent possible absorption transitions between singlet states. Emission from the triplet state T_1 represents phosphorescence and occurs on a timescale very much longer than emission from singlet states.

The process of fluorescence is one possible pathway by which a molecule can return to the ground state once excited. However, many alternative de-excitation pathways exist such as internal conversion, intersystem crossing, intramolecular charge transfer, collisional depopulation and conformational change [1].

The fluorescence lifetime and quantum yield are particularly important features of a fluorophore. The quantum yield is defined as the number of emitted photons relative to the number of absorbed photons. Fluorescence dye probes such as rhodamine6G possess quantum yields in excess of 95% at room temperature [6]. The fluorescence lifetime is defined as the interval during which the intensity of fluorescence has fallen to $1/e$ of its maximum value. This characteristic is particularly important as it determines

the average length of time an excited molecule can interact with its environment and therefore defines the time window available for observation of dynamic processes.

1.3 Polarised Photoselection, Fluorescence Anisotropy and Isotropic Rotational Diffusion

Most experiments involving fluorescence are carried out using polarized light sources [3]. In this situation the fluorescence emission after excitation is also polarized. The polarized emission is a result of the interaction between the transition dipole moment of the fluorophore and the electric vector of the excitation source. The transition dipole moment is oriented relative to the molecular axis, so in an isotropic environment where the molecules are randomly distributed the transition dipole moments are also oriented randomly. Those fluorophores which possess transition dipole moments aligned parallel to the electric vector of the excitation source are then preferentially excited as shown in figure 1.2.

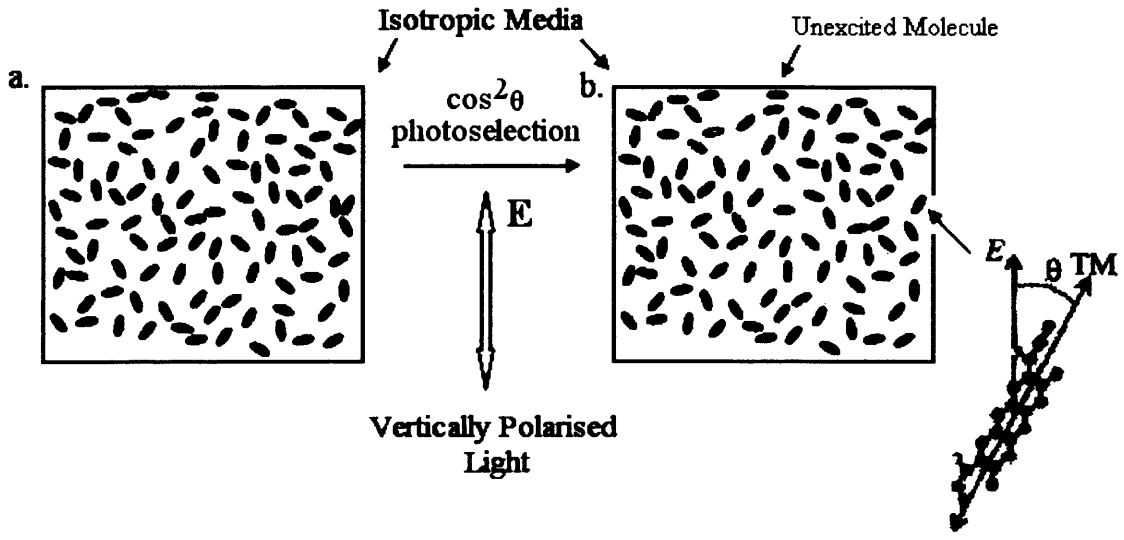

Figure 1.2: A schematic representation of single-photon photoselection in an isotropic medium. The probability of absorption is dependent on the orientation of the transition dipole moment relative to the electric vector of the of the excitation source. Those fluorophores which possess absorption dipoles which make a small angle with respect to the E field will be preferentially excited relative to those oriented close to the perpendicular plane.

The electric dipole moment need not necessarily be aligned precisely parallel to the electric vector of the excitation source to absorb light. As the probability of excitation is

proportional to the square of the transition dipole moment and the electric vector, for vertically polarised light the resultant photoselected excited-state population is made up of fluorophores which are symmetrically orientated about the Z-axis as shown in figure 1.3b.

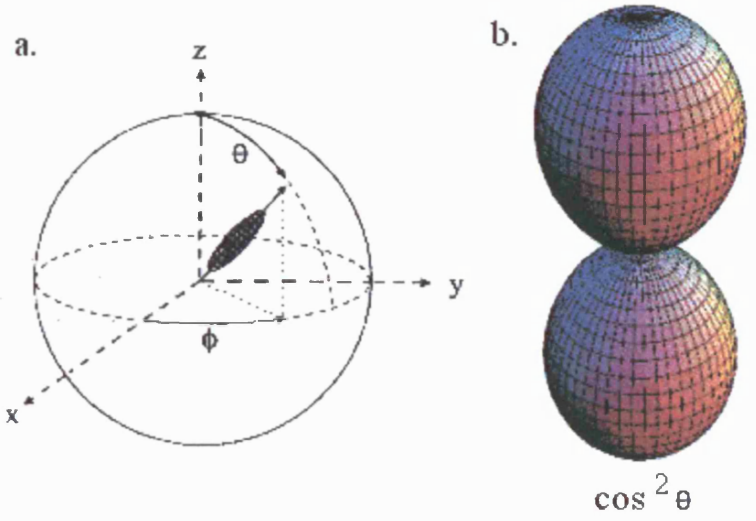

Figure 1.3: a) Polar coordinate geometry representation of the probability of finding a molecule oriented between θ to θ + dθ and φ to φ + dφ. b) The excited-state distribution immediately after single-photon excitation for an isotropic medium. The transition probability yields a $\cos^2\theta$ distribution.

On de-excitation the fluorescence photon is polarised parallel to the emission dipole moment of the molecule which, provided the emitting state is not substantially different to the absorbing state, is expected to be near parallel to the absorption dipole moment. The extent of polarization of the emission in the laboratory frame therefore contains information on the alignment of the emitting population. The degree of orientational order remaining in the excited state ensemble is normally described in terms of the fluorescence anisotropy R(t). The fluorescence anisotropy for an excitation pulse polarised parallel to the Z-axis (vertically polarised), is given by

$$R(t) = \frac{I_V(t) - I_H(t)}{I_V(t) + 2I_H(t)} \qquad [1.1]$$

where $I_V(t)$ and $I_H(t)$ are the vertically and horizontally polarized fluorescence emission

intensities respectively. For a cylindrically symmetric system these are given by [1]

$$I_V(t) \propto N_{EX}(t)[1 + 2R(t)] \qquad [1.2a]$$

$$I_H(t) \propto N_{EX}(t)[1 - R(t)] \qquad [1.2b]$$

Here $N_{EX}(t)$ is the excited state population remaining at time t following excitation. From symmetry considerations it can be shown that the fluorescence anisotropy is proportional to the degree of second-order alignment present in the excited state [8, 9]:

$$R(t) \equiv \frac{\langle \alpha_{20}^{ex}(t) \rangle}{\sqrt{5}} = \sqrt{\frac{4\pi}{5}} \int_0^{2\pi} \int_0^{\pi} Y_{20}^{*}(\theta,\varphi) P_{ex}(\theta,\varphi,t) \sin\theta d\theta d\varphi \qquad [1.3]$$

where P_{ex} is the probability of finding the molecule aligned between the polar angles θ to $\theta + d\theta$ and φ to $\varphi + d\varphi$ (figure 1.3a) and Y^*_{20} is a spherical harmonic of the form

$$Y_{20}^{*}(\theta,\varphi) = \sqrt{\frac{5}{16\pi}} \left(3\cos^2\theta - 1\right) \qquad [1.4]$$

Inserting equation 1.3 into 1.4 yields

$$R(t) = \frac{1}{2}\left(3\langle \cos^2\theta(t) \rangle - 1\right) \qquad [1.5]$$

where $\langle\ \rangle$ denotes an average over the distribution. For an isotropic distribution the initial single-photon maximum anisotropy is 2/5 [1].

In the condensed phase molecules cannot undergo free rotation as in the gas phase but are subject to rapid solute-solvent collisions $10^{-13}s^{-1}$ [7]. In this case the reorientation is assumed to occur in small steps resulting in the randomisation of the ensemble of molecular orientations (Appendix II). Due to the continuous interactions with their neighbours molecules rotating in a liquid experience friction. This can be described by simple hydrodynamic theory where the behaviour is related to the size and shape of the fluorescent molecule and the relative viscosity of the local environment. Effects on the

rotational dynamics of the molecule depend on the boundary conditions, which are broadly classified as either stick or slip depending on the degree to which molecular rotation involves cooperative movement of the surrounding solvent (this is discussed in detail in Chapter 2). Such rotational diffusion occurs during the lifetime of the excited state and causes a displacement of the emission dipole and the extent of the fluorescence depolarization caused by rotational diffusion, yields information on the motion of the fluorescent molecule in the host environment. If the absorption and emission transition dipole moments are approximately parallel and lie along or in the vicinity of the molecular axis, then the diffusion approximates to that of a symmetric rotor [10]. In this case the fluorescence anisotropy is given by

$$R(t) = R(0)\exp\left(\frac{-t}{\tau_{ROT}}\right) \qquad [1.6]$$

where τ_{ROT} is the rotational diffusion time given by

$$\tau_{ROT} = \frac{1}{6}D \qquad [1.7]$$

and D is defined as the rotational diffusion coefficient (s^{-1}). From equation 1.8 it can be seen that the rotational diffusion time is proportional to the molecular hydrodynamic volume V and the solvent viscosity η. It is also inversely proportional to the thermal energy kT. The molecular shape factor f and the boundary coefficient C, which accounts for the interaction between the solvent and solute, are two constants which modify the relationship giving the rotational diffusion time as

$$\tau_{ROT} = fC\left(\frac{\eta V}{kT}\right) \qquad [1.8]$$

The rotational dynamics described above refer to an isotropic fluid, where rotational diffusion is relatively straightforward and diffusion times for small molecular probes vary from a few nanoseconds to several hundred picoseconds [5]. This is not the case for fluorescent probes used to investigate locally structured environments such as membranes or the mesophases of a liquid crystal. Similarly complex behaviour occurs

with naturally occurring fluorescent probes found in large molecules such as proteins. In these environments, the fluorescent probe is no longer free to rotate, but is in fact restricted by the local geometry of the media. Although the overall orientational distribution of the macro environment is isotropic, the steady state orientational distribution of the fluorescent probe locally, is no longer isotropic. These characteristics are manifest in bi-exponential anisotropy decays indicating degrees of local order and global order within the host environment. Providing the local and global rotational diffusion times are independent of each other, the fluorescence anisotropy is defined as the product of the correlation function [2]:

$$R(t) = \exp\left(\frac{-t}{\tau_{SLOW}}\right)\left[(R(0) - R_{DOMAIN})\exp\left(\frac{-t}{\tau_{FAST}}\right) + R_{DOMAIN}\right] \qquad [1.9]$$

where $R(0)$ and R_{DOMAIN} are the limiting values of the anisotropy in the absence of motion of the domains. The ratio of the two pre-exponential factors in equation 1.9 reveals the degree of the local restricted motion of the fluorescent probe. These factors can be used to determine the angular width of the probe environment from equation 1.10.

$$\sqrt{\frac{R_{DOMAIN}}{R(0)}} = \frac{1}{2}\left[\cos\theta_{max}\left(1 + \cos\theta_{max}\right)\right] \qquad [1.10]$$

From such R(t) measurements it is possible to determine conformational changes and local structure in complex protein molecules such as Human Serum Albumin (HSA). Human serum albumin (HSA) is the most abundant protein found in plasma and performs many important functions including the transport, distribution and metabolism of many endogenous and exogenous ligands (e.g. fatty acids, amino acids, steroids and numerous pharmaceuticals) [10, 11]. Studies undertaken by Chadborn et al revealed the ligand dependent conformational changes induced by binding Oleic acid to the protein [11]. The results revealed that that the presence of the Oleate increased the rotational diffusion time of the protein and decreased the restricted rotational motion of the tryptophan probe [11] confirming that structural change in HSA could be induced by ligand binding (Figure 1.4).

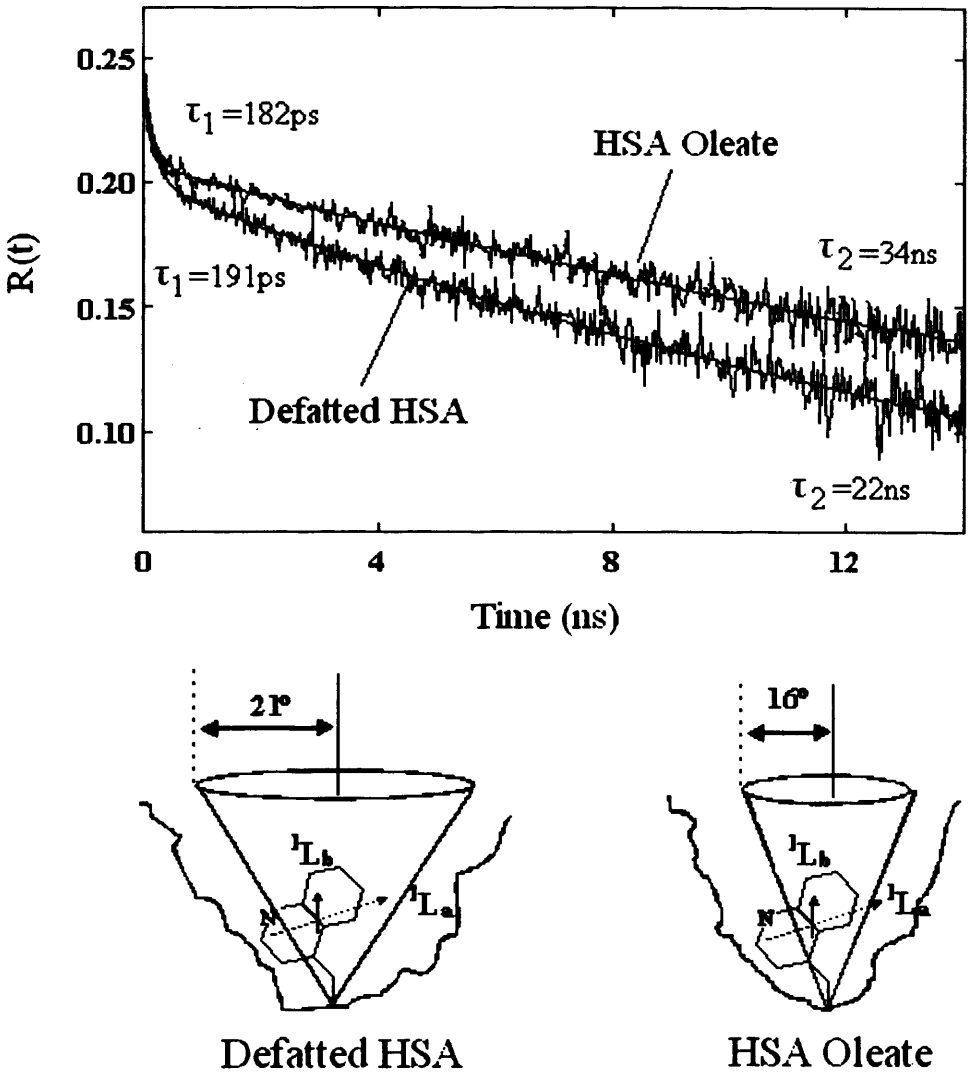

Figure 1.4: Observed fluorescence anisotropy decays of the tryptophan 214 in HSA as measured by Chadborn et al [11]. The fast picosecond decay component is due to the local tryptophan motion whereas the slower nanosecond decay component results from the overall rotation of the HSA molecule. Binding of the oleic acid molecules to HSA is seen to give rise to a conformational change in the protein affecting the local environment of tryptophan 214 located towards the centre of the protein. It can be seen that the protein becomes more compact with a change in cone angle from 21° to 14°.

1.4 Probe Behaviour in Highly Ordered Environments

Highly ordered systems are found throughout nature and the presence of order can have a profound effect on the intrinsic properties and behaviour of a system. The optical [13] and photophysical behaviour [14], the chemical reactivity [15] and the molecular dynamics of a system [16] all depend on the degree of order. In biological systems membranes contain highly organized molecular assemblies that mediate important processes such as energy transduction, active transport, nerve impulse conduction, sensory reception, and hormonal integration [17]. In the ordered environment of liquid crystals the ability for the molecules to respond to external electric fields has generated industrial applications in the form of liquid crystal displays, optical imaging and recording. The probing of molecular order to obtain structural, functional and dynamical information is therefore of considerable scientific interest and the use of time resolved photoselection techniques, have facilitated studies in the behaviour of ordered environments.

In environments such as the nematic phase of a liquid crystal there exists a significant degree of molecular order and polarised fluorescence from such systems is seen to depart from that behaviour observed in isotropic media. In the highly ordered ground state of an anisotropic medium the orientation of the fluorescence probe is confined such that the polarization is no longer entirely randomized and the fluorescence anisotropy decays to some non-zero steady state value. Furthermore, in contrast to an isotropic environment, θ and φ diffusion rates are not necessarily equivalent [10].

Given an isotropic ground state where the population is excited by a Z-polarized pulse (as shown in figure 1.3) the resultant fluorescence anisotropy depends solely on the evolution of the cylindrically symmetric excited state alignment $\langle \alpha_{20}^{ex}(t) \rangle$ [10]. Excited state arrays generated in this manner possess inherent cylindrical symmetry. This implies that the fluorescence anisotropy R(t) is sensitive only to θ relaxation and any angular averaging in the X-Y plane (φ-diffusion) is not observed [18].

In an isotropic system θ and φ diffusion is wholly equivalent. In an anisotropic environment this is not necessarily the case. By varying the excitation polarisation angle β with respect the laboratory fixed axis (figure 1.5), the preparation of cylindrical asymmetric $\left\{\left\langle \alpha_{22}^{ex}(t)\right\rangle + \left\langle \alpha_{2-2}^{ex}(t)\right\rangle\right\}$ as well as cylindrically symmetric $\left\langle \alpha_{20}^{ex}(t)\right\rangle$ initial probe alignment is possible [8, 12]. In the example of a doped nematic liquid crystal aligned parallel to the laboratory Z-axis (described in Chapter 2) an excitation polarisation angle β=0° creates a cylindrically symmetric excited state with respect to the nematic director **n**. Relaxation of this distribution can be observed only in θ averaging.

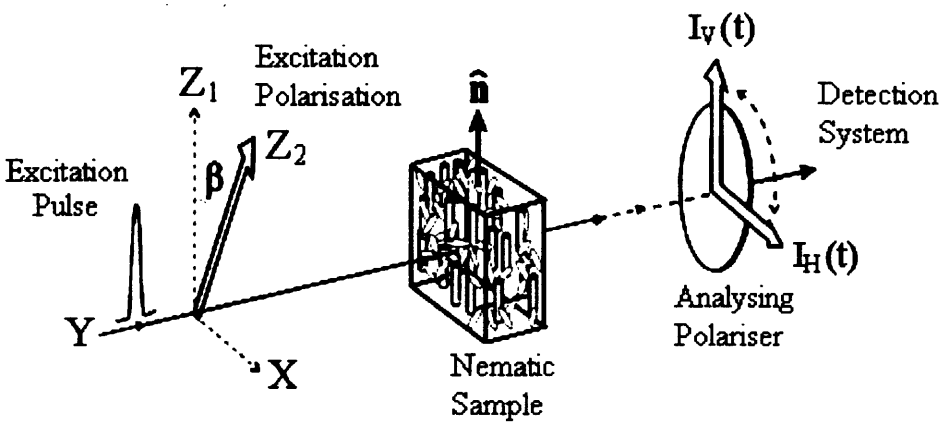

Figure 1.5: Experimental arrangement for time resolved photoselection using a variable polarised excitation pulse. Photoselection is achieved using single-photon excitation in a 180° excitation-detection geometry. Variation of the polarisation angle β is with respect to the nematic director n. The vertically (I_V) and horizontally (I_H) polarised emission intensities are used to construct the fluorescence anisotropy R(t, β). The technique is described in detail in Chapter 2.

In contrast, for β=90° a significant degree of asymmetric excited state alignment is created which principally relaxes by φ diffusion. Given an arbitrarily ordered excited state it is possible to determine the fluorescence anisotropy based on the degrees of symmetric and asymmetric probe alignment, which in the coordinate system (Z_1) as defined in figure 1.5, is given by equation 1.11 [8]:

$$R(t)=\frac{I_V(t)-I_H(t)}{I_V(t)+2I_H(t)}=\frac{1+\frac{\langle\alpha^{ex}_{20}(t)\rangle}{\sqrt{5}}-\sqrt{\frac{3}{10}}\left\{\langle\alpha^{ex}_{2+2}(t)\rangle+\langle\alpha^{ex}_{2-2}(t)\rangle\right\}}{1-\frac{\langle\alpha^{ex}_{20}(t)\rangle}{\sqrt{5}}+2\sqrt{\frac{3}{10}}\left\{\langle\alpha^{ex}_{2+2}(t)\rangle+\langle\alpha^{ex}_{2-2}(t)\rangle\right\}} \qquad [1.11]$$

Fluorescent probe studies utilising variable excitation polarisation photoselection techniques carried out by Monge et al have highlighted the extent of the difference in θ and φ diffusion rates for the fluorescent dye probe molecule Oxazine 4 in the nematic phase of n-cyanobiphenyl liquid crystals [2, 10]. This is shown in figure 1.6 where it is clear that the orientational relaxation for a cylindrically symmetric population created with an excitation polarisation angle aligned parallel to the nematic director ($\beta=0^o$) is considerably slower than that for a population aligned predominantly perpendicular to the nematic director ($\beta=90^o$).

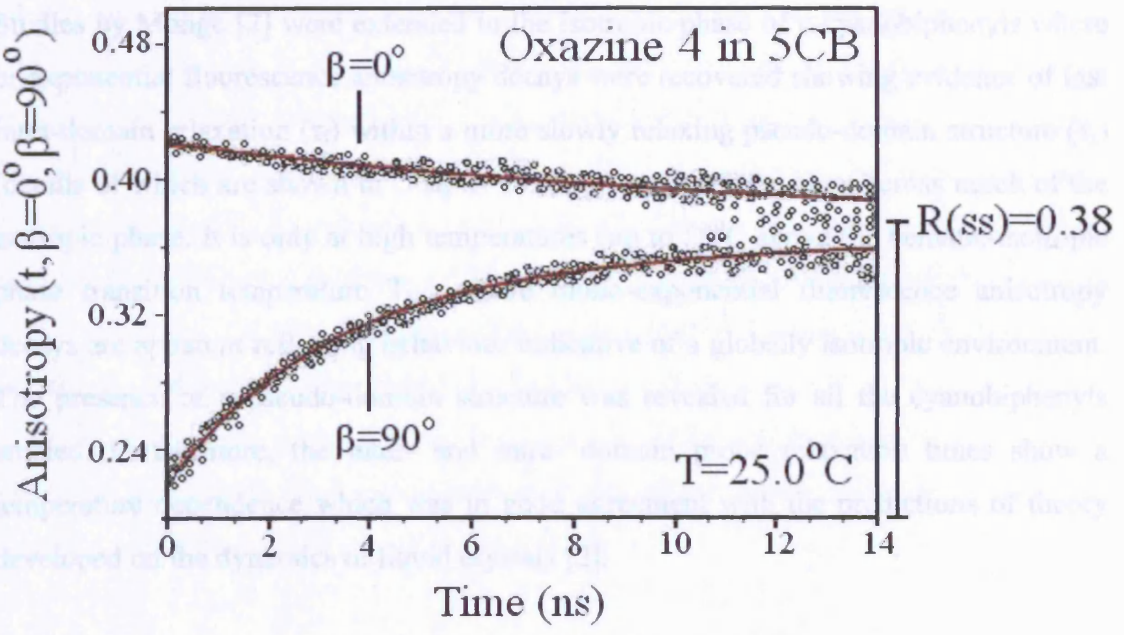

Figure 1.6: Fluorescence anisotropy decays for polarisation angles β=0° and β=90° for the fluorescent probe Oxazine 4 in the nematic phase of the liquid crystal 5-cyanobiphenyl at T=25°C. It is evident that the fluorescence anisotropy decays to a non-zero steady state value (Rss=0.38).

The full temperature dependent variation in the symmetric and asymmetric relaxation times resulting from excitation at polarisation angles β=0° and β=90° relative to the nematic director has been measured for several probes in this group and is discussed in detail in Chapter 2 and Chapter 3.

From the anisotropy decays created via time resolved single-photon excited fluorescence in a highly aligned environment, it is not only possible to determine the excited state rotational relaxation times of a fluorescence probe but also the ground state order parameters $\langle \alpha_{20}^{gs}(ss) \rangle$ and $\langle \alpha_{40}^{gs}(ss) \rangle$ [9] (Appendix I). However symmetry constraints limit the sensitivity of single-photon emission to the K=2 alignment moments of an excited state configuration, irrespective of its overall orientational distribution [3, 8]. The direct measurement of higher ground state alignment moments (K=6) is only possible if the interaction of the electric field with the aligned molecular population is defined by a higher order interaction such as two-photon excitation. To this end Monge and Armoogum [2, 18] have combined both single and two-photon fluorescence anisotropy measurements to determine the previously concealed (K=6) moments of the ground state probe distribution function.

Studies by Monge [2] were extended to the isotropic phase of n-cyanobiphenyls where bi-exponential fluorescence anisotropy decays were recovered showing evidence of fast intra-domain relaxation (τ_f) within a more slowly relaxing pseudo-domain structure (τ_s) (details of which are shown in Chapter 2). This structure is evident across much of the isotropic phase. It is only at high temperatures (up to 50^0C above the nematic-isotropic phase transition temperature T_{NI}) where mono-exponential fluorescence anisotropy decays are apparent reflecting behaviour indicative of a globally isotropic environment. The presence of a pseudo-domain structure was revealed for all the cyanobiphenyls studied. Furthermore, the inter- and intra- domain probe relaxation times show a temperature dependence which was in good agreement with the predictions of theory developed on the dynamics of liquid crystals [2].

1.5 Time Resolved Two-Photon Excited Fluorescence

Two-photon absorption is a non linear optical process which provides a variety of new capabilities in various scientific fields. The first quantum calculations were performed by Maria Goppert-Mayer in 1931, who predicted that a molecule could absorb two-photons simultaneously in the same quantum event [19]. The probability of two-photon excitation is sensitive to different molecular and ensemble parameters than single photon. As well as a quadratic dependence on the intensity of the exciting laser light, its temporal properties are also important [7]. The transition also can not be characterized by a single absorption dipole moment, the orientational dependence of the transition probability is instead described by the transition tensor [20]. (These differences are discussed in greater detail in Chapter 4).

Due to these inherent differences compared to single photon absorption two-photon excited fluorescence is strongly dependent on the focal properties of the excitation source. Two-photon absorption is maximised in the Rayleigh region of a focused Gaussian beam [4]. This inherent depth resolution has made two-photon fluorescence a highly useful tool in the life sciences especially in fluorescence microscopy [21]. As a result there has been considerable effort in recent years to produce fluorophores with high two-photon absorption cross-sections and optimised fluorescence yields [22]. In this respect the work of Blanchard-Desce and co-workers at the CNRS Institute, Rennes has been particularly successful and involves the design and synthesis of an extensive series of quadrupolar and octupolar push-push (electron donating) and push-push (electron withdrawing) polyenes [22, 23, 24, 25].

1.6 Stimulated Emission Depletion (STED)

The technique of far-field fluorescence light microscopy has been plagued by the diffraction resolution limit, the fundamental limit below which it is impossible to distinguish between two objects. The research of Ernst Abbe put a minimum limit on the distance over which it is possible to distinguish between two objects using light microscopy as approximately $1/3\lambda$ where λ is the wavelength of light [26]. This intrinsic property of far field microscopy has been found to be particularly restraining in the case

of fluorescence imaging of biological specimens such as live cells. However recent research has shown that these limits can be overcome by combining fluorescence microscopy with stimulated emission depletion (STED) [27] the principle of which is outlined as follows (a detailed explanation is given in Chapter 5). For single-photon stimulated emission depletion the excitation or 'pump' pulse is focused into the sample, producing an excited state population which is manifest by an ordinary diffraction limited spot. The 'pump' pulse is followed by a time-delayed, red-shifted depletion or 'dump' pulse. By spatially displacing the 'pump' and 'dump' pulses, it is possible to form an intense, localized fluorescent region in the sample. The volume from which spontaneous emission then follows is effectively restricted and with appropriate spatial and temporal shaping of the 'dump' pulse, the fluorescent spot can be progressively narrowed down, theoretically without limit so breaking the fundamental diffraction barrier. Although STED microscopy to date has been limited to single-photon excited states, the engineering and development of chromophores optimised for two-photon absorption which have proven STED capabilities, coupled with advancements in precision imaging may provide improved optical microscopy techniques and enhanced biological imaging.

Further advances in stimulated emission depletion techniques have recently been demonstrated by Armoogum et al who have developed a new approach to time resolved fluorescence spectroscopy based on stimulated emission depletion of two-photon excited states [18, 28]. In combining streak camera measurements of excited state population depletion and two-photon fluorescence anisotropy measurements, the stimulated emission cross section and the ground state vibrational relaxation time has been measured in the fluorescent dye probes rhodamine 6G and fluorescein. The studies have been further extended to incorporate high two-photon absorption cross section push-push polyenes [29] and enhanced green fluorescent protein (EGFP) [30]. STED has also been used as a way of probing higher order excited state moments $\langle \alpha_{40}^{ex} \rangle$ [18] whereby the normal electric dipole selection rules which restrict the amount of information available in conventional single-photon fluorescence spectroscopy are circumvented allowing access to previously 'hidden' information on molecular structure, dynamics and geometry.

1.7 Chapters Overview

Time resolved photoselection techniques rely on the fluorescent properties of well characterised fluorophores to study the local environment of molecular systems. As a consequence of the strong influence of the host medium, fluorescent probes that have readily interpretable photophysical properties can be specifically inserted into ordered environments to reveal facets of their structure and dynamics. Experiments detailed within Chapter 2 and Chapter 3 have been carried out using such time resolved photoselection techniques, to measure the molecular order and molecular dynamics of the nematic liquid crystal 4-n-pentyl-4'-cyanobiphenyl (5CB) whilst doped with the coumarin fluorescent dye probe derivatives Coumarin 6 and Coumarin 153. Previous work in the group has concentrated on the behaviour of four common Xanthene dyes in 5CB: Rhodamine B, Rhodamine 6G, Oxazine 4 and Oxazine 1. Although Coumarin 6 shows similar characteristics and is well described by conventional models, Coumarin 153 in contrast exhibits substantial solvatochromic effects.

Studies have been carried out to investigate the structural and photophysical properties of several quadrupolar and octupolar chromophores in the solvent toluene. The wavelength dependence of the two-photon absorption cross-section of several quadrupolar and octupolar push-push polyenes has been investigated. These measurements have been combined with wavelength dependent two-photon fluorescence anisotropy measurements yielding information on the structure of the two-photon transition tensor. These detailed investigations are outlined in Chapter 4. Furthermore, by combining anisotropy measurements with stimulated emission depletion measurements the stimulated emission cross-section and ground state vibrational relaxation time for a branched octupolar derivative (OM77) has been determined. This study is detailed in Chapter 5.

References

[1] Bernard Valeur *"Molecular Fluorescence; Principles and Applications"* Second Reprint, Wiley-VCH (2005)

[2] E M Monge, Ph. D. Thesis, University College London (2003)

[3] A J Bain and A.J. McCaffery, J. Chem. Phys., **83**, 2627 (1985)

[4] B Larijani and A J Bain, *"Biological Applications of Single and Two-Photon Fluorescence"* in *"Biological Chemistry"* Eds B Larijani, C A Rosser and R Woscholski, Wiley London (2006)

[5] J R Lakowicz, *"Principles of Fluorescence Spectroscopy"* Second Edition, Kluwer Academic (1999)

[6] I B Berlmann, *"Handbook of Fluorescence Spectra of Aromatic Molecules"* Second Edition, Academic Press, NewYork (1971)

[7] G R Fleming, *"Chemical Applications of Ultrafast Spectroscopy"* Clarendon (1986)

[8] A J Bain, P Chandna and J Bryant, J. Chem. Phys., **112**, 10418 (2000)

[9] D L Andrews and A A Demidov (Ed.) *"An Introduction to Laser Spectroscopy"* Second Edition, Kluwer (2002)

[10] J Bryant, Ph. D. Thesis, University of Essex, (2000)

[11] N Chadborn, J Bryant, A.J.Bain and P. O'Shea, Biophysical J., **76**, 2198 (1999)

[12] A J Bain, P Chandna, G Butcher and J Bryant, J. Chem. Phys., **112**, 10435 (2000)

[13] W R Thomkins, M S Malcut, R W Boyd and J E Sipe, J. Opt. Soc. Am., **6**, 757 (1990)

[14] D L Andrews and D Juzelinas, J. Chem. Phys., **95,** 5513 (1995)

[15] P A Anfinrud, D E Hart and W S Struve, J. Phys. Chem., **92,** 4067 (1988)

[16] H J Loesch, E Stenzel and B Wustenecker, J. Phys. Chem., **95,** 3841 (1991)

[17] J Yguerabide and L Stryer, Proc. Nat. Acad. Sci. **68,** 1217 (1971)

[18] D A Armoogum, Ph. D. Thesis, University College London (2004)

[19] C Xu and W W Webb, J. Opt. Soc. Am. B., **3**, 481 (1996)

[20] P N Butcher and D Cotter, *"The Elements of Nonlinear Optics"* Cambridge University Press, Cambridge (1998)

[21] W Denk, J H Strickler and W W Webb, Science., **248**, 73 (1990)

[22] F Terenziani, C Le Droumaguet, C Katan, O Mongin, M H V Werts, S Tretiak and M Blanchard-Desche. SPIE-Int. Soc. Opt. Eng., **5935** (2005)

[23] C Katan, F Terenziani, O Mongin, M H V Werts, L.Porres, T Pons, J Mertz, S Tretiak and M Blanchard-Desche, J. Chem. Phys. A., **109**, (2005)

[24] C Katan, F Terenziani, O Mongin, M H V Werts, C Le Droumaguet, L Porres, T Pons, J Mertz, S Tretiak and M Blanchard-Desche, J. Phys. Chem. A., **109**, 13, (2005)

[25] L Porres, C Katan, O Mongin, T Pons, J Mertz and M Blanchard-Desche, J. Mol. Struct., **704**, (2004)

[26] R Kopelman and W Tan, Science., **262,** 1382 (1993)

[27] O Mongin, L Porres, M Charlot, C Katan and M Blanchard-Desche. Chem. Eur. J., **13** (2007)

[28] R J Marsh, D A Armoogum and A J Bain, Chem. Phys. Lett., **366**, 398 (2002)

[29] R J Marsh, N D Leonczek, D A Armoogum, O Mongin, L Porres, M Blanchard-Desche and A J Bain, SPIE-Int. Soc. Opt. Eng., **5510** (2004)

[30] T Masters, D A Armoogum, R J Marsh and A J Bain, *to be published*

Chapter 2

Studies in the Nematic and Isotropic Phase of 5-Cyanobiphenyl Part I: Coumarin 6

2.1 Introduction

In the next two chapters short picosecond pulsed photoselection and time resolved fluorescence polarisation and intensity measurements are used to investigate the behaviour of two coumarin probes in the isotropic and nematic phases of 5-cyanobiphenyl (5CB). Previous work in the group has concentrated on the alignment and rotational dynamics of ionic fluorescent probes such as Rhodamine 6G, Rhodamine B, Oxazine 1 and Oxazine 4 [1, 2]. Coumarin dyes, whilst polar, are non-ionic and hydrophobic in nature; consequently the nature of their positioning into a cyanobiphenyl host should be substantially different to that of an ionic fluorophore with a greater propensity to association with the alkyl tail environment of the 5CB molecules. Coumarin 6 (C6) and Coumarin 153 (C153) whilst possessing the same fluorescent core differ substantially both in shape and excited state properties. Both probes have significant ground state dipole moments (7D for C6 and 6.68D for C153 [3]). However, in contrast to Coumarin 6, on excitation to the S_1 state C153 experiences a substantial increase in dipole moment of c.a. 90% (see table 2.0). In non-ordered solvents this leads to a time-dependent Stokes shift due to reorganisation of the solvent in reaction to the new excited state dipole moment. Such effects are well understood in C153 which has been the subject of numerous experimental and theoretical studies over recent years [4-10]. However, solvation dynamics in an ordered environment have until now not been studied experimentally.

Substantial solvent-solute reorganisation in an ordered system presents a number of experimental challenges and the use of fluorescence anisotropy measurements may be compromised. For this reason the experimental studies and analysis of Coumarin 6 and Coumarin 153 fluorescence data are substantially different. Coumarin 6 undergoes a much smaller increase in dipole moment (c.a. 1D) and can be treated in an analogous manner to experiments using non-strongly solvating ionic dyes (Rhodamine 6G,

Rhodamine B, Oxazine 1 and Oxazine 4). Experiments on Coumarin 6 are covered in this chapter and a modified procedure involving global analysis of polarised intensity decays for Coumarin 153 are covered in Chapter 3.

2.2 Fluorescence Probes

Time resolved photoselection techniques rely on the fluorescent properties of well characterised fluorophores to study the local environment of molecular systems. As a consequence of the strong influence of the host medium, fluorescent probes that have readily interpretable photophysical properties can be specifically inserted into ordered isotropic environments to reveal facets of their structure and dynamics. It is therefore desirable to investigate molecular systems with a variety of fluorescent probes characterized by different photophysical properties. The properties of a system can be measured directly if naturally occurring fluorescent species exist within the system; however such intrinsic fluorescent probes are limited. Some of the few existing examples are green fluorescent protein, tryptophan and tyrosine. Where the molecule is non-fluorescing or has low quantum yield then extrinsic probes such as rhodamine and oxazine are attached to the media and their properties are measured indirectly.

2.2.1 Coumarin

The role of coumarin fluorescent dyes in spectroscopy had traditionally been limited to laser dye applications; however with the rapid rise in the use of solid-state laser technology coumarin derivatives are now increasingly utilised as fluorescence probes. Coumarins are formed by fusing benzene with an auxochromic non-fluorescing α-pyrone [11], and although they are themselves poor emitters with low quantum yield, appropriate substitution can form fluorescent compounds which emit in the blue-green region of the visible spectrum. The two coumarin derivatives employed in this thesis are the 7-aminocoumarins Coumarin 6 and Coumarin 153. The fluorescence yield for 7-aminocoumarins depends on the pattern of substitution of the amine function [12]. The molecular structure of the parent chromophore along with the derivatives is shown in figure 2.0. Coumarin 6 is formed with substitution of position 7 by the delocalising substituent group $N(H_5C_2)_2$ and substitution of position 3 with the electron donating benzothiazol group. Coumarin 153 is formed with substitution of position 4 by the

electron-withdrawing group CF_3 whilst the main amine function is coupled with a quinoline group. The molecular structure of the parent chromophore along with the derivatives is shown in figure 2.0.

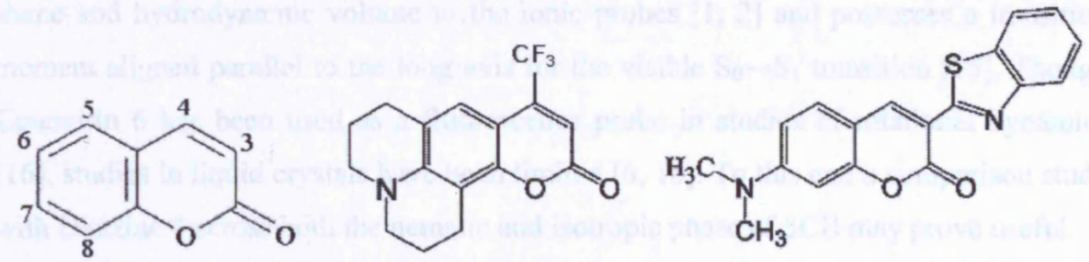

Figure 2.0: Molecular structure of the parent chromophore coumarin, and the derivatives Coumarin 153 and Coumarin 6.

The absorption and emission spectra of Coumarin 6 and Coumarin 153 are characterised by a relatively broad featureless structure with a Stokes shift of approximately 50nm and 100nm respectively, this is shown in figure 2.1.

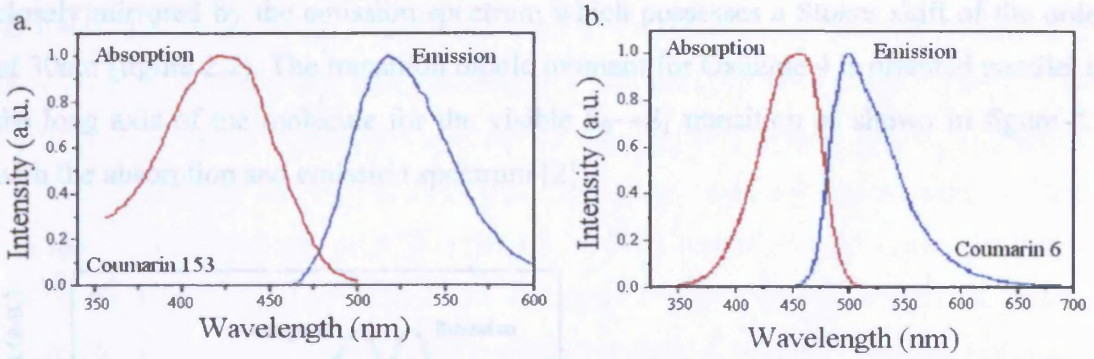

Figure 2.1: Normalised steady state absorption and emission spectra of (a) Coumarin 153 in DMF (Original data from W C Flory & G J Blanchard, Applied Spectroscopy 52(1), 82 (1998) and (b) Coumarin 6 in ethanol [13]

2.2.2 Coumarin 6

Coumarin 6 was chosen as a fluorescence probe to investigate the nematic and isotropic phases of the liquid crystal 4-n-pentyl-4'-cyanobiphenyl (5CB) and the isotropic liquid ethylene glycol for a number of reasons. It possesses strong single-photon absorption cross-sections and high fluorescence quantum yields at room temperature (0.9 in cyclohexane [14]) and absorbs well in the blue region of the visible spectrum, wavelengths which are accessed via readily available laser sources. The photophysical

behaviour of Coumarin 6 is highly receptive to the polarity and viscosity of the solvent host [14] which makes it a good candidate for fluorescence experiments requiring low concentration molecular probes. Though spectrally different, Coumarin 6 is of similar shape and hydrodynamic volume to the ionic probes [1, 2] and possesses a transition moment aligned parallel to the long axis for the visible $S_0 \rightarrow S_1$ transition [15]. Though Coumarin 6 has been used as a fluorescence probe in studies of rotational dynamics [16], studies in liquid crystals have been limited [6, 16]. To this end a comparison study with Oxazine 4 across both the nematic and isotropic phase of 5CB may prove useful.

2.2.3 Oxazine 4

Work by Bryant, Monge et al [1, 2] on order and motion in the cyanobiphenyls, demonstrated that of the ionic probes, Oxazine 4 is the most accurate probe of 5CB order and correlates well with the local ordering of 5CB in the nematic phase. As such Oxazine 4 has been chosen as the probe molecule best suited for comparison with Coumarin 6. Oxazine 4 is a planar, rigid molecule and behaves as single axis prolate rotational diffuser [2]. The long wavelength absorption spectrum for Oxazine 4 is closely mirrored by the emission spectrum which possesses a Stokes shift of the order of 30nm (figure 2.2). The transition dipole moment for Oxazine 4 is oriented parallel to the long axis of the molecule for the visible $S_0 \rightarrow S_1$ transition as shown in figure 2.2 with the absorption and emission spectrum [2].

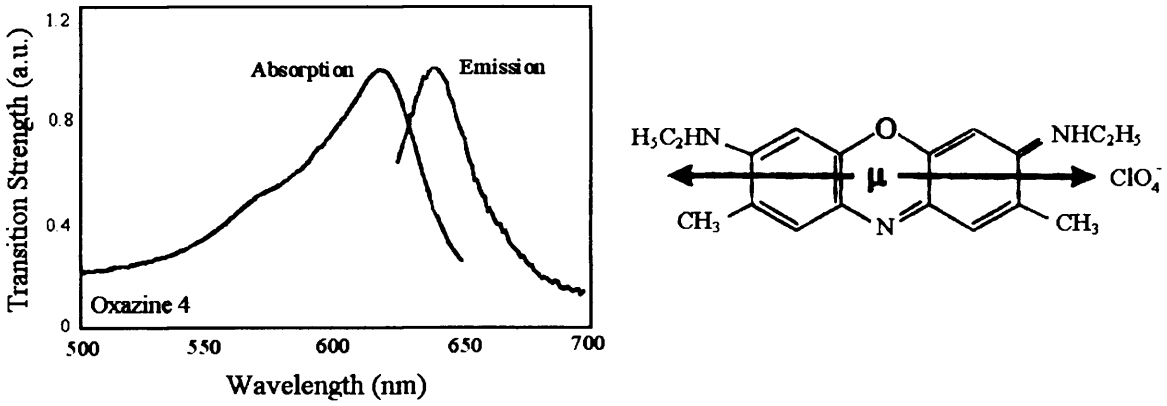

Figure 2.2: The absorption and emission spectra of Oxazine 4. The molecular structure and transition dipole moment direction are also shown.

Property	Oxazine 4
Composition	$C_{18}H_{22}N_3O_5Cl$
Quantum Yield	0.63
Absorption Maximum	615nm
Emission Maximum	649nm
Molar Absorptivity (L mol^{-1} cm^{-1})	$10.9x10^4$
Molecular Weight (g/mol)	395.84
Hydrodynamic Volume	313Å$^{3[2]}$

Table 2.1: A summary of the basic photophysical properties of Oxazine 4[a].

[a]: Absorption and emission measurements are in ethanol

2.3 Liquid Crystals

Ordered environments are found throughout nature and the presence of order has a profound effect on the intrinsic properties and behaviour of a system. The optical and photophysical behaviour, the chemical reactivity and the molecular dynamics of a system [1] all depend on the degree of order. In biological systems membranes contain highly organized molecular assemblies that mediate important processes such as energy transduction, active transport, nerve impulse conduction, sensory reception, and hormonal integration [17]. In the ordered environment of liquid crystals the ability for the molecules to respond to external electric fields has generated industrial applications in the form of liquid crystal displays, optical imaging and recording [18]. The probing of molecular order to obtain structural, functional and dynamical information is therefore of considerable scientific interest and the use of optical processes such as Raman Scattering [1], laser induced fluorescence [19] and, more recently, time resolved photoselection techniques [20], have applied to studies of ordered molecular systems.

Liquid crystals are an intermediate state of matter with characteristics that fall between that of a crystalline solid and isotropic liquid. The diffusion properties and flow behaviour of liquid crystals are similar to those of an ordinary liquid, however, some orientational and or positional order of the order of a few molecular lengths is maintained [21]. This produces anisotropic behaviour which can be measured in the optical, electromagnetic and elastic properties of the system [2]. Liquid crystals possess mesophases (mesomorphic phases) and can be classified according to the mechanisms that drive their self organization [22]. The ability for molecules to form liquid crystal phases depends upon a number of factors the most important of which is the degree of geometric anisotropy in the shape of the molecule [23].

The liquid crystal may pass through several mesophases before transformation to the isotropic state. They are generally composed of rod-like molecules and are broadly classified as nematic, smectic or cholesteric depending on the difference in the degree of orientational and/or positional ordering of the constituent molecules as shown in figure 2.3.

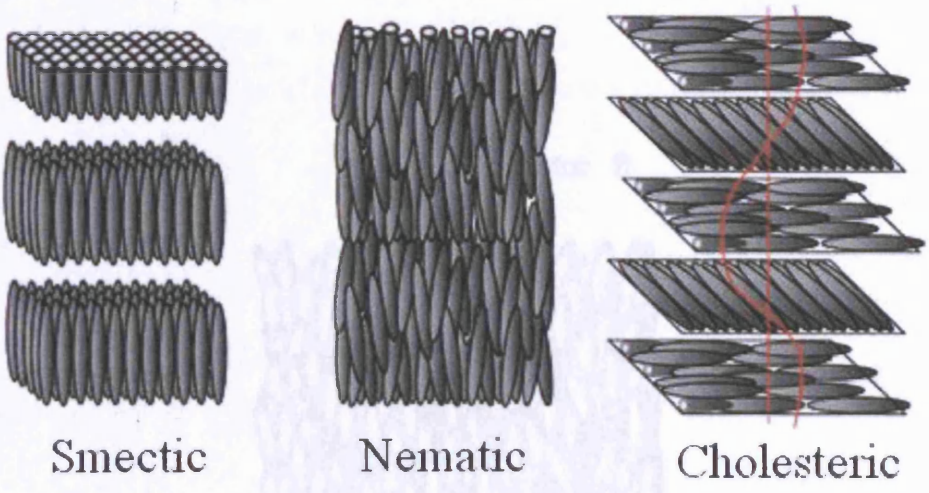

Figure 2.3: Illustration of the positional and orientational ordering in the nematic, smectic and cholesteric liquid crystal phases. The nematic state is characterised by molecules that have no positional order but tend to point in the same direction along the nematic director ñ. In the smectic state, the molecules maintain the general orientational order of nematics, but also tend to align themselves in layers or planes. The cholesteric liquid crystal phase is typically composed of nematic mesogenic molecules containing a chiral center which produces intermolecular forces that favour alignment between molecules at a slight angle to each other.

Thermotropic liquid crystals are characterised by thermally induced phase transitions and the intermediate states develop only as a result of thermal processes. Lyotropic liquid crystals are defined by phase transitions induced by changes in solvent concentration and temperature. These molecules are essentially surfactants made up of two distinct parts, a tail which is essentially hydrophobic and a head which is hydrophilic. Lyotropic molecules are able to form ordered structures in both polar and non polar solvents. Common examples of lyotropic liquid crystals are soap and phospholipids [22].

The simplest of all the mesophases is the nematic phase. The nematic phase is characterised by a high degree of long-range orientational order with no long range

translational order of the constituent molecules, as shown in figure 2.4. Nematic order is determined primarily by molecular shape, nematogenic molecules are calamitic in that they are essentially elongated structures with a long axis significantly greater than the short axis. This gives rise to a preferential alignment of the long axis parallel to some common axis or director defined by the unit vector **n̂.** The elongated shape of a nematogen is maintained by a degree of rigidity in the core.

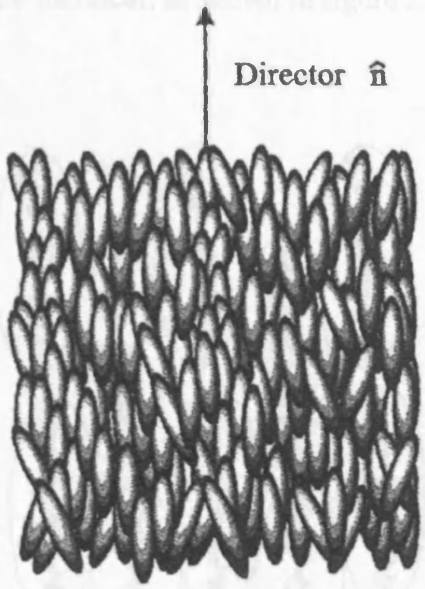

Figure 2.4: Schematic structure of the nematic phase. The orientation of the individual molecules is correlated, but no positional correlation to the nematic director n̂ exists.

There is a general structural template which determines the morphology of calamitic mesogens. This template usually takes the form of two core units A and B sometimes bridged by a linking group Y as shown in figure 2.5. The linearly linked group provides the rigidity necessary to produce anisotropic molecular structures. The terminal groups R and R' are generally alkyl [24] or alkoxy chains with one terminal end a small polar substituent [25] (CN, F, NCS, NO_2). The end groups ensure that the structure has the degree of flexibility necessary to provide low melting points and stabilisation of the molecular alignment in the mesophases. The end groups can either be linked directly to the core or via the groups X and Z. Finally the lateral substituents M and N are used to modify the morphology of the mesophases depending on the properties of the liquid crystal required for a particular application.

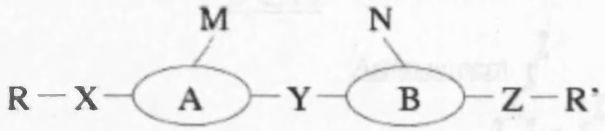

Figure 2.5: General structural template for calamitic mesogens.

In addition nematic mesophases are centrosymmetric, having equivalent numbers of molecules aligned parallel as anti parallel to the nematic director, hence the states of the nematic director **n** and **–n** are identical, as shown in figure 2.6.

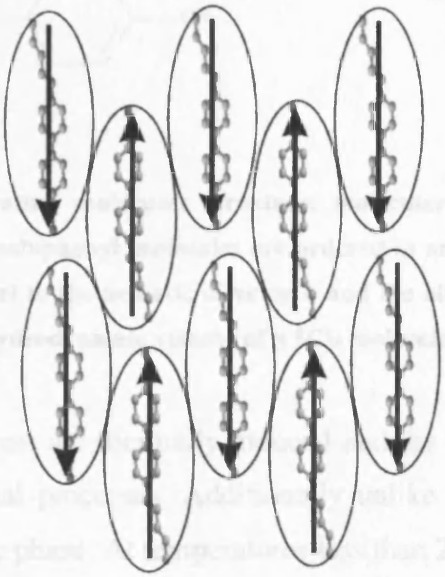

Figure 2.6: Molecules which possess a permanent dipole moment and form a nematic liquid crystal have equal numbers of dipole moments oriented parallel as anti-parallel relative to the nematic director ñ. The polar nematic liquid crystal molecules of the compound 4-n-pentyl-4'-cyanobiphenyl are represented inside the ellipsoid.

2.3.1 4-n-pentyl-4'-cyanobiphenyl: 5CB

The liquid crystal host material used in this thesis is the polar nematic liquid crystal 4-n-pentyl-4'-cyanobiphenyl (5CB). 5CB belongs to a class of liquid crystals known as cyanobiphenyls and exhibits a nematic liquid crystal mesophase. 5CB molecules are uniaxial and calamitic. The elongated shape is maintained by a degree of rigidity in the core of the molecule which enables the molecule to produce interactions which favour alignment. Figure 2.7 illustrates the packing order and structure of 5CB.

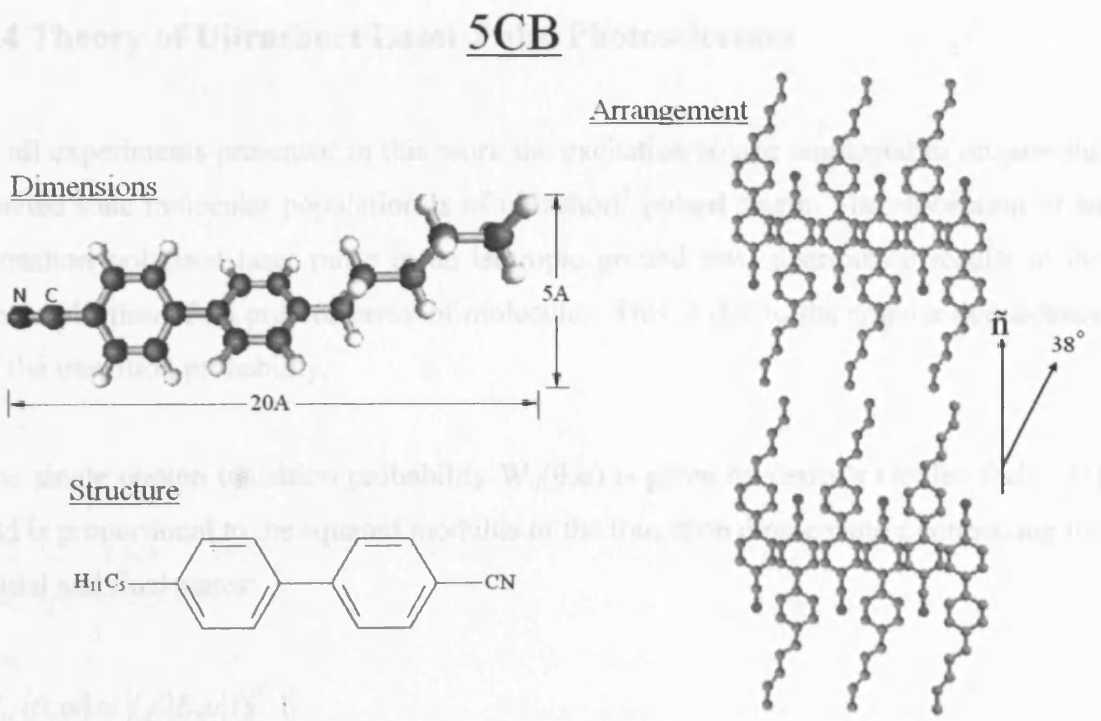

Figure 2.7: Diagram illustrating molecular structure, molecular arrangement and molecular dimensions of 5CB. The cyanobiphenyl molecules are ordered in an anti-parallel fashion with the cyano groups aligning parallel to the nematic director ñ and the alkyl groups making an angle of c.a. 38° to the director. The hydrodynamic volume of a 5CB molecule is c.a. 264Å^3 [26].

In 5CB the phase transitions are thermally induced and the intermediate states develop only as a result of thermal processes. Additionally unlike other cyanobiphenyls 5CB does not possess a smectic phase. At temperatures less than 24°C, 5CB is in a crystalline state. At 24°C the liquid crystal undergoes a crystalline-nematic phase transition and remains in the nematic state up to 35.3°C [26]. At this temperature the liquid crystal undergoes a second phase transition and becomes isotropic.

2.4 Theory of Ultrashort Laser Pulse Photoselection

In all experiments presented in this work the excitation source employed to prepare the excited state molecular population is of ultrashort† pulsed origin. The absorption of an ultrashort polarised laser pulse in an isotropic ground state distribution results in the photoselection of an ordered array of molecules. This is due to the angular dependence of the transition probability.

The single photon transition probability $W_{if}(\theta,\varphi)$ is given by Fermi's Golden Rule [27] and is proportional to the squared modulus of the transition dipole matrix connecting the initial and final states:

$$W_{if}(\theta,\varphi) \propto \left|\langle f|E.\mu|i\rangle\right|^2$$

$$\propto \left|\mu_{if}\right|^2 I^2 \cos^2\theta \qquad [2.0]$$

Here μ_{if} is the instantaneous transition dipole moment between i and f and I is the incident laser irradiance, θ defines the angle between the polarisation vector of the incident laser pulse and the transition dipole moment direction as shown in figure 2.8.

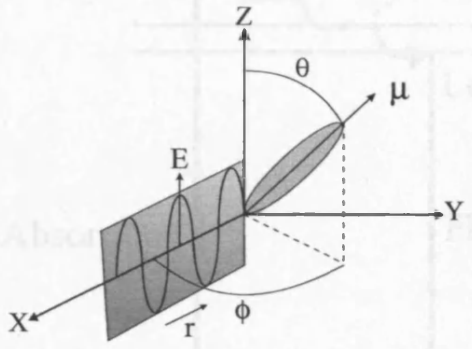

Figure 2.8: The polar coordinate system defines the direction of propagation of the incident electromagnetic radiation r, the plane of polarisation and the amplitude of the electric field E.

†*Ultrashort in this case means a pulse very much shorter than the lifetime of the excited state.*

If only a small fraction of the isotropic ground state population is removed, the excited state population distribution is given by

$$N_{ex}(\theta,\varphi) = N_{gs} W_{if}(\theta,\varphi) \qquad [2.1]$$

For Z-polarised excitation this becomes

$$N_{ex}(\theta,\varphi) \propto N_{gs} \cos^2 \theta \qquad [2.2]$$

All the molecular probes used in this thesis are four level systems as outlined in figure 2.9. Initial excitation takes place from the lower molecular ground state vibrational levels (level 1) to a vibrationally excited but rapidly deactivating population in the excited state (level 2). This population relaxes by the mechanism of internal conversion to a thermally equilibriated excited state (level 3) and emits to higher vibration levels in the ground state (level 4), which quickly relax via the internal conversion process, quickly reaching thermal equilibrium (level 1).

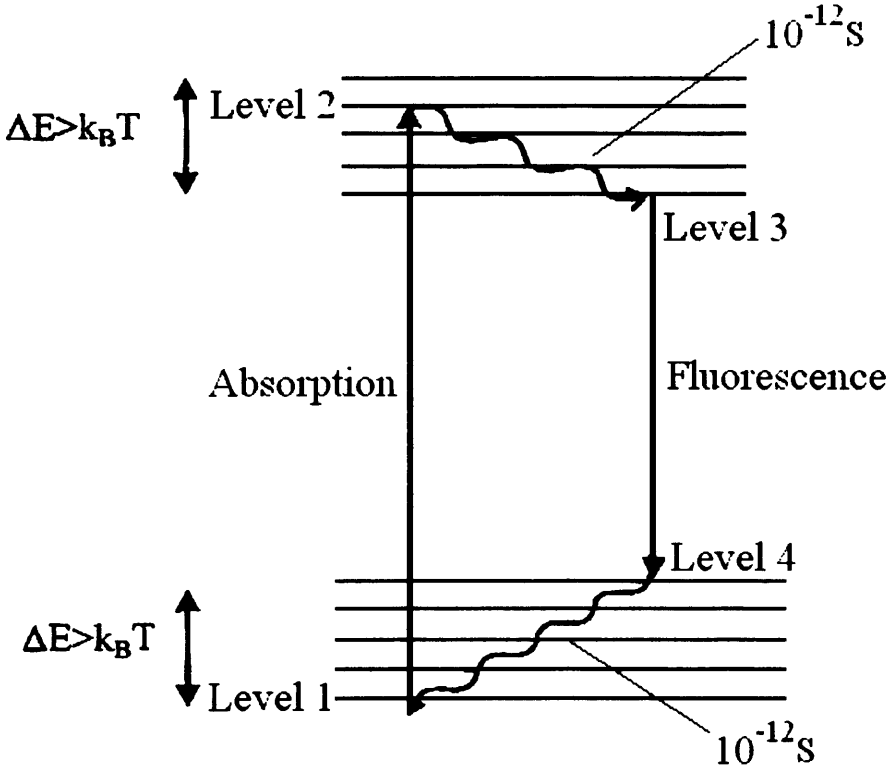

Figure 2.9: The basic four level excitation-emission cycle of the molecular probes used in this work.

Assuming that the rate of transfer from level 1 to level 2 is very fast, the change in population of level 3 can be given in the form of a rate equation as

$$\frac{dN_3}{dt} = \frac{\sigma I(t)}{h\nu} N_1 - N_3 \gamma_{34} \qquad [2.3]$$

where σ is the single photon absorption cross-section (cm^2) and γ_{34} is the spontaneous emission from the low lying vibrational levels in S_1 (level 3) to the high lying ground state vibrational levels in S_0 (level 4). As the excitation is weak ($N_3 << N_1$) and the pulse duration is ultrashort, then integrating over I(t) gives

$$N_3 = \frac{\sigma N_1}{h\nu} \int I(t) dt \qquad \left[\left(= \frac{\sigma}{h\nu A} \int \frac{dE_P(t)}{dt} dt \right) \right] \qquad [2.4]$$

$$= \frac{\sigma E_P N_1}{h\nu A} = S N_1 \qquad [2.5]$$

where E_P is the laser pulse energy and A is the area of illumination. Equation 2.5 defines the transition probability for single photon absorption, also known as the transition saturation parameter S where in the weak excitation limit $S << 1$. For experiments undertaken in Chapter 2 and Chapter 3 for typical excitation pulse parameters of $\sigma \approx 10^{-}16 cm^{-2}$, $E_p \approx 1.6 \times 10^{-14} J$, $h \approx 6.6 \times 10^{-34}$, $\nu \approx 5 \times 10^{14} s^{-1}$ and $A \approx 10^{-5} cm^{-2}$, the saturation parameter was found to be

$$S = \frac{\sigma E_P}{h\nu A} \approx \frac{1x6}{33} \left(\frac{10^{-16} x 10^{-14}}{10^{-34} x 10^{14} x 10^{-5}} \right) \approx 5x10^{-6}$$

Given that the ground state orientational distribution function is isotropic such that $P^{GS}(\theta,\varphi)$ is independent of θ and φ (Appendix I) and excitation is in the weak regime then the excited state orientational distribution function directly follows the form of the transition probability $W_{if}(\theta,\varphi)$ stated in equation 2.0. Expressing $\cos^2\theta$ in terms of spherical harmonics gives

$$\cos^2\theta = \frac{\sqrt{4\pi}}{3} \left[Y_{00}(\theta,\varphi) + \frac{2}{\sqrt{5}} Y_{20}(\theta,\varphi) \right] \qquad [2.6]$$

In the limit of weak excitation the photoselected excited state population N_{ex} is given by

$$N_{ex}(\theta,\varphi) = N_{gs} P_{ex}(\theta,\varphi) \qquad [2.7]$$

The orientational distribution function $P(\theta,\varphi)$ in terms of a spherical harmonic expansion is given by (Appendix1)

$$P(\theta,\varphi) = \Sigma_{KQ} \langle C_{KQ} \rangle Y_{KQ}(\theta,\varphi) \qquad [2.8]$$

Substituting equations 2.6 and 2.7 into equation 2.8 and equation 2.2 yields for $P_{ex}(\theta,\varphi)$ and $N_{ex}(\theta,\varphi)$:

$$P_{ex}(\theta,\varphi) = C\frac{\sqrt{4\pi}}{3}\left[Y_{00}(\theta,\varphi) + \frac{2}{\sqrt{5}} Y_{20}(\theta,\varphi)\right] \qquad [2.9]$$

$$N_{ex}(\theta,\varphi) = CN_{ex}\frac{\sqrt{4\pi}}{3}\left[Y_{00}(\theta,\varphi) + \frac{2}{\sqrt{5}} Y_{20}(\theta,\varphi)\right] \qquad [2.10]$$

where C is a constant of proportionality. Integrating over all angular coordinates and normalising to unity yields the total excited state population as

$$N_{ex} = C\frac{\sqrt{4\pi}}{3}\int_0^{2\pi}\int_0^{\pi}\left[Y_{00}(\theta,\varphi) + \frac{2}{\sqrt{5}} Y_{20}(\theta,\varphi)\right]\sin\theta d\theta d\varphi \qquad [2.11]$$

therefore

$$C = \frac{3}{4\pi} N_{ex} \qquad [2.12]$$

and

$$P_{ex}(\theta,\varphi) = \frac{1}{\sqrt{4\pi}}\left[Y_{00}(\theta,\varphi) + \frac{2}{\sqrt{5}} Y_{20}(\theta,\varphi)\right] \qquad [2.13]$$

The excited state orientational distribution function created from an isotropic ground state distribution is thus characterised by population ($Y_{00}(\theta,\varphi)$) and cylindrically symmetric alignment moments ($Y_{20}(\theta,\varphi)$).

2.5 Emission of Fluorescence: Anisotropy

In time-resolved fluorescence depolarisation experiments linearly polarized light is used to photoselect, via ultrashort pulsed excitation, an initially ordered excited state population. This population has an anisotropic distribution of absorption and emission transition dipole moments [1]. The orthogonally polarized emission components are then no longer equivalent. The depolarisation function, the fluorescence anisotropy, is defined in terms of two experimental quantities, these are the time dependent fluorescent intensities polarised parallel ($I_{\parallel}$) and perpendicular ($I_{\perp}$) to the excitation polarisation direction. The detection of the two orthogonally polarized emission intensities are used to construct the fluorescence anisotropy as follows

$$R(t)=\frac{I_{\parallel}(t)-I_{\perp}(t)}{I_{\parallel}(t)+2I_{\perp}(t)} \qquad [2.14]$$

The observation of fluorescence emission in conventional fluorescence experiments is made using right-angled excitation-detection geometry, where the polarisation vector of the excitation beam determines the z-axis, figure 2.10a. As the excitation process is cylindrically symmetric about the z-axis, wholly equivalent information can also be obtained by adopting a collinear excitation-detection geometry where the fluorescence linearly polarised parallel and perpendicular to the excitation polarisation direction corresponds to the Z(||) and X(⊥) directions respectively as shown in figure 2.10b. Throughout chapters two and three a collinear excitation-detection geometry was employed with the aim of making measurements in a thin sample

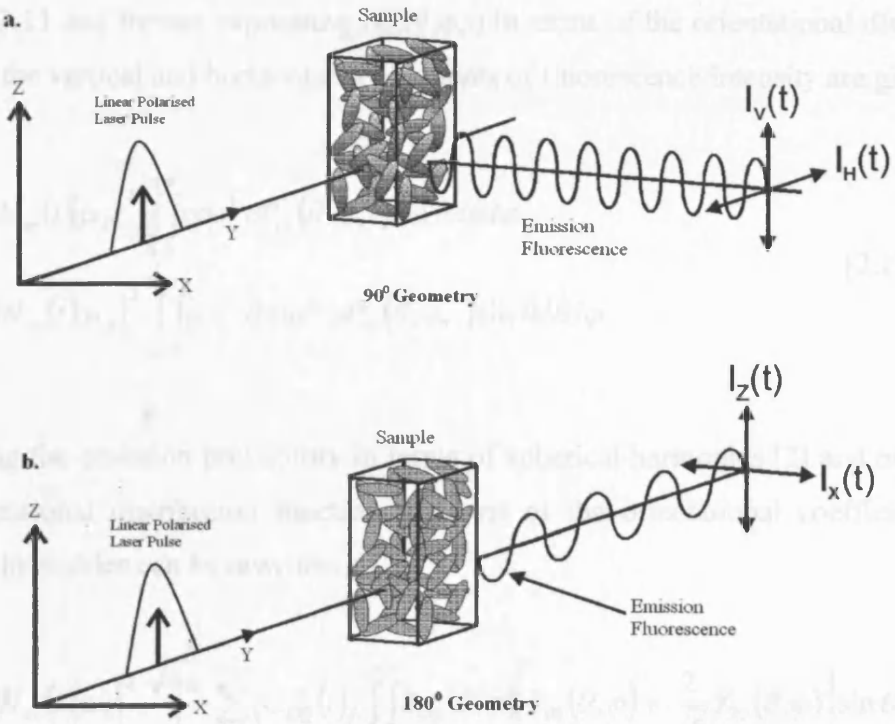

Figure 2.10: Geometries for the experimental measurement of fluorescence anisotropy in isotropic or cylindrically symmetric environments. (a) The conventional geometry where the orthogonal components are collected at 90^0 to the excitation direction. (b) The 180^0 geometry where fluorescence is collected collinear to the excitation direction.

In the laboratory frame, the intensity of the linearly polarised emission fluorescence (defined by a linear polarisation vector, $\hat{e}_i$) of the $S_1 \rightarrow S_0$ transition is given by [4]

$$I_i(t) = B \int_0^{2\pi} \int_0^{\pi} \left| \langle f | \mu . \hat{e}_i | i \rangle \right|^2 N_{ex}(\theta, \varphi, t) \sin\theta d\theta d\varphi \qquad [2.15]$$

where B is a constant of proportionality, and the initial and final molecular states are defined by $|i\rangle$ and $|f\rangle$ respectively. For the vertical (Z) and horizontal (X) components of fluorescence, $\hat{e}_i$ is given by

$$\begin{aligned} \hat{e}_V &= \cos\theta \\ \hat{e}_H &= \sin\theta \sin\varphi \end{aligned} \qquad [2.16]$$

where θ and φ are polar coordinates defined in figure 2.8. Applying these expressions to equation 2.11 and further expressing $N_{ex}(\theta,\varphi,t)$ in terms of the orientational distribution function, the vertical and horizontal components of fluorescence intensity are given as

$$I_V(t) = BN_{ex}(t)\left|\mu_{fi}\right|^2 \int_0^{2\pi}\int_0^{\pi} \cos^2\theta P_{ex}(\theta,\varphi,t)\sin\theta d\theta d\varphi$$
$$I_H(t) = BN_{ex}(t)\left|\mu_{fi}\right|^2 \int_0^{2\pi}\int_0^{\pi} \sin^2\theta\sin^2\varphi P_{ex}(\theta,\varphi,t)\sin\theta d\theta d\varphi \qquad [2.17]$$

Expressing the emission probability in terms of spherical harmonics [2] and expanding the orientational distribution function in terms of the orientational coefficients, the emission intensities can be rewritten as

$$I_V(t) = BN_{ex}(t)\left|\mu_{fi}\right|^2 \frac{\sqrt{4\pi}}{3}\sum_{KQ}\left\langle C_{KQ}^{ex}(t)\right\rangle \int_0^{2\pi}\int_0^{\pi} Y_{KQ}(\theta,\varphi)\left[Y_{00}(\theta,\varphi)+\frac{2}{\sqrt{5}}Y_{20}(\theta,\varphi)\right]\sin\theta d\theta d\varphi$$

$$I_H(t) = BN_{ex}(t)\left|\mu_{fi}\right|^2 \frac{\sqrt{4\pi}}{3}\sum_{KQ}\left\langle C_{KQ}^{ex}(t)\right\rangle \int_0^{2\pi}\int_0^{\pi} Y_{KQ}(\theta,\varphi)\left[\begin{array}{l} Y_{00}(\theta,\varphi) \\ -\frac{1}{\sqrt{5}}Y_{20}(\theta,\varphi) \\ +\sqrt{\frac{3}{10}}\{Y_{22}(\theta,\varphi)+Y_{2-2}(\theta,\varphi)\}\end{array}\right]\sin\theta d\theta d\varphi \qquad [2.18]$$

The solution of these integrals yields [2]

$$I_V(t) = BN_{ex}(t)\left|\mu_{fi}\right|^2 \frac{\sqrt{4\pi}}{3}\left[\left\langle C_{00}^{ex}\right\rangle + \frac{2}{\sqrt{5}}\left\langle C_{20}^{ex}(t)\right\rangle\right] \qquad [2.19a]$$

$$I_H(t) = BN_{ex}(t)\left|\mu_{fi}\right|^2 \frac{\sqrt{4\pi}}{3}\left[\left\langle C_{00}^{ex}\right\rangle - \frac{1}{\sqrt{5}}\left\langle C_{20}^{ex}(t)\right\rangle + \sqrt{\frac{3}{10}}\left\{\left\langle C_{22}^{ex}(t)\right\rangle + \left\langle C_{2-2}^{ex}(t)\right\rangle\right\}\right] \qquad [2.19b]$$

The polarised components of the fluorescence intensity evolve according to the time invariant population term $\langle C_{00}^{ex} \rangle$ and the time dependent $\{\langle C_{22}^{ex}(t) + C_{2-2}^{ex}(t) \rangle\}$ and $\langle C_{20}^{ex}(t) \rangle$ moments. By normalising each moment to the population term and substituting the fluorescence intensity components into equation 2.12, the expression for the fluorescence anisotropy is given by,

$$R(t) = \frac{\frac{1}{\sqrt{5}}\langle \alpha_{20}^{ex}(t) \rangle - \frac{1}{\sqrt{30}}\{\langle \alpha_{22}^{ex}(t) \rangle + \langle \alpha_{2-2}^{ex}(t) \rangle\}}{1 + \frac{2}{\sqrt{30}}\{\langle \alpha_{22}^{ex}(t) \rangle + \langle \alpha_{2-2}^{ex}(t) \rangle\}} \qquad [2.20]$$

where $\langle \alpha_{KQ} \rangle = \frac{\langle C_{KQ} \rangle}{\langle C_{00} \rangle}$.

As can be seen from equation 2.20 and outlined in Chapter 1, the fluorescence anisotropy can be defined in terms of the orientational distribution of the photoselected excited state. This expression further shows that from a single photon photoselected excited state, the fluorescence anisotropy is sensitive only to the K=2 (alignment) moments of the population, and depends on a cylindrically symmetric moment (Q=0) and cylindrically asymmetric moment (Q=±2). The evolution of these moments is determined by the diffusive nature of molecular motion in the liquid phase. The non-equilibrium photoselected excited state order is dissipated due to randomising collisions with solvent molecules.

2.6 Variable Angle Photoselection in Anisotropic Media

In conventional time resolved fluorescence anisotropy experiments in isotropic environments, the laboratory z-axis is determined by the excitation polarisation vector of the excitation pulse and only cylindrically symmetric degrees of excited state alignment are created. Furthermore the cylindrical symmetry inherent within the excited state arrays means R(t) is invariant to any angular variation in the XY plane (φ rotation). It is possible however, to create cylindrically asymmetric excited state alignment by varying the excitation polarisation angle β with respect to the laboratory axis as defined

by the analysing polarisation geometry (see figure 2.11). In such an arrangement fluorescence observables are sensitive to θ and φ averaging in the laboratory frame- which in an isotropic system are wholly equivalent. However in an ordered environment θ and φ diffusion dynamics can be markedly different [20].

A collinear excitation-detection geometry is employed for all variable angle photoselection experiments carried out in this work. The polarisation vector is varied between 0^0 and 90^0 with respect to the laboratory fixed axis (Z_1) as shown in figure 2.11.

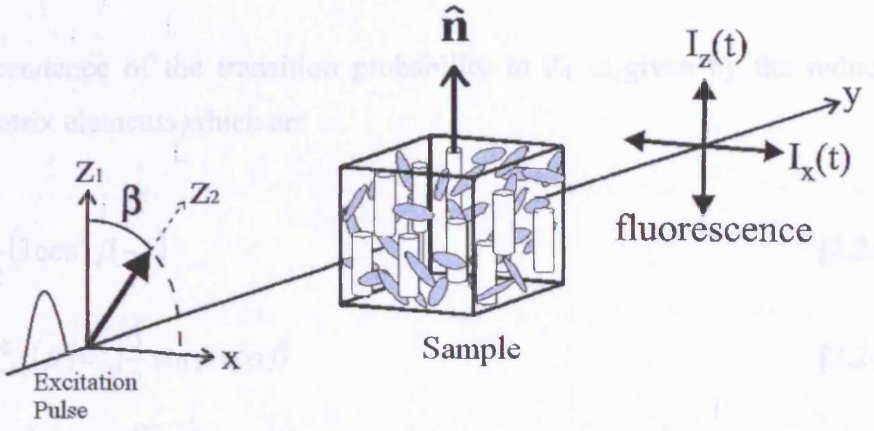

Figure 2.11: Variation of the excitation polarisation angle β with respect to the laboratory fixed axis (Z_1) which is aligned parallel to the nematic director ñ for the case of an aligned medium.

In the axis frame defined by the polarisation vector of the excitation pulse the angle dependent excitation probability is given by,

$$W(\theta',\varphi',t)_{Z_2} = BI(t)\left|\vec{\mu}_a\right|^2 \frac{\sqrt{4\pi}}{3}\left[Y_{00}(\theta',\varphi') + \frac{2}{\sqrt{5}}Y_{20}(\theta',\varphi')\right] \qquad [2.21]$$

where θ' and φ' are the polar angles defining the orientation of the absorption transition dipole moment μ_a in the reference frame that is defined by the excitation pulse polarisation vector (Z_2). The pulse intensity and B is a proportionality constant [9]. The initial polarisation of the excitation beam defines the laboratory frame (Z_1) and all measurements are collected relative to the laboratory frame. Furthermore the light and laboratory axis systems are connected by the Euler rotation D(0,-β,0) where β is the

angle between the polarisation vector (Z_2) and the laboratory axis (Z_1). In the laboratory frame equation 2.21 becomes in terms of spherical harmonics [20]

$$W(\theta,\varphi,t)_{Z_1} = BI(t)|\vec{\mu}_a|^2 \frac{\sqrt{4\pi}}{3}\left[Y_{00}(\theta',\varphi') + \frac{2}{\sqrt{5}}\sum_{Q=-2}^{2} d^2_{0Q}(-\beta)Y_{2Q}(\theta',\varphi')\right] \qquad [2.22]$$

where $d^2_{0Q}(-\beta)$ is a reduced Euler rotation matrix [29]

$$d^K_{QQ'}(-\beta) = \int Y^*_{KQ'}(\theta,\varphi)D(0,-\beta,0)Y_{KQ}(\theta',\varphi')d\Omega \qquad [2.23]$$

The β dependence of the transition probability in Z_1 is given by the reduced Euler rotation matrix elements which are

$$d^2_{00}(\beta) = \frac{1}{2}\left(3\cos^2\beta - 1\right) \qquad [2.24.a]$$

$$d^2_{10}(\beta) = d^2_{-10}(\beta) = \sqrt{\frac{3}{2}}\sin\beta\cos\beta \qquad [2.24.b]$$

$$d^2_{20}(\beta) = d^2_{-20}(\beta) = \sqrt{\frac{3}{8}}\sin^2\beta \qquad [2.24.c]$$

For weak excitation conditions the initial excited state orientational distribution is given by the product of the ground state orientational distribution function and the excitation operator:

$$P_{ex}(\theta,\varphi) = P_{gs}(\theta,\varphi)W(\theta,\varphi) \qquad [2.25]$$

In equation 2.25 only the population term is present in $P_{gs}(\theta,\varphi)$ for an isotropic ground state and the angular dependence of the excitation probability determines the excited state distribution. In a nematic environment the equilibrium order is symmetric about the nematic director **n**. The initial excited state distribution is therefore given by

$$P_{ex}(\theta,\varphi,\beta,t=0)=\frac{C}{3\sqrt{4\pi}}\sum_{K'even}\left\langle C^{gs}_{K'0}\right\rangle Y_{K'0}(\theta,\varphi)\left[Y_{00}(\theta,\varphi)+\frac{2}{\sqrt{5}}\sum_{Q}d^{2}_{0Q}(\beta)Y_{2-Q}(\theta,\varphi)\right] \quad [2.26]$$

where C is a constant of proportionality, and the moments of the excited state orientational distribution function are given by [22]

$$\left\langle C^{ex}_{KQ}(0)\right\rangle = C\frac{\sqrt{4\pi}}{3}\sum_{K'}\left\langle C^{gs}_{K'0}\right\rangle\left\langle KQ\left|\left[Y_{00}(\theta,\varphi)+\frac{2}{\sqrt{5}}\sum_{Q'}d^{2}_{0Q'}(-\beta)Y_{2Q'}(\theta,\varphi)\right]\right|K'0\right\rangle \quad [2.27]$$

which yields for $P_{ex}(\theta,\varphi)$ [22].

$$P_{ex}(\theta,\varphi)=C\frac{\sqrt{4\pi}}{3}\sum_{K=2,4,6..}\left(\left\langle C_{K0}\right\rangle Y_{K0}(\theta,\varphi)\right)\left[Y_{00}(\theta,\varphi)+\frac{2}{\sqrt{5}}\sum_{K=2}^{-2}d^{2}_{0K}(\beta)Y_{2K}(\theta,\varphi)\right] \quad [2.28]$$

The excited state moments observable in fluorescence measurements are given by

$$\frac{\left\langle\alpha^{ex}_{20}(0,\beta)\right\rangle}{\sqrt{5}}=\frac{\frac{1}{5}\left(3\cos^2\beta-1\right)+\frac{\left\langle\alpha^{gs}_{20}\right\rangle}{\sqrt{5}}\left(1+\frac{2}{7}\left\{3\cos^2\beta-1\right\}\right)+\frac{6\left\langle\alpha^{gs}_{40}\right\rangle}{35}\left(3\cos^2\beta-1\right)}{1+\frac{\left\langle\alpha^{gs}_{20}\right\rangle}{\sqrt{5}}\left(3\cos^2\beta-1\right)} \quad [2.29]$$

$$\frac{\left\langle\alpha^{ex}_{22}(0,\beta)\right\rangle+\left\langle\alpha^{ex}_{2-2}(0,\beta)\right\rangle}{\sqrt{30}}=\frac{\frac{1}{5}\sin^2\beta\left(1-\frac{10\left\langle\alpha^{20}_{gs}\right\rangle}{7\sqrt{5}}+\frac{\left\langle\alpha^{gs}_{40}\right\rangle}{7}\right)}{1+\frac{\left\langle\alpha^{gs}_{20}\right\rangle}{\sqrt{5}}\left(3\cos^2\beta-1\right)} \quad [2.30]$$

and combining equations 2.29 and 2.30 yields the initial fluorescence anisotropy

$$R(0,\beta)=\frac{\frac{2}{5}\left(\cos^2\beta-\sin^2\beta\right)+\frac{\left\langle\alpha^{gs}_{20}\right\rangle}{\sqrt{5}}\left[1+\frac{4}{7}\cos^2\beta\right]+\frac{\left\langle\alpha^{gs}_{40}\right\rangle}{35}\left(19\cos^2\beta-7\right)}{1+\frac{2}{5}\sin^2\beta+\frac{\left\langle\alpha^{gs}_{20}\right\rangle}{\sqrt{5}}\left[\frac{25\cos^2\beta-11}{7}\right]+\frac{\left\langle\alpha^{gs}_{40}\right\rangle}{35}2\sin^2\beta} \quad [2.31]$$

For β=0° it can be seen that the there is no contribution to the fluorescence anisotropy from the cylindrically asymmetric moments $\left(\left\langle \alpha_{22}^{ex}(t,\beta)\right\rangle + \left\langle \alpha_{2-2}^{ex}(t,\beta)\right\rangle\right)$. The fluorescence anisotropy can therefore be defined purely in terms of the cylindrically symmetric moment $\left\langle \alpha_{20}^{ex}(t,\beta)\right\rangle$. Fluorescent anisotropy measurements in this configuration will be solely sensitive to θ diffusion dynamics. For excitation polarisation angles β>0 the fluorescent anisotropy will contain both cylindrically symmetric and asymmetric degrees of molecular alignment. As will be seen below the specific excitation polarisation settings can be used to highlight the cylindrically symmetric alignment relaxation dynamics.

Figure 2.12 shows the dependence of fluorescence observables on the excitation polarisation angle β, for both isotropic and nematic ground state distributions.

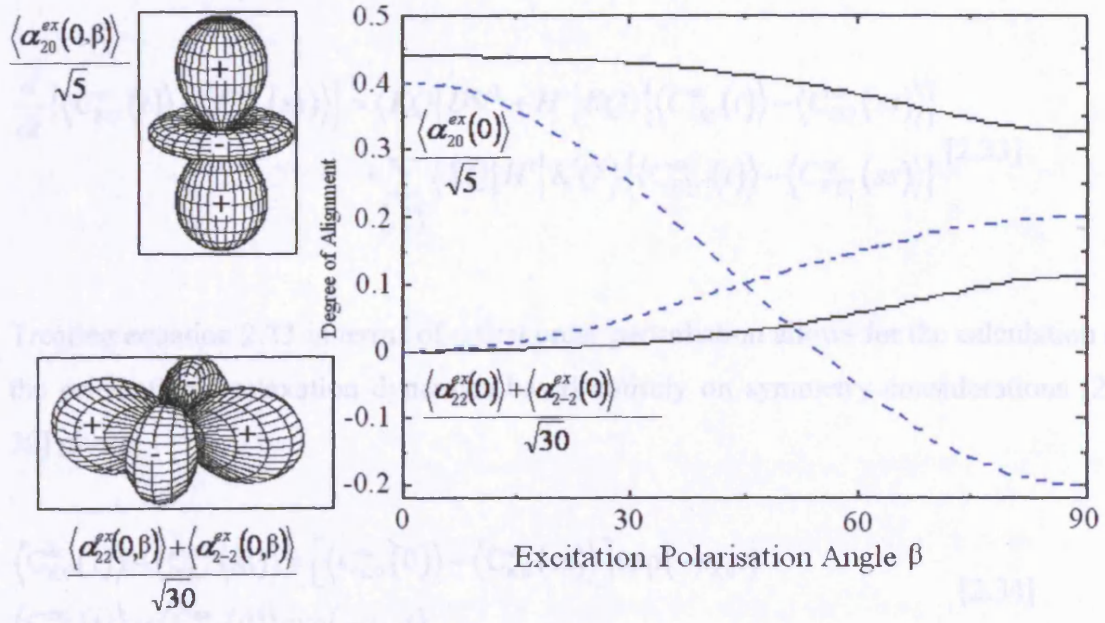

Figure 2.12: Variation in the excitation polarisation angle β for excitation from an isotropic ground state (broken blue lines) and from a ground state with an arbitrary net alignment (solid lines) determines the contributions of fluorescence observables to the initial excited state anisotropy.

2.7 Molecular Relaxation Dynamics in Ordered Environments

If rapid collisions occur between probe and host molecules whilst in a fluid environment [28] and each collision event is restricted to only a small angular variation, then the molecular dynamics are well described by the Debye small step diffusion model (Appendix II). However in an anisotropic medium the model must be modified, thereby considered as a static perturbation H' in the isotropic excited state according to [29]

$$\frac{d}{dt}P_{ex}(\theta,\varphi,t)=\left[D\nabla^2+H'\right]P_{ex}(\theta,\varphi,t) \qquad [2.32]$$

If H' is to be considered a perturbation, then to a first order approximation, $D\nabla^2$ must be very much larger than H'. Furthermore H' must retain the initial symmetry of the medium. In terms of distribution moments equation 2.32 becomes

$$\frac{d}{dt}\left\{\left\langle C_{KQ}^{ex}(t)\right\rangle-\left\langle C_{KQ}^{ex}(ss)\right\rangle\right\}=\left\langle KQ\left|D\nabla^2+H'\right|KQ\right\rangle\left\{\left\langle C_{KQ}^{ex}(t)\right\rangle-\left\langle C_{KQ}^{ex}(ss)\right\rangle\right\}+\sum_{\substack{K'\neq K\\ Q'\neq Q}}\left\langle KQ\left|H'\right|K'Q'\right\rangle\left\{\left\langle C_{K'Q'}^{ex}(t)\right\rangle-\left\langle C_{K'Q'}^{ex}(ss)\right\rangle\right\} \qquad [2.33]$$

Treating equation 2.33 in terms of a first order perturbation allows for the calculation of the orientational relaxation dynamics based entirely on symmetry considerations [29, 30] giving

$$\left\langle C_{K0}^{ex}(t)\right\rangle-\left\langle C_{K0}^{ex}(ss)\right\rangle=\left[\left\langle C_{K0}^{ex}(0)\right\rangle-\left\langle C_{K0}^{ex}(ss)\right\rangle\right]\exp(-\gamma_{K0}t)$$
$$\left\langle C_{KQ}^{ex}(t)\right\rangle=\left\langle C_{KQ}^{ex}(0)\right\rangle\exp(-\gamma_{KQ}t) \qquad [2.34]$$

In environments defined by axial symmetry, the diffusion tensor in the laboratory frame of reference is diagonal with $D_{XX} = D_{YY} \neq D_{ZZ}$ ($D_{\|}$ and $D_{\perp}$, respectively). Under these circumstances the γ_{KQ} decay rates are given by [30],

$$\gamma_{KQ}=D_{\perp}\left[K(K+1)-Q^2\right]+D_{\|}Q^2+\left\langle KQ\left|H'\right|KQ\right\rangle \qquad [2.35]$$

As the perturbation is small in the first order approximation, the dominant mechanism in orientational relaxation is due to the presence of anisotropic viscosity, this phenomena in turn yields unequal values of $D_{\parallel}$ and $D_{\perp}$

$$\gamma_{20} = 6D_{\perp} \qquad [2.36]$$

$$\gamma_{22} = 2D_{\perp} + 4D \qquad [2.37]$$

2.8 Time Dependent Fluorescence Anisotropy

Considering the first order relaxation dynamics outlined in section 2.5, the rate of change of displacement of a particular excited state moment from its equilibrium position obeys first order kinetics:

$$\frac{d}{dt}\left[\left\langle \alpha_{KQ}^{ex}(t)\right\rangle - \left\langle \alpha_{KQ}^{ex}(ss)\right\rangle\right] = -\gamma_{KQ}\left[\left\langle \alpha_{KQ}^{ex}(t)\right\rangle - \left\langle \alpha_{KQ}^{ex}(ss)\right\rangle\right] \qquad [2.38]$$

where (ss) denotes the steady state value of the moment. Equation 2.38 has a solution of the form

$$\left\langle \alpha_{KQ}^{ex}(t)\right\rangle = \left\{\left\langle \alpha_{KQ}^{ex}(0)\right\rangle - \left\langle \alpha_{KQ}^{ex}(ss)\right\rangle\right\}\exp\left(-\gamma_{KQ}t\right) + \left\langle \alpha_{KQ}^{ex}(ss)\right\rangle \qquad [2.39]$$

From equation 2.20, the fluorescence anisotropy is dependent upon the $\left\langle \alpha_{20}^{ex}\right\rangle$ and $\left\{\left\langle \alpha_{22}^{ex}\right\rangle + \left\langle \alpha_{2-2}^{ex}\right\rangle\right\}$ moments, and from equation 2.5 in Appendix I.II, the steady state distribution function is characterised by moments of even rank K and projection Q of zero for an axially symmetric medium. That is $\left\langle \alpha_{2\pm2}^{ex}(ss)\right\rangle$=0, which yields for the time dependent fluorescence anisotropy

$$R(t) = \frac{\frac{1}{\sqrt{5}}\left[\left\{\left\langle \alpha_{20}^{ex}(0)\right\rangle - \left\langle \alpha_{20}^{ex}(ss)\right\rangle\right\}e^{(-\gamma_{20}t)} + \left\langle \alpha_{20}^{ex}(ss)\right\rangle\right] - \frac{1}{\sqrt{30}}\left[\left\langle \alpha_{22}^{ex}(0)\right\rangle + \left\langle \alpha_{2-2}^{ex}(0)\right\rangle\right]e^{(-\gamma_{22}t)}}{1 + \frac{2}{\sqrt{30}}\left[\left\langle \alpha_{22}^{ex}(0)\right\rangle + \left\langle \alpha_{2-2}^{ex}(0)\right\rangle\right]e^{(-\gamma_{22}t)}}$$

[2.40]

which upon substitution of equations 2.29 and 2.30 and $R_{SS} = \langle \alpha_{20}^{ex} \rangle / \sqrt{5}$ gives the expression

$$R(t,\beta) = \frac{\left[\frac{(3\cos^2\beta - 1)}{35}\{7+6b\} + \frac{a}{7}(6\cos^2\beta + 5) - R_{ss}(1 + a(3\cos^2\beta - 1))\right]\exp(-\gamma_{20}t) - \frac{1}{5}\sin^2\beta\left(1 - \frac{10}{7}a + \frac{b}{7}\right)\exp(-\gamma_{22}t) + R_{ss}(1 + a(3\cos^2\beta - 1))}{(1 + a(3\cos^2\beta - 1)) + \frac{2}{5}\sin^2\beta\left(1 - \frac{10}{7}a + \frac{b}{7}\right)\exp(-\gamma_{22}t)} \quad [2.41]$$

where $a = \langle \alpha_{20}^{gs} \rangle / \sqrt{5}$ and $b = \langle \alpha_{40}^{gs} \rangle$ are the normalised ground state alignment moments. From the β dependence of the initial fluorescence anisotropy equation 2.41 allows for the degrees of $\langle \alpha_{20}^{gs}(ss) \rangle$ (quadrupolar) and $\langle \alpha_{40}^{gs}(ss) \rangle$ (hexadecapolar) alignment to be determined.

2.9 Phase Transition Characteristics and Isotropic Orientational Dynamics of Nematic Liquid Crystals

2.9.1 Phase Transitions

It is well known that any substance of fixed chemical composition can exist in several homogeneous forms. Such macroscopic states which exist under specific conditions are called phases and are defined by the distinct arrangement of the constituent molecules and differ in their thermal, optical and mechanical properties [31, 32, 33]. The phases of a material can be represented pictorially in a phase diagram as shown in figure 2.13. Along the boundary line a substance can coexist in several phases simultaneously, although the properties of the material change discontinuously. In fluid systems defined with state variables pressure and temperature (p, T), phase transitions occur when a thermodynamic potential such as the Gibbs free energy (F) of one state of matter ceases to be in equilibrium with another [34]. Evidence of a phase transition is signaled by a singularity in the Gibbs free energy given by

$$F = H + PV - TS \quad [2.42]$$

where H is the enthalpy, T the temperature and S the entropy.

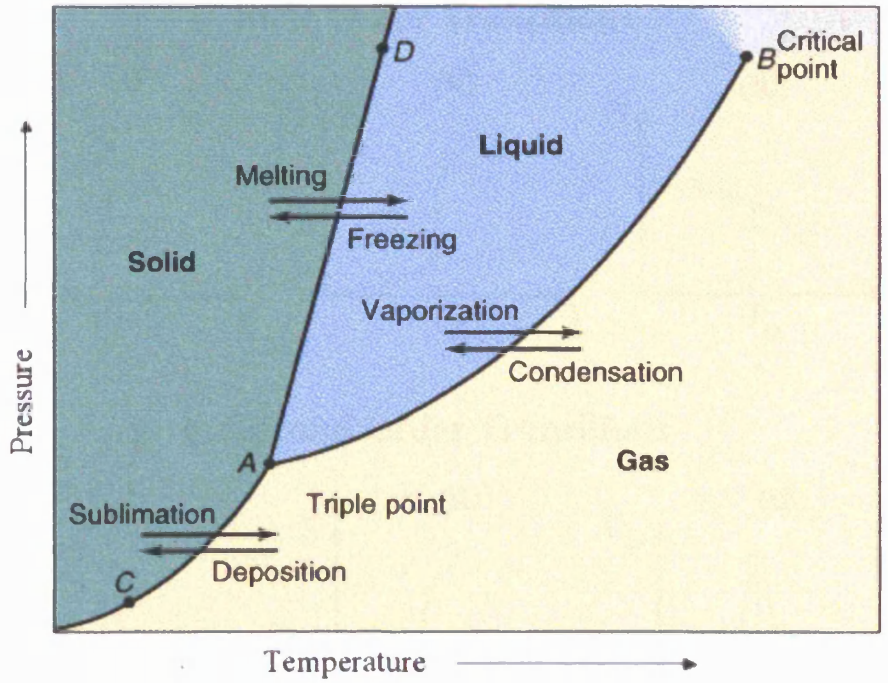

Figure 2.13: Schematic phase diagram for water. The triple point (A) defines the point at which three phases coexist in equilibrium, the critical point (B) is the point at which the liquid and gaseous state of a pure stable substance become identical. The black lines represent phase boundaries where two phases coexist simultaneously. Points A-D indicate the melting temperature of the solid as a function of pressure and points A-C indicate the vapor pressure of the solid as it sublimes at different temperatures.

Phase transitions are classified as first order if they possess a finite discontinuity in the first derivative in one or more of the appropriate thermodynamic potentials (i.e. entropy, density as shown in figure 2.14a) or more generally if the transition is associated with the existence of latent heat. For second or continuous order transitions the first-order derivatives are continuous, while the second order derivatives with respect to the state variables are discontinuous or infinite [35] (as shown in figure 2.14b). This type of transition corresponds to a critical point at which the correlation length extends over macroscopic scales (i.e. long range order develops in the system). Furthermore the correlation function which defines the degree of correlated order in the system decays as a power law [36].

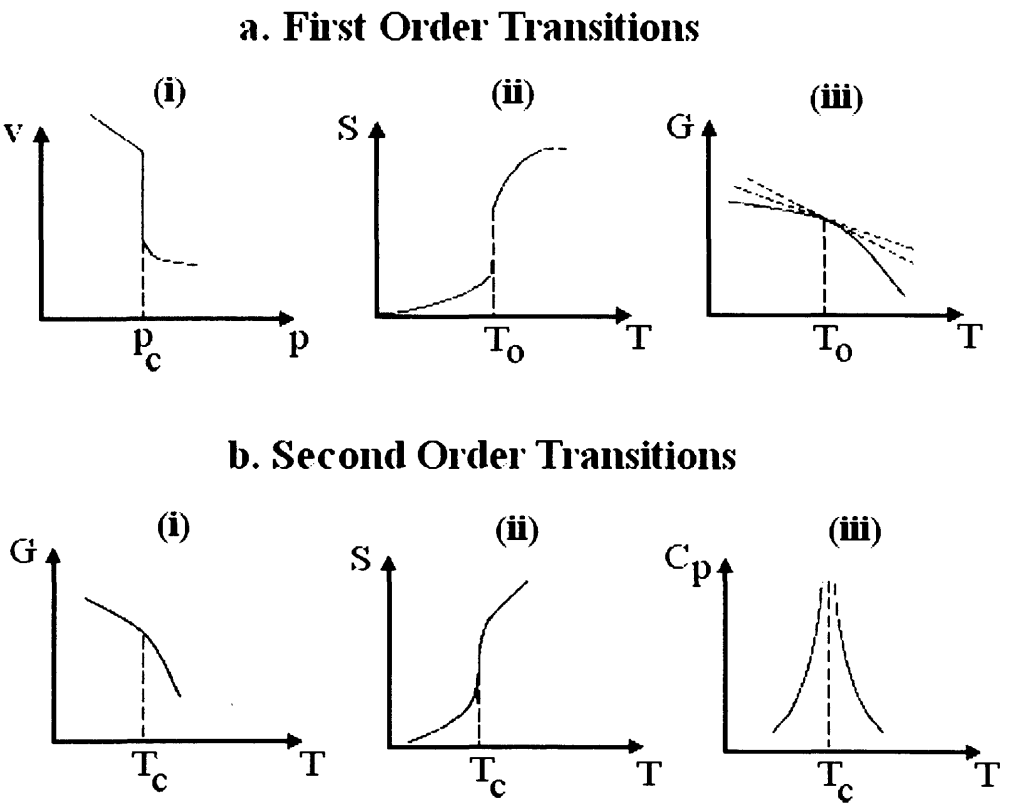

Figure 2.14: First and second order phase transitions (a). There is a finite discontinuity in the first order derivatives in (i) and (ii) at the phase transition whereas the Gibbs free energy potential (iii) is continuous in the transition (b). The first order derivatives with respect the free energy and associated quantities are continuous in (i) and (ii) however the second derivative with respect the specific heat at constant pressure (iii) is not continuous and is seen to diverge at T_C.
After P Papon, J Leblond and P H E Meijer, Springer (2006)

2.9.2. Phase Transitions in Liquid Crystals

The phenomenological model provided by the theory of Landau-De-Gennes best describes the thermodynamic behaviour of liquid crystals in the vicinity of the nematic-isotropic (N-I) phase transition. The theory predicts the development of the order parameter <S> in the vicinity of the N-I transition i.e. as <S> approaches 0, by considering a Taylor expansion of the excess Gibbs free energy F, as a function of <S> [37],

$$F = F_0 + K(T)\langle S\rangle + \frac{1}{2}A\langle S\rangle^2 - \frac{1}{3}B\langle S\rangle^3 + \frac{1}{4}C\langle S\rangle^4 ..., \qquad [2.43]$$

where K, B and C are constants. In the vicinity of the transition A varies as [34]

$$A = A_0\left(T - T^*\right) \qquad [2.44]$$

where A_0 and T* are constants and T^* is the second order phase transition temperature known as the virtual temperature and lies below the phase transition temperature T_{NI} (typically 1-2K below T_{NI} [38]) which is constant for a particular dye-host solution. The states of equilibrium of the system must satisfy the following equations

$$\frac{\partial F}{\partial \langle S \rangle} = 0 \ , \ \frac{\partial^2 F}{\partial \langle S \rangle^2} > 0 \qquad [2.45]$$

so the minimum of the free energy F can be obtained by evaluating the first derivative of the free energy with respect the order parameter S [39] giving an expression, neglecting higher order terms, of the order parameter at T_{NI} of,

$$S_{NI} = \frac{2B}{3C} \qquad [2.46]$$

By further considering that the virtual temperature lies below the phase transition temperature we can write [40]

$$T_{NI} = T^* + \frac{2B^2}{9A_0C} \qquad [2.47]$$

Since the nematic-isotropic phase transition is a weak first order transition [2] for calamitic molecules such as 5CB, the magnitude of B is small [39]. Therefore the value of $\left(T_{NI} - T^*\right)$ is expected to be small also.

Though the order parameter reduces to zero at the nematic-isotropic phase transition, (i.e. such that it is zero above T_{NI}), an appreciable degree of order persists above the phase transition and extends over a microscopic distance, $0 \le S \le \xi(T)$, where $\xi(T)$ is the correlation length. In the isotropic phase a liquid crystal sample is macroscopically isotropic but microscopically anisotropic. When considering a distance scale short

compared to a correlation length ξ, the local structure is like that of a nematic liquid crystal, creating what can be described as pseudo-nematic domains. These domains of local order however are not correlated to one another, as shown in figure 2.15.

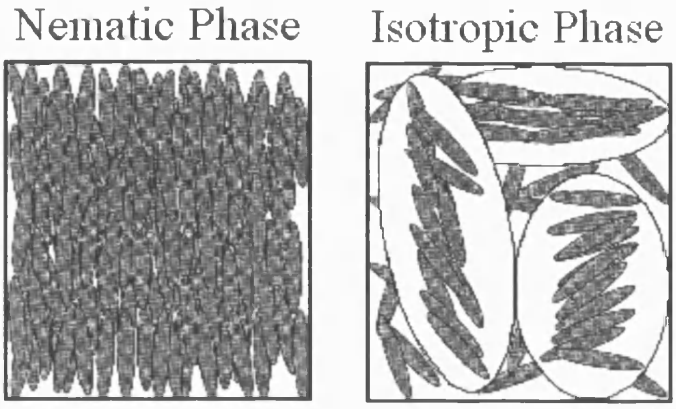

Figure 2.15: Illustration of the contrast in order in the nematic and isotropic phase of a nematic liquid crystal. For the nematic phase order persists over macroscopic distances whereas for the isotropic phase local order persists over distances ξ, which are larger than the molecular size.

The existence of pseudo-nematic domains in liquid crystals such as 5CB and MBBA has been confirmed from dynamic light scattering [41] and electric birefringence experiments [42]. The domain sizes vary typically from 10-20 molecular lengths to approximately 200Å near the phase transition temperature [43]. This is in accordance with predictions made by the theory of Landau-De-Gennes whereby the correlation length ξ is described in terms of the molecular length and the virtual temperature T^* as

$$\xi(T) = \xi_0 \sqrt{\frac{T^*}{T - T^*}} \qquad [2.48]$$

As a result of the existence of local domains, the orientational relaxation dynamics of nematogens in the isotropic phase of liquid crystals is complex. Recently a series of time resolved polarised fluorescence experiments designed to measure the molecular ordering and orientational dynamics in the isotropic phase of 5CB have been carried out by the group [1, 2]. These studies along with studies by Gootke et al [44, 45] have revealed that the dynamics can be divided into two timescales, a long (nanosecond) time and short time of the order of several hundred picoseconds.

On a long time scale the orientational relaxation of the pseudo-nematic domains is exponential in nature and is highly temperature dependent. The nanosecond dynamics are described by an exponential functional form predicted by the theory of Landau-De-Gennes [46]. The function decays with relaxation time τ_{LDG} which diverges at the virtual transition temperature T^* as

$$\tau_{LDG} = \frac{V_{eff}\eta(T)}{T - T^*} \qquad [2.49]$$

where V_{eff} is the nematogen effective volume, $\eta(T)$ is the viscosity and T is the temperature. Pseudo-nematic domains of this nature are seen to persist up to approximately 70°C above the nematic-isotropic phase transition temperature [1, 2, 47].

The observed short time dynamics are attributed to the collective motions of the nematogens within the pseudo-nematic domains. The dynamics do not follow Landau-De-Gennes behaviour and are instead described in terms of a power law decay. They are found to be temperature independent up to c.a. T_{NI}+70°C. The temperature independence associated with the fast reorientation can be explained by expressing the free energy of the isotropic phase as an expansion in terms of S(**q**), where **q** is the wavevector which describes the fluctuations in the order parameter S due to the uncorrelated domains [40]. This leads to the dispersion relation [1]

$$\frac{1}{\tau} = \frac{1}{\eta_1}\left(q^2 + \frac{1}{\xi^2}\right) \qquad [2.50]$$

By taking limits of the fluctuation wave vectors **q** corresponding to length scales from molecular size to domain correlation length, this approach reproduces the slow orientational component (consistent with Landau-De-Gennes theory) [40] as well as recovering the fast component of the reorientation. In the limit of $q\xi >> 1$ the fluctuation mode relaxation time (τ_f) becomes

$$\frac{1}{\tau_f} = \frac{Dq^2}{\eta} \qquad [2.51]$$

where D is a constant. The fast dynamics that are observed on a time scale short compared to the slow orientational dynamics (τ_{LdG}) are referred to in terms of intra-domain relaxation. Recently Fayer and co workers (using analysis based on density functional theory as previously proposed by Bagchi [47]) have presented a revised model in which longer temporal scales are considered [44]. From this a linear relationship has been established between what can be described as intermediate times (relative to the long (nanosecond) and short (picosecond) times) τ_{fast} and viscosity given by

$$\tau_{FAST} \approx \frac{\eta V_{eff}}{k_B T} \qquad [2.52]$$

2.10 Local Ordering of Fluorescence Probes in the Isotropic Phase of Nematic Liquid Crystals

The local order and restricted dynamics of ionic probes in the isotropic phase of cyanobiphenyls have been studied in detail by Bryant, Monge and co-workers [1, 2]. For all systems studied within a temperature range of T_{NI} to T_{NI}+50K the fluorescence anisotropy whilst decaying to an isotropic background (R_{SS}=0) was strongly bi-exponential in stark contrast to the single exponential decays obtained for the probes in non-self organising solvents. Close to T_{NI}, anisotropy decays were characterised by 'fast' and 'slow' relaxation (c.a. 2.3-1.8ns and 16-1.8ns) with the onset of a single exponential decay at temperature above T_{NI}+50K as shown in figure 2.16. Below this 'isotropic' temperature the variation in the two decay times was distinctly different, indicating the presence of two independent orientational relaxation mechanisms. Fluorescence intensity decays across the isotropic phase, as in the nematic phase, were seen to fit well to single exponential decays.

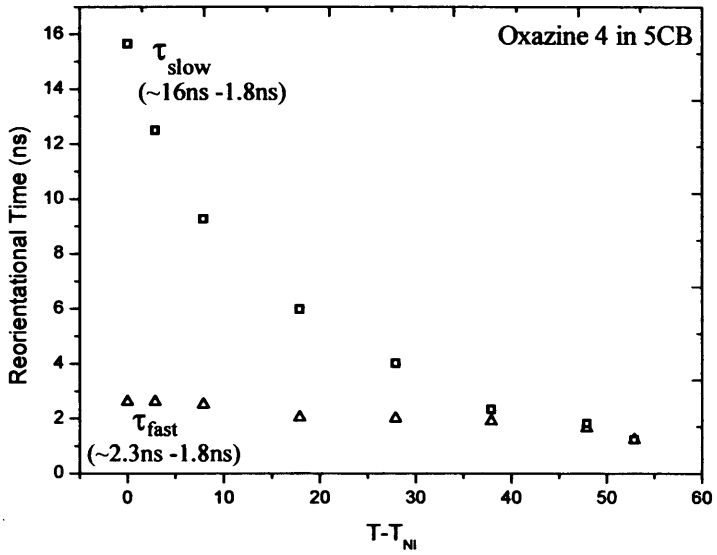

Figure 2.16: Isotropic phase dynamics of Oxazine4 in 5CB. The fluorescence anisotropy is bi-exponential corresponding to restricted rotational diffusion within an isotropically diffusing domain structure. Normal (mono-exponential) orientational relaxation is observed for $T>T_{NI}+50°C$.

Given highly restricted rotational diffusion of probe molecules in the nematic phase within a fixed (or extremely slowly diffusing) host environment the isotropic phase dynamics were modeled assuming fast restricted rotational diffusion within a more slowly diffusing pseudo-nematic domain structure. In this limit, anisotropy dynamics should resemble that of a fluorescent probe constrained in a slowly diffusing host.

$$R(t) = \exp\left(\frac{-t}{\tau_{SLOW}}\right)\left[(R(0) - R_{DOMAIN})\exp\left(\frac{-t}{\tau_{FAST}}\right) + R_{DOMAIN}\right] \qquad [2.53]$$

Where R(0) and R_{DOMAIN} are the limiting values of the anisotropy in the absence of domain motion. With the loss of local structure R_{DOMAIN} tends to zero and the times τ_{fast} and τ_{slow} converge yielding a single exponential functional form for equation 2.53. Local probe order within the domain structure can be deduced from a consideration of the long-time behaviour of the orientational correlation function [49, 50] in which a local order parameter S ($<P_2>_{local}$) is given by

$$S = \sqrt{\frac{R_{DOMAIN}}{R(0)}} \qquad [2.54]$$

Interpretation of S is achieved using the 'wobbling' in a cone model [49] in which a cylindrically symmetric probe tumbles locally within a cone of angle θ_{MAX} (fig. 2.17).

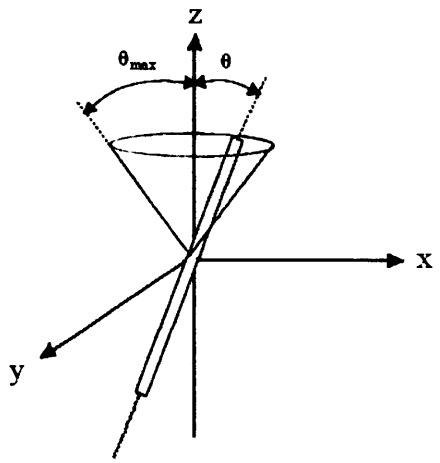

Figure 2.17: The restricted rotational motion of a cylindrically symmetric probe fluorescent probe embedded in a host environment of restrictive geometry. The extent of the free rotation is set by the limits of the cone of angular width θ_{MAX}

2.11 Experiment

The experimental technique of Time Correlated Single Photon Counting (TCSPC) was used to measure the fluorescence intensities and fluorescence anisotropies in all experiments described in this chapter. The experimental apparatus is illustrated in figures 2.18 and 2.19. Prior to undertaking experiments in 5CB it was deemed prudent to determine the type of rotational diffusive behaviour exhibited by Coumarin 6 in a simple liquid, experiments in the isotropic solvent ethylene glycol were therefore undertaken where a 90° excitation-detection set-up was employed. Measurements of single photon fluorescence anisotropy in 5CB were undertaken in homogenously aligned cells of c.a. 100μm path length and utilised collinear excitation-detection geometry (180°). For all experiments detailed in this chapter procedures were undertaken prior to collection of fluorescence emission data from the samples. Initially the instrument response function (IRF-Appendix IV) was checked and the FWHM was found to be c.a. 80ps. The detection efficiency for vertically and horizontally polarised scattered laser light was measured (G-Factor) at a polarisation angle of 45° in an isotropic sample. This should yield unbiased detection where equivalent decays are recovered. Any difference between the two decays is an indication that some polarisation bias exists and adjustments are made to the optical components until any

bias is eliminated. The vertical (I_Z) and horizontal (I_V) emission intensities were recorded for 10 second periods by alternating a polaroid sheet attached to a stepper motor controlled by a PC with a synchronous change in the MCB memory address. A non-commercial program written by Dr Gary Holtom (Pacific North Western Research Laboratory) was used to stop and start the experiment; W.J.Noad (formerly of the Rutherford Appleton Laboratory) has developed a polarisation data collection program which was run in conjunction with the Holtom program.

Coumarin 6 and Oxazine 4 were used without further purification. Sample concentrations for solutions in ethylene glycol were c.a. $5x10^{-6}$M and for solutions in 5CB the concentrations were c.a. $5x10^{-4}$M. For all experiments involving Coumarin 6 in 5CB single photon excitation (λ_{excite}:470nm) was achieved using the output of a regeneratively amplified Ti:Sapphire pumped tunable optical parametric amplifier (OPA) delivering 200-250fs pulses at a repetition rate of 250kHz with an average output power of 80mW and tuning range 450nm-700nm. The OPA output was attenuated using neutral density wheels and filtered to remove any harmonics associated with the Ti:Sapphire and any residual from the white light continuum generated in the OPA, using a range of long pass filters (Schott RD530,550,570). A fraction (4%-6%) of the output beam from the OPA was split from the main beam and focused into the fast photodiode (protected by a set of neutral density filters), the signal from which provided the "stop" trigger for the TCSPC measurements [48]. The remainder of the output beam was passed through a set of variable neutral density filters and a half wave plate, allowing for polarisation control and further attenuation of all on-sample powers. Selection of the excitation polarisation angle (β) was made using a high quality Glan Taylor polariser cube (extinction ratio 10^6:1) mounted in a precision rotation stage (Photon Control RM100). The laser beam was focused into the sample which was held in a precision temperature controlled heat stage (±0.1°C, Mettler FP82) via a 10cm achromatic lens (Melles Griot). Detection of the generated fluorescence was made using a 6.3cm focal length lens (Melles Griot). A polaroid sheet placed within a computer controlled mount was used to isolate detection of the vertically or horizontally polarised components of the fluorescence. Beam blocks and cut-off filters (Corion LS500, LS550, Schott RG570, RG590) were employed to block and filter any laser light where appropriate. For excitation polarisation angles β=0°, 90° and 54.7° the vertical (I_Z) and horizontal (I_X) intensities were measured from the nematic temperature 27°C to the

nematic-isotropic phase transition temperature $T_{NI,}$ which is made apparent by the abrupt increase in laser scattering due to the loss of order in the system. In the vicinity of T_{NI} the increments in temperature between subsequent measurements was decreased from c.a. 0.5° at T_{NI}-2°C to c.a. 0.1 at T_{NI}-0.5°C

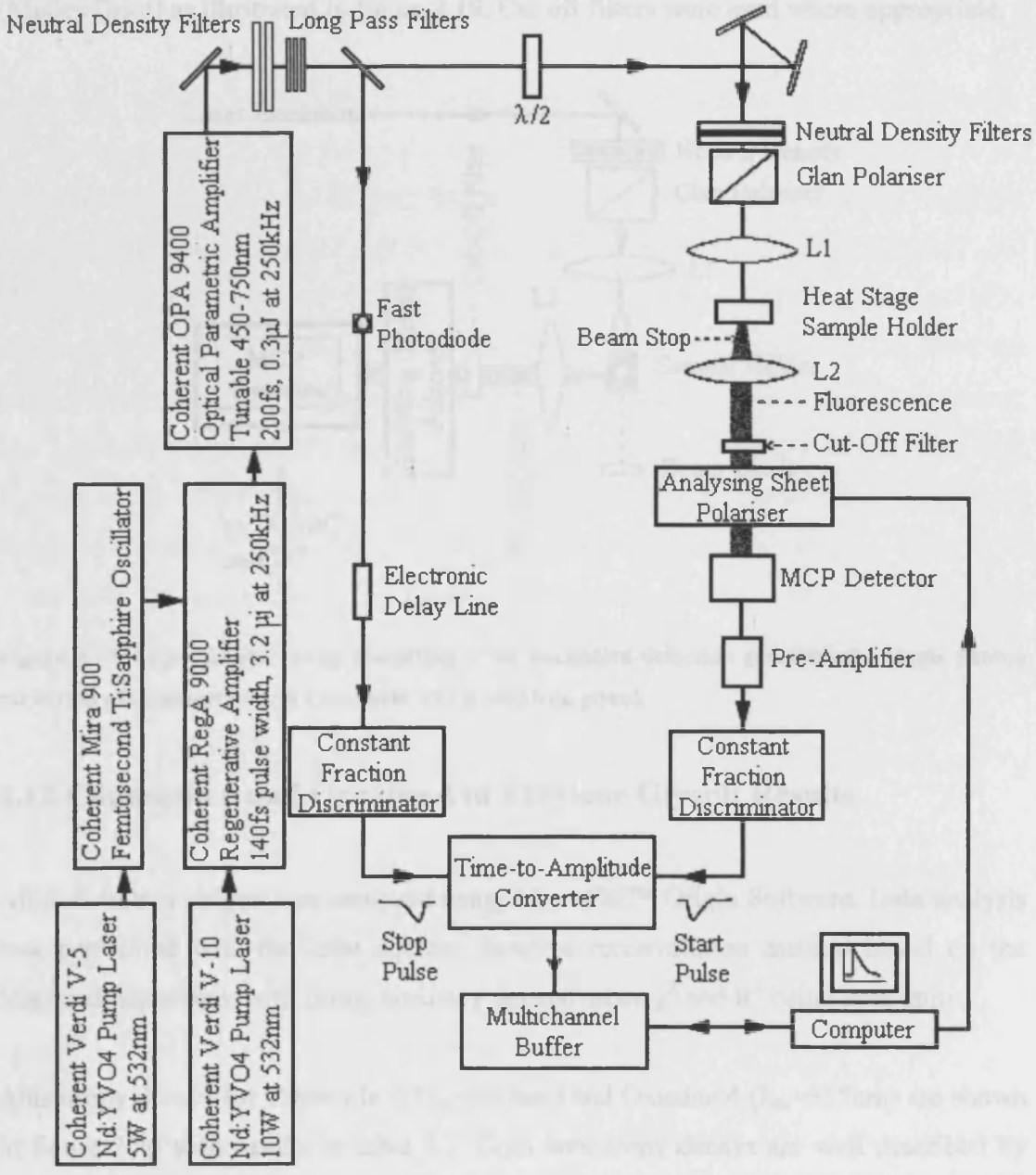

Figure 2.18: Experimental system consisting of collinear excitation-detection geometry for single photon excitation of Coumarin 6 (λ=470nm) and Coumarin 153 (λ=440nm) in 5-cyanobiphenyl.

For experiments involving ethylene glycol, the excitation source is as described in this section. The samples were contained in a 1cm cuvette (Hellma) with four optical windows and all measurements were carried out at room temperature (21°C +/-1°C). The laser beam was focused into the sample via a 10cm achromatic lens (Melles Griot). Detection of the generated fluorescence was made at 90° using a 6.3cm focal length lens (Melles Griot) as illustrated in figure 2.19. Cut off filters were used where appropriate.

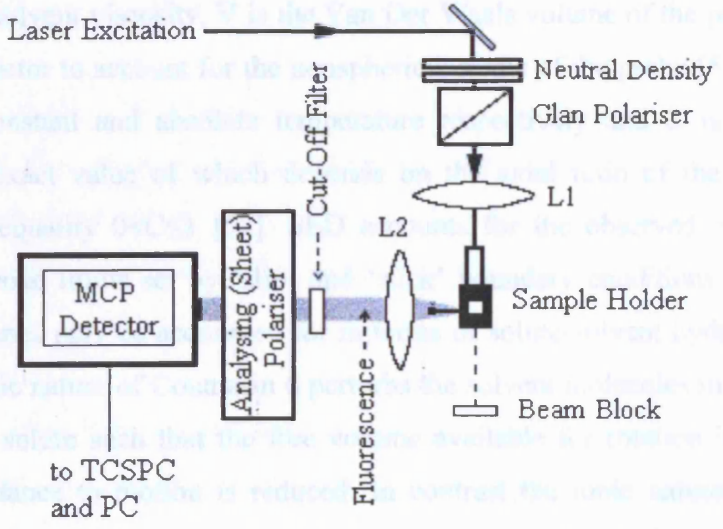

Figure 2.19: Experimental set-up consisting of 90° excitation-detection geometry for single photon excitation of Coumarin 6 and Coumarin 153 in ethylene glycol.

2.12 Coumarin 6 and Oxazine 4 in Ethylene Glycol: Results

All data in this chapter was analysed using MicroCal™ Origin Software. Data analysis was performed with the least squares iterative reconvolution method based on the Marquadt algorithm, with fitting accuracy dependent on χ^2 and R^2 being near unity.

Anisotropy decays for Coumarin 6 (λ_{ex}=490nm) and Oxazine 4 (λ_{ex}=615nm) are shown in figure 2.20 with results in table 2.1. Both anisotropy decays are well described by single exponential functions typical of isotropic rotational diffusion of a symmetric rotor. Though the initial anisotropies for Oxazine 4 and Coumarin 6 are of similar magnitude (c.a. 0.390 and 0.379 respectively) the rotational time for Coumarin 6 is found to be faster (c.a. 22%) than that of Oxazine 4. This is somewhat unusual given that Coumarin 6 has a hydrodynamic volume c.a. 29% larger than Oxazine 4 (436Å^3

and 313Å^3 respectively). According to the hydrodynamic model of Stokes-Einstein-Debye (SED) the rotational reorientation time depends on the size and shape of the rotating molecule and the bulk viscosity of the solvent as given by [1, 49]

$$\tau_r = \frac{\eta V}{KT}(fC) \qquad [2.55]$$

where η is the solvent viscosity, V is the Van Der Waals volume of the probe molecule, *f* is the shape factor to account for the nonspherical shape of the probe [51], k and T are Boltzmann's constant and absolute temperature respectively and C is the boundary condition the exact value of which depends on the axial ratio of the molecule and satisfies the inequality $0<C\leq 1$ [52]. SED accounts for the observed reorientation in terms of the broad limits set by 'slip' and 'stick' boundary conditions. The observed reorientation times may be accounted for in terms of solute-solvent hydrogen bonding. The hydrophobic nature of Coumarin 6 perturbs the solvent molecules in the immediate vicinity of the solute such that the free volume available for rotation increases. As a result the resistance to motion is reduced. In contrast the ionic nature of Oxazine 4 reacts with the hydrophilic solvent molecules resulting in 'stick' boundary conditions where there is cooperative motion between solvent and solute molecules.

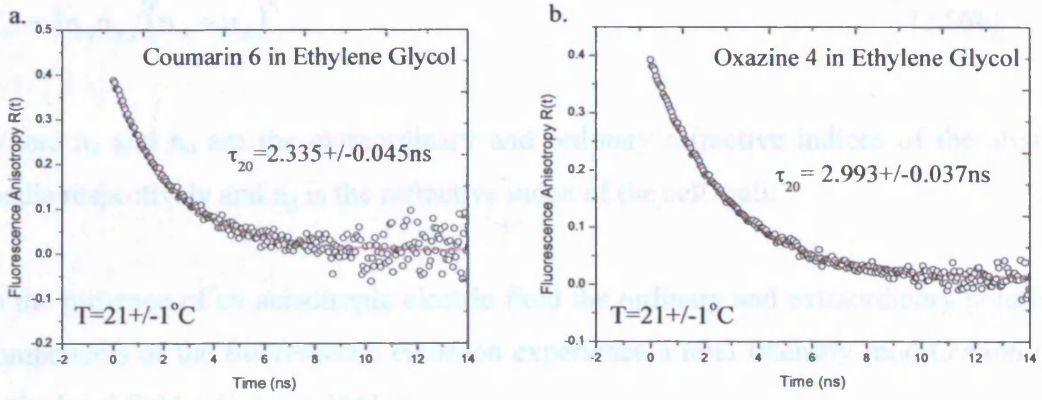

Figure 2.20: Anisotropy decays for (a) Coumarin 6 and (b) Oxazine 4 in the isotropic solvent ethylene glycol at room temperature (T=21°+/-1°C). Both fit to single exponential decays indicating that the emission dipole moments are parallel to the long axis of the molecules.

Probe	Solvent	Con^c (M)	λ_{EXCITE} (nm)	τ_{LIFE} (ns)	R(0)	τ_{ROT} (ns)
Coumarin 6	EthG	$5x10^{-6}$	490	2.359 +/- 0.002	0.379 +/- 0.004	2.335 +/- 0.045
Oxazine 4	EthG	$5x10^{-6}$	615	2.916 +/- 0.001	0.390 +/- 0.003	2.993 +/- 0.037

Table 2.2: Summary of lifetime and rotational anisotropy decays for Coumarin 6 and Oxazine 4 in ethylene glycol.

2.13 Fluorescence Signals in Anisotropic Media

In the nematic phase of cyanobiphenyl liquid crystals, the constituent molecules are highly aligned. This creates optical anisotropy (birefringence) of the medium and anisotropic local field effects which have a significant influence on the emitted intensities. Fluorescent probe studies within such media are complicated by these factors.

The transmission of light (T) through a boundary between two media with different refractive indices can be expressed in terms of a Fresnel coefficient given by [53]

$$T_e = 4n_e n_g / \left(n_e + n_g\right)^2 \qquad [2.56a]$$

$$T_o = 4n_o n_g / \left(n_o + n_g\right)^2 \qquad [2.56b]$$

Where n_e and n_o are the extraordinary and ordinary refractive indices of the aligned media respectively and n_g is the refractive index of the cell wall.

In the presence of an anisotropic electric field the ordinary and extraordinary polarised components of the fluorescence emission experience a total intensity modification due to the local field anisotropy [54] as

$$I_Z(observed) \propto I_Z(i)\left(n_e^2 + 2\right) \qquad [2.57a]$$

$$I_X(observed) \propto I_X(i)\left(n_o^2 + 2\right) \qquad [2.57b]$$

where the intensity for the emission in an anisotropic dielectric of unit refractive index is denoted by (i). The Z and X polarised components of fluorescence anisotropy are then modified such that

$$I_Z(observed) \propto I_Z(i)\frac{(n_e^2+2)4n_e n_g}{(n_e+n_g)^2} \equiv I_Z(i)\cdot a \qquad [2.58a]$$

$$I_X(observed) \propto I_X(i)\frac{(n_o^2+2)4n_o n_g}{(n_o+n_g)^2} \equiv I_X(i)\cdot b \qquad [2.58b]$$

By defining a parameter k=a/b the fluorescence anisotropy can be written as

$$R = \frac{kI_Z(i) - I_X}{kI_Z(i) + 2I_X} \qquad [2.59]$$

where the parameter k is given by

$$k = \frac{(n_o^2+2)n_e(n_o+n_g)^2}{(n_o+2)n_o(n_e+n_o)} \qquad [2.60]$$

The measured fluorescence anisotropy for anisotropic rotational diffusion in a cylindrically symmetric medium is then given by [2, 54]

$$R(t) = \frac{(k-1) + \frac{\langle \alpha_{20}^{ex}(t)\rangle}{\sqrt{5}}(2k+1) - \sqrt{\frac{3}{10}}\{\alpha_{2+2}^{ex}(t) + \alpha_{2-2}^{ex}(t)\}}{(k+2) - \frac{\langle \alpha_{20}^{ex}(t)\rangle}{\sqrt{5}}(2k-2) + 2\sqrt{\frac{3}{10}}\{\alpha_{2+2}^{ex}(t) + \alpha_{2-2}^{ex}(t)\}} \qquad [2.61]$$

Fluorescence anisotropy measurements in highly aligned media are thus characterized by two degrees of alignment relaxation and the optical anisotropy of the environment. All three quantities are temperature dependent and the determination of k in a fluorescent anisotropy experiment is essential if accurate measurements of molecular order and alignment relaxation are to be obtained. Values for k can be obtained from refractive index data where this available. Bulk refractive index data for undoped 5CB

for a wide range of wavelengths and temperatures has been measured by Wu et al [55]. However in the study of doped liquid 5CB and in general ordered systems for which refractive index data is not readily available it is advantageous to be able to measure k within the context of a time resolved fluorescence experiment

2.13.1 Depolarisation Factor Ā

The maximum theoretical value of the initial fluorescence anisotropy in an isotropic medium following single photon excitation is 0.4 [15] however experimentally this value is found to be less. The depolarisation of fluorescence can be attributed to a number of molecular and experimental factors such as the absorption and emission transition dipole moments being non-parallel self-absorption due to high sample concentration, imperfect optical alignment and scattering [56]. The effect of these factors is to modify the alignment components from their true values by an amount defined by the parameter Ā given by

$$\bar{A} = \frac{R(0)^{iso}_{mol}}{0.4} \qquad [2.62]$$

Determination of Ā can be achieved by measuring the variation in the initial fluorescence anisotropy with excitation polarisation angle for an isotropic sample [2]. From 2.31 R(0,β) in an isotropic sample is defined by

$$R(0,\beta) = \frac{\frac{2}{5}\left(\cos^2\theta - \sin^2\theta\right)}{1 + \frac{2}{5}\sin^2\beta} \qquad [2.63]$$

The value of Ā for Coumarin 6 in 5cb was determined by raising the temperature to 10°C above the nematic-isotropic phase transition temperature T_{NI} and fitting data collected at R(0,β) (where β=0°,35.3°,45°,54.7° and 90°) to equation 2.63.This yields a value of 0.844.

2.13.2 Fluorescence Intensity Decay Analysis in Nematic 5CB

In a cylindrically symmetric medium measurement of the total fluorescence intensity I_Z+2I_X yields a fluorescence signal which only contains population terms [57]. For a nematic liquid crystal the presence of birefringence (differential reflection losses) coupled with local field effects perturbs the fluorescence observables such that the total intensity for Z-polarised excitation ($\beta=0^o$ relative to the nematic director) is [2]

$$I_Z + 2I_X(\beta = 0^O) = A\exp\left(\frac{-t}{\tau_f}\right)\left[\frac{k+2}{\overline{A}} + \frac{2(k-1)}{\sqrt{5}}\left\langle\alpha_{20}^{ex}(\beta = 0^o, t)\right\rangle\right] \qquad [2.64]$$

where A is a proportionality constant. In the nematic phase of liquid crystals k>1 therefore the alignment term is non-vanishing and will make a small contribution to the fluorescence signal. The full time dependence of equation 2.64 is given by

$$I_Z + 2I_X(\beta = 0^O) = A\exp\left(\frac{-t}{\tau_f}\right)\left[\frac{k+2}{\overline{A}} + \frac{2(k-1)}{\sqrt{5}}\left\{\begin{array}{l}\left[\left\langle\alpha_{20}^{ex}(0)\right\rangle - \left\langle\alpha_{20}^{ex}(ss)\right\rangle\right]\exp\left(\frac{-t}{\tau_{20}}\right) \\ + \left\langle\left(a_{20}^{ex}(ss)\right)\right\rangle\end{array}\right\}\right] \qquad [2.65]$$

$$\equiv A\exp\left(\frac{-t}{\tau_f}\right)\left[\frac{k+2}{\overline{A}} + \frac{2(k-1)}{\sqrt{5}}R(t, \beta = 0^o)\right] \qquad [2.66]$$

The Z-polarised component of fluorescence emission following excitation at $\beta=54.7^o$ is given by [2]

$$I_Z(\beta = 54.7^o) = A' \exp\left(\frac{t}{\tau_f}\right)\left[\frac{1}{\overline{A}} + \frac{2}{\sqrt{5}}\left\langle\alpha_{20}^{ex}(t, \beta = 54.7^o)\right\rangle\right] \qquad [2.67]$$

where A' is a constant of proportionality. With an excitation polarisation angle of $\beta=54.7^o$ and a cylindrically symmetric ground state, the initial excited state cylindrically symmetric alignment is equal to that of the equilibrium alignment in the ground state [2]. From equation 2.39, the fluorescence intensity can then be given by

$$I_Z(\beta = 54.7^o) = A' \exp\left(\frac{t}{\tau_f}\right)\left[\frac{1}{A} + \frac{2}{\sqrt{5}}\left(\left\{\left\langle \alpha_{20}^{gs}(ss)\right\rangle - \left\langle \alpha_{20}^{ex}(ss)\right\rangle\right\}\exp\left(\frac{-t}{\tau_{20}}\right) + \left\langle \alpha_{20}^{ex}(ss)\right\rangle\right)\right] \quad [2.68]$$

Comparison of the two intensity decays corresponding to 2.65 and 2.68 allows k to be determined. Providing the difference in ground and excited state degrees of equilibrium alignment is small then equation 2.68 should closely resemble a single exponential decay with a lifetime τ_f.

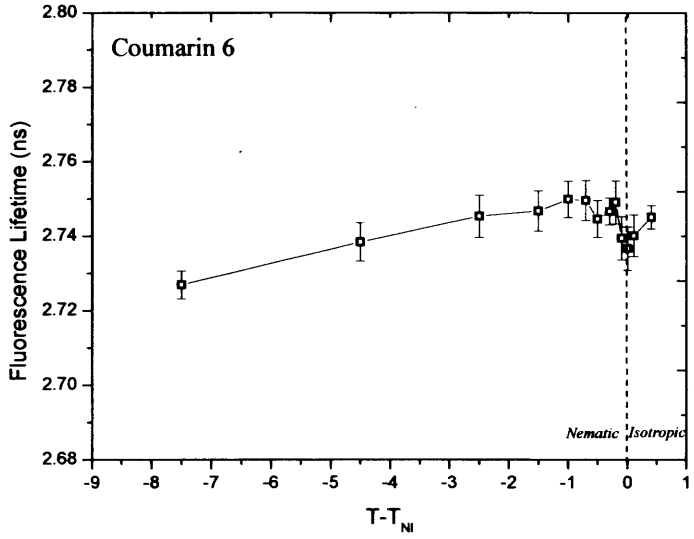

Figure 2.21: Fluorescence lifetime against reduced temperature for Coumarin 6 in the nematic phase of 5CB extracted from equation 2.62b. The lifetime shows a slight increase with temperature across the nematic phase.

2.13.3 Determination of the Optical Correction Factor k

In order to determine k the following systematic approach was applied

1. A single exponential fit was made to equation 2.66 to give the fluorescence lifetime τ_f.
2. From the intensity decays comprising equation 2.65 a double exponential fit was made to $I_Z(\beta=0^o)$ to give the reorientational lifetime τ_{20} and a second approximate value for τ_f
3. k uncorrected values for the steady state anisotropy R_{SS}, the initial anisotropy R_0 and the reorientational lifetime τ_{20} were obtained from fits to $R(t,\beta=0^o)$.

4. Custom functions generated in Origin based on the intensity components of equation 2.65 were then used to find k. As it was necessary to determine three parameters accurately (R_{SS}, R_0 and τ_{20}) the values found in steps two and three were used as initial approximate values. Accurate determination of the fluorescence lifetime has been achieved in step 1 and this value was fixed for both fits. All other parameters were allowed to float within the constraints of the errors found in the initial fits. In simultaneously fitting the functions global analysis was possible and accurate determination of the correction factor k was made by taking ratio of the pre-exponential factors generated as a result of fitting three parameters to the customised fitting function.

This method has since been superseded with the purchase of global analysis software allowing for determination of all parameters without the need for separate simultaneous fitting.

2.14 Nematic Order of Coumarin 6 in 5CB

The initial fluorescence anisotropies for excitation polarisation angles of $\beta=0^{\circ}$ and $\beta=90^{\circ}$ were measured for Coumarin 6. These anisotropies when combined with the nematic correction factor k and the depolarisation factor $\bar{A}$ yield values of the K=2 and K=4 moments of the ground state distribution function. A Mathematica program written in collaboration with Dr Richard Marsh allows for the determination of the K=2 and K=4 moments of 5CB. The results are shown in figure 2.22a for Coumarin 6 and 2.22b for Oxazine 4, as a function of reduced temperature ($T-T_{NI}$).

It is clear that Coumarin 6 has similar alignment to that of Oxazine 4, characterised by positive values of $\langle \alpha_{20}^{gs} \rangle / \sqrt{5}$ and negative values of $\langle \alpha_{40}^{gs} \rangle$. The value of $\langle \alpha_{20}^{gs} \rangle / \sqrt{5}$ decreases gradually with temperature to T_{NI}-0.5 where there is a sudden collapse to zero at T_{NI}. This behaviour is mirrored by the K=2 moment of 5CB as shown in figure 2.23. As with Oxazine 4, Coumarin 6 shows a notable increase in the negative value of $\langle \alpha_{40}^{gs} \rangle$ with increasing temperature, which persists to within close vicinity of the nematic-isotropic phase transition temperature (T_{NI}-0.2) where there is a sudden collapse to zero (isotropic) at T_{NI}.

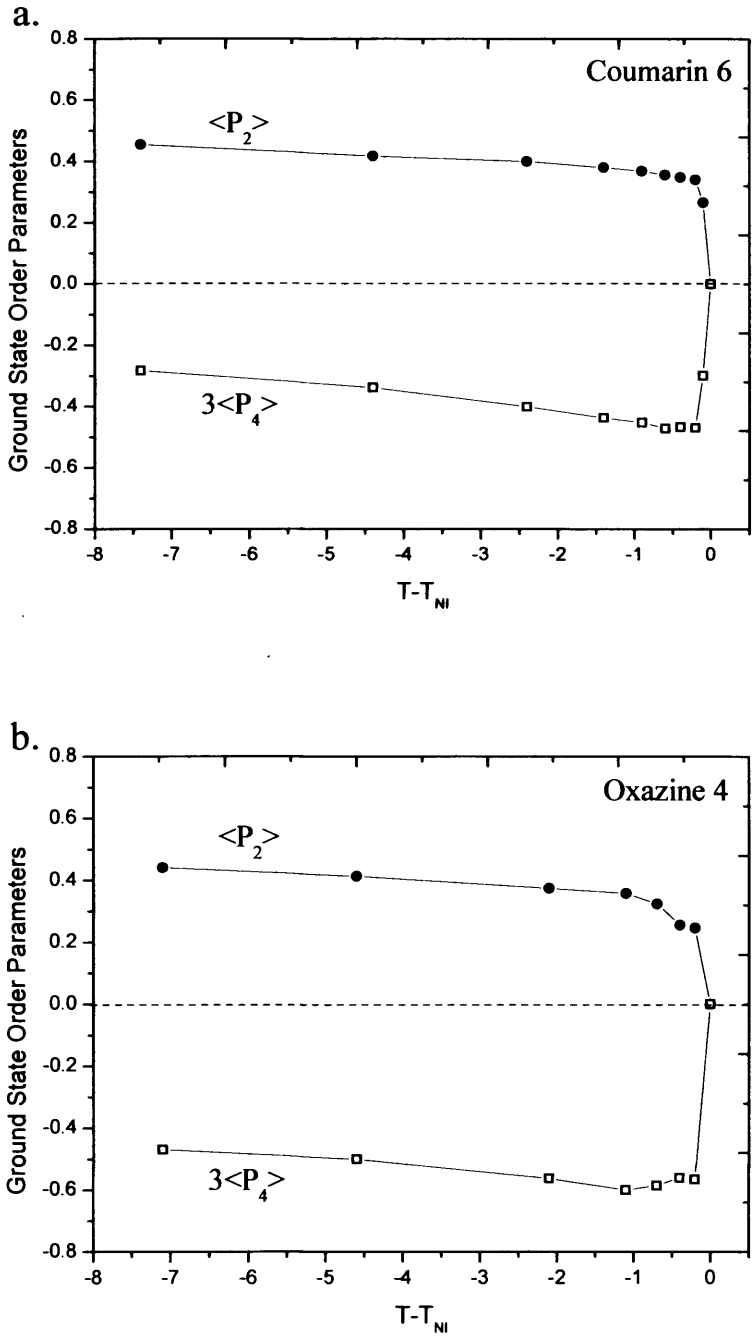

Figure 2.22: Second order $\left(\left\langle \alpha_{20}^{gs} \right\rangle / \sqrt{5} = \left\langle P_2 \right\rangle\right)$ and fourth order $\left(\left\langle \alpha_{40}^{gs} \right\rangle = 3\left\langle P_4 \right\rangle\right)$ parameters for (a) Coumarin 6 and (b) Oxazine 4 in 5CB [6]. For both probes the ground state order parameters demonstrate similar temperature dependence with decreasing positive alignment and increasing negative alignment across the temperature range.

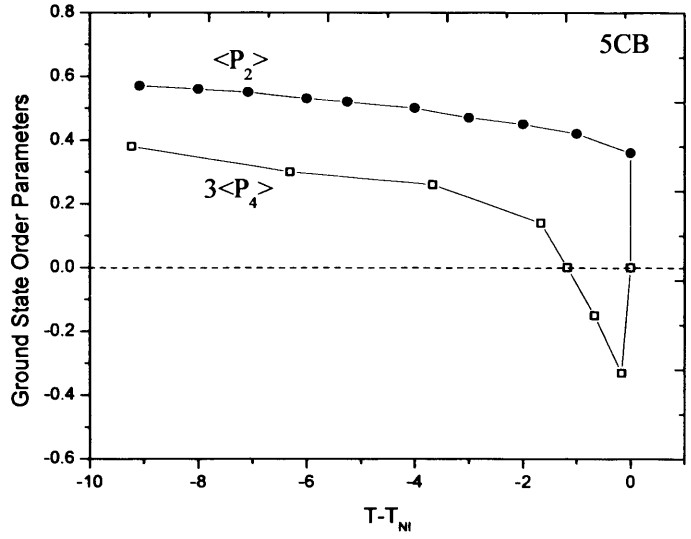

Figure 2.23: Temperature variation in the ground state alignment moments of 5CB across the nematic phase [51]

2.15 Cone Model: Modification of Existing Analytical Techniques

A more detailed picture of the environment of the probe molecules in the nematic host can be obtained if the full orientational distribution function is known. For a cylindrically symmetric system this is given by

$$P_{gs}(\theta,\varphi)=\frac{1}{4\pi}\left[1+\sqrt{4\pi}\sum_{K>0}\left\langle\alpha_k^{gs}(ss)\right\rangle Y_{K0}(\theta,\varphi)\right] \qquad [2.69]$$

Work by Bryant, Monge, Armoogum and co-workers revealed that with moments truncated at K=4, the distributions were physically unreal manifest in regions of negative probability. By applying the method of Shen and co-workers reasonable estimates for the higher moments were made. With the sole constraint that the distribution retains a single maximum between 0° and 90° trial values were added sequentially such that $P^{gs}(\theta, \varphi)\geq 0$. Using this approach for Oxazine 4, the resulting distribution functions approximated well to Gaussian distributions centred about a peak angle θ_{MAX}.

In order to better relate the order in the nematic phase to that in the isotropic phase a cone model has been adapted whereby the probability distribution in θ resembles a cone with equal probability of being between two limits described as $\theta_{MAX} - \frac{1}{2}\theta_{FWHM}$ and $\theta_{MAX} + \frac{1}{2}\theta_{FWHM}$ given by

$$\langle \alpha_{K0} \rangle = \frac{\sqrt{4\pi} \int_0^{2\pi} \int_{\theta_1}^{\theta_2} Y_{K0}(\theta, \vartheta) \sin(\theta) d\theta d\vartheta}{\int_0^{2\pi} \int_{\theta_1}^{\theta_2} \sin(\theta) d\theta d\vartheta} \qquad [2.70]$$

where $\theta_1 = \theta_{MAX} - \frac{1}{2}\theta_{FW}$ and $\theta_2 = \theta_{MAX} + \frac{1}{2}\theta_{FW}$ and K = 2,4.

A Mathematica program has been written in collaboration with Dr R Marsh which allows determination of the peak angle (θ_{MAX}) and full width half maximum ($\Delta\theta_{FWHM}$) of the distribution functions based on equation 2.70 (Appendix III). The temperature dependent variation in the peak angle (θ_{MAX}) of the ground state distribution function of Coumarin 6 in the nematic phase of 5CB is shown in figure 2.24a. Equation 2.70 has been applied to re-analyse data from measurements of Oxazine 4 in the nematic phase of 5CB (Bryant, Monge and co-workers) and is presented in figure 2.24b. For Coumarin 6 θ_{MAX} is found to vary between 32.6° and 42.2° across the nematic temperature range. The peak angle maintains a near positive linear dependence (c.a.1.1°/°C) though in close vicinity of T_{NI} the peak angle decreases (c.a. 2°).Oxazine 4 also maintains a near linear dependence (c.a.0.5°/°C) however in contrast to Coumarin 6, θ_{MAX} peaks sharply in the vicinity of T_{NI} (c.a. 4-5°). In the nematic phase, the 5CB molecules are ordered in an anti-parallel fashion; the cyano groups aligning parallel to the nematic director with the alkyl groups making an angle (θ_{ALKYL}) of c.a. 38° to **n** [6], (figure 2.4). It is interesting to note that for Coumarin 6 θ_{MAX} is oriented at an angle greater than θ_{ALKYL} for most of the nematic temperature range whereas Oxazine 4 maintains a peak angle close to θ_{ALKYL}.

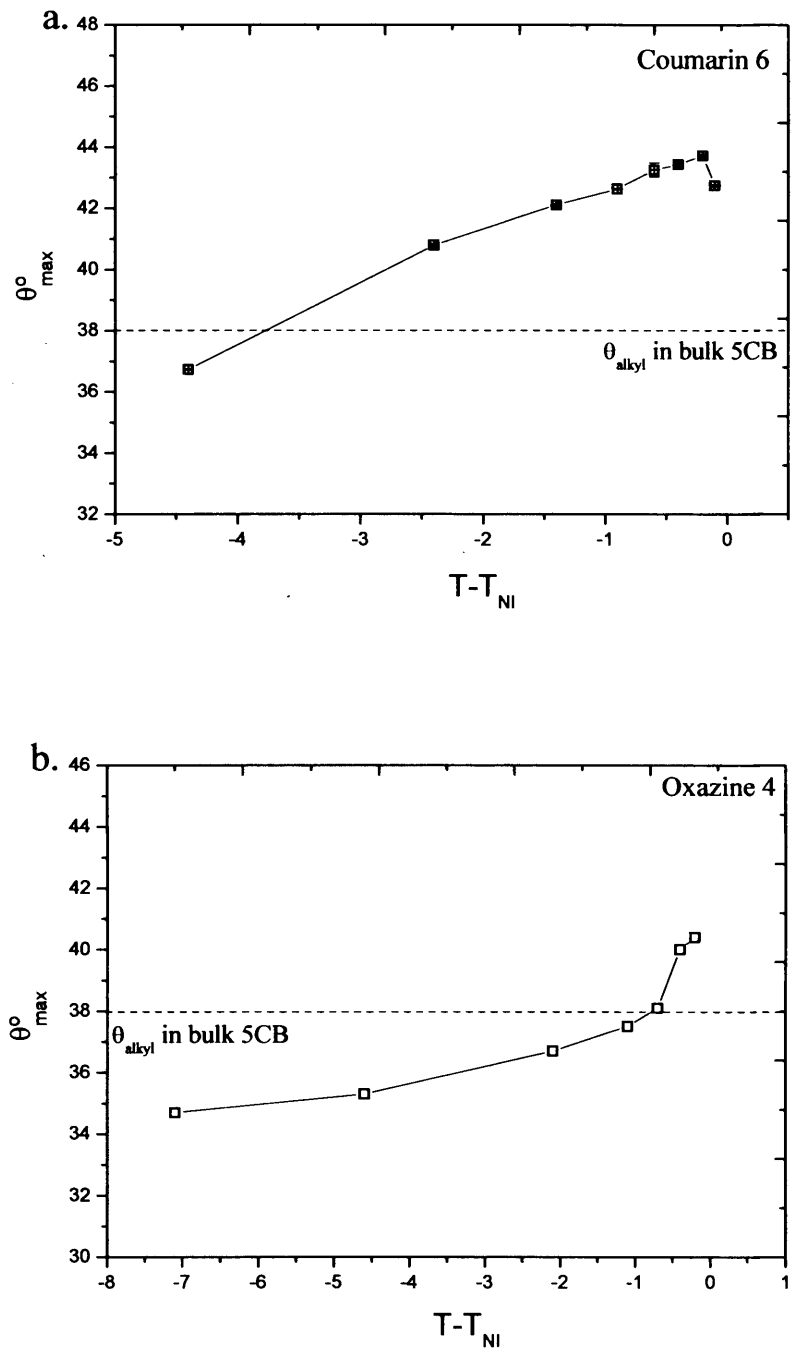

Figure 2.24: Graph illustrating variation in the peak angle of the orientational distribution function with reduced temperature for (a) Coumarin 6 and (b) Oxazine 4 in nematic 5CB. Coumarin 6 follows an almost linear increase to within close vicinity of T_{NI} and has orientational distribution functions peaked at higher angles than Oxazine 4 across the whole temperature range.

The variation in the width of the distribution function for Coumarin 6 and Oxazine 4 as a function of reduced temperature is shown in figure 2.25.

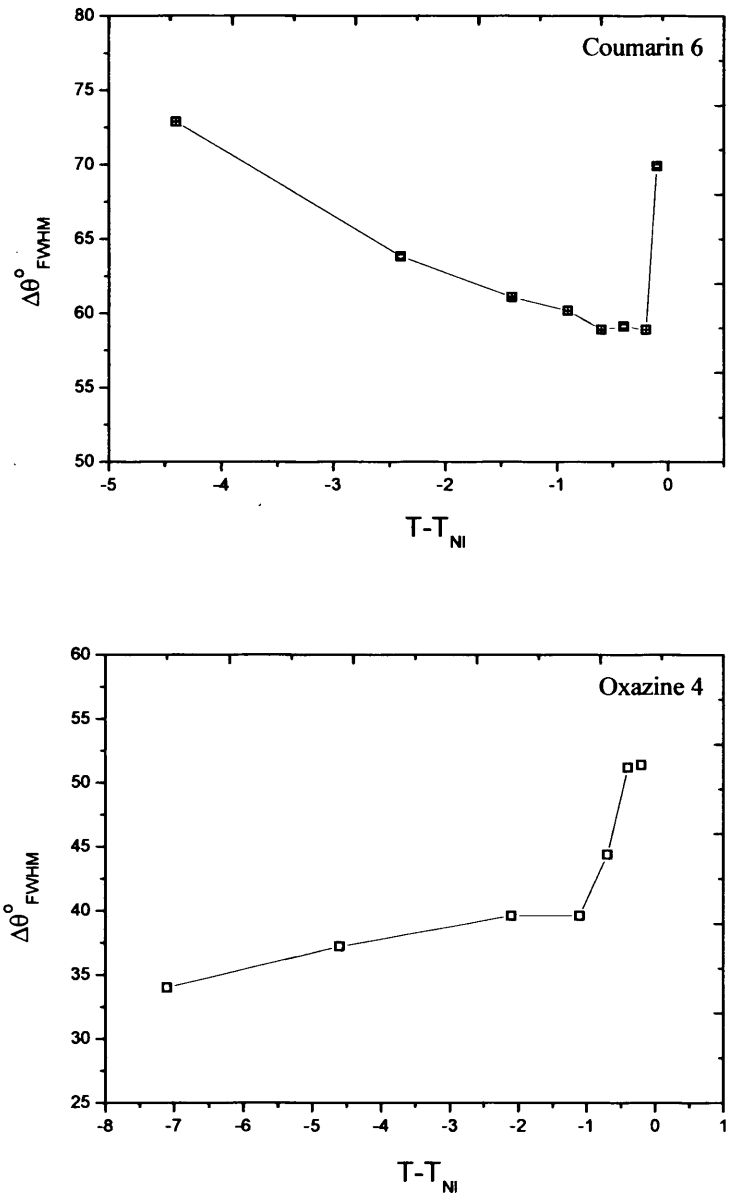

Figure 2.25: Variation of the width of the orientational distribution functions with reduced temperature for Coumarin 6 and Oxazine 4 in nematic 5CB.

It is clear that the variation in the width of the distribution for the two probes is markedly different. For Coumarin 6 the width of the distribution decreases sharply (c.a.2.44°/°C) and this behaviour is maintained to within close vicinity of T_{NI} where the width reaches a minimum at T_{NI}-0.6 and then widens sharply (c.a. 20°) at T_{NI}-0.1° to T_{NI}. For Oxazine 4 $\Delta\theta_{FWHM}$ shows a small (c.a.3-4°) increase with temperature with a

distinct widening of c.a. 12° in the region close to T_{NI}. This is consistent with the probes adopting different sites within the nematic host structure. Cyanobiphenyl molecules are known to be ordered in a 'head to tail' configuration [58]. It was suggested by Bryant and Monge that the elimination of one cyanobiphenyl dimer allows the formation of a pocket of approximately the correct symmetry and volume for the oxazine probe molecule to occupy [2]. This is consistent with the width of the distribution which is tightly constrained about θ_{ALKYL} suggesting that the position of the Oxazine 4 molecule is well correlated with the 5CB structure. In contrast Coumarin 6 shows a very broad orientational distribution; although this decreases with temperature it does not become as narrow as Oxazine 4. Additionally θ_{MAX} does not correlate as well with θ_{ALKYL} showing stronger temperature dependence. This suggests that Coumarin 6 adopts a less ordered position within 5CB than Oxazine 4. This may possibly be due to either the presence of Coumarin 6 causing a greater disruption of the local 5CB structure or its adoption of a significantly different position within the host environment.

2.16 Coumarin 6 Orientational Relaxation Dynamics in Nematic 5CB

2.16.1 Determination of the Cylindrically Asymmetric Relaxation Time τ_{22}

Modification of the technique to extract the cylindrically asymmetric relaxation time has been undertaken by Monge and co-workers. Originally resolved from anisotropy data collected at a polarisation angle of $\beta=90^{o}$ relative to the nematic director, determination of the asymmetric relaxation time τ_{22} is now based upon the analysis of the vertically (I_Z) and horizontally (I_X) polarised fluorescence intensities at an excitation polarisation angle of $\beta=54.7^{o}$ [2]. At this angle (assuming only a small degree of excited state reorientation such that $\langle \alpha_{20}^{ex}(0) \rangle \approx \langle \alpha_{20}^{gs}(ss) \rangle$) the polarised fluorescence intensities are given by

$$I_Z(\beta = 54.7^{o}) = C' \exp\left(\frac{-t}{\tau_f}\right)\left[\frac{1}{A} + \frac{2}{\sqrt{5}}\langle \alpha_{20}^{ex}(ss) \rangle\right] \qquad [2.71]$$

$$I_X(\beta = 54.7^{o}) = C'' \exp\left(\frac{-t}{\tau_f}\right)\left[\frac{1}{A} + \sqrt{\frac{3}{10}}\left\{\langle \alpha_{22}^{ex}(0) \rangle + \langle \alpha_{2-2}^{ex}(0) \rangle\right\}\exp\left(\frac{-t}{\tau_{22}}\right)\right] \qquad [2.72]$$

The ratio of the two intensities solely contains the asymmetric alignment dynamics τ_{22}

$$\frac{I_X}{I_Z}\left(\beta = 54.7^O\right) = C''' \left[\frac{\frac{1}{\overline{A}} + \sqrt{\frac{3}{10}} \left\{ \left\langle \alpha_{22}^{ex}(0) \right\rangle + \left\langle \alpha_{2-2}^{ex}(0) \right\rangle \right\} \exp\left(\frac{-t}{\tau_{22}} \right)}{\frac{1}{\overline{A}} + \frac{2}{\sqrt{5}} \left\langle \alpha_{20}^{ex}(ss) \right\rangle} \right] \qquad [2.73]$$

The variation in τ_θ and τ_φ with reduced temperature for Coumarin 6 is shown in figure 2.26 along with the values of τ_θ and τ_φ for Oxazine 4 in 5CB as per Monge, Bryant and co-workers.

The cylindrically symmetric (τ_{20}) times were determined from equation 2.6 the cylindrically asymmetric times (τ_{22}) were determined using equation 2.73. Providing the orientational distributions are dominated by anisotropic friction, the small θ dependence present in τ_{22} can be removed yielding a pure φ diffusion time [2, 15] through the equation

$$\tau_\varphi = \frac{2\tau_{20}\tau_{22}}{3\tau_{20} - \tau_{22}} \qquad [2.74]$$

The reorientational lifetimes (τ_θ and τ_φ) for Coumarin 6 are approximately equal (within experimental error bars) indicating that the relaxation of the symmetric alignment (θ-diffusion) is very similar to that of the asymmetric alignment (φ-diffusion). This is somewhat unusual as it demonstrates behaviour expected in a wholly isotropic medium where θ-diffusion and φ-diffusion are necessarily equal. This is not generally the case for an ordered medium where symmetry considerations of perturbed rotational diffusion demand that the two times are unequal [20]. Only in the region of the phase transition temperature does Coumarin 6 show any change as τ_θ decreases in the approach to T_{NI}. This is in marked contrast to θ and φ motion for Oxazine 4 where τ_θ and τ_φ are clearly different and described by approximately temperature independent φ-diffusion (similar to that seen in Coumarin 6) although it slows in the approach to T_{NI}, and θ-diffusion which is considerably slower and decreases across the nematic temperature range converging with τ_φ at T_{NI}.

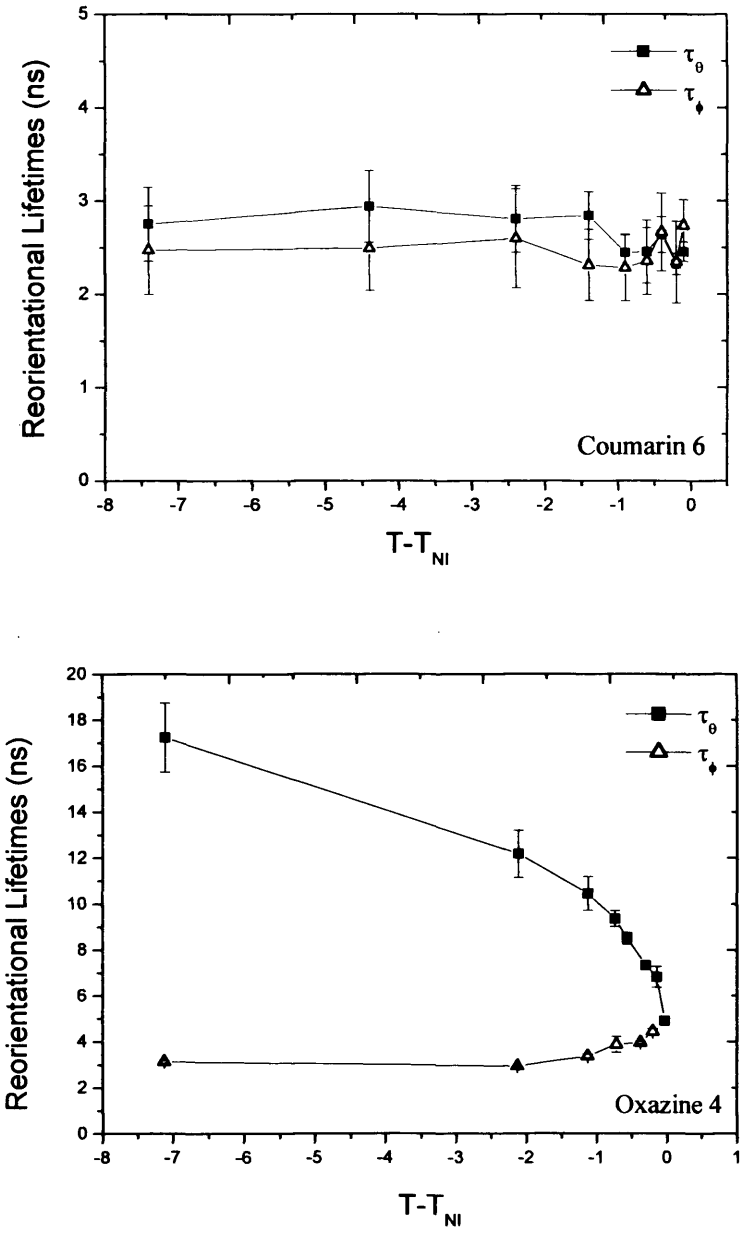

Figure 2.26: Variation in the orientational relaxation times (τ_θ) and (τ_φ) with reduced temperature for Coumarin 6 and Oxazine 4 in the nematic phase of 5CB.

It is clear from the results that Coumarin 6 possesses rotational dynamics that are largely isotropic ($\tau_\theta \approx \tau_\varphi$) unlike those of Oxazine 4 where $\tau_\theta >> \tau_\varphi$. The differences in τ_θ and τ_φ for Oxazine 4 have been accounted for by Bryant and Monge in terms of the effective friction (i.e. viscosity) experienced by θ and φ motions of the probe [1, 2]. As Oxazine 4 is seen to correlate strongly with the order of the liquid crystal host, the rotational diffusion of the probe exhibits a similar asymmetry to that of the nematic host in which the bulk viscosity is highly anisotropic [58]. In this case θ motion becomes less

restricted whilst the slowing of φ motion was accounted for in terms of the uncorrelated motion of different segments of the tails of individual cyanobiphenyl molecules whose interference acts to hinder φ-diffusion [1, 2]. This is not the case for Coumarin 6 where the difference in θ and φ motion appears negligible, indicative of a much more isotropic environment for the probe. Additionally θ-diffusion is observed to be much faster than for Oxazine 4 at a rate more akin to unrestricted diffusion in a simple liquid (section 2.12). The slow θ-diffusion times for Oxazine 4 were attributed to the tight structural constraints on the probe leading to predominantly 'stick' dynamics. The much faster θ-diffusion times coupled with the isotropic diffusional behaviour for Coumarin 6 however suggest predominantly 'slip' boundary conditions.

The diffusion dynamics discussed above combined with the lower orientational constraints compared with Oxazine 4 suggest that Coumarin 6 occupies a much less structured environment with much greater orientational freedom. This can be further highlighted by a plot of the proportion of orientational space the molecule can occupy as shown in figure 2.27.

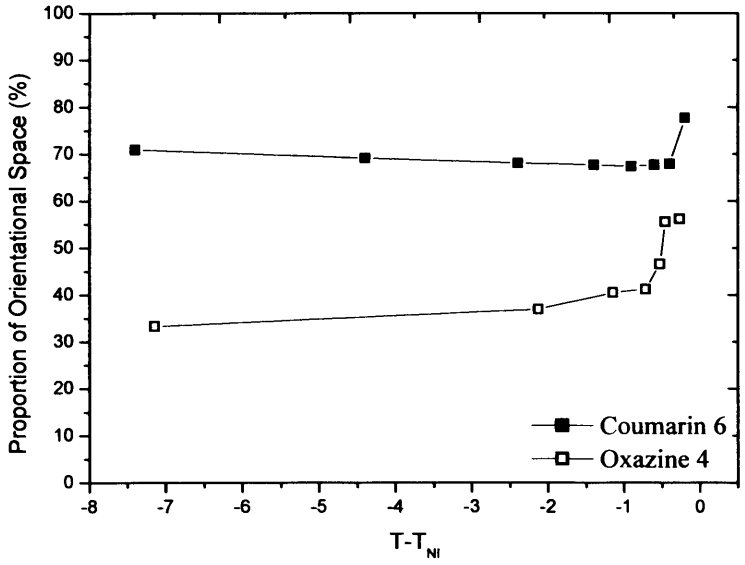

Figure 2.27: Graph showing proportion of unit sphere occupied by the probe using the cone model. It is evident that Coumarin 6 is in a much less restricted environment than Oxazine 4 and is temperature invariant.

This plot combined with the experimental results above strongly suggest that Oxazine 4 is in a much more restrictive environment than Coumarin 6 and that this environment is sensitive to the temperature dependent anisotropic behaviour of the host. In contrast Coumarin 6 appears to adopt a position within the local environment which is insensitive to the behaviour of the 5CB molecules across the nematic phase. A possible reason for this is the up-take of the probe into the alkyl tail region of the liquid crystal host possibly combined with distortion of the local nematic structure due to the larger size and hydrophobic nature of Coumarin 6.

2.17 Orientational Dynamics and Local Order of Coumarin 6 in Isotropic 5CB

2.17.1 Results

For all experiments undertaken in the isotropic phase of 5CB, the phase transition was identified by a sudden loss in scattered laser light from the sample and confirmed when the fluorescence anisotropy $R(t, \beta)$ was seen to decay to zero irrespective of polarisation angle β. Subsequent measurements were carried out with the polarisation angle set at $\beta=0^{o}$ as θ and φ diffusion are equivalent in an isotropic environment.

The orientational lifetimes showing the behaviour of both the fast component τ_{fast} and slow component τ_{slow} of the fluorescence anisotropy decays of both dyes as a function of reduced temperature across the isotropic phase of 5CB is shown in figure 2.28.

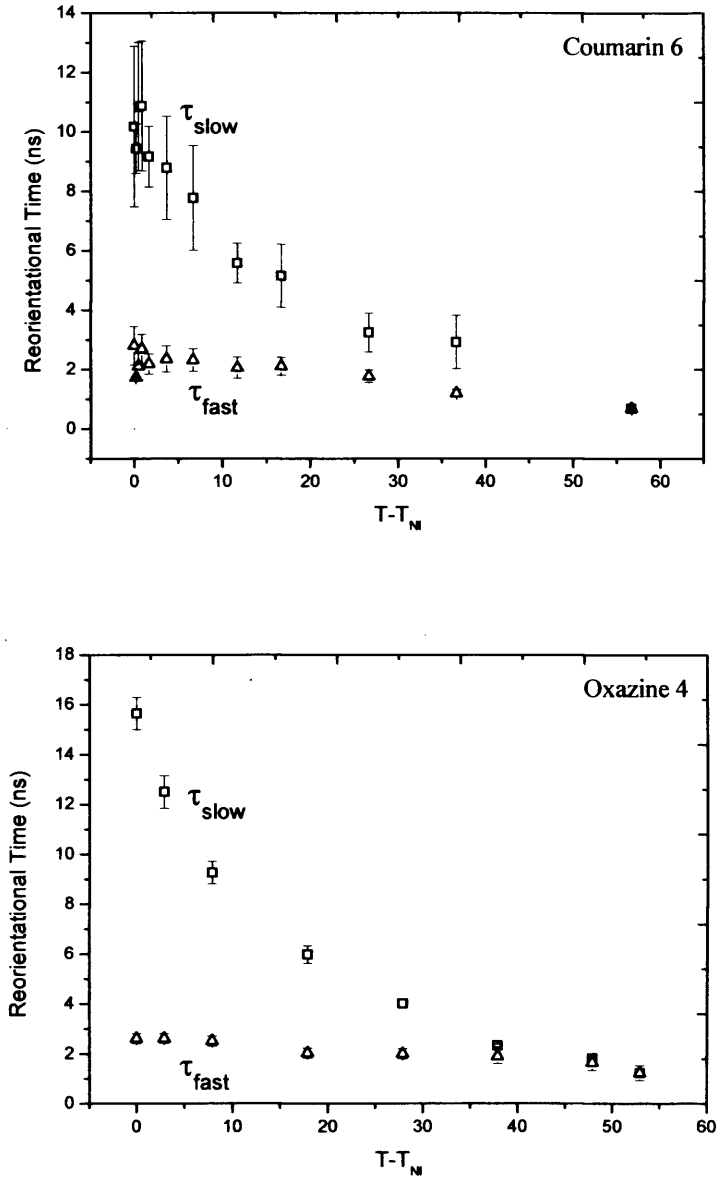

Figure 2.28: Variation with temperature in the fast and slow orientational relaxation times (τ_{fast} and τ_{slow}) for Coumarin 6 and Oxazine 4 in 5CB.

The slow overall diffusion time (τ_{slow}) variation with temperature is related to the temperature dependent shear viscosity of the liquid crystal in the isotropic phase by

$$\tau_S \approx \frac{1}{k_B}\frac{\eta(T)V_{eff}}{(T-T^*)} + \tau_0 \qquad [2.75]$$

where V_{eff} is the hydrodynamic volume of the Coumarin 6 dye molecule, τ_0 is the free rotor correlation time, k_B the Boltzmann constant and T* is the virtual transition

temperature the value of which (c.a. 292K extracted from equation 2.75) was found to be lower than that of pure 5CB (c.a. 307K) [1]. For Coumarin 6 to demonstrate LDG then a plot of τ_s versus $\eta(T)/(T-T^*)$ from equation 2.75 should yield a straight line. As can be seen from figure 2.29 Coumarin 6 is not as LDG compliant as Oxazine 4 which displays a far more linear dependence.

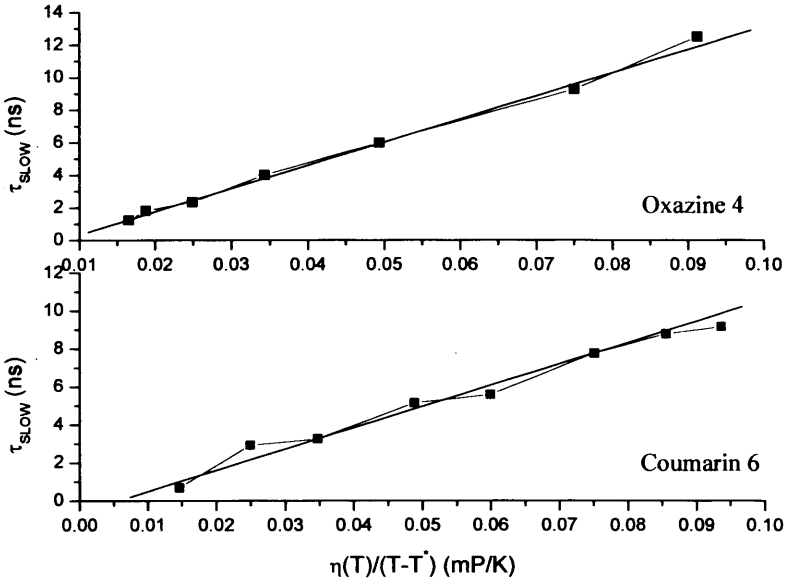

Figure 2.29: Comparison of the compliance of Coumarin 6 with LDG by measuring the slow reorientational time τ_s against $\eta(T)/(T-T^*)$. Oxazine 4 (which shows good LDG behaviour) is shown for comparison. {The original data for Oxazine 4 is taken from work by Bryant [1].

The fast relaxation time (τ_{fast}) is largely temperature independent and does not follow the LDG model. A number of theories have been proposed by Fayer and co-workers whereby the fast and slow time dynamics are related to the intra and inter domain relaxation processes [47]. Previous work by Monge and Bryant found that the reorientational dynamics of the Xanthene probes in the isotropic phase of n-cyanobiphenyls were in broad agreement with these theories. Dutt and co-workers [59] have measured the rotational dynamics of Coumarin 6 in the isotropic phase of the liquid crystal MBBA and found that the reorientation dynamics follow basic hydrodynamic theory (SED) rather than the model of LDG. Though the fluorescence lifetimes recovered for Coumarin 6 in 5CB (2.75ns) are comparable to those in MBBA (2.58-2.10ns), the anisotropy decays are found to be markedly different. Values of the initial anisotropy for Coumarin 6 in 5CB as a function of reduced temperature are shown in figure 2.30. The values of R(0) (c.a. 0.367-0.312) show a slight decrease with

temperature, whilst not substantially different, is larger than that observed in xanthenes [1, 2]. The temperature dependence of R(0) suggests that depolarisation may be affected by a fast solvation component which is beyond the detection capabilities of the experimental set-up. Dutt and co-workers recovered relatively low initial values of R(0) (c.a. 0.12) increasing with temperature. Such depolarisation was accounted for in terms of limitations in the ability to detect fast intra-domain relaxation dynamics. It is apparent that for Coumarin 6 in 5CB the intra-domain dynamics are of a detectable timescale so in this instance cannot account for the decreasing value of the initial anisotropy with increasing temperature.

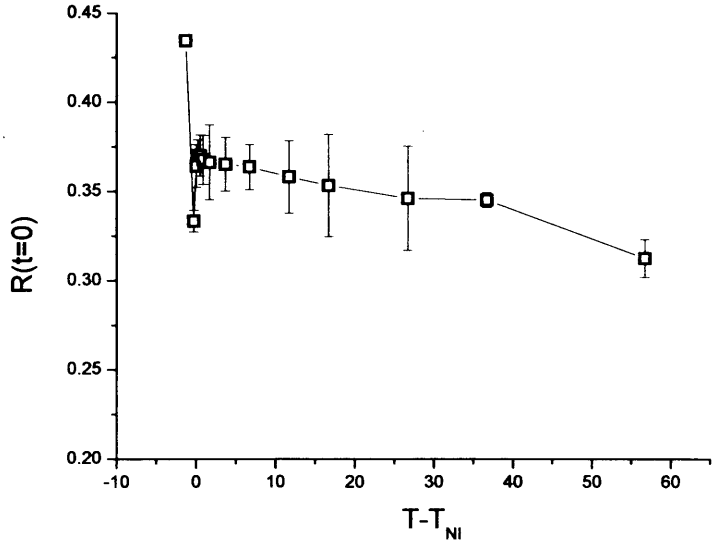

Figure 2.30: Values of the initial anisotropy for coumarin 6 in the isotropic phase of 5CB. Values extracted from anisotropy decay at β=0°.

The variation in the cone angle (as defined in section 2.8) for Coumarin 6 and Oxazine 4 in the isotropic phase of 5CB along with the full width half maximum of the cone model fits to the probe distribution function in the nematic phase are shown in figure 2.31. For Coumarin 6 the isotropic cone angle remains approximately constant from T_{NI}-T_{NI}+16.7 where the width increases sharply (c.a. 39°) to T_{NI}+36.7. Beyond this temperature there is a rapid collapse to a wholly isotropic environment. This collapse was also observed in Oxazine 4 by Bryant and Monge but at a slightly higher temperature. Furthermore the near independence of the cone angle of Oxazine 4 with temperature is not observed in Coumarin 6.

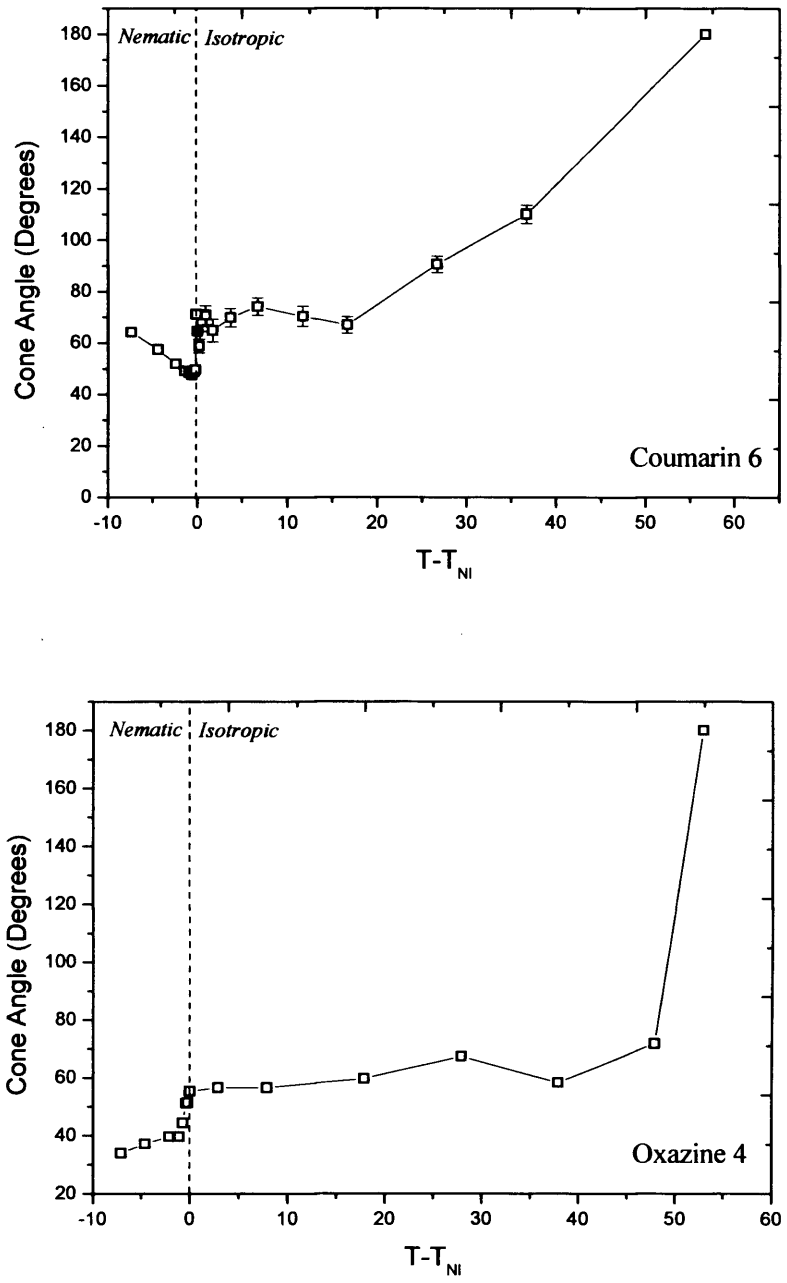

Figure 2.31: Cone angle for Coumarin 6 and Oxazine 4 in 5CB as a function of reduced temperature in both the nematic and isotropic phases of 5CB. Also shown is the FWHM angle dependence of the probe molecules in the nematic phase.

This would tend to indicate the local environment around Oxazine 4 is not sufficiently changing as the size of the pseudo-domains reduces with temperature. Conversely Coumarin 6 seems to have even greater orientational freedom as the correlation length reduces. A second notable difference in the behaviour of the two probes is seen in the rotational diffusion times at the phase transition as shown in figure 2.32. For Oxazine 4

τ_θ and τ_φ approach 5ns at T_{NI} however in the isotropic phase τ_{fast} which represents the rotational diffusion time within the liquid crystal domain corresponds to the mid-nematic range diffusion time τ_φ.

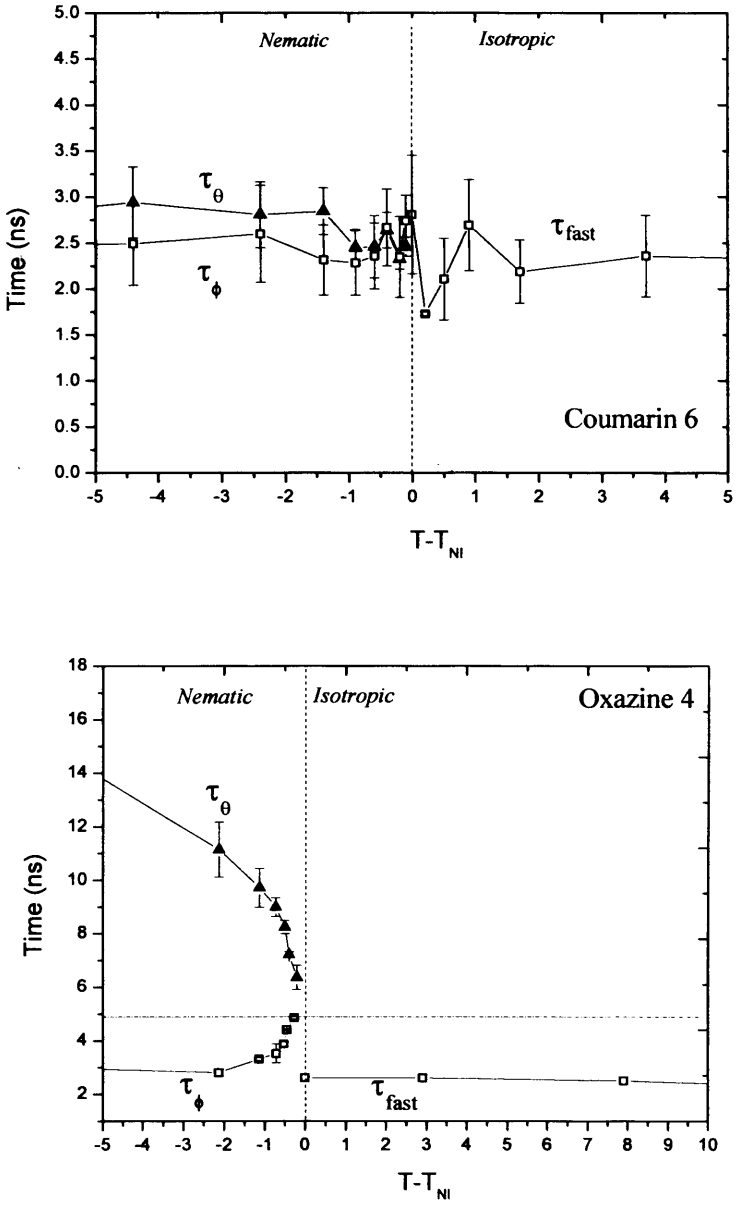

Figure 2.32: Comparison of the intra-domain relaxation times with θ and φ-diffusion times either side of the phase transition for Coumarin 6 and Oxazine 4 in 5CB.

This behaviour is not observed in Coumarin 6 where there is essentially no change in the diffusion dynamics. This tends to support the findings from the nematic phase results which indicate that the orientational motion of Oxazine 4 is highly coupled to the liquid crystal host (i.e. stick boundary conditions) and therefore sensitive to the

structural changes at the phase transition. In contrast Coumarin 6 is in a more isotropic and possibly distorted environment that does not change significantly through the phase transition.

Bryant and Monge also studied other Xanthene probes in 5, 6 and 7 CB and similar behaviour was observed as for Oxazine 4 in 5CB. A slight departure form this behaviour was observed for Rhodamine B which showed a smaller difference between θ and φ-diffusion times and a slightly larger centre angle. These differences are small when compared to those of Coumarin 6 in this work.

2.18 Conclusion

To the best of our knowledge this study represents the first investigation of the full angular motion and molecular order of Coumarin 6 in a highly aligned nematic liquid crystal. Coumarin 6 dynamics are seen to depart considerably from those of Oxazine 4 in the nematic phase. Rotational diffusion with respect to the (global) nematic director is seen to be both fast and isotropic with $\tau_{\theta} \approx \tau_{\varphi}$. This indicates the predominance of slip boundary conditions. The width of the distribution function further suggests that the orientation of Coumarin 6 is only weakly correlated to the liquid crystal host unlike Oxazine 4 and other Xanthene dyes [1, 2]. Isotropic phase behaviour further supports these conclusions. Both the poor LDG behaviour and lack of sensitivity of the dynamics to the phase transition also suggest poor correlation between probe and host.

As described in section 2.3 the defining characteristics of the nematic phase of a liquid crystal is the strong propensity of the individual molecules to self-align with each other. This is manifest by a high degree of anisotropy in both bulk and microscopic properties. Oxazine 4 is seen to closely follow this behaviour and the corresponding changes with temperature. It has been argued by Bryant and Monge, supported by further analysis in this work that Oxazine 4 occupies a position between the phenyl cores of the 5CB molecules with little disruption to the surrounding structure, hence the strong correlation with the host. This is consistent with the hydrophilic nature of Oxazine 4. In contrast Coumarin 6 does not show anisotropic diffusional behaviour or the associate temperature dependence, coupled with much greater orientational freedom. It is

therefore suggested that Coumarin 6 occupies a position amongst the alkyl tails of the 5CB molecules along with associated disruption of the local structure due to the larger volume of Coumarin 6 thus causing the molecule to feel a much more isotropic environment. This would be consistent with the much more hydrophobic nature of Coumarin 6 when compared with Oxazine 4 thus preventing its up-take in a similar position. It has been shown that for Coumarin 6 in squalane (a viscous alkane environment) slip hydrodynamic conditions predominate [60] which is consistent with our observations in 5CB. A feature of the Oxazine 4 data was the slowing of φ-diffusion close to the phase transition temperature. This has been explained as increasing entanglement of the alkyl tails with temperature ('bi-axial fluctuation') [1, 61]. The presence of Coumarin 6 in the alkyl region may hinder this process thereby accounting for the temperature invariance of the diffusion times. Additionally it is possible that in the isotropic phase, disruption to the local ordering within the pseudonematic domains might account for the apparent break up of the domains at a lower temperature than for Oxazine 4. Furthermore this may also account for the increase in orientational freedom of the probe as the temperature increases and the correlation length decreases. The lessening tendency of the 5CB molecules to self align as the temperature increases aids disruption of the structure by the presence of the probe. A proposed position of Coumarin 6 within the host is shown in figure 2.33 alongside that previously suggested for Oxazine 4.

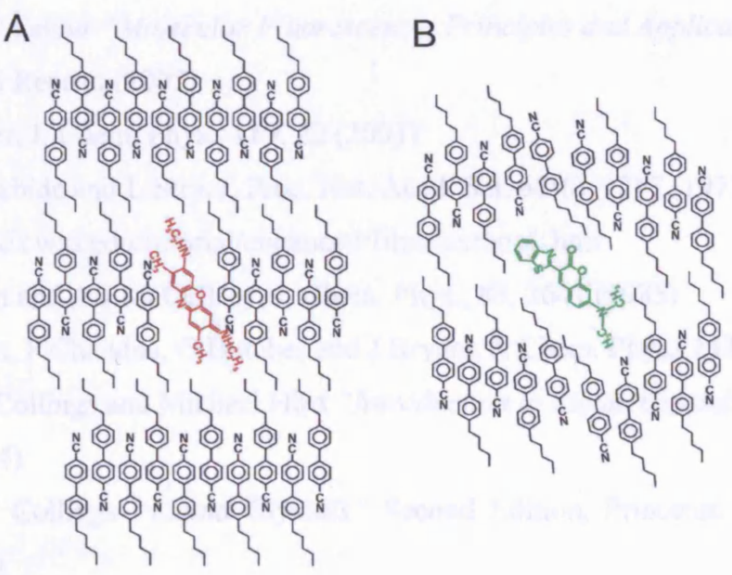

Figure 2.33: Illustration of the suggested positions of (a) Oxazine 4 and (b) Coumarin 6 in 5CB. Oxazine 4 is assumed to adopt a position between the phenyl cores whereas Coumarin 6 is assumed to be located in the alkyl tails.

References

[1] J. Bryant, Ph. D. Thesis, University of Essex, (2000)

[2] E M Monge, Ph.D. Thesis, University of London (2003)

[3] P K McCarthy and G J Blanchard J. Chem. Phys., **97**, 47 (1993)

[4] M L Horng, J A Gardecki and M Maroncelli, J. Phys. Chem. A, **101**, 6 (1997)

[5] H Jin, G A Baker, S Arzhantsev, J Dong and M Maroncelli, J. Phys. Chem. B., **111**, 25 (2007)

[6] J Rau, C Ferrante, E Kneuper, F-W Deeg and C Bräuchle, J. Phys. Chem. A., **105**, 24 (2001)

[7] N. Ito, S. Arzhantsev, M. Heitz, and M. Maroncelli, J. Phys. Chem. B., **108**, 18 2004

[8] M. El-Kemary and W. Rettig, Phys. Chem. Chem. Phys., **5**, 5221 (2003)

[9] V Kapko and D V Matyushov, J. Chem. Phys, **124**, 114904 (2006)

[10] K A Nguyen, P N Day and R Pachter, J. Chem. Phys., **126**, 094303 (2007)

[11] Theodore G. Pavlopoulos, Applied Optics., **36**, 21 (1997)

[12] G. A. Reynolds and K. H. Drexhage, Optics Commun., **13**, 222 (1975)

[13] Oregon Medical Laser Center PhotoChemCAD Spectra
URL: http://omlc.ogi.edu/spectra/PhotochemCAD/html/index.html

[14] G Jones II, W R Jackson, C Choi, W R Bergmark, J. Chem. Phys., **89**, 2 (1985)

[15] Bernard Valeur *"Molecular Fluorescence; Principles and Applications"* Wiley-VCH Second Reprint (2005)

[16] G B Dutt, J. Chem. Phys., **119**, 22 (2003)

[17] J Yguerabide and L Stryer, Proc. Nat. Acad. Sci. **68**(6), 1217 (1971)

[18] http://plc.cwru.edu/tutorial/enhanced/files/textbook.htm

[19] A J Bain and A J McCaffrey, J. Chem. Phys., **83**, 2641 (1985)

[20] A J Bain, P Chandna, G Butcher and J Bryant, J. Chem. Phys., **112**, 10435 (2000)

[21] Peter J Collings and Michael Hird *"Introduction to Liquid Crystals"* Taylor and Francis (2004)

[22] Peter J Collings *"Liquid Crystals"* Second Edition, Princeton University Press (1992)

[23] W H de Jeu *"Physical Properties of Liquid Crystalline Materials"* Liquid Crystal Monographs Volume 1, Gordon and Breach (1980)

[24] G W Gray and K J Harrison, UK Patent 1 433 130

[25] H Kelker and B Scheurle, Angew. Chem., **8**, 884 (1969)

[26] LiqCryst Online http://liqcryst.chemie.uni-hamburg.de/lolas-www/main.html

[27] P W Atkins, *"Molecular Quantum Mechanics"* Second Edition, Oxford University Press (1992)

[28] G R Fleming and M Cho, Ann. Rev. Phys. Chem., **47**, 109 (1996)

[29] A J Bain, P Chandna, G Butcher and J Bryant, J. Chem. Phys. **112**, 10418 (2000)

[30] D.L. Andrews and A.A. Demidov (Ed.) *"An Introduction to Laser Spectroscopy"* Second Edition, Kluwer, (2002)

[31] M de Podesta *"Understanding the Properties of Matter"* Second Edition, Taylor and Francis (2002)

[32] W D Callister Jr, "*Materials Science and Engineering*" (5th Ed.), Wiley (2000)

[33] B H Flowers and E Mendoza, "*Properties of Matter*" Third Edition, Wiley (1991)

[34] S Elliott *"The Physics and Chemistry of Solids"* Wiley (2005)

[35] F Mandl *"Statistical Physics"* Second Edition, Wiley (1994)

[36] P Papon, J Leblond and P H E Meijer "*The Physics of Phase Transitions*" Second Edition, Springer (2006)

[37] D Demus, J Goodby, G W Gray, H-W Spiess and V Vill "*Handbook of Liquid Crystals Volume 2A*" First Edition Wiley-VCH (1998)

[38] J Bryant and A J Bain, Chem. Phys. Lett., **286**, 121 (1998)

[39] S Chandrasekhar *"Liquid Crystals"* Second Edition, Cambridge University Press (1992)

[40] A Sengupta and M D Fayer, J. Chem. Phys., **102**, 10 (1995)

[41] W Stinson and J D Lister, Phys. Rev. (Lett)., **25**, 503 (1970)

[42] H J Coles, Mol. Crystl. Liq. Cryst (Lett)., **49**, 67 (1978)

[43] F W Deeg, J J Stankus, S R Greenfield, V J Newell and M D Fayer, J. Chem. Phys., **90**, 6893 (1989)

[44] S.D. Gottke, D.D. Brace, H. Cang, B. Bagchi and M.D. Fayer, J. Chem. Phys. **116,** 360 (2002)

[45] S.D. Gottke, H. Cang, B. Bagchi and M.D. Fayer, J. Chem. Phys. **116**, 6339 (2002)

[46] K Kinosita, S Kawato and A Ikagami, Biophys. J., **20**, 289 (1977)

[47] J J Stankus, R Torre, C D Marshall, S R Greenfield, A Sengupta, A Tokmakoff, M.D. Fayer, Chem. Phys. (Lett)., **194,** 213 (1992)

[48] D V O'Connor and D V Phillips, *"Time Correlated Single Photon Counting"* Academic Press (1984)

[49] P Debye, *"Polar Molecules"*, Dover, New York (1929)

[50] G Vertogen and B W van der Meer, Phys. Rev. A **19**, 370-374 (1979)

[51] F Perrin, J .Phys. Radium., **5**, 497 (1934)

[52] C M Hu and R Zwanzig, J Chem. Phys., **60**, 4354 (1974)

[53] D M Brink and G R Satchler, *"Angular Momentum"* Second Edition, Clarendon Press, (1968)

[54] S D Durbin and Y R Shen, Phys. Rev. A., **30**(3), 1419 (1984)

[55] S T Wu and C S Wu, Opt. Eng., **32**(8), 1775 (1993)

[56] J R Lakowicz, *"Principles of Fluorescence Spectroscopy"* Second Edition, Kluwer Academic, (1999)

[57] A. J. Bain and A. J. McCaffery, J. Chem. Phys., **80**, 5893 (1984)

[58] A Arcioni, F Bertinelli, R Tarroni and C Zannoni, Molecular Physics., **61** (5), 1161 (1987)

[59] G B Dutt, J. Phys., Chem **119**, 22 (2003)

[60] G B Dutt and A Sachdeva, J. Chem. Phys., **118**, 18 (2003)

[61] S V Dvinskikh, I Furo, H Zimmerman and A Maliniak, Phys. Rev. E., **65**, 061701 (2002)

Chapter 3

Studies in the Nematic and Isotropic Phase of 5 Cyanobiphenyl Part II: Coumarin 153

3.1 Introduction

The solvatochromic properties of Coumarin 153 have been studied extensively in a variety of polar and non-polar plain solvents [1] but little is known about the behaviour in aligned polar environments. In fact there have been few publications in the field of solvation dynamics in nematic liquid crystals [2, 3, 4]. It is well known that shifts in absorption and emission bands can be induced by a change in solvent nature or composition. A probe molecule such as Coumarin 153 undergoes intra-molecular charge transfer on excitation such that the dipole moment in the excited state is significantly higher than that in the ground state. The resulting solvent relaxation around the probe lowers the free energy of the excited state causing a red-shift in the emission (figure 3.1). The degree of red-shift will depend on the relative polarity of both the solvent and solute, and the rate of solvent relaxation is dependent on solvent viscosity.

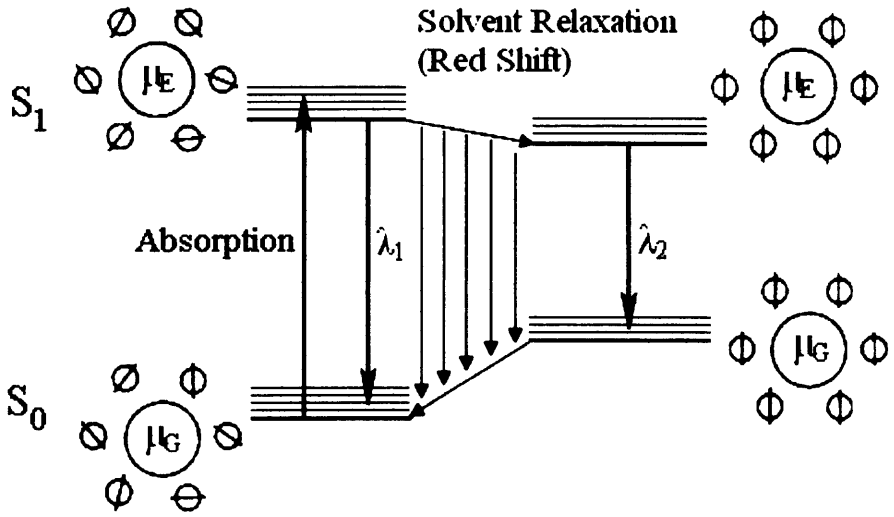

Figure 3.1: Schematic illustrating solvent relaxation and associated red shift in emission around a probe such as Coumarin 153 which possesses a large difference between its ground and excited state dipole moments. λ_1 and λ_2 represent blue emission and red-shifted emission respectively

In a completely isotropic environment the torque applied by all the solvent-solute interactions sums to zero; thus solvent relaxation only involves reorientation of the solvent about the solute [5]. However if the solvation shell is highly anisotropic considerable net torque may be applied to the solute resulting in reorientation of both solvent and solute molecules to minimize the free energy. This is notable where the solvent is highly viscous or orientationally constrained such as in a liquid crystal [6].

In this chapter Coumarin 153 is used to investigate the highly aligned nematic and isotropic phases of 5CB and compared to the behaviour of Coumarin 6 (Chapter 2). The detailed investigation of Coumarin 153 in 5CB is carried out in three distinct spectral regions (455-500nm {Blue}, >530nm, >570nm {Red}). In spectrally resolving the emission into blue and red edge components the solvatochromic properties of Coumarin 153 are enhanced. However the large difference in ground and excited state dipole moments on excitation and the subsequent substantial solvent-solute reorganization negates the method developed in Chapter 2 (section 2.13) for calculating the correction factor k and complicates the procedure to determine the value of τ_{22} in the nematic phase, from the ratio of the intensities I_H/I_V (β=54.7°) [7]. Therefore in order to determine the orientational dynamics of Coumarin 153 in the nematic phase of 5CB it has been necessary to develop a procedure involving global analysis of polarised intensity decays.

To date work in this group has concentrated on probes which do not show solvation effects in the cyanobiphenyls. Coumarin 153 is known to exhibit strong solvation in many plain solvents and it would therefore be surprising if it did not demonstrate more complex behaviour than probes previously studied by the group. Such behaviour will challenge conventional methods developed to date in analysing the behaviour of dye probes doped in 5CB resulting in novel analytical techniques.

	Coumarin 6	Coumarin 153
Composition	$C_{20}H_{18}N_2O_2S$	$C_{16}H_{14}NO_2F_3$ ·
Quantum Yield	0.78[8]	0.90[9]
Absorption Maximum	458nm	423nm
Emission Maximum	505nm	530nm
Molar Absorptivity ($L\ mol^{-1}\ cm^{-1}$)	$5.4x10^4$	$1.89x10^4$
Molecular Weight (g/mol)	350.43	309.29
Hydrodynamic Volume	436Å^3 [10]	246Å^3 [11]
Ground State Dipole Moment [12]	7.00D	6.68D
Excited State Dipole Moment [12]	8.60D	13.64D
$\Delta\mu$ (μ_e - μ_g)	1.60D	6.96D

Table 3.1: The photophysical and hydrodynamic properties of Coumarin 6 and Coumarin 153

3.2 Coumarin 153 in Ethylene Glycol: Results

All measurements in section 3.2 have been carried out using the same experimental set-up described in section 2.11 and the results analysed in the same manner using MicroCal™ Origin software. A single photon excitation wavelength of 470nm was chosen and a long pass filter (Schott RD530) was used to isolate all emission long of 530nm. The anisotropy decay for Coumarin 153 in ethylene glycol is shown in figure 3.2.

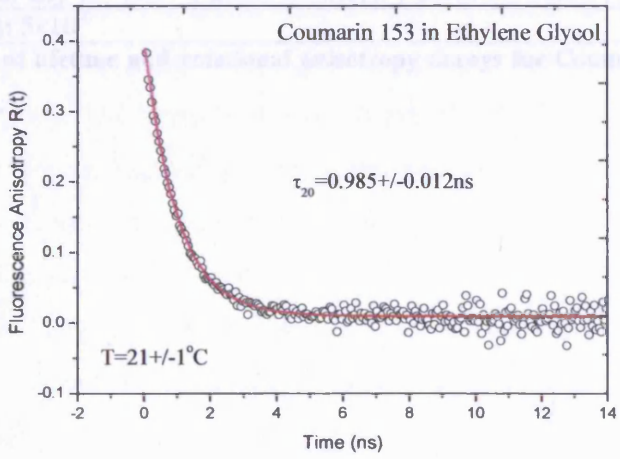

Figure 3.2: Single photon anisotropy decay for Coumarin 153 in the isotropic solvent ethylene glycol at room temperature (T=21°+/-1°C) using an excitation wavelength of 470nm and emission filtered long of 530nm. The decay fits a single exponential function indicating isotropic rotational diffusion.

It can be seen that the anisotropy decay for Coumarin 153 fits well to a single exponential function typical of diffusion in a simple isotropic liquid. Maroncelli et al have undertaken fluorescence up-conversion studies for Coumarin 153 in ethylene glycol [1] and found non-exponential anisotropy decays comprising a very fast picosecond component (44ps) coupled with a slow longer time component (880ps) of similar magnitude to that recovered in this experiment (985ps). The rationale for such findings was described in terms of the non-Markovian nature of the friction on the rotational motion of the probe molecule. Values of the initial anisotropy R(0) are similar (0.380) to those found by Maroncelli and co-workers (0.369). It may still be possible that a faster component is present in the anisotropy decay which cannot be resolved due to the limitations in the single photon counting system. The rotational diffusion times for Coumarin 153 were found to be considerably faster than those of Coumarin 6 (c.a. 60%). This is consistent with the 'slip' and 'stick' hydrodynamic theory proposed by Stokes-Einstein-Debye (SED). In this instance Coumarin 153 has a rotational time which is approximately 60% faster than that of Coumarin 6 whilst possessing a hydrodynamic volume approximately twice as small (table 3.2).

Probe	**Solvent**	**λ_{EXCITE} (nm)**	**τ_{LIFE} (ns)**	**r(0)**	**τ_{ROT} (ns)**
Coumarin 153	Eth-Gly	470	3.539 +/- 0.003	0.380 +/- 0.003	0.985 +/- 0.012
Coumarin 6	Eth-Gly	490	2.359 +/- 0.002	0.379 +/- 0.004	2.335 +/- 0.045
Concentration (M): $5x10^{-6}$					

Table 3.2: Summary of lifetime and rotational anisotropy decays for Coumarin 6 and Coumarin 153 in ethylene glycol.

3.3 Coumarin 153 in 5CB: Experiment

The experimental set-up for measurements of Coumarin 153 in 5CB is illustrated in figure 3.3. Before commencing any data collection the instrument response function (IRF) (Appendix IV) was checked and the experimental G-Factor measured as described in Chapter 2. Single-photon excitation (440nm) was achieved via the frequency doubled output of a modelocked ultrafast Ti:Sapphire oscillator (Coherent Mira 900) pumped by a solid state diode pump laser (Coherent Verdi V10) and tuned to 880nm providing laser pulse energies of c.a.10nJ with 140fs pulse width at a repetition rate of 76MHz. A single pulse selector (APE) was used to divide the 76MHz repetition rate output ensuring adequate on-sample powers. The single pulse selector is designed for optimum use with mode locked lasers that possess repetition rates between 70 and 85 MHz and its operation is based on the acousto-optic effect. By applying a modulating RF signal to a piezoelectric transducer bonded to the TeO_2 crystal an acoustic wave is generated in the crystal. The modulating acoustic signal forms areas of compression and rarefaction so modifying the refractive index of the crystal. As a result an incident laser beam which interacts with the acoustic wave at the Bragg angle is diffracted. By varying the RF signal it is possible to control the frequency and direction of the diffracted beam. The pulse from the MIRA was reduced using an adjustable internal frequency divider with the division ratio of the laser repetition rate set at 1:20. This gave a repetition rate of 3.8MHz and an output pulse energy c.a. 60% of the incident pulse energy. Frequency doubling of the output was achieved via a Lithium Triborate (LBO) crystal. The beam was focused into the crystal using a 25cm focusing lens and angle tuned for maximum power so minimising the potential for beam walk-off. A pair of telescopic lenses was also used to minimise the degree of beam divergence on exiting the doubling crystal. The subsequent laser beam path is described in Chapter 2 section 11 (page 50). A long pass filter (Schott RD530) placed in front of the MCP detector was used to isolate fluorescence long of 530nm.

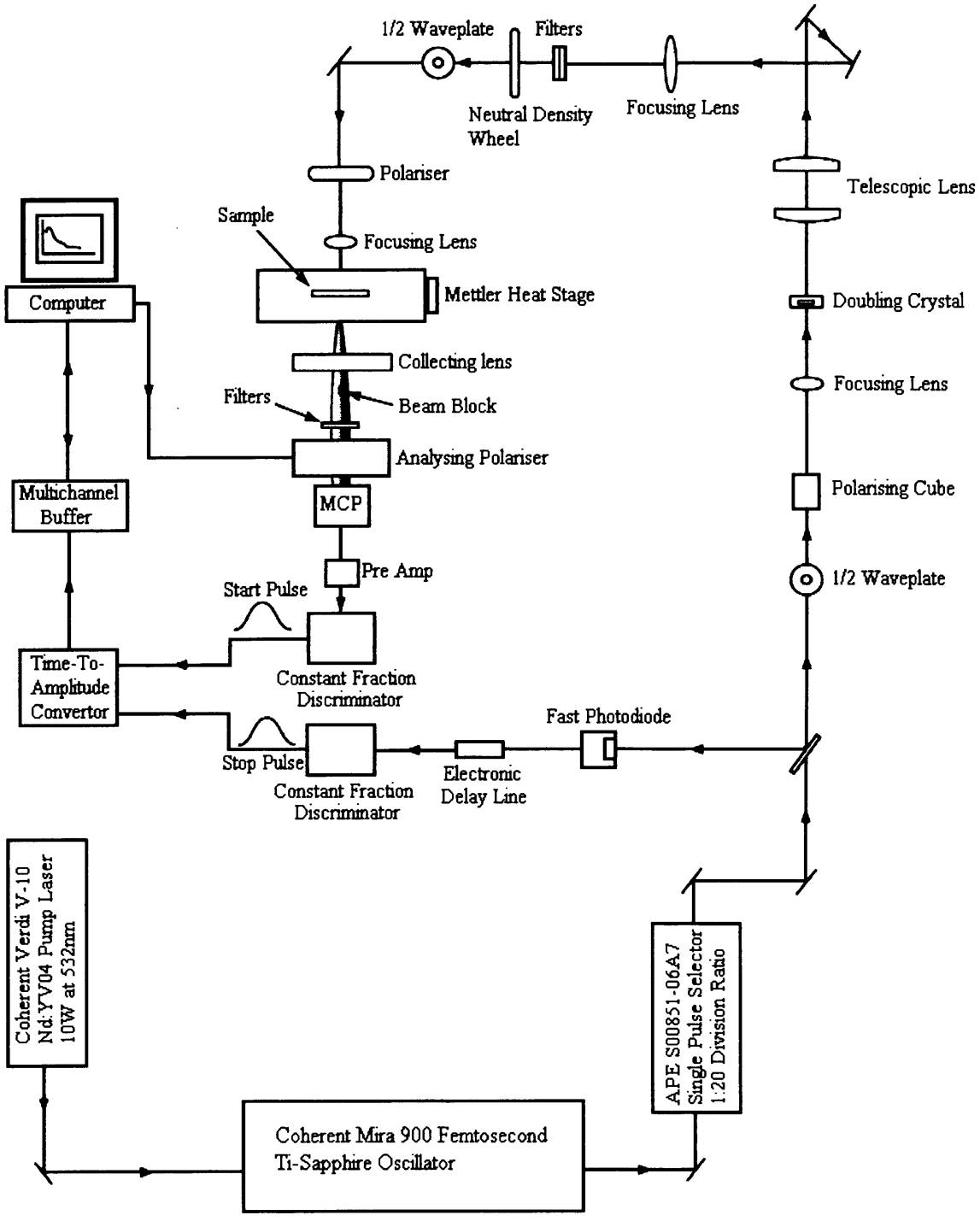

Figure 3.3: Experimental set-up for Coumarin 153 in 5CB incorporating the single-pulse selector and LBO doubling crystal. The excitation wavelength was chosen to be 440 nm with emission isolated long of 530nm using a Schott RD530 long-pass filter.

3.4 Correction Factor k

In Chapter 2, the correction factor k for the nematic phase of 5CB doped with Coumarin 6 was found from the technique described in Chapter 2, section 2.13.2. However application of the same technique for Coumarin 153 is not possible due to the large difference in the ground and excited state dipole moment which is known to cause significant solvation relaxation [5, 13]. The assumption that the initial excited state cylindrically symmetric alignment is equal to that of the equilibrium alignment in the ground state does not hold. To circumvent this problem determination of k was made using a different method. As k is a product of two components (the local field factor and the differential reflection losses for o and e rays at the birefringent sample boundary with the cell wall), it is possible to calculate the value of k for varying wavelengths and temperatures from equation 2.60 (Chapter 2, section 2.13) using existing published data for n_e and n_o for 5CB [14] coupled with refractive index data for the glass used in constructing the thin cells (n_g=1.479 at λ=486.1nm [15]). The calculated values of k across the nematic temperature range of 5CB doped with Coumarin 153 are shown in figure 3.4

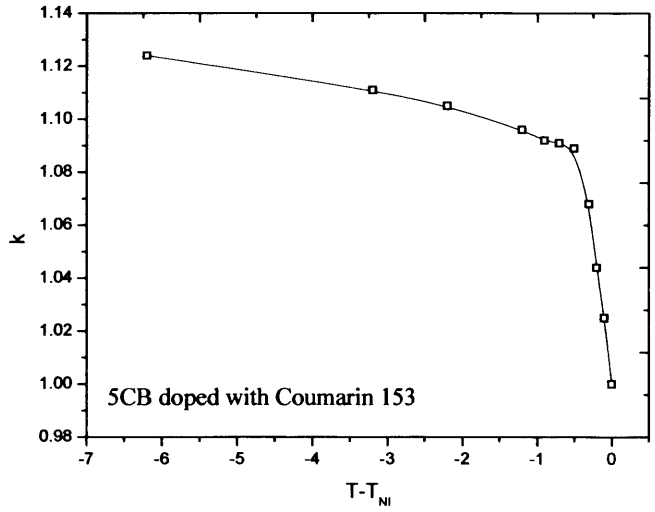

Figure 3.4: The correction factor k for 5CB doped with Coumarin 153 extrapolated from published data [14, 15]

Once k had been determined, the value for the depolarization factor Ā and the K=2 and K=4 moments were determined as described in Chapter 2 section 2.13.1 and 2.14 respectively.

3.5 Nematic Order of Coumarin 153 in 5CB

The variation in the ground state order parameters as a function of reduced temperature for Coumarin 153 in 5CB are shown in figure 3.5. The procedure to determine the peak angle (θ_{MAX}) and width of the distribution ($\Delta\theta_{FWHM}$) is described in Chapter 2, section 2.15.

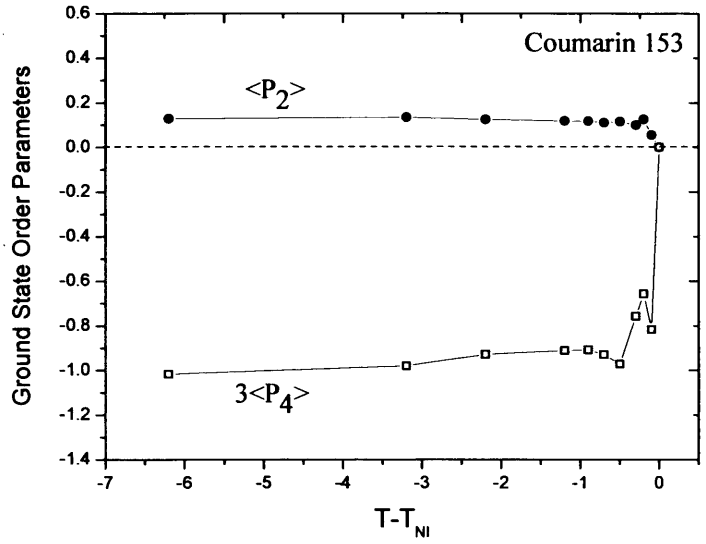

Figure 3.5: Second order $\left(\left\langle \alpha_{20}^{gs} \right\rangle / \sqrt{5} = \left\langle P_2 \right\rangle\right)$ and fourth order $\left(\left\langle \alpha_{40}^{gs} \right\rangle = 3\left\langle P_4 \right\rangle\right)$ parameters for Coumarin 153 in 5CB. It is evident that both order parameters are at variance to those of Coumarin 6 and Oxazine 4.

Coumarin 153 is characterised by positive values of $\left\langle \alpha_{20}^{gs} \right\rangle / \sqrt{5}$ though the degree of K=2 alignment in the nematic host is considerably lower (c.a. 12%) when compared to that of Coumarin 6 (c.a. 45%). The degree of positive alignment is constant to T_{NI}-0.5 where there is an abrupt collapse to zero at T_{NI}. The degree of negative alignment $\left\langle \alpha_{40}^{gs} \right\rangle$ also shows little variation to within close vicinity of the phase transition

The temperature dependent variation in the peak angle (θ_{MAX}) of the ground state distribution function of Coumarin 153 in the nematic phase of 5CB, compared to that of Coumarin 6 is shown in figure 3.6. The peak angle for the orientational distribution function of Coumarin 153 in 5CB shows little temperature dependence (c.a. 51.75±0.5°) across the nematic temperature range to within close vicinity of T_{NI} (T_{NI}-0.5) where there is a small fluctuation (±1°). It is further apparent that Coumarin 153 maintains a

peak angle $\theta_{MAX}>\theta_{ALKYL}$ across the entire nematic temperature range. Furthermore the distribution functions for Coumarin 153 are peaked at larger angles (c.a. 10^{o}-17^{o}) than those of Coumarin 6 and Oxazine 4 at equivalent reduced temperatures (see Chapter 2 figure 2.24 for Oxazine 4)

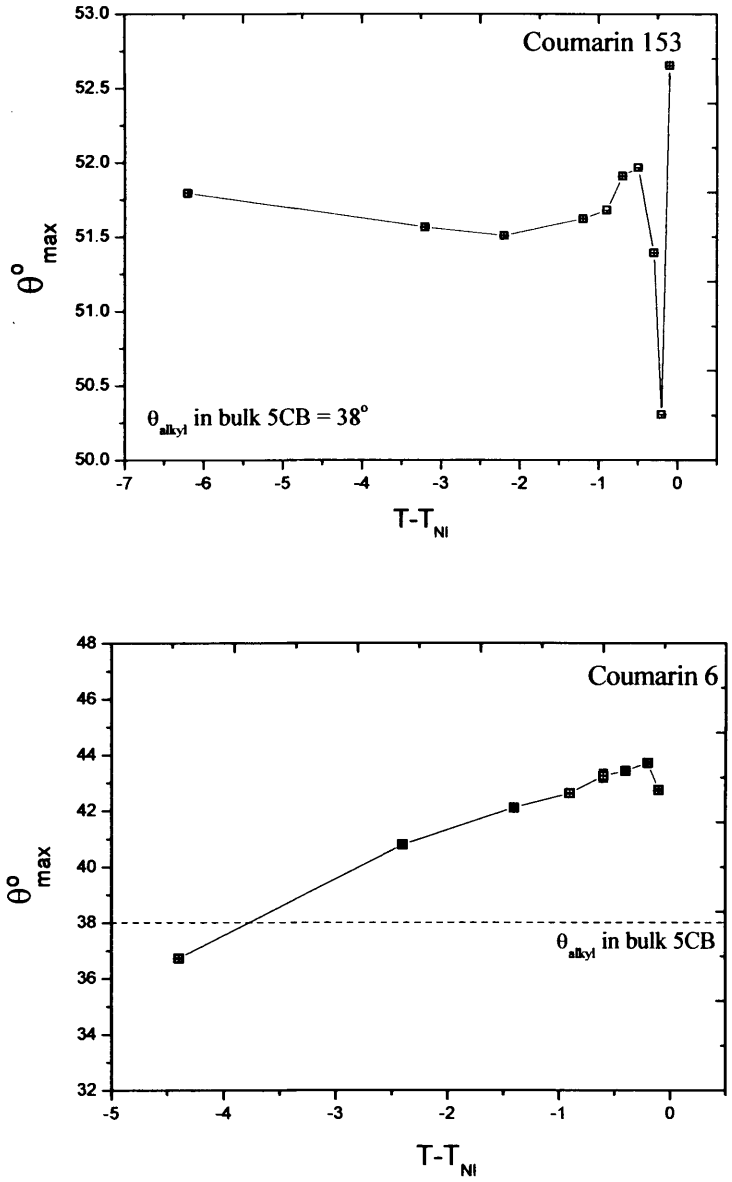

Figure 3.6: Graphs illustrating variation in the peak angle of the orientational distribution function with reduced temperature for Coumarin 153 and Coumarin 6 in nematic 5CB. Coumarin 153 exhibits only a slight variation in peak angle when compared to the behaviour of Coumarin 6.

The variation in the width of the distribution function with temperature for Coumarin 153 compared to that of Coumarin 6 is shown in figure 3.7.

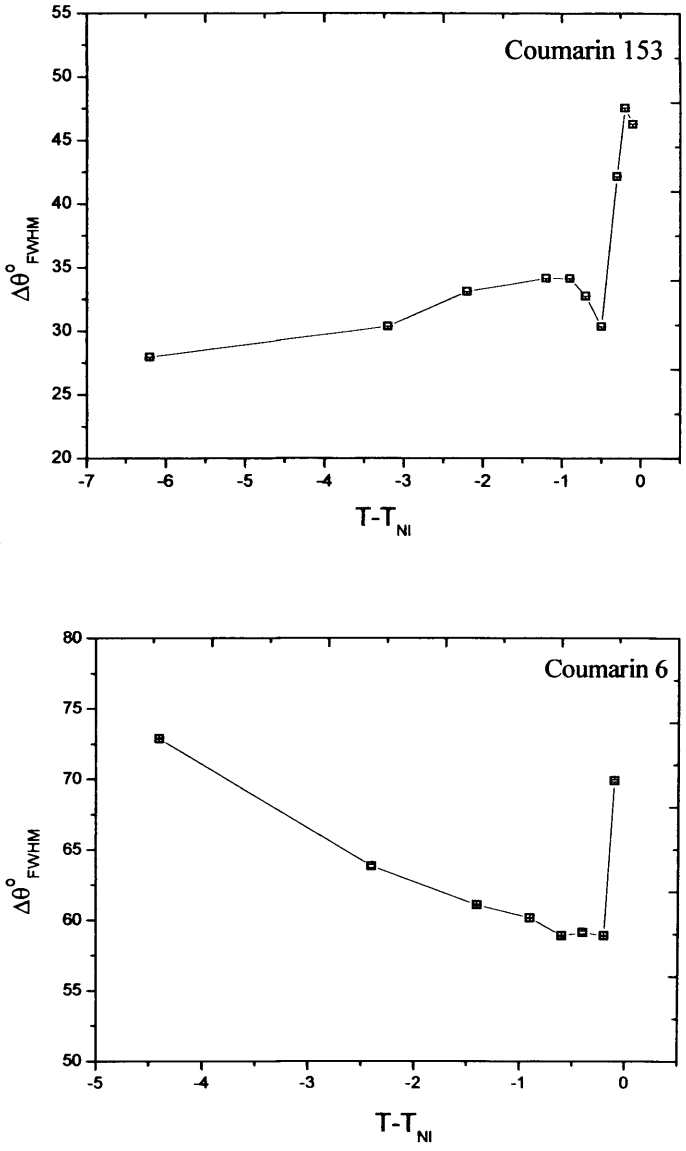

Figure 3.7: Comparison of the variation of the width of the orientational distribution functions with reduced temperature for Coumarin 153 and Coumarin 6 in nematic 5CB. The width of the distribution is different across the nematic phase with $\Delta\theta_{FWHM}$ widening with temperature for Coumarin 153 and narrowing for Coumarin 6.

Coumarin 153 shows a gradual increase in the width of the orientational distribution (c.a. 0.94°/°C) from T_{NI}-7.4 - T_{NI}-0.6. In the vicinity of T_{NI} the width of the distribution is seen to decrease slightly (c.a. 5°) before a distinct widening (c.a. 20°) to T_{NI}. It is apparent that the orientational distribution is much narrower (c.a. 45°-27°) than that of Coumarin 6 over the entire nematic temperature range and the behaviour is markedly different suggesting that Coumarin 153 has adopted an environment significantly different to that of Coumarin 6. Moreover there would appear to be an abrupt change in

the probe ordering close to the phase transition which could indicate a slight shift in probe position or some local re-ordering of the host around the probe.

3.6 Orientational Relaxation Dynamics of Coumarin 153 in 5CB

In Chapter 2 determination of the cylindrically symmetric relaxation time was based on the assumption that k was non-varying over the orientational relaxation timescale. This assumption may not hold for Coumarin 153 where the large difference in ground and excited state dipole moment is known to cause large solvation effects [5, 13]. Reordering of solvent and solute molecules during the excited state lifetime would cause the intensity ratio $I_V(t)/I_H(t)$ to vary distorting both the population and alignment relaxation data. Therefore the orientational relaxation times for cylindrically symmetric alignment (τ_θ) were instead determined using polarised intensity decays (Appendix V). The orientational relaxation times for cylindrically asymmetric alignment (τ_φ) were determined as for Coumarin 6 in Chapter 2 section 2.13.2, as the observed decay rates are independent of k (equation 2.68).

The variation in τ_θ and τ_φ with reduced temperature for Coumarin 153 across the nematic range of 5CB is shown in figure 3.8.

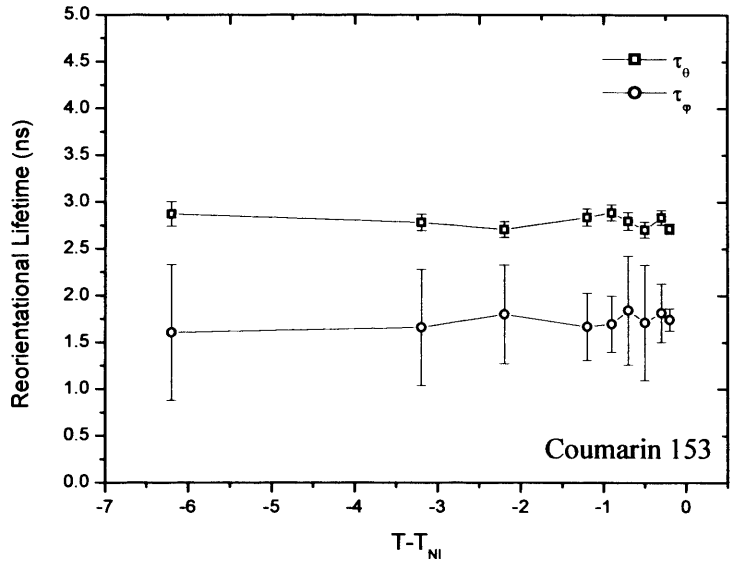

Figure 3.8: Variation in orientational relaxation times (τ_θ) and (τ_φ) with reduced temperature for Coumarin 153 in the nematic phase of 5CB. It is evident that both θ-diffusion and φ-diffusion are largely temperature independent.

As with Coumarin 6, the diffusion dynamics (τ_θ and τ_φ) of Coumarin 153 show little temperature dependence remaining largely constant across the nematic temperature range. However, Coumarin 153 shows distinct anisotropic diffusional behaviour with $\tau_\theta > \tau_\varphi$ across the nematic temperature range with no convergence at T_{NI}, unlike that seen with Oxazine 4. The results show no indication of slowing of the φ-diffusion times with temperature ('bi-axial fluctuations') as mentioned in the previous chapter. Both Coumarin 6 and Coumarin 153 are highly hydrophobic [2, 8, 16]. Coumarin 153 would therefore also be expected to position itself within the alkyl tail region. A similarly large θ_{MAX} to Coumarin 6 is consistent with this assumption. However, the much lower hydrodynamic volume of Coumarin 153 [1] (table 3.1) is expected to cause far less disruption of the nematic structure. This may well explain the extremely narrow angular distribution and the observation of some anisotropy in the diffusion dynamics as the orientation of the probe is still partially correlated to the host. The much lower volume of Coumarin 153 would normally suggest faster orientational diffusion than Coumarin 6 (table 3.2). The similar rates of diffusion for the two probes in 5CB, but with some directional anisotropy for Coumarin 153, would suggest that although 'slip' conditions prevail they are not as predominant as they are for Coumarin 6. Rau et al [2] measured rotational diffusion dynamics for Coumarin 153 in isotropic 8-cyanobiphenyl (8CB) and have suggested that slip conditions prevail.

3.7 Orientational Dynamics and Local Order of Coumarin 153 in Isotropic 5CB: Results

The variation in fast and slow rotational times for Coumarin 153 in the isotropic phase of 5CB is shown in figure 3.9. It is unclear whether the slow overall diffusion time follows a Landau-de Gennes type dependence of the form described by equation 2.47. An initial indication of LDG compliance is the virtual phase transition temperature T^* which was found to be c.a.290K. This is well below that expected in 5CB (307K [7]).

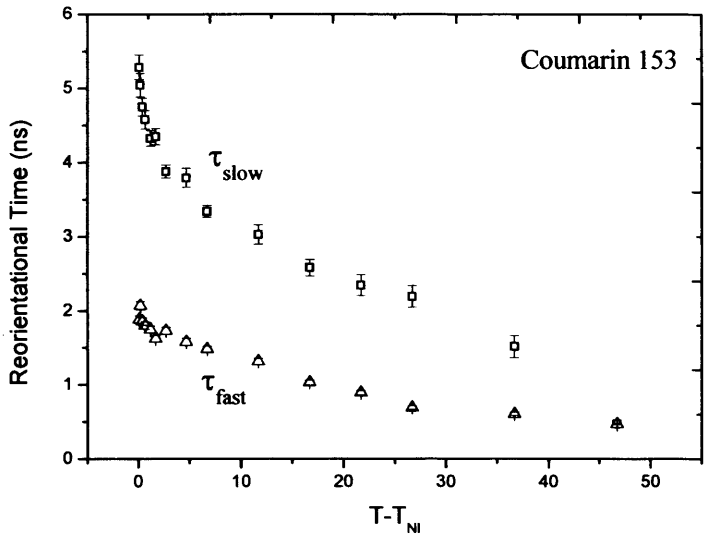

Figure 3.9: Temperature dependence of the fast (τ_{fast}) and slow (τ_{slow}) orientational relaxation times for Coumarin 153 in 5CB. There is evidence of a decreasing fast orientational relaxation time (τ_{fast}) which is not apparent in Coumarin 6 in 5CB or Oxazine 4 in 5CB.

The slow rotational time variation with temperature is related to the temperature dependent shear viscosity of the liquid crystal in the isotropic phase by [17]

$$\tau_S \approx \frac{\eta(T)V_{eff}}{k_B(T-T^*)} + \tau_0 \qquad [3.1]$$

where V_{eff} is the hydrodynamic volume of the dye molecule, τ_0 is the free rotor correlation time and k_B the Boltzmann constant. If Coumarin 153 is to demonstrate LDG behaviour then a plot of τ_S versus $\eta(T)/(T-T^*)$ should yield a straight line. As can be seen from figure 3.10 the linear dependence is less marked when compared to that of Oxazine 4 which shows good LDG compliance. Unlike Coumarin 6 and Oxazine 4 the fast relaxation time (τ_{fast}) does show some temperature dependence, decreasing from c.a. 2.2ns at T_{NI} to c.a. 0.5ns at T_{NI} + 46°C.

The variation in the cone angle for Coumarin 153 in the isotropic phase of 5CB is shown in figure 3.11. The nematic phase orientational distribution function width is also shown.

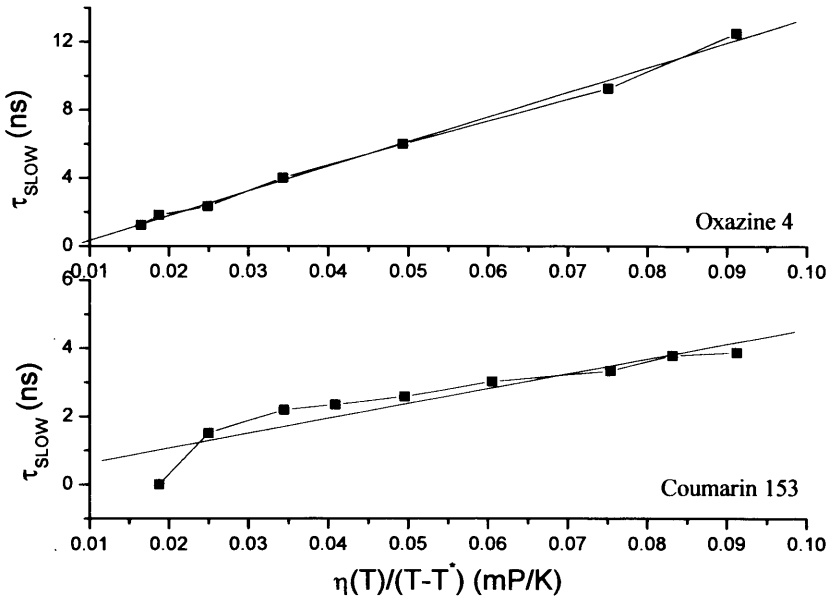

Figure 3.10: Comparison of the compliance of Coumarin 153 with LDG by measuring the slow reorientational time τ_S against η(T) / (T-T*). Oxazine 4 (which shows good LDG behaviour) is shown for comparison. {The original data for Oxazine 4 is taken from work by J Bryant [18]}

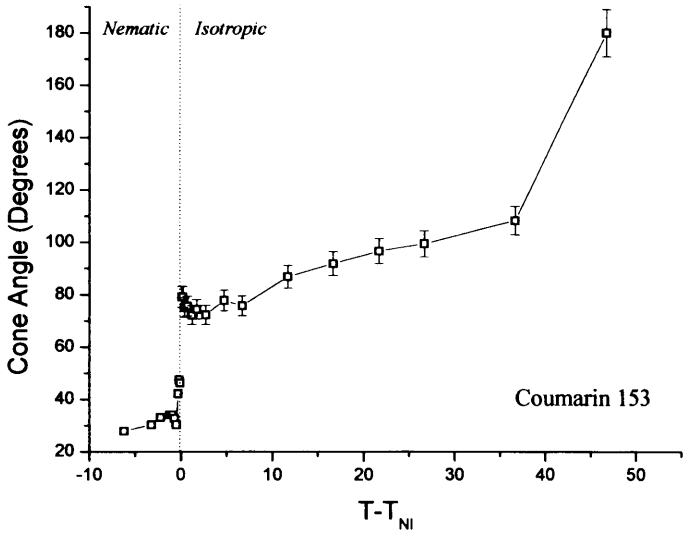

Figure 3.11: The variation with temperature in cone angle for Coumarin 153 in the nematic and isotropic phases of 5CB. It is evident that there is a discontinuity at the phase transition temperature.

Coumarin 153 shows only a gradual increase in cone angle across the isotropic phase (0.94°/°C) to T_{NI}+ 36.7 where there is a rapid collapse to a wholly isotropic environment. This collapse takes place at a similar temperature to that for Coumarin 6

(figure 2.31). However, there is evidence of a discontinuity at T_{NI}, in stark contrast to the behaviour of Coumarin 6 which increases sharply in the vicinity of T_{NI} but does not show any discontinuity at the phase transition. If the probe was more highly correlated with the liquid crystal host it would be expected to show sensitivity to the structural changes at the phase transition [19]. Furthermore the reduction of the correlation length with temperature in the isotropic phase does not give rise to the same degree of broadening in the cone angle as seen with Coumarin 6. These two factors further support the idea that Coumarin 153 causes less disruption to the local nematic ordering of the host than Coumarin 6.

The temperature variation in the initial fluorescence anisotropy for Coumarin 153 in the isotropic phase of 5CB is shown in figure 3.12. It is evident that across the isotropic phase the initial anisotropy is significantly lower than that for Oxazine 4 in ethylene glycol (c.a. 0.39) and Coumarin 6 (c.a. 0.38) (Chapter 2, figure 2.20). Departure of the initial fluorescent anisotropy from 0.4 can arise from non-parallel absorption and emission transition dipole moments [5] or from fast orientational relaxation which occurs on a sub-instrument response time [1]. Fast (sub picosecond) orientational relaxation of Coumarin 153 has been observed in a number of solvents. The decrease in the measured initial anisotropy with increasing temperature for Coumarin 153 in the isotropic phase of 5CB would indicate that orientational relaxation on a timescale shorter than c.a. 83ps (fwhm of the instrument response function) is taking place.

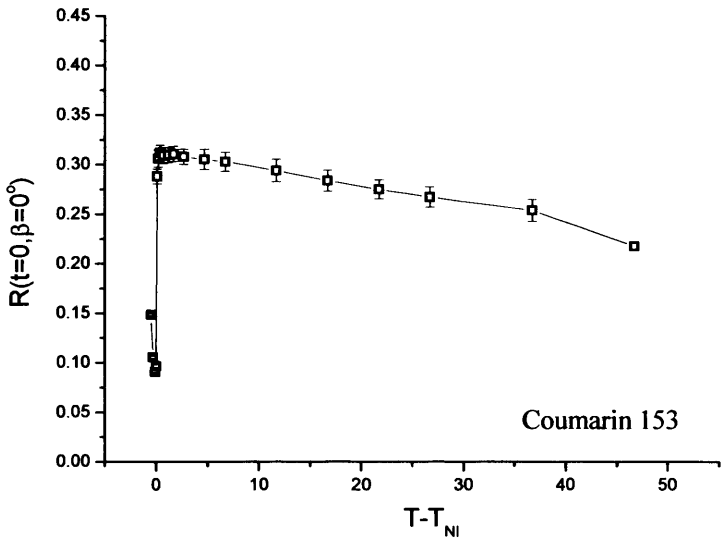

Figure 3.12: Variation in R(0) with reduced temperature for Coumarin 153 in 5CB.

3.8 Lifetime Behaviour in the Nematic Phase of 5CB

As shown in Chapter 2 section 2.13.2, given an excitation polarisation angle of β=54.7° and assuming a cylindrically symmetric ground state, the initial excited state cylindrically symmetric alignment is equal to that of the equilibrium alignment in the ground state [20] the fluorescence intensity from equation 2.68 is given by

$$I_Z(\beta = 54.7^o) = A \exp\left(\frac{t}{\tau_f}\right)\left[\frac{1}{A} + \frac{2}{\sqrt{5}}\left(\left\{\left\langle \alpha_{20}^{gs}(0)\right\rangle - \left\langle \alpha_{20}^{ex}(ss)\right\rangle\right\}\exp\left(\frac{-t}{\tau_{20}}\right) + \left\langle \alpha_{20}^{ex}(ss)\right\rangle\right)\right] \quad [3.2]$$

For ground and excited state degrees of alignment that are close to or equal the time dependence of equation 3.2 will be dominated by population decay. Providing the alignment change is slowly varying and small then equation 3.2 should closely resemble the population decay. Unlike the analysis of Coumarin 6 and Oxazine 4, the decay is not well described by a single exponential. This is evident in undeconvoluted data analysis using MicroCal™ Origin software where the decays are in fact described by three exponential times. A c.a. 6ns slow component which showed little variation across the nematic temperature, a c.a. 3ns fast component which exhibited a slight decrease with increasing temperature and a c.a. 500ps rapid component. The temperature variation of the three times along with the pre-exponential factors is shown in figure 3.13.

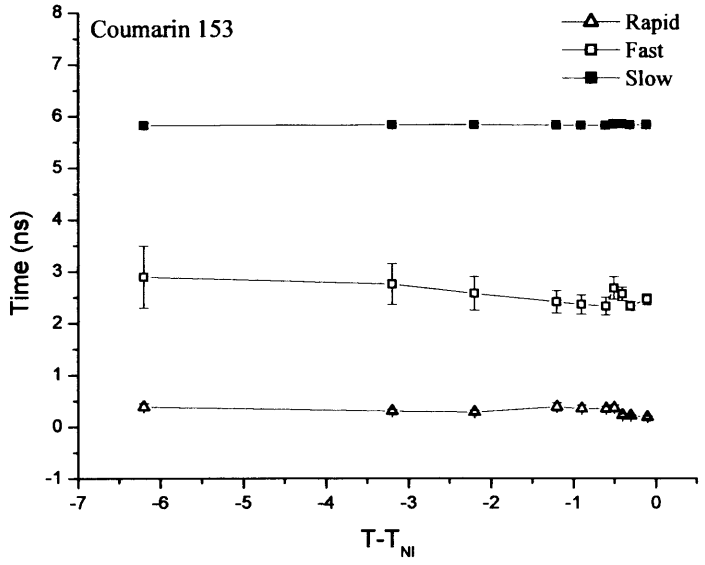

Figure 3.13: The fluorescence lifetime as a function of reduced temperature for Coumarin 153 in the nematic phase of 5CB along with the pre-exponential factors for each time. There is clear evidence of multi exponential decays.

It is unlikely that the triple exponential decay can be attributed solely to the lifetime. Non-exponential decays can arise for a variety of reasons. For example, orientational relaxation if not recovered from intensity decay will lead to a bi-exponential decay as is seen in conventional anisotropy measurements in isotropic fluids. Multi component decays for Coumarin 153 have been observed by Maroncelli et al in a number of solvents [1, 13] where the rapid time is defined in terms of solvation. In this case the failure of equation 3.2 to provide a single population decay is evident where as well as the picosecond component there are two nanosecond components one of which can be attributed to the fluorescence lifetime (c.a. 6ns, as it not modulated by any other decay) and the other, when deconvoluted from the fluorescence lifetime is very similar to the θ-diffusion times (net reorientation of the excited state molecules $\langle \alpha_{20}^{gs}(0) \rangle \neq \langle \alpha_{20}^{ex}(ss) \rangle$ in equation 3.2) obtained for the $\beta=0^{o}$ measurements shown above.

The variation in the cone angle for Coumarin 153 in the isotropic phase of 5CB is shown in figure 3.9. The nematic phase orientational distribution function width is also shown.

3.9 Coumarin 153: Results for Blue and Red Edge Filtered Emission in the Nematic Phase of 5CB

Further to discussions at the beginning of this chapter regarding the solvatochromic properties of Coumarin 153 and the potential effects on fluorescence measurements in an aligned environment such as 5CB, the same experiments were repeated with the emission resolved into two spectral windows at either end of the spectrum. Evidence of a solvatochromic shift should be made apparent by examination of the decays in the respective spectral windows. Such a shift should be manifest by a decay of population in one spectral window with a corresponding rise in the other.

The experimental set-up is described in section 3.3, however in order to accurately resolve the emission into two spectral windows appropriate filters (Corion LS500, Schott RD570) were incorporated into the set-up. The emission spectrum was measured as a function of temperature using an Ocean Optics Spectrometer (USB4000–VIS-NIR (350nm-1000nm)) placed between the Mettler Heat Stage and MCP detector (figure

3.2). Any background contamination of the emission spectrum was minimised by carrying out all measurements in low light with data collected for an integration time of 10s at each temperature. The spectral windows were then chosen appropriately. Figure 3.13 shows the emission spectrum and the proportion of the emission in the spectral windows as a function of temperature. These windows were chosen to be 455-500nm (blue edge) and >570 nm (red edge). The temperature dependent emission spectrum is shown in figure 3.14 along with the emission windows. Though there is evidence of discontinuity at and around the phase transition temperature, this can be accounted for in terms of the characteristic beam scatter around T_{NI}, the degree of which is wavelength dependent. It is apparent therefore that there is negligible temperature dependence to the emission.

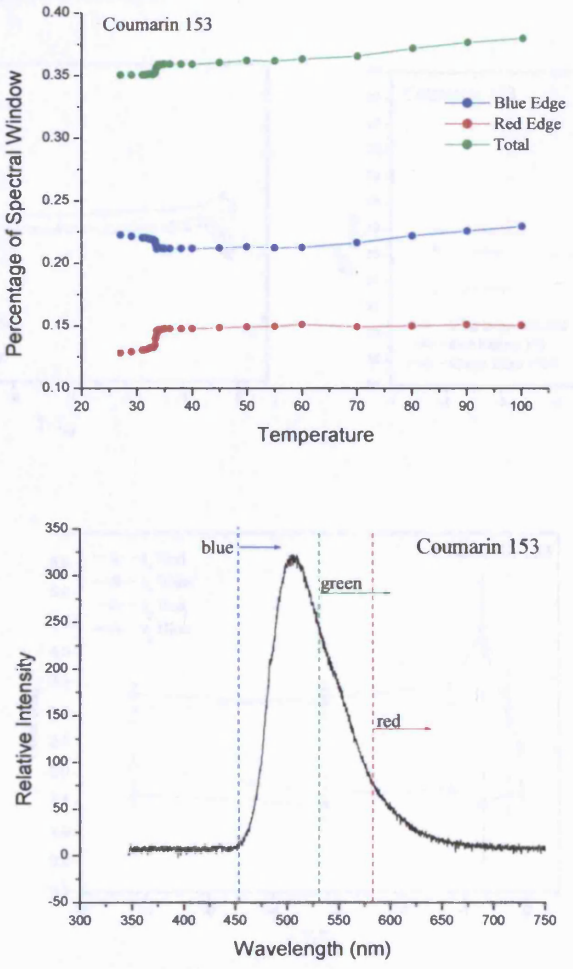

Figure 3.14: The proportion of emission in the blue and red windows as a function of temperature shown with the emission spectrum for Coumarin 153 in 5CB at T=27°C. The blue (455-500nm) and red (>570 nm) edge spectral windows are shown alongside the emission window originally selected (>530nm).

Elements of the nematic and isotropic phase measurements described above were repeated for the blue and red edge filtered emission. The peak angle (θ_{MAX}) and width of the orientational distribution function (θ_{FWHM}) are shown along with rotational diffusion time for the nematic phase in figure 3.15 and compared with the previous analysis of emission measured long of 530nm for Coumarin 153 in 5CB. It is evident that there is little difference in the probe orientation or diffusion dynamics for the different regions of the spectrum. The slight discrepancy observed in the width of the distribution between the filtered emission and previous results may be accounted for by sample inhomogeneity as these measurements were performed at different times. The lack of significant variation of these distribution function and rotational orientation times across the emission spectrum suggest all the molecules within the excitation region are in essentially the same environment.

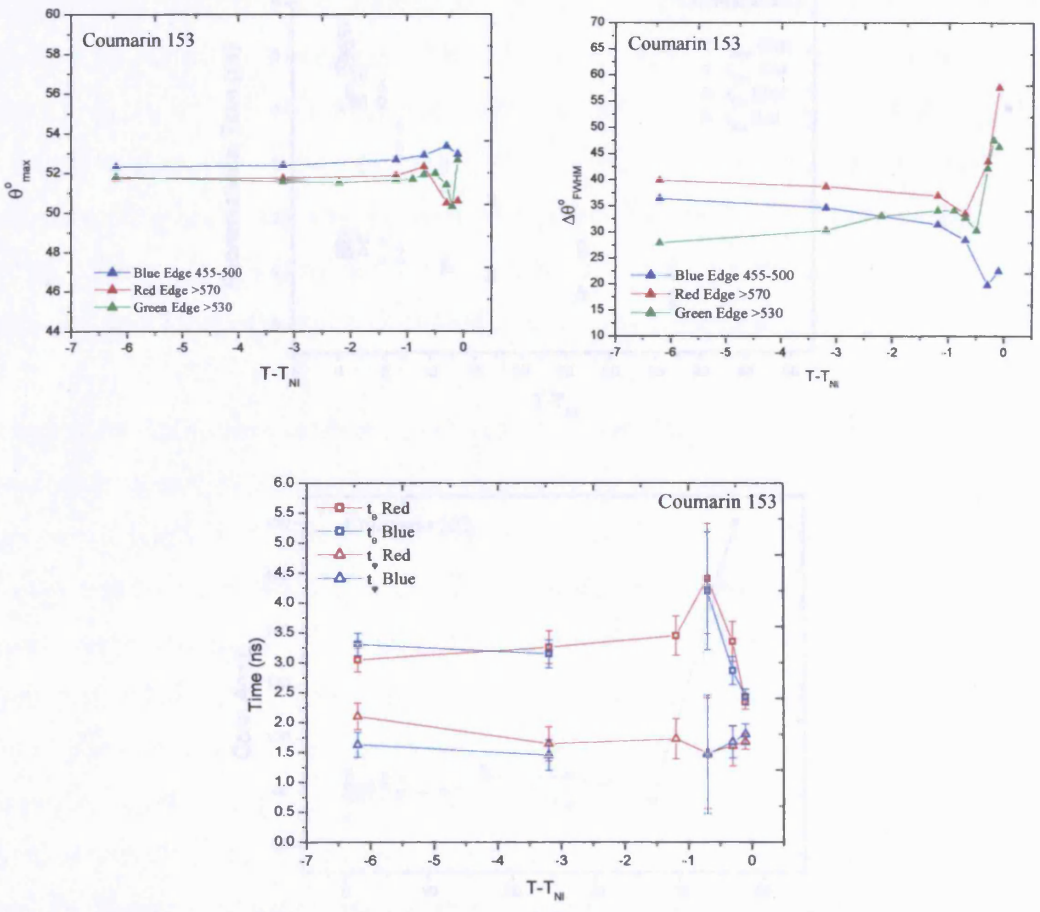

Figure 3.15: Graphs displaying the peak angle, distribution width and rotational diffusion times for blue edge and red edge emission windows for Coumarin 153 in 5CB. There is no significant difference in the measured parameters for varying emission wavelength.

3.10 Coumarin 153: Results for Blue and Red Edge Filtered Emission in the Isotropic Phase of 5CB

The intradomain and interdomain diffusion times and variation in the cone angle with temperature are shown in figure 3.16. As with the nematic phase, there is little difference in the blue and red edge emission results and those of >530nm (green edge) described earlier in this chapter. They show similarly poor LDG behaviour and the cone angle is also invariant with temperature. The partial correlation of the probe with the pseudo-domain and the temperature invariance of the cone angle further supports the idea that the molecule adopts an orderly position in the alkyl region of the liquid crystal host.

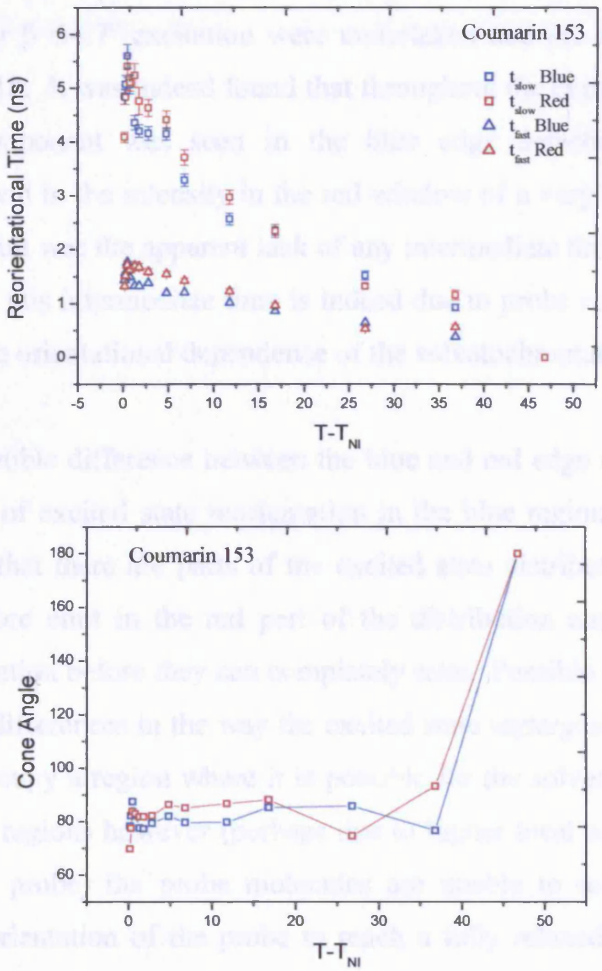

Figure 3.16: Variation in inter and intra domain relaxation times and cone angle for blue and red edge filtered emission for Coumarin 153 in the isotropic phase of 5CB. There is little difference between the blue and red edge results and the previous measurements (figure 3.8).

3.11 Blue and Red Edge Lifetime Analysis

Without accurate knowledge of k the most reliable determination of the fluorescence lifetime is from equation 3.2. For experiments carried out in the green edge a tri-exponential decay was recovered, manifest in slow, intermediate and rapid times. The slow time was taken to be the fluorescence lifetime, the intermediate time was taken to be the reorientational time given the remarkable similarity with the time recovered for θ-diffusion and the rapid time was ascribed to solvation as a result of the solvatochromic properties of the probe. If indeed the rapid time is indicative of a dynamic red-shift in the emission spectrum due to solvent relaxation then rapid intensity decay in the blue emission window should be matched by a corresponding rapid growth in the red. To further examine this, tri-exponential fits to the vertically polarised intensity decays for $\beta=54.7^{o}$ excitation were undertaken and the results are shown in figures 3.17 and 3.18. It was indeed found that throughout the entire temperature range a rapid decay component was seen in the blue edge detection window with a corresponding growth in the intensity in the red window of a very similar timescale. A more surprising result was the apparent lack of any intermediate time in the red window intensity decays. If this intermediate time is indeed due to probe reorientation then this would suggest some orientational dependence of the solvatochromatic shift.

The greatest discernible difference between the blue and red edge measurements is the apparent existence of excited state reorientation in the blue region and not in the red. This would imply that there are parts of the excited state distribution that are already relaxed and therefore emit in the red part of the distribution and other regions that experience reorientation before they can completely relax. Possible explanations for this behaviour include differences in the way the excited state undergoes solvent relaxation: some molecules occupy a region where it is possible for the solvent to reorient around the probe; in other regions however (perhaps due to higher local ordering of the liquid crystal around the probe) the probe molecules are unable to re-orientate as freely, requiring some reorientation of the probe to reach a fully relaxed state. However the persistence of the intermediate decay time in the blue spectral window throughout the isotropic phase (where the absence of k means no alignment terms should be detected) is at variance with this interpretation. In this host phase, loss of intensity from this

spectral region should result only from fluorescence decay or solvent shift. The close similarity between this intermediate time and the θ diffusion times suggest a correlation of the solvent relaxation with orientational diffusion. Although this has not been observed experimentally it has been postulated by Kapko et al [21] whose calculations showed a slight dependence of solvent shift on probe orientation for this system.

To investigate further the variation in the number of decay components observed in the two fluorescence windows, a commercial deconvolution software package (PicoQuant Fluorofit) was used to fit some representative data sets to determine precisely this number. Observations of the residuals did indeed confirm the existence of only two significant decay components in the red spectral window. Furthermore, intensity decays in the blue could not be accurately fitted without the presence of a third decay component of significant amplitude. An example of these fits is shown in figure 3.19.

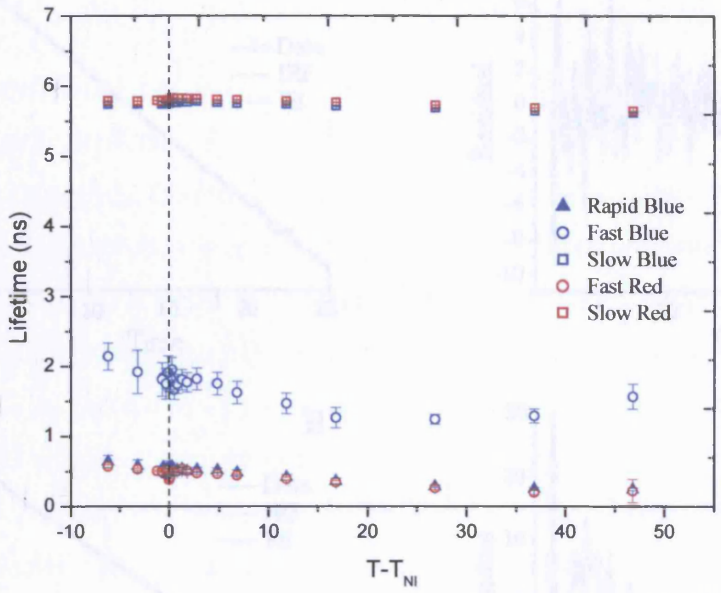

Figure 3.17: Tri-exponential and bi-exponential lifetime components for blue and red edge filtered emission for Coumarin 153 in 5CB. There is no change in behaviour at the phase transition. However there is evidence of a decrease with temperature in both the fast blue component and the rapid blue and red components. The fluorescence lifetime remains temperature invariant.

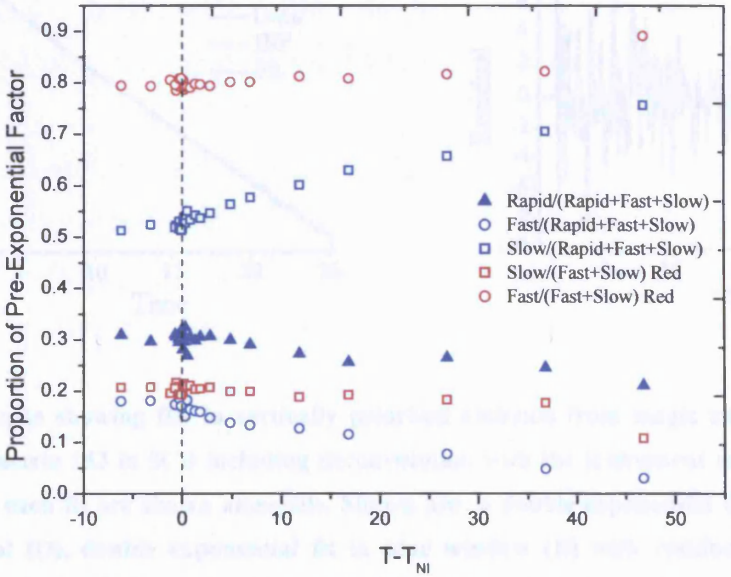

Figure 3.18: The proportion of the pre exponential factor for each decay component as a function of the totadetected fluorescence for the blue and red edge filtered emission. Actual values are shown in Appendix VI

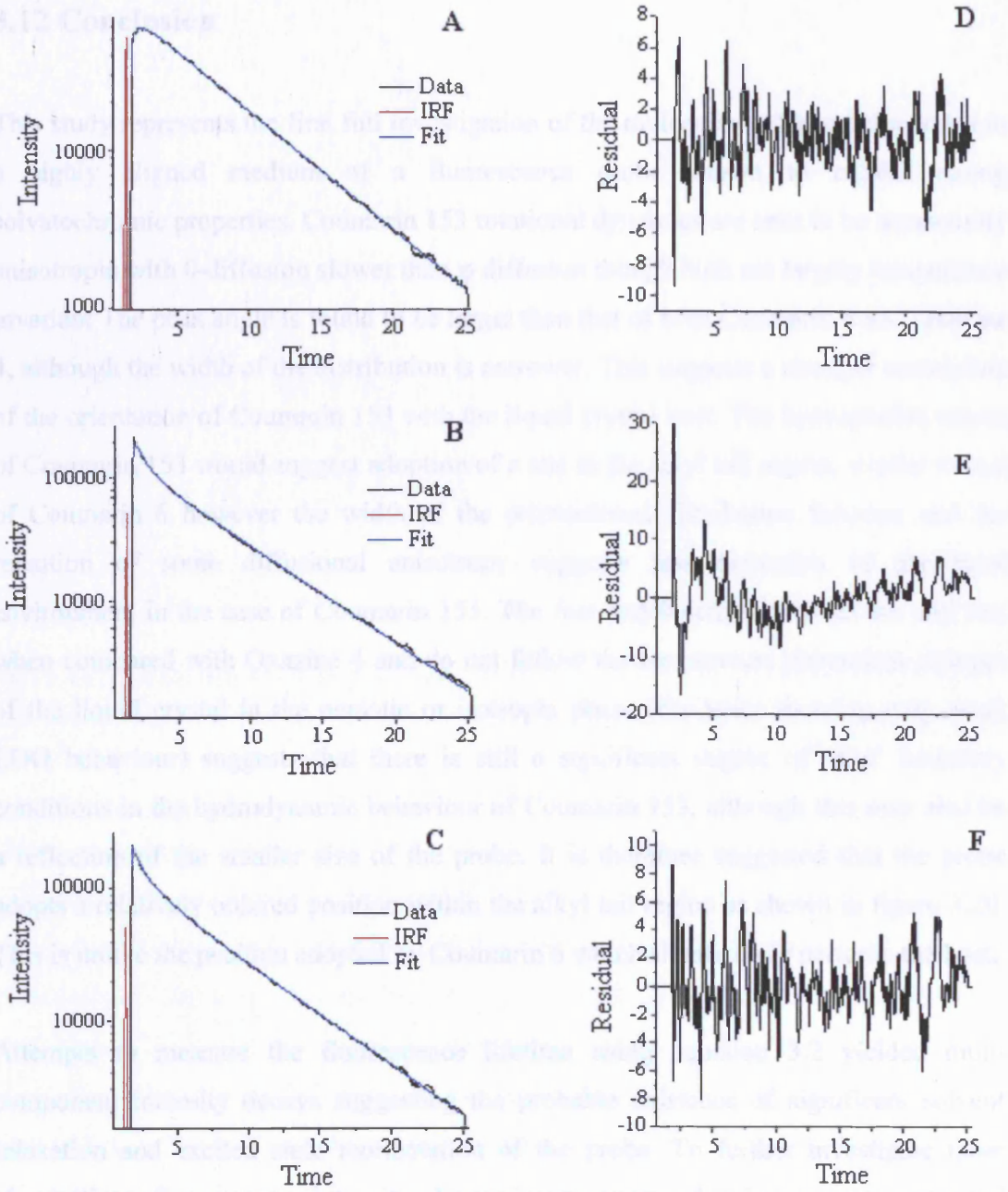

Figure 3.19: Graphs showing fits to vertically polarised emission from magic angle excitation at T=27°C for Coumarin 153 in 5CB including deconvolution with the instrument response function. The residuals of each fit are shown alongside. Shown are: a double exponential fit to red window (A) with residual (D), double exponential fit to blue window (B) with residual (E) and triple exponential fit to blue window (C) with residual (F) clearly indicating the presence of a third exponential decay in the blue window. Reduced χ^2 for (A), (B) and (C) are 4.1, 17.8 and 5.5 respectively.

3.12 Conclusion

This study represents the first full investigation of the molecular order and dynamics in a highly aligned medium of a fluorescence probe known to exhibit strong solvatochromic properties. Coumarin 153 rotational dynamics are seen to be measurably anisotropic with θ-diffusion slower than φ diffusion though both are largely temperature invariant The peak angle is found to be larger than that of both Coumarin 6 and Oxazine 4, although the width of the distribution is narrower. This suggests a stronger correlation of the orientation of Coumarin 153 with the liquid crystal host. The hydrophobic nature of Coumarin 153 would suggest adoption of a site in the alkyl tail region, similar to that of Coumarin 6 however the width of the orientational distribution function and the retention of some diffusional anisotropy suggests less distortion of the local environment in the case of Coumarin 153. The fact that θ-diffusion times are still fast when compared with Oxazine 4 and do not follow the temperature dependent changes of the liquid crystal in the nematic or isotropic phase (the latter showing only weak LDG behaviour) suggests that there is still a significant degree of 'slip' boundary conditions in the hydrodynamic behaviour of Coumarin 153, although this may also be a reflection of the smaller size of the probe. It is therefore suggested that the probe adopts a relatively ordered position within the alkyl tail region as shown in figure 3.20. This is unlike the position adopted by Coumarin 6 which significantly perturbs the host.

Attempts to measure the fluorescence lifetime using equation 3.2 yielded multi component intensity decays suggesting the probable existence of significant solvent relaxation and excited state reorientation of the probe. To further investigate these observations fluorescence intensity decays were measured using narrower spectral windows at either end of the emission spectra. Comparison of the ground state order parameters and the diffusion dynamics in the observed spectral regions (i.e. red edge, blue edge or green edge) displayed negligible difference. Further extending the measurements into the isotropic phase produced no noticeable variation with emission wavelength. This would tend to imply a high degree of ground state homogeneity

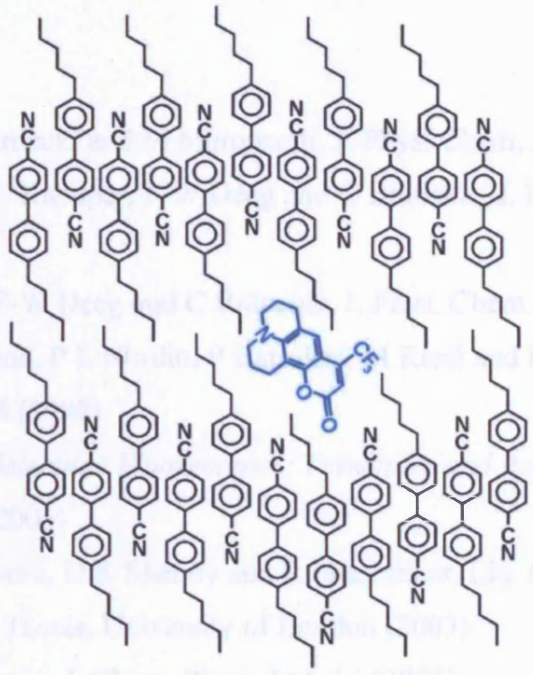

Figure 3.20: Illustration of the suggested position of Coumarin 153 within the liquid crystal host. The results suggest a position of strong correlation with the alkyl tails of the host without significant disruption to the biphenyl core.

However investigation of the lifetime behaviour from equation 3.2 reveals significant variation between the different regions of the emission spectrum. These are manifested as substantial solvent shifts in the emission spectrum on the timescale of a few hundred picoseconds. The decay rate of this solvent relaxation component is seen to increase significantly over the entire temperature range probably indicating the reducing viscosity of the solvent. This may not be the only solvation component. Although not shown here, both blue and red spectral windows display very similar initial anisotropies to the green edge data in the isotropic phase. Therefore, if a sub instrument response decay component exists (as discussed above) there is no evidence of it varying over the emission profile.

References

[1] M L Horng, J A Gardecki and M Maroncelli, J. Phys. Chem. A., **101**, 6 (1997)

[2] J Rau, C Ferrante, E Kneuper, F-W Deeg and C Bräuchle, J. Phys. Chem. A., **105**, 24 (2001)

[3] J Rau, C Ferrante, F-W Deeg and C Bräuchle, J. Phys. Chem. B., **103**, 24 (1999)

[4] G Saielli, A Polimeno, P L Nordio, P Bartolini, M Ricci and R Righini J. Chem. Soc, Faraday Trans., **94** (1998)

[5] Bernard Valeur *"Molecular Fluorescence; Principles and Applications"* Second Reprint, Wiley-VCH (2005)

[6] M L Dark, M H Moore, D K Shenoy and R Shashidhar, Liq. Crystals., **33**, 1 (2006)

[7] E M Monge, Ph.D. Thesis, University of London (2003)

[8] G B Dutt and S Raman, J. Chem. Phys., **114**, 15 (2001)

[9] G Jones II, W R Jackson, C Choi and W R Bergmark, J. Chem. Phys., **89**, 2 (1985)

[10] M L Horng, J A Gardecki and M Maroncelli, J. Phys. Chem. A., **101**, 6 (1997)

[11] G B Dutt, J. Phys. Chem **119**, 22 (2003)

[12] P K McCarthy and G J Blanchard J. Chem. Phys., **97**, 47 (1993)

[13] L Reynolds, M L Horng, J A Gardecki, S J V Frankland and M Maroncelli, J. Phys. Chem., **100**, 10337 (1996)

[14] S T Wu and C S Wu, Opt. Eng. **32**, 1775 (1993)

[15] Melles Griot Catalogue, 4.15 (2007)

[16] M Maroncelli, J. Chem. Phys., **106**, 4 (1997)

[17] S Chandrasekhar "Liquid Crystals" Second Edition, Cambridge University Press (1992)

[18] J Bryant, Ph. D. Thesis, University of Essex (2000)

[19] P G de Gennes, *"The Physics of Liquid Crystals"* Clarendon, Oxford (1974)

[20] A J Bain, P Chandna, G Butcher and J Bryant, J. Chem. Phys. **112**, 10435 (2000)

[21] V Kapko and D M Matyushov, J. Chem. Phys., **124**, 114904 (2006)

Chapter 4

Two-Photon Transitions in Quadrupolar and Branched Fluorophores

4.1 Introduction

The development of high quantum yield fluorescent probes with enhanced two-photon absorption cross-sections has attracted significant interest in recent years This stems from advances in broadband and tunable femtosecond near-infra red laser systems and their use in scanning fluorescence microscopy [1-3]. Two–photon excitation is an intensity dependent process and for a focused Gaussian laser beam the transition probability peaks sharply in the Rayleigh range about the beam waist. Two-photon excited fluorescence thus offers inherent optical sectioning. In contrast, single-photon excited fluorescence requires a confocal optical geometry which rejects the significant degree of fluorescence that is excited from other regions of the sample. The difference between the two excitation techniques can be clearly seen in figure 4.1. Near infra-red two-photon fluorescence in principle affords greater penetration of biological samples, reduced photodamage [4] and with excitation confined to a small (ca. femtolitre) confocal volume [5]. In practice however the two-photon absorption cross-sections of naturally occurring fluorescent chromophores are not large, nor are those for conventional (synthetic) probes optimised for single-photon absorption and spontaneous emission (see table 4.1). There is therefore a need to engineer molecules with high two-photon cross-sections in the near infra-red coupled with efficient single- photon fluorescence from the emitting state.

Two-photon absorption is a third order nonlinear optical process and thus common to all molecules [6]. From quantum mechanical considerations the two-photon absorption rate (s^{-1}) is given by

$$R_{TPA} = \frac{\sigma^{(2)} I^2(t) G^{(2)}}{2(h\nu)^2} \qquad [4.1]$$

where $\sigma^{(2)}$ is the two photon absorption cross-section ($cm^4 s\ photon^{-1}$), $I(t)$ is the

instantaneous optical intensity (Wcm^{-2}) and $G^{(2)}$ is the second order degree of coherence of the light. If I(t) has a Gaussian temporal profile τ at full width half maximum and the excitation source is well mode-locked ($G^{(2)}=1$) then integration of equation 4.1 yields the two-photon absorption transition probability

$$P_{TPA} = \frac{\sigma^{(2)}}{2(h\nu)^2}\left(\frac{E_{TP}}{A}\right)^2 \times \frac{0.664}{\tau} \qquad [4.2]$$

where E_{TP} is the laser pulse energy (J) and A is the area of illumination (cm^2). As can be seen from equation 4.2, the transition probability is proportional to the square of the photon flux $E_{TP}/h\upsilon A$ and inversely proportional to the excitation pulse width τ. Typical values for two-photon absorption cross-sections range from 10^{-50}-10^{-48} cm^4s $photon^{-1}$ $molecule^{-1}$ (table 4.1). This limits the ability to excite a molecule using two-photon excitation to regions of high photon flux and necessitates the use of short (sub-picosecond) high intensity laser pulses to create suitable two-photon excitation conditions. Two-photon cross-sections are often quoted in units of *Göppert-Meyer* (GM), such that $1GM=1x10^{-50}$ cm^4s/photon.

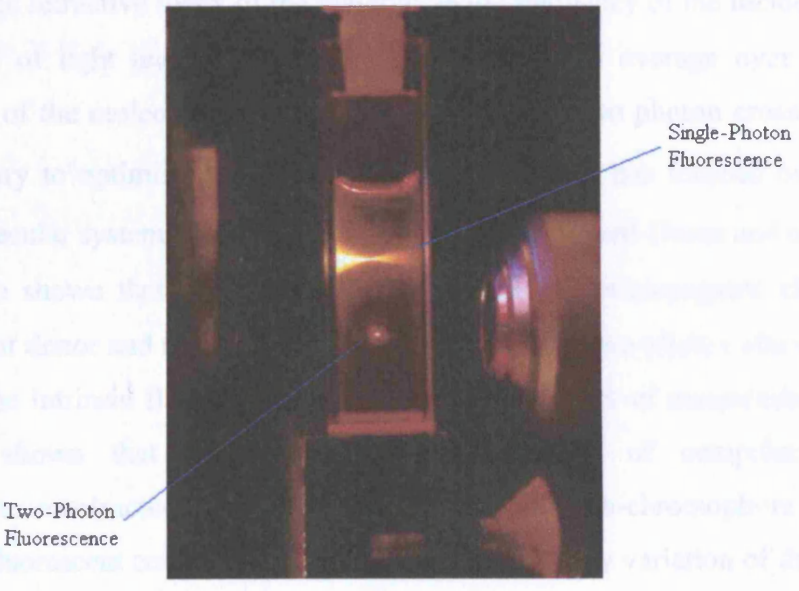

Figure 4.1: A direct comparison between the spatial dependence of two- and single-photon absorption from a fluorescent probe in an isotropic solution contained in a cuvette and viewed at 90° to the excitation direction. Single-photon excitation at 488nm produces fluorescence throughout the sample whereas the restriction of two-photon fluorescence (excited at 800nm) to the Rayleigh range around the laser focus is clearly evident. The photograph is provided courtesy of Dr Mireille Blanchard-Desce (CNRS UMR 6510 Rennes).

A: Naturally Occurring Fluorophores				
Fluorophore	**GFP (wild type)**	**NADH**	**Serotonin**	**Dopamine**
$\sigma^{(2)}$ (GM)	6	0.02	43	1.2
Exc. Wavelength (nm)	800	700	560	560
B: Synthetic (single-photon) Fluorophores				
Fluorophore	**Rhodamine 6G**	**Fluorescein**	**Bis-MSB**	**Indo-1(free)**
$\sigma^{(2)}$ (GM)	11	38	6.3	12
Exc. Wavelength (nm)	700	782	691	700

Table 4.1: Two-photon cross-sections of (A) naturally occurring fluorophores and (B) synthetic fluorescent probes optimised for single-photon excited fluorescence.

Non-linear optical processes are in general governed by hyperpolarisabilities which determine molecular behaviour due to the presence of a static or perturbing (oscillating) optical electric field. The two-photon cross-section is related to the diagonal part of the second hyperpolarisability γ_I via

$$\gamma_I = \frac{4\pi^2\hbar\omega^3}{n^2c^3}\langle \mathrm{Im}(\gamma(-\omega;\omega,\omega-\omega))\rangle \qquad [4.3]$$

where n is the refractive index of the material, ω the frequency of the incident radiation, c the speed of light and the angle brackets indicate an average over all possible orientations of the molecule. In order to achieve a high two photon cross-section it is thus necessary to optimise $\langle \mathrm{Im}\ (\gamma_I)\rangle$; to this end research has focused on conjugated organic molecular systems [7-9]. Recent work by M Blanchard-Desce and co-workers at Rennes have shown that the quadrupolar substitution of π-conjugated chromophores with different donor and acceptor groups can increase the two-photon absorption cross-section of the intrinsic fluorescent unit by up to two orders of magnitude [4]. Further work has shown that the two-photon cross-sections of octupolar (branched) chromophores constructed from the gathering of dipolar sub-chromophore units around a common fluorescent core can be significantly enhanced by variation of the connecting unit or the conjugated branch length. Large two-photon cross-sections (c.a. 10^3GM) have been achieved using an ambivalent core with conjugated rods made from arylene-vinylene or arylene ethyneylene oligomers [4].

The work in this chapter consists of two studies undertaken in collaboration with the Blanchard-Desce group; firstly the measurement of two-photon cross-sections for a series of quadrupolar fluorophores and a branched quadrupolar fluorophore was extended to shorter wavelengths (typically 700nm to 540nm) that lie outside the Ti:Sapphire tuning range – this was achieved using a tunable ultrafast optical parametric amplifier. These measurements were accompanied by theoretical time-dependent density functional calculations of wavelength dependence of the two-photon transition undertaken at Rennes and at Los Alamos National Laboratory by Tretiak and co-workers. Subsequent to these studies a high repetition rate optical parametric oscillator and Ti:Sapphire laser (in conjunction with time correlated single-photon counting) was used to investigate the difference in the two-photon cross-sections for linearly and circularly polarised excitation as a function of wavelength (infra red-visible region), and the degree of initial fluorescence anisotropy created in both excitation processes. These measurements can be used to provide information on the structure of the two-photon transition tensor; significant structural differences were observed between branched and unbranched fluorophores, which can be attributed to delocalisation of the excitation over the branched structure rather than localisation on a single arm.

4.2 Quadrupolar and Branched Two-Photon Fluorescent Probes

The molecules studied in this thesis were three quadrupolar species: OM49, TM11 and BH101, and a branched system: OM77. These are representative of the design strategy employed by the Blanchard-Desce Group to both tailor and optimise the two-photon absorption and single-photon fluorescence emission of a molecular system. The principle is to engineer the absorption and emission properties of an ultraviolet absorbing and emitting core with the addition of electron donating end groups coupled to the core by the appropriate molecular linkers (figure 4.3). OM49 and TM11 both contain a biphenyl fluorescent core with the same electron donating end groups and differ only in the connector (acetylenic vs. ethylinic) between these and the core. The change in linker from triple bond (acetylenic) to a double bond (ethylinic) gives rise to a red shift in single-photon absorption and emission spectra with a rise in fluorescence lifetime. A change in the fluorescent core from biphenyl to the planar and rigid fluorene system (BH101) is accompanied by a red shift (bathochromic) in the single-photon

absorption spectrum - the emission spectra of the two fluorophores are however similar. The more rigid fluorene core is found to give rise to an increase in the two-photon cross-section. OM77 is the branched analogue of BH101; the combination of three quadrupolar molecules into a branched structure is accompanied by a red shift in absorption and fluorescence with little apparent change in fluorescence lifetime and quantum yield (all absorption and emission spectra are shown in figure 4.4). The branched structure is however expected to produce an enhanced two-photon cross-section with excitation delocalised over the structure.

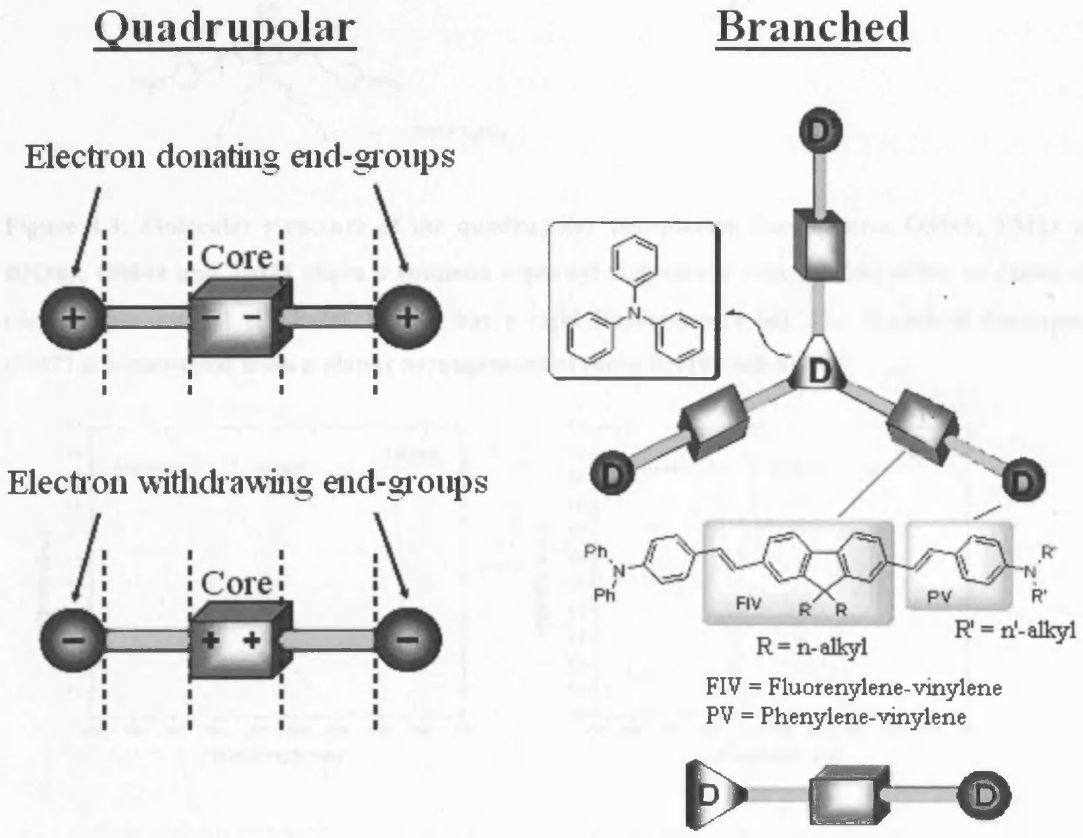

Figure 4.2: Structures of the two-photon polyenes developed by the Blanchard-Desce group and studied in this thesis. Two-photon absorbers are based around a fluorene or a biphenyl core with electron donating end groups (+)† and are designed to undergo a quadrupolar intramolecular charge redistribution upon two-photon excitation. The branched systems consist of a (near) planar arrangement of quadrupolar chromophores about a nitrogen core.

†electron withdrawing substituents (-) have also been synthesised but are not part of this study.

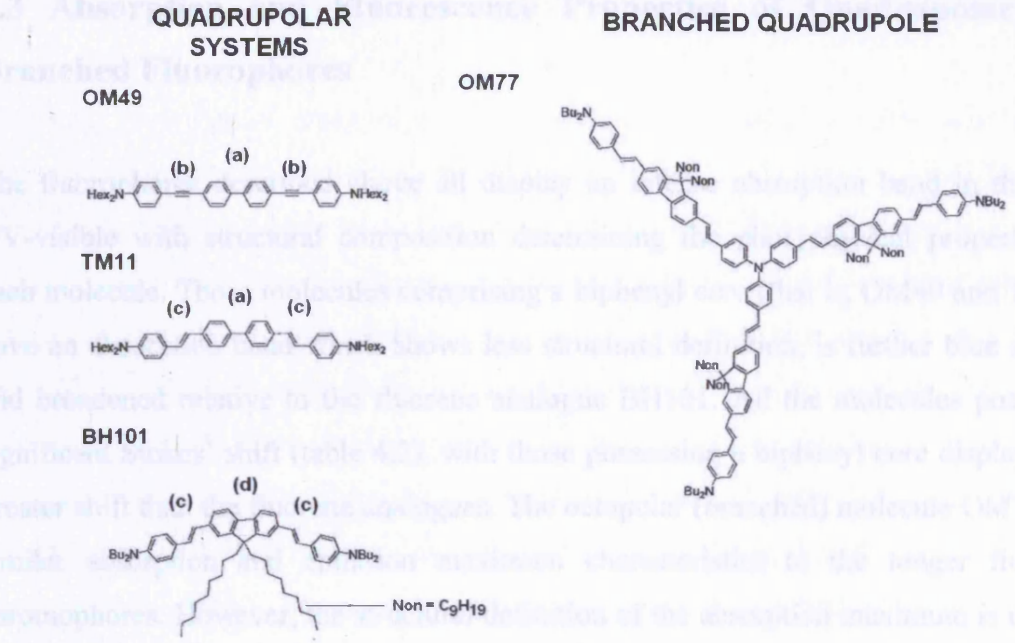

Figure 4.3: Molecular structure of the quadrupolar two-photon fluorophores OM49, TM11 and BH101. OM49 and TM11 share a common biphenyl fluorescent core (a) but differ in connectors ((b)vinylinic and (c) ethylinic). BH101 has a rigid fluorene core (d). The branched fluorophore OM77 is constructed from a planar arrangement of three BH101 sub units.

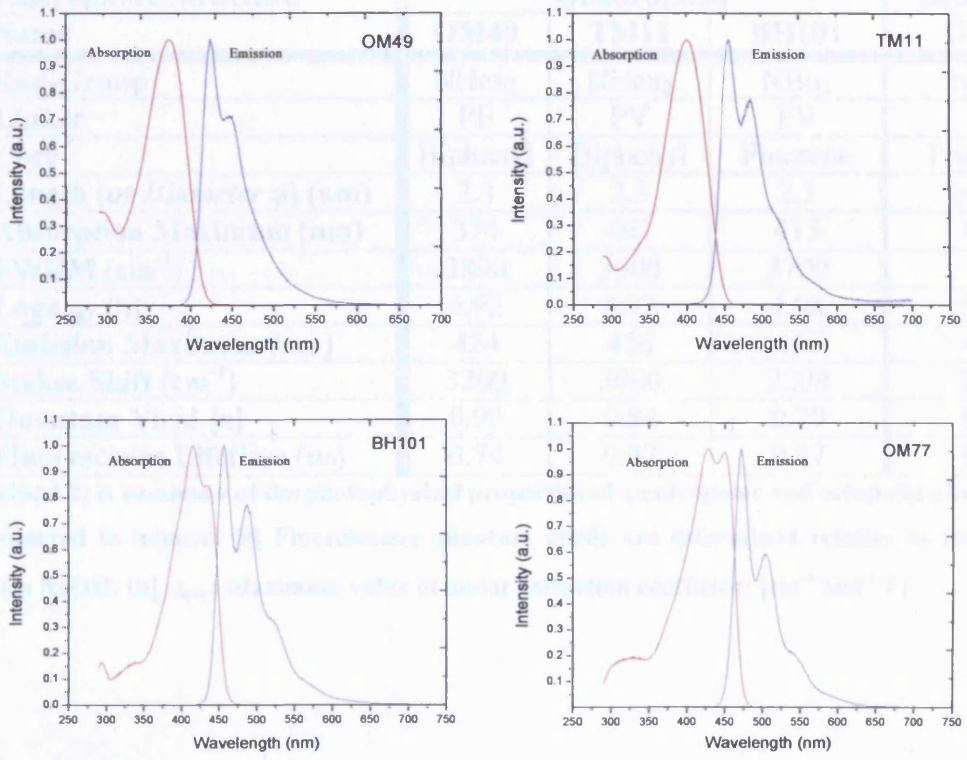

Figure 4.4: Absorption and emission spectra of the two-photon quadrupolar chromophores OM49, TM11 and BH101 and the branched fluorophore OM77

4.3 Absorption and Fluorescence Properties of Quadrupolar and Branched Fluorophores

The fluorophores described above all display an intense absorption band in the near UV-visible with structural composition determining the photophysical properties of each molecule. Those molecules comprising a biphenyl core (that is, OM49 and TM11) have an absorption band which shows less structural definition, is further blue shifted and broadened relative to the fluorene analogue BH101. All the molecules possess a significant Stokes' shift (table 4.2), with those possessing a biphenyl core displaying a greater shift than the fluorene analogues. The octupolar (branched) molecule OM77 has similar absorption and emission maximum characteristics to the longer fluorene chromophores. However, the structural definition of the absorption maximum is unique in that there are two maxima (c.a. 425nm and c.a. 447nm) of very similar magnitude. All the molecules exhibit good quantum yields ranging from 0.47 to 0.90 and similar excited state lifetimes. Their photophysical properties are set out in table 4.2.

Fluorophore Structure	**Quadrupolar**			**Branched**
Name	**OM49**	**TM11**	**BH101**	**OM77**
End-Group	$NHex_2$	$NHex_2$	NBu_2	NBu_2
Linker	PE	PV	PV	-
Core	Biphenyl	Biphenyl	Fluorene	Triphenyl
Length (*or Diameter φ*) (nm)	2.4	2.3	2.3	φ=4.3
Absorption Maximum (nm)	374	401	415	428
FWHM (cm^{-1})	3800	3900	3700	-
Logε_{max} [b]	4.92	4.92	4.98	5.39
Emission Maximum (nm)	424	456	457	445
Stokes Shift (cm^{-1})	3200	3000	2200	2100
Quantum Yield [a]	0.90	0.84	0.79	0.74
Fluorescence Lifetime (ns)	0.74	0.87	0.87	0.85

Table 4.2: A summary of the photophysical properties of quadrupolar and octupolar chromophores measured in toluene. [a] Fluorescence quantum yields are determined relative to fluorescein in 0.1m NaOH. [b] ε_{max}: Maximum value of molar extinction coefficient [cm^{-1} mol^{-1} L]

4.4 Two Photon Photoselection and Fluorescence Anisotropy

Molecular two-photon absorption and spontaneous emission is illustrated in the Jablonski diagram of figure 4.5. Initial excitation from low-lying vibrational levels in the ground electronic state (S_0) takes place with the simultaneous absorption of two (non-resonant) near infra red photons. Two-photon absorption can be thought of as two instantaneously consecutive single-photon transitions that take place via a set of "virtual" intermediate states. Virtual states are those which can be coupled (allowed) by single-photon transitions to the ground and excited states. Molecular two-photon absorption generally involves the absorption of red to near infra-red photons, wavelengths for which there are no single-photon electronic transitions. The virtual states are thus strongly off-resonance and as a result exist on a time scale Δt (lifetime) that is governed by the uncertainty principle,

$$\Delta E \Delta t \approx \hbar \qquad [4.4]$$

where

$$\Delta E = E_{State} - h\upsilon \qquad [4.5]$$

The nearest electronic state that in principle could act as a virtual state would be the first excited (singlet) state with a transition energy corresponding to photons in the visible to ultraviolet regions. The energy gap ΔE is therefore on the order of $h\upsilon$, for a typical near-infra red two-photon excitation wavelength of 800nm this yields a value of 4.2×10^{-16} seconds (0.42 femtoseconds). This is less than the oscillation period for light at 800nm. Thus, for two-photon absorption to occur (given a favourable quantum mechanical transition probability) both photons must in effect interact with the molecule instantaneously as illustrated below.

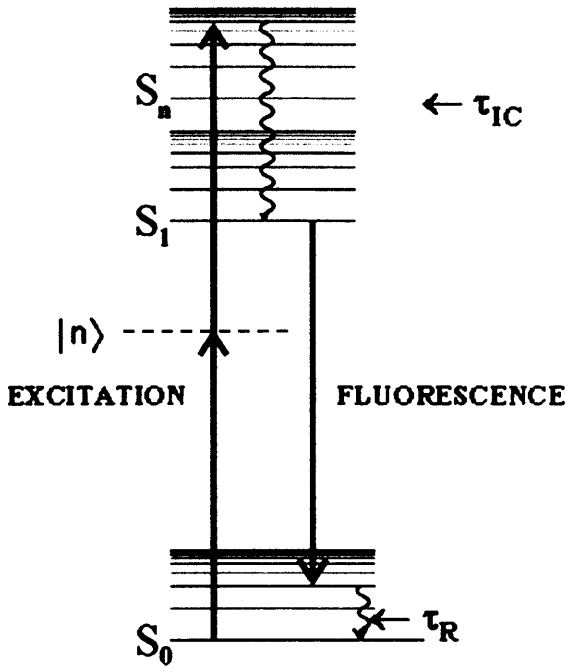

Figure 4.5: A Jablonski diagram showing the excitation and relaxation pathways in two-photon excited fluorescence. Excitation occurs from the molecular ground state S_0 via a virtual state $|n\rangle$ to an excited singlet state S_n. This is followed by rapid (τ_{IC}: sub-picosecond) internal conversion and vibrational relaxation to lower vibrational levels of S_1. Spontaneous emission (nanoseconds) takes place to high vibrational levels in the ground state with fast (τ_R sub-picosecond) collisional relaxation returning molecules to the initially populated levels.

The initially excited state (S_n) undergoes rapid (sub-picosecond) internal conversion and vibrational relaxation in collisions with surrounding solvent molecules leading to the population of lower vibrational levels in S_1. In the absence of external perturbations the population in S_1 decays by spontaneous emission (as in the case of single-photon excitation from S_0 to S_1) to upper vibrational levels of S_0 consistent with the Franck-Condon principle. Solvent 'cooling' of the vibrationally hot ground state population is correspondingly rapid. As well as possessing an intensity dependent transition probability, two-photon excitation is also distinct from single-photon excitation in that the absorption probability is polarisation dependent. A fundamental property of single-photon transitions in an isotropic medium is that the transition probability is independent of the polarisation of the incident light [10]; this restriction is relaxed in ordered systems as seen in Chapters 2 and 3 where there is a direct correspondence between the molecular and laboratory frames of reference. However for two-photon

absorption the transition does not involve a simple dipolar rearrangement of electronic charge density; rather, it involves products of the allowed single-photon transition dipoles between the ground intermediate and final states. In quantum mechanical terms the cross-section for the absorption of two photons of polarisations α and β between states $|g\rangle$ and $|e\rangle$ is proportional to the squared modulus of the tensor $W_{\alpha\beta}^{g\to e}$ defined by a sum of transitions involving the intermediate (virtual) states $|n\rangle$,

$$\left|W_{\alpha\beta}^{g\to e}\right|^2 = \left|\sum_n \left(\frac{\alpha\cdot\langle g|r|n\rangle\langle n|r|e\rangle\cdot\beta}{\upsilon_n - \upsilon_\alpha + i\Gamma_n} + \frac{\beta\cdot\langle g|r|n\rangle\langle n|r|e\rangle\cdot\alpha}{\upsilon_n - \upsilon_\beta + i\Gamma_n} \right)\right|^2 \qquad [4.6]$$

where υ_n and Γ_n are the transition frequency and homogeneous linewidth of $|n\rangle$ respectively. In the molecular frame of reference the transition tensor can have 9 elements S_{AB} where A, B=X, Y or Z,

$$\left|W_{\alpha\beta}^{g\to e}\right|^2 \equiv \left|\sum_{A,B=X,Y,Z} S_{AB}\right|^2 \qquad [4.7]$$

For the absorption of two identical photons $S_{AB}=S_{BA}$. For planar aromatic molecules the two-photon transition is dominated by moments in the plane (XY) of the molecule. The relative absorption strengths for linearly and circularly polarised two-photon absorption define the parameter Ω which can be determined from the integrated fluorescence intensity for linearly and circularly polarised absorption as shown in figure 4.6.

$$\Omega = I_{ABS}^{C} / I_{ABS}^{L} = \int I_F^C(t)dt \Big/ \int I_F^L(t)dt \qquad [4.8]$$

The total fluorescence intensity can be obtained from a 'magic angle' polarisation measurement at 54.7° to the symmetry axis (axis of cylindrical symmetry for the transition).

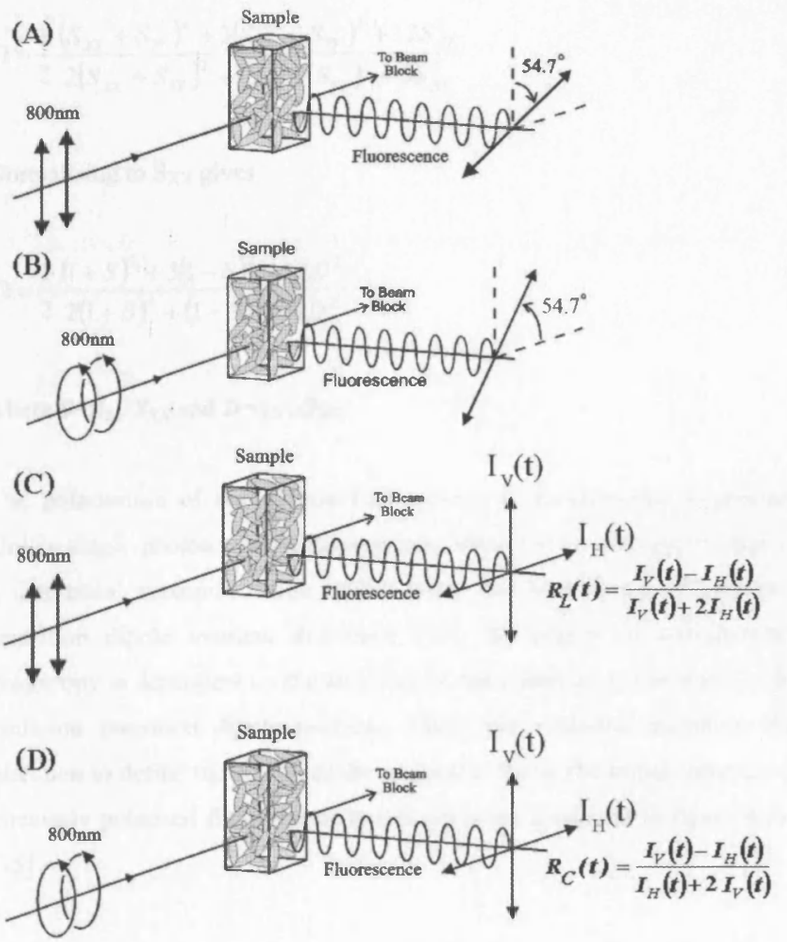

Figure 4.6: Excitation-detection geometries for the determination of the transition strength for (A) linearly polarised and (B) circularly polarised two-photon excitation. Fluorescence intensity measurements are made at magic angle polarisation settings with respect to the quantisation (symmetry) axis for the two polarisations. Alternatively the fluorescence intensity can be constructed from $I_V(t)+2I_H(t)$ and $2I_V(t)+I_H(t)$ measurements for linear and circular polarisations respectively. (C) and (D): Excitation-detection geometries for fluorescence anisotropy measurements following linearly and circularly polarised two-photon excitation.

In terms of a planar transition tensor, Ω is given by [11-13]

$$\Omega = \frac{1}{2}\frac{(S_{XX}+S_{YY})^2 + 3(S_{XX}-S_{YY})^2 + 12S_{XY}^2}{2(S_{XX}+S_{YY})^2 + (S_{XX}-S_{YY})^2 + 3S_{XY}^2} \qquad [4.9]$$

Normalising to S_{XX} gives

$$\Omega = \frac{1}{2}\frac{(1+S)^2 + 3(1-S)^2 + 12D^2}{2(1+S)^2 + (1-S)^2 + 4D^2} \qquad [4.10]$$

where $S=S_{YY}/S_{XX}$ and $D=S_{XY}/S_{XX}$.

The polarisation of two-photon fluorescence is an important experimental quantity. Unlike single-photon excited fluorescence which (in an isotropic medium) departs from a theoretical maximum value of 0.4 solely due to different absorption and emission transition dipole moment directions [14], the degree of two-photon fluorescence anisotropy is dependent on the structure of the transition tensor and the direction of the emission transition dipole moment. Using the emission transition dipole moment direction to define the X axis of the molecular frame the initial (time-zero) linearly and circularly polarised fluorescence anisotropies (as measured in figure 4.5) are given by [15]

$$R_L(0) = \frac{I_V(0) - I_H(0)}{I_V(0) + 2I_H(0)} = \left(\frac{1}{7}\right)\frac{2(S_{XX}+S_{YY})^2 + (S_{XX}-S_{YY})^2 + 4S_{XY}^2 + 9(S_{XX}^2 - S_{YY}^2)}{2(S_{XX}+S_{YY})^2 + (S_{XX}-S_{YY})^2 + 4S_{XY}^2} \qquad [4.11]$$

$$R_C(0) = \frac{I_V(0) - I_H(0)}{I_H(0) + 2I_V(0)} = \left(\frac{1}{7}\right)\left[\frac{3(S_{XX}-S_{YY})^2 - (S_{XX}+S_{YY})^2 + 12S_{XY}^2 + 6(S_{XX}^2 - S_{YY}^2)}{(S_{XX}+S_{YY})^2 + 3(S_{XX}-S_{YY})^2 + 12S_{XY}^2}\right] \qquad [4.12]$$

For an emission transition dipole moment with X and Y components [4.11] and [4.12] become [16]

$$R_L(0)=\left(\frac{1}{7}\right)\left[1+\frac{9(1-S^2)(\cos^2\theta-\sin^2\theta)+4D(1+S)\sin\theta\cos\theta}{2(1+S)^2+(1-S)^2+4D^2}\right] \qquad [4.13]$$

$$R_C(0)=\left(\frac{1}{7}\right)\left[1+\frac{6\left[(1-S^2)(\cos^2\theta-\sin^2\theta)+4D(1+S)\sin\theta\cos\theta\right]-2(1+S)^2}{(1+S)^2+3(1-S)^2+12D^2}\right] \qquad [4.14]$$

For the simplest two-photon transition tensor S and D have zero values (i.e. S_{XX} is the sole non-zero element), yielding

$$\Omega=\frac{2}{3},\ R_L(0)=\left(\frac{4}{7}\right)\left[\frac{3\cos^2\theta-1}{2}\right],\ R_C(0)=\left(\frac{2}{7}\right)\left[\frac{\left[(3\cos^2\theta-1)\right]}{2}\right] \qquad [4.15]$$

These are recognisable as the values obtained for two sequential single-photon transitions via a 'real' intermediate state with parallel (absorption) transition dipole moments at an angle θ to the emission transition dipole moment. Such a one dimensional situation might be approximated by a linear molecule but in a system with significant two dimensional charge displacement ***S*** and ***D*** should be significant. For example, for a system with S≈1,

$$\Omega=\frac{2+6D^2}{8+4D^2},\ R_L(0)=\left(\frac{1}{7}\right)\left[1+\frac{8D\sin\theta\cos\theta}{8+4D^2}\right]\ R_C(0)=\left(\frac{1}{7}\right)\left[1+\frac{12D\sin\theta\cos\theta-2}{1+3D^2}\right] \qquad [4.16]$$

4.5 Measurement of Two-Photon Absorption Cross-Sections

Although it is possible to measure the two-photon absorption cross-section of a fluorophore directly by measuring the amount of light absorbed by the sample, this procedure is highly problematic as the need for high incident powers leads to saturation, photobleaching, stimulated emission and self-quenching [17]. These factors greatly complicate the interpretation of such measurements. Alternatively two-photon absorption cross-sections can be determined by measuring the two-photon fluorescence signal generated via two-photon absorption. The resulting two-photon excitation (TPE)

action cross-section σ_{TPE} is linearly proportional to the two-photon absorption cross-section σ_2:

$$\sigma_{TPE} = \eta_2 \sigma_2 \qquad [4.17]$$

where η_2 is the fluorescence quantum yield of the fluorophore. For a two-photon process the number of photons absorbed per unit time N_{abs}, (providing there is no saturation, photobleaching, self-quenching or stimulated emission) is related to the number of fluorescence photons *F(t)* detected per unit time by the experimental apparatus, according to

$$F(t) = \frac{1}{2}\varphi \eta_2 N_{abs} \qquad [4.18]$$

where φ is the fluorescence collection efficiency of the measurement system, a function of the collection efficiency of the objective lens, the transmission optics and detector. The fact that two photons are absorbed for every excitation event is incorporated in the factor of ½. During the experiment it is the time-averaged fluorescence emission $\langle F(t) \rangle$ which is measured. If the excitation source is of pulsed origin, then the time averaged emission detected can be expressed as [17]

$$F(t) = \frac{1}{2}\varphi \eta_2 \sigma_2 C \left(\frac{g_p}{f\tau} \right) \left(\frac{8n\langle P(t) \rangle^2}{\pi \lambda} \right) \qquad [4.19]$$

where *C* is the molecular concentration, *n* is the refractive index of the sample, $\langle P(t) \rangle$ is the time averaged power of the excitation source (photons s^{-1}) and λ is the excitation wavelength (cm). In equation 4.19 the second order temporal coherence of the optical pulse $G^{(2)}$ has been written as $g_p/f\tau$ where *f* is the repetition rate of the pulsed excitation source and g_p is a dimensionless parameter equal to unity [18].

In TPE cross-section measurements the absorption rates depend strongly on the temporal coherence of the excitation pulse. The measurement of TPE cross-sections requires detailed knowledge of $G^{(2)}$ in the focal region of the sample. However,

obtaining this information is complicated and alternative methods have been developed to allow accurate determination of the TPE action cross-sections. The fluorescence signal of a standard calibration sample of known TPE action cross section and emission spectrum can be used to calibrate the fluorescence signal for the new molecular fluorophore. By taking the ratio of the two signals it is possible to determine the value of the TPE action cross section of the new fluorophore without accurate knowledge of $G^{(2)}$. The value of $G^{(2)}$ at any given excitation wavelength is the same for both the calibration sample and the new fluorophore and from equation 4.19, the ratio of the time averaged fluorescence that is detected becomes

$$\frac{\langle F(t)\rangle_{cal}}{\langle F(t)\rangle_{new}} = \frac{\varphi_{cal}\eta_{2cal}\sigma_{2cal}C_{cal}\eta_{cal}\langle P_{cal}(t)\rangle^2}{\varphi_{new}\eta_{2new}\sigma_{2new}C_{new}\eta_{new}\langle P_{new}(t)\rangle^2} \qquad [4.20]$$

where $\langle P_{cal}(t)\rangle$ and $\langle P_{new}(t)\rangle$ are the incident powers for the calibration sample and the new fluorophore. Rearranging equation 4.20 gives the TPE action cross-section of the fluorophore under investigation as

$$\sigma_{2new}(\lambda)\eta_{2new} = \frac{\varphi_{cal}\eta_{2cal}\sigma_{2cal}(\lambda)C}{\varphi_{new}C_{new}}\frac{\eta_{cal}}{\eta_{new}}\frac{\langle P_{cal}(t)\rangle^2}{\langle P_{new}(t)\rangle^2}\frac{\langle F(t)\rangle_{new}}{\langle F(t)_{cal}\rangle} \qquad [4.21]$$

4.6 p-Bis (o-methylstyryl)-benzene (bis-MSB): Calibration Sample

All two-photon absorption cross-section measurements described in this chapter were calibrated relative to the absolute two-photon absorption (TPA) cross section of the reference compound p-Bis (o-methylstyryl)-benzene (bis-MSB) in cyclohexane. The two-photon absorption properties of bis–MSB have been well documented [19]. The compound is characterized by an absorption spectrum ranging from 470-720nm, a pure power squared dependence (i.e. no single-photon or sequential two-photon processes) across the wavelength range examined (540-700nm) and a fluorescence quantum yield of 0.95 (cyclohexane) at ambient temperatures. Significantly the compound possesses a satisfactory two-photon absorption cross-section (72GM at 570nm) which avoids the

use of high powers for sample excitation. The TPA cross sections for the wavelength range 540-700nm are shown in figure 4.7.

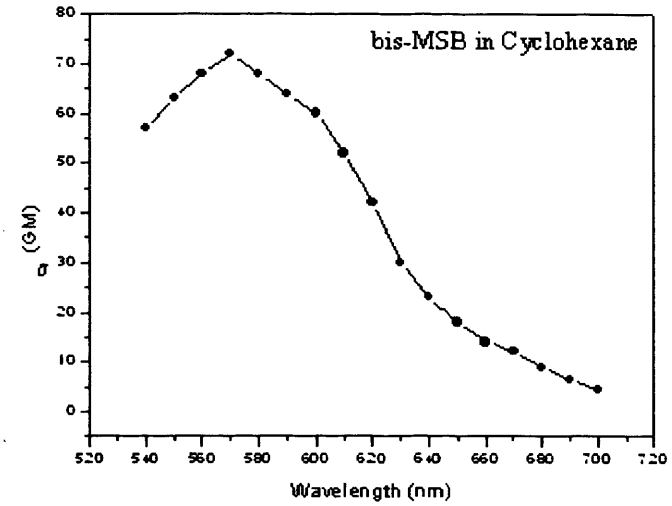

Figure 4.7: Graph of the two-photon absorption cross-section for bis-MSB in the solvent cyclohexane for the wavelength range 540-700nm. (Supplied by Dr M Wertz Rennes)

4.7 Experimental Procedure

The experimental apparatus designed to measure the two-photon absorption cross section of OM49, TM11, BH101 and OM77 from 540-700nm is illustrated in figure 4.8. It is based on a regeneratively amplified Ti:Sapphire pumped tunable optical parametric amplifier delivering 200-250fs pulses at a repetition rate of 250kHz with an average power of 70mW. The output power was controlled using neutral density wheels and filtered using a range of long pass filters (Schott RD530-665) to remove any harmonics associated with the Ti:Sapphire and any residual fundamental Ti:Sapphire radiation from the white light continuum. The OPA output was chopped at 220Hz by an optical chopper (Stanford SR540), passed through a 2.5mm aperture and focused into a 45μl optical cuvette (Hellma) using a 25mm achromatic lens (Melles Griot). Detection of the generated fluorescence was made at 90^0 using a 25mm focal length lens and passed through an analyzing polarizer (Polaroid) set for magic angle detection (54.7^o) to the excitation polarization. Short pass filters (Corion LS500 and LS550) were employed to filter any scattered laser light where appropriate. Emitted fluorescence signals were detected using a photomultiplier (Hamamatsu 943-02) coupled to a lock-in amplifier (Stanford SRS 540).

Corrections to the fluorescence signals were made for differences in the spectral overlap between the emitted fluorescence and the spectral sensitivity of the detector (300-700nm). To confirm that single-photon absorption was not contributing to the signal, the quadratic dependence of the fluorescence intensity on the excitation intensity was verified for each sample at each wavelength, by measuring the fluorescence signal before and after placing an appropriate filter (NG5-50% Transmission) in the beam path.

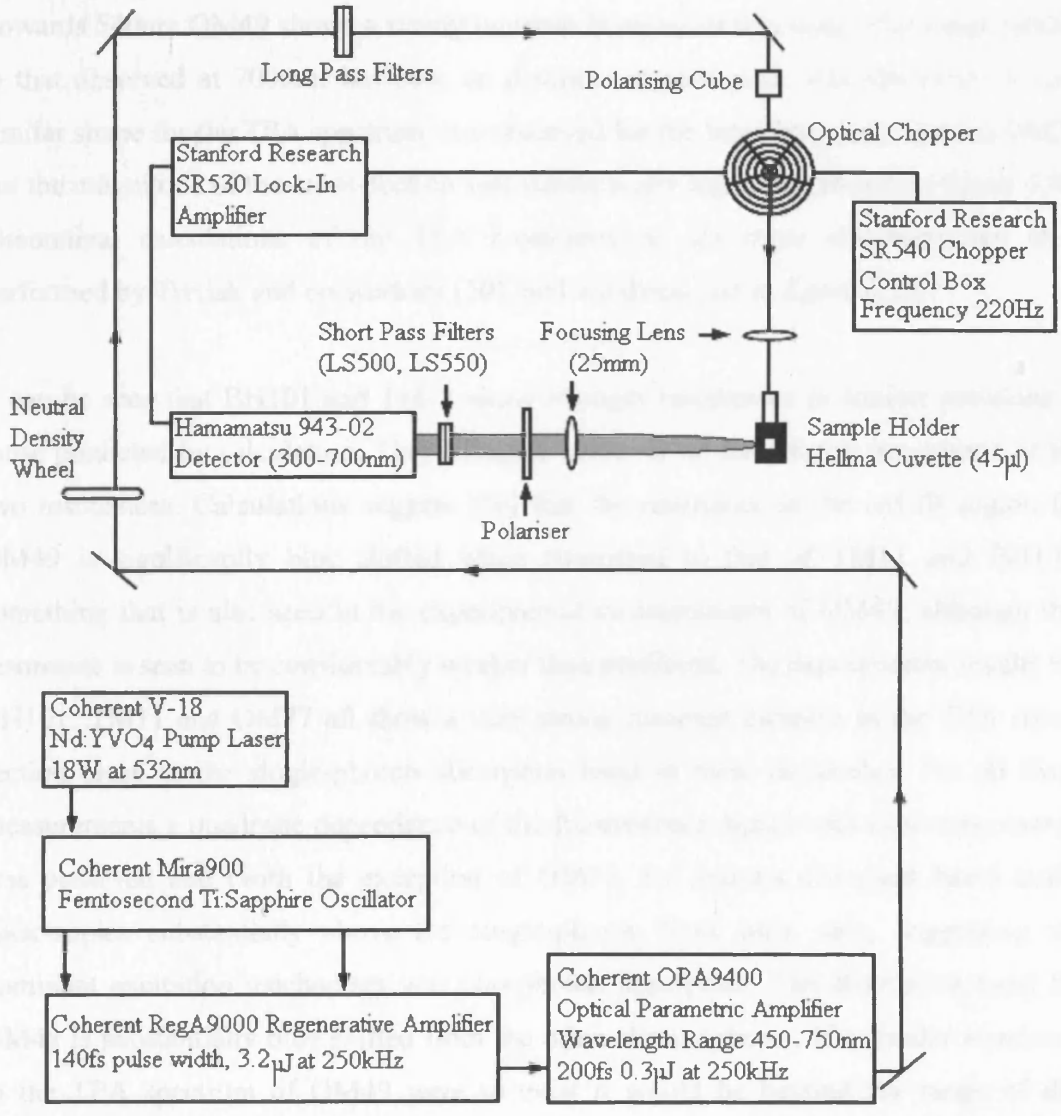

Figure 4.8: Experimental set-up for the steady state detection of two-photon excited fluorescence. In this arrangement the pulsed optical beam is chopped and the reference output is used to lock the lock-in amplifier to the chopper frequency. The sensitivity of the lock-in amplifier allows for measurement of reference signals otherwise lost in background noise.

4.8 Results

Experimental TPA spectra of OM49, TM11 and BH101 are shown in figure 4.9a. The lowest energy TPA maximum of each of the three chromophores is significantly blue shifted with respect to twice the one-photon absorption maximum and occurs between 690-760nm. The notable feature of the visible cross-section measurements is the growth of a very substantial resonance at wavelengths shorter than 600nm in TM11 and BH101 which significantly exceeds their respective near infrared cross-section maxima. Towards 540nm OM49 shows a steady increase in cross-section with values comparable to that observed at 700nm; however no distinct resonant peak was observed. A very similar shape for the TPA spectrum was observed for the branched chromophore OM77 but the magnitude of the cross-section was substantially higher, as shown in figure 4.9b. Theoretical calculations of the TPA cross-sections for these chromophores were performed by Tretiak and co-workers [20]. and are displayed in figure 4.10.

It can be seen that BH101 and TM11 show stronger resonances in similar positions to those predicted by calculation. They disagree however on the relative magnitude of the two resonances. Calculations suggest [20] that the resonance in the red-IR region for OM49 is significantly blue shifted when compared to that of TM11 and BH101, something that is also seen in the experimental measurements of OM49, although this resonance is seen to be considerably weaker than predicted. The experimental results for BH101, TM11 and OM77 all show a very strong resonant increase in the TPA cross-section close to the single-photon absorption band in these molecules. For all these measurements a quadratic dependence of the fluorescence signal with excitation energy was observed and (with the exception of OM77, for reasons discussed later) initial anisotropies substantially above the single-photon limit were seen, suggesting the dominant excitation mechanism was two-photon absorption. The absorption band for OM49 is substantially blue shifted from the other chromophores. If a similar resonance in the TPA spectrum of OM49 were to exist it would be beyond the range of this experiment. The possibility of a large second resonance in the blue region can be seen in the calculated TPA spectrum.

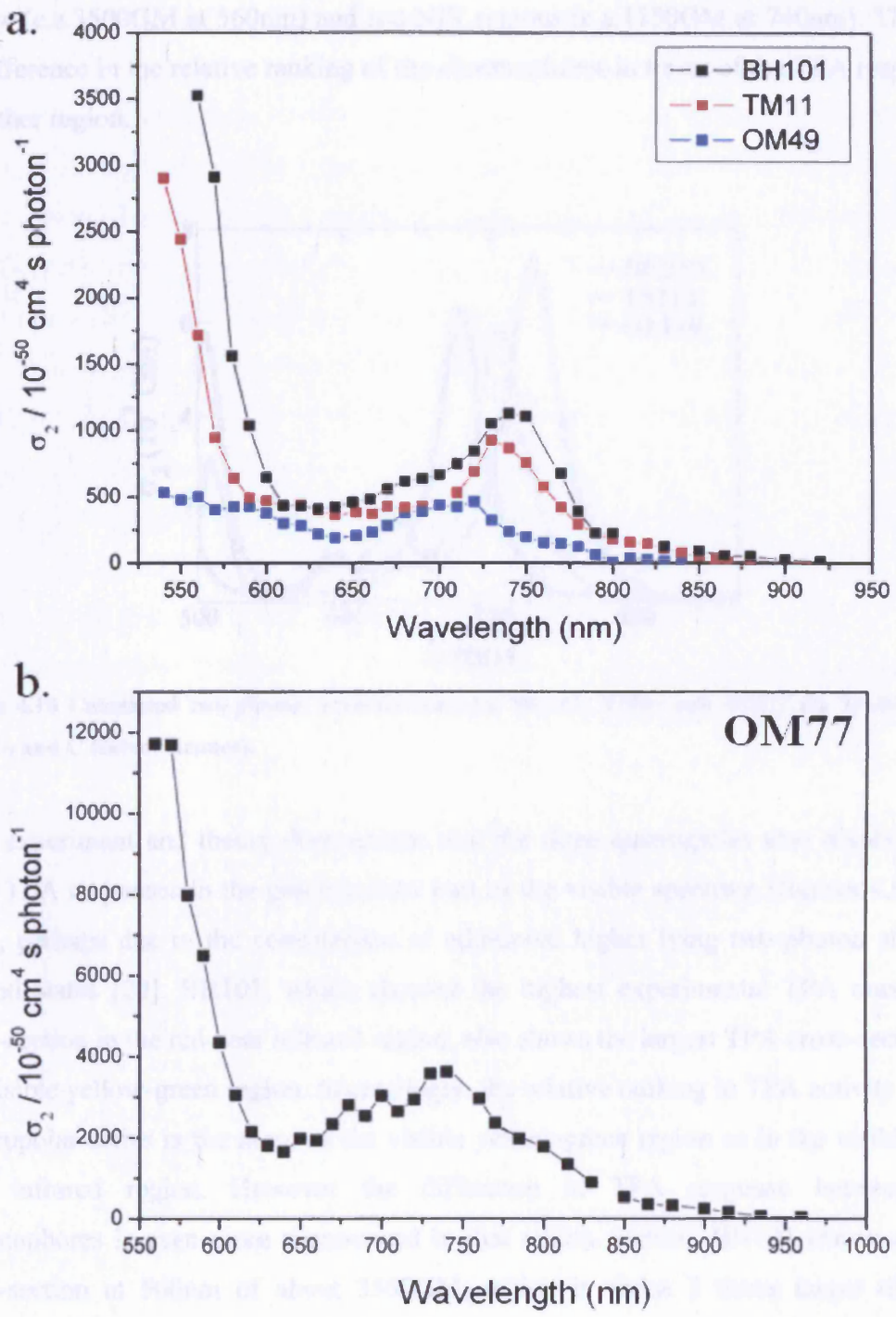

Figure 4.9 The measured two-photon absorption spectra for (a) BH101, OM49 and TM11, and (b) OM77 for the wavelength range 540nm-960nm. The cross-section data at wavelengths above 700nm were measured by the Rennes group. Cross-section data for wavelengths 540nm-700nm measured in collaboration with N.Leonczek.

In line with theoretical predictions (figure 4.10) [20] the fluorene cored molecule BH101 shows the highest TPA maximum cross-sections in both the visible green-yellow (c.a.3500GM at 560nm) and red-NIR regions (c.a.1150GM at 740nm). There is no difference in the relative ranking of the chromophores in terms of the TPA responses for either region.

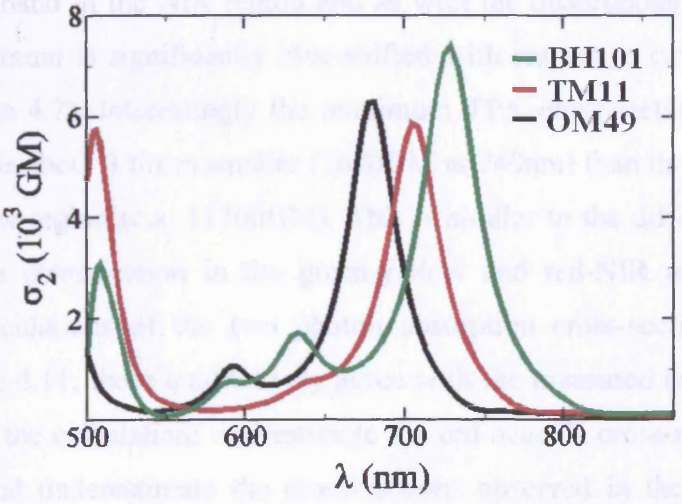

Figure 4.10 Calculated two-photon cross-sections for BH101, TM11 and OM77 (S. Tretiak, Los Alamos and C Katan, Rennes).

Both experiment and theory demonstrate that the three quadrupoles also display very large TPA responses in the green-yellow part of the visible spectrum (figures 4.9a and 4.10), perhaps due to the contribution of additional higher lying two-photon allowed excited states [20]. BH101, which showed the highest experimental TPA maximum cross-section in the red-near infrared region, also shows the largest TPA cross-section in the visible yellow-green region. Interestingly, the relative ranking in TPA activity in the quadrupolar series is the same in the visible yellow-green region as in the visible red-near infrared region. However the difference in TPA response between the chromophores is even more pronounced in that region. Indeed, BH101 shows a TPA cross-section at 560nm of about 3500GM, which is about 3 times larger than its maximum TPA cross-section in the NIR. By comparison OM49 shows similar maximum TPA activity in the two distinct spectral regions (i.e. yellow-green and red-NIR) while TM11 shows a TPA cross-section at 560 nm which is 5 times larger that its maximum TPA cross-section in the NIR (i.e. about 1500GM). Since quadrupoles TM11 and BH101 have the same number of π-electrons in the conjugated system as well as the

same number of effective electrons [16], this indicates that the geometrical conformation (i.e. the planar fluorene core in BH101), favouring increased conjugation, leads to dramatically higher TPA responses in the green-yellow region.

The branched chromophore OM77 has the highest TPA cross-section (c.a.11900GM at 560nm) over both the visible green-yellow and red-NIR range. The TPA spectrum shows a broad band in the NIR region and as with the quadrupolar chromophores the first TPA maximum is significantly blue-shifted with respect to twice the one photon maximum (table 4.2). Interestingly the maximum TPA cross-section of OM77 in the red-NIR range is about 3 times smaller (3600GM at 740nm) than its maximum value in the green-yellow region (c.a. 11700GM). This is similar to the difference between the TPA maximum cross-section in the green-yellow and red-NIR regions for BH101. Theoretical calculations of the two photon absorption cross-section for OM77 are shown in figure 4.11; these qualitatively agree with the measured cross-section data in figure 4.9a, all the calculations overestimate the red-near IR cross-sections of the four fluorophores and underestimate the cross-sections observed in the green-yellow; the former is attributed to the choice of line width for the transition in the calculations, and a limited treatment of solvent effects; the latter, principally by the practical limitations to the number of excited states that could be included in the calculation [20]. The effective enhancement in the TPA cross-section for OM77 over BH101 can be visualised by normalising to the number of quadrupolar branches and the resulting cross-sections are displayed in figure 4.12. The TPA magnitude shows almost additive behaviour near the first TPA maximum but with a sizeable enhancement in the NIR and visible sides indicating the utility of the branching strategy in the design of two-photon absorbers. Differences between the structure of the transition tensor between BH101 and OM77 in the NIR transition are marked and will be discussed further below. A summary of the measured two-photon cross-section data for the four compounds are displayed in table 4.3.

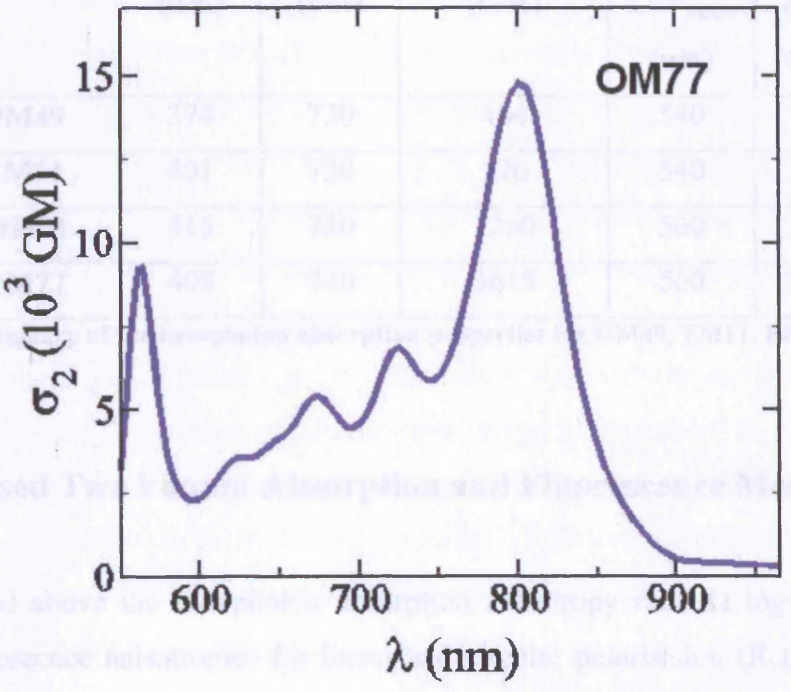

Figure 4.11: Theoretical two-photon absorption spectrum of OM77 calculated by C Katan and S Tretiak [20].

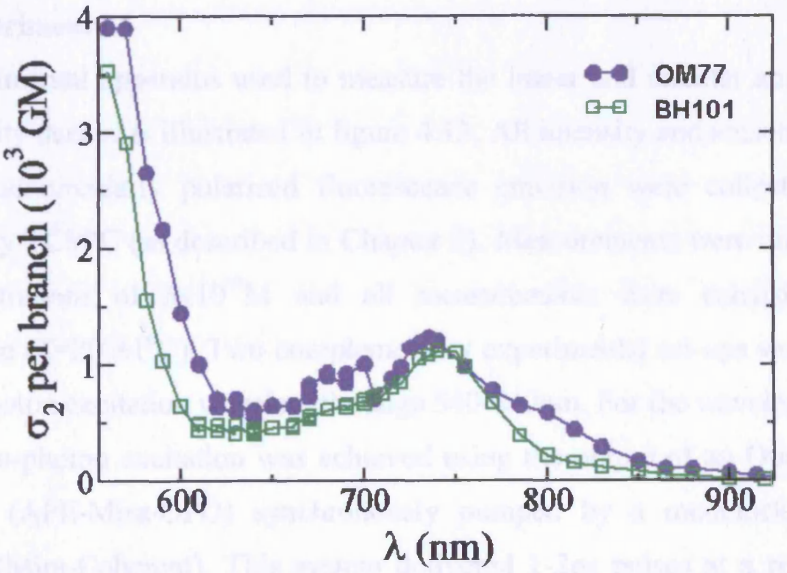

Figure 4.12: Experimental TPA cross-sections normalised for the number of branches of OM77 (3) and BH101 (1).

Fluorophore	λ^{OPA}_{MAX} (nm)	λ^{TPA}_{MAX} (nm)	σ_2 at λ^{TPA}_{MAX} (GM)	Wavelength Range 540nm-700nm	
				λ^{TPA}_{MAX} (nm)	$\sigma_{2\,MAX}$ (GM)[a]
OM49	374	720	464	540	529
TM11	401	730	926	540	2901
BH101	415	730	1260	560	3527
OM77	408	740	3615	560	11712

Table 4.3: Summary of the two-photon absorption properties for OM49, TM11, BH101 and OM77 in toluene.

4.9 Polarised Two Photon Absorption and Fluorescence Measurements

As discussed above the two-photon absorption anisotropy ratio Ω together with the initial fluorescence anisotropies for linear and circular polarisation ($R_L(0)$ and $R_C(0)$) give information on the relative magnitudes of the elements of the two-photon transition tensor. Measurements of Ω, $R_L(0)$ and $R_C(0)$ were performed over 540-820nm for the three quadrupolar systems and OM77.

4.9.1 Experiment

The experimental apparatus used to measure the linear and circular anisotropy decays and intensity decays is illustrated in figure 4.13. All intensity and anisotropy decays for linearly and circularly polarised fluorescence emission were collected at 90° and analysed by TCSPC (as described in Chapter 2). Measurements were made of solutions at concentrations of $5x10^{-4}$M and all measurements were carried out at room temperature (T=20°±1°C). Two complementary experimental set-ups were used to span the two-photon excitation wavelength range 540-840nm. For the wavelength range 540-750nm two-photon excitation was achieved using the output of an Optical Parametric Oscillator (APE-Mira-OPO) synchronously pumped by a modelocked Ti:Sapphire oscillator (Mira-Coherent). This system delivered 1-2ps pulses at a repetition rate of 76MHz with an average pulse energy of 2nJ and tuning range 505nm-750nm. For the wavelength range 750-840nm, two-photon excitation was achieved using a Ti:Sapphire oscillator (Coherent) providing 100fs pulses at 76MHz with an average pulse energy of

1nJ and tuning range 750-900nm. The subsequent beam path is identical for both wavelength ranges in that a single pulse selector (APE) was used to select a portion of the 76MHz repetition rate (as described in Chapter 3), the division ratio of which was set at 1:20 giving a repetition rate of 3.8MHz and an output pulse energy c.a. 60% of the incident pulse energy. The output power was controlled using neutral density wheels and filtered using a range of short pass (LS700) and long pass (OG645) filters where appropriate. The beam was focused into a 45μl small volume cuvette (Hellma) with three optical windows using a 25mm achromatic lens (Melles Griot). Detection of the generated fluorescence was made at 90° using a 6.3cm focal length lens (Melles Griot). A polaroid sheet placed within a computer controlled mount was used to isolate vertically or horizontally polarised components of the fluorescence. In order to obtain circularly polarised light an adjustable phase retardation plate (Alphalas) was introduced to the set-up. Production of fully circularly polarized light was obtained by adjusting the retardation plate such that on rotating an analysing polarizer in the beam path through 360°, the transmitted power remained constant.

In order to determine Ω, fluorescence population decays were obtained from 'magic angle' settings of the analysing polariser relative to the cylindrical symmetry axis of the excitation process. This corresponded to a setting of 54.7° from vertical for linear polarisation or 35.3° from vertical for circular polarisation as illustrated in figure 4.5. To obtain an accurate value of Ω, a sequence of alternating linearly polarised and circularly polarised measurements were carried out for each sample. The value of Ω at each excitation wavelength was calculated from the integrated fluorescence intensities as described by equation 4.8. Measurement of the linearly and circularly polarised fluorescence anisotropy decays was performed by alternating collection of $I_V(t)$ and $I_H(t)$ decays as described in Chapter 2.

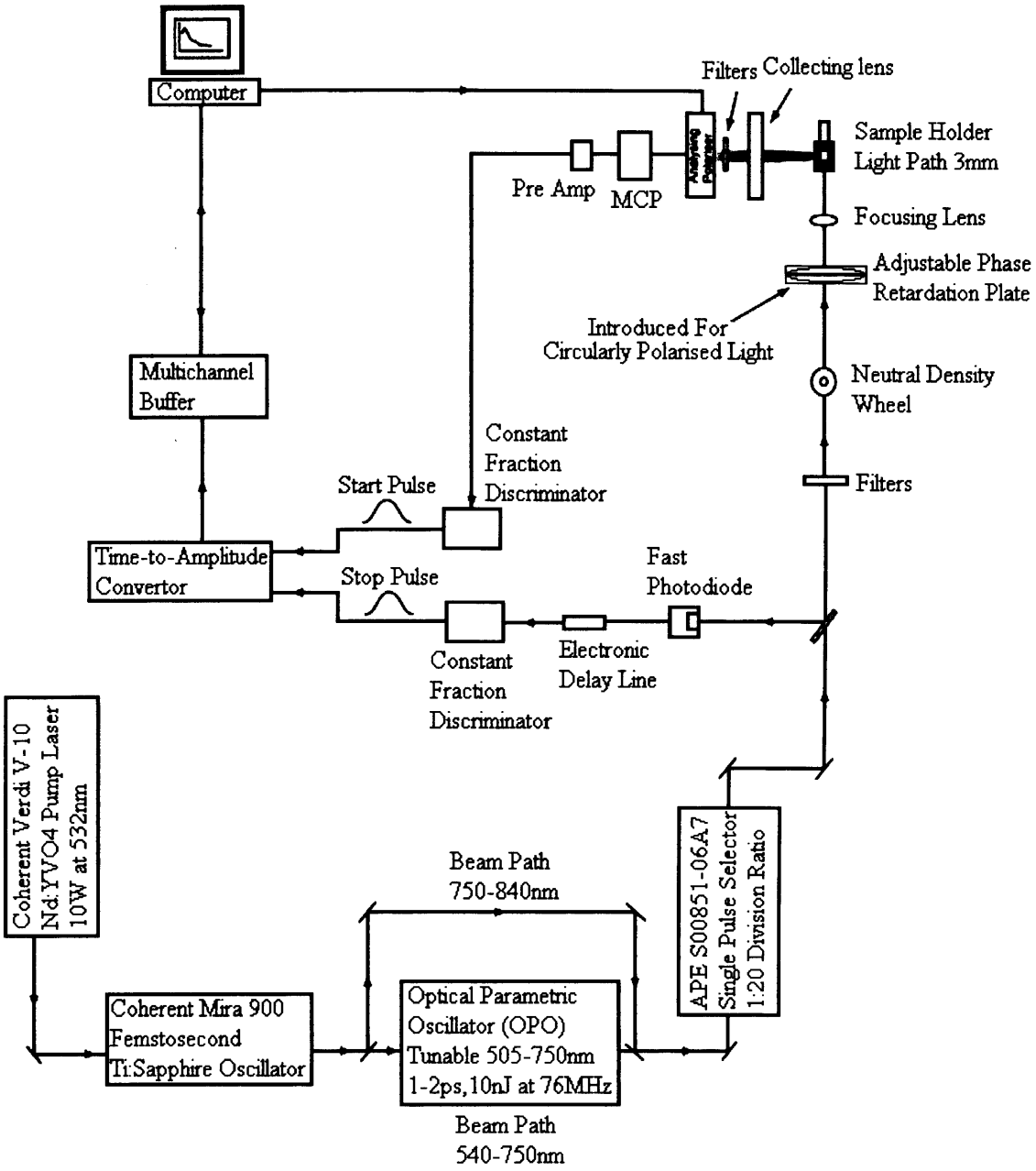

Figure 4.13: Experimental set-up for time resolved polarised two-photon fluorescence anisotropy and anisotropic absorption measurements. Two beam paths are shown in the set-up. In order to generate excitation wavelengths from 540nm-750nm the beam is passed through an Optical Parametric Oscillator (OPO). For those wavelengths between 750nm-840nm the Mira is tuned to the required excitation wavelength.

4.9.2 Results

The two-photon excitation ratios (Ω) and initial fluorescence anisotropies ($R(0)_L$ and $R(0)_C$ are displayed in figure 4.14. The two biphenyl cored quadrupolar molecules OM49 and TM11 show essentially no variation of Ω with wavelength. TM11 particularly shows initial anisotropies that are near independent of wavelength. OM49 shows a slight downward trend for the anisotropies with increasing wavelength but no discernible variation in the red-IR resonance. In contrast the fluorene cored quadrupolar chromophore BH101 shows greater variations in the observed parameters with excitation wavelength. However there is no sign of any distinct structure in the TPA resonance in the red-IR region of the spectrum. The branched chromophore OM77 however shows great deviation from the above described behaviour. Here substantial variations in Ω and $R(0)_C$ are observed in the region of the resonance. though $R(0)_L$ appears largely unaffected.

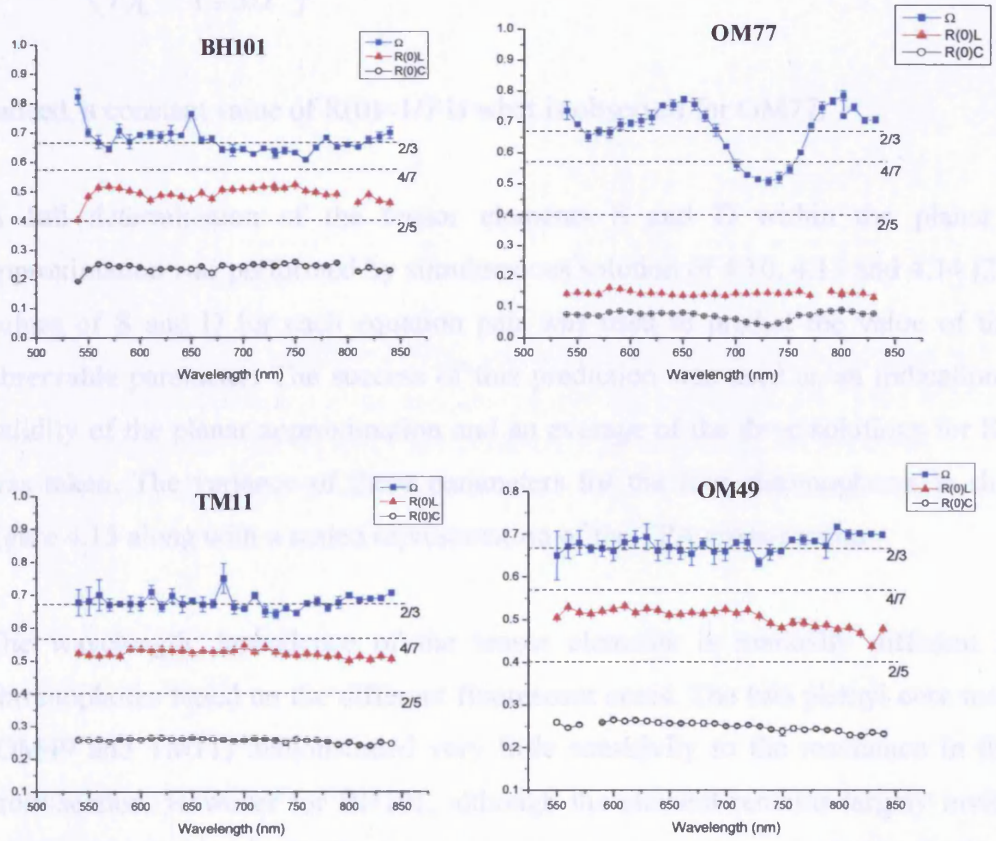

Figure 4.14: The measured linearly and circularly polarised initial anisotropies and excitation ratios for BH101, OM77, TM11 and OM49.

This behaviour might be explained by closer inspection of equation 4.13: if the tensor element is assumed to be 1 corresponding to equivalent excitation along X and Y in the molecular frame, the dependence on the other tensor element is removed and an expression for $R(0)_L$ reduces to

$$R(0)_L = 1/7 \qquad [4.22]$$

and the corresponding expression for Ω and $R(0)_C$ are

$$\Omega = \frac{1+3D^2}{4+2D^2} \qquad [4.23]$$

$$R_C(0) = \left(\frac{1}{7}\right)\left[1+\frac{-2}{1+3D^2}\right] \qquad [4.24]$$

Indeed, a constant value of $R(0) \approx 1/7$ is what is observed for OM77.

A full determination of the tensor elements S and D within the planar tensor approximation was performed by simultaneous solution of 4.10, 4.13 and 4.14 [21]. The values of S and D for each equation pair was used to predict the value of the third observable parameter. The success of this prediction was used as an indication of the validity of the planar approximation and an average of the three solutions for S and D was taken. The variance of these parameters for the four chromophores is shown in figure 4.15 along with a scaled representation of the TPA cross-section.

The wavelength dependence of the tensor elements is markedly different for the chromophores based on the different fluorescent cores. The two phenyl core molecules (OM49 and TM11) demonstrated very little sensitivity to the resonance in the TPA cross-section. However for BH101, although the element remains largely invariant to excitation wavelength, the D element appears to show some variation in the red-IR resonance. The difference in the behaviour of the two tensor elements for OM77 is clearly evident. The S element remains close to 1 through the entire excitation

wavelength range despite the off diagonal element D reducing dramatically through the region of the resonance.

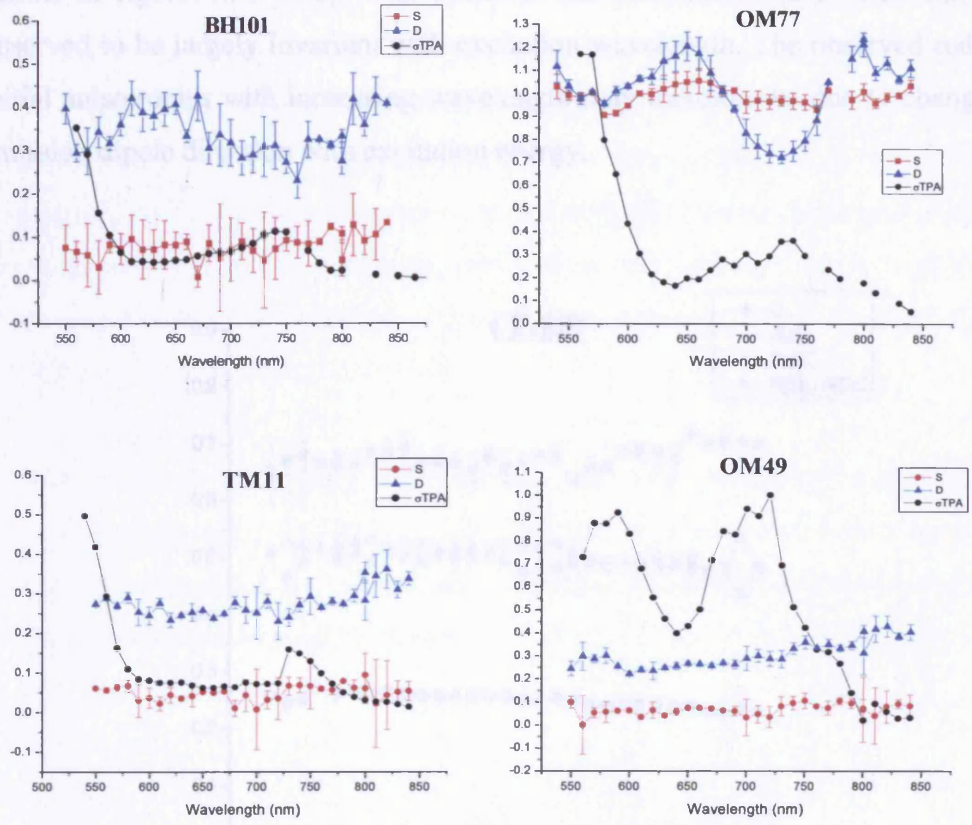

Figure 4.15: Absorption anisotropy ratios and initial fluorescence anisotropies for linearly and circularly polarised excitation in the three quadrupolar fluorophores OM49, TM11, BH101 and the branched quadrupolar fluorophore OM77. Overlayed for comparison are the scaled TPA spectra. The correlation of changes in the tensor elements with the red-IR resonance is clearly seen in OM77.

Whilst the fluorene core chromophore BH101 showed some sensitivity in the red-IR resonance in the TPA cross-section, the branched chromophore OM77 based on three fluorene cores displayed large tensor fluctuations at this resonance. Neither these chromophores nor those possessing biphenyl cores displayed any significant change to the tensor elements at the much larger second resonance close to the single-photon absorption band. It is clear that the combination of three quadrupolar chromophores gives rise to a two-photon transition of markedly different symmetry to that of the single fluorophore.

The observed slow increase in the tensor elements of OM49 with increasing wavelength may have an alternative explanation. It is seen from figure 4.13 that Ω is largely invariant and that both anisotropies display a slow monotonic increase. These are re-shown in figure 4.16 along with ratios of the two anisotropies. This ratio is also observed to be largely invariant with excitation wavelength. The observed reduction in initial anisotropies with increasing wavelength may therefore be due to changes in the emission dipole direction with excitation energy.

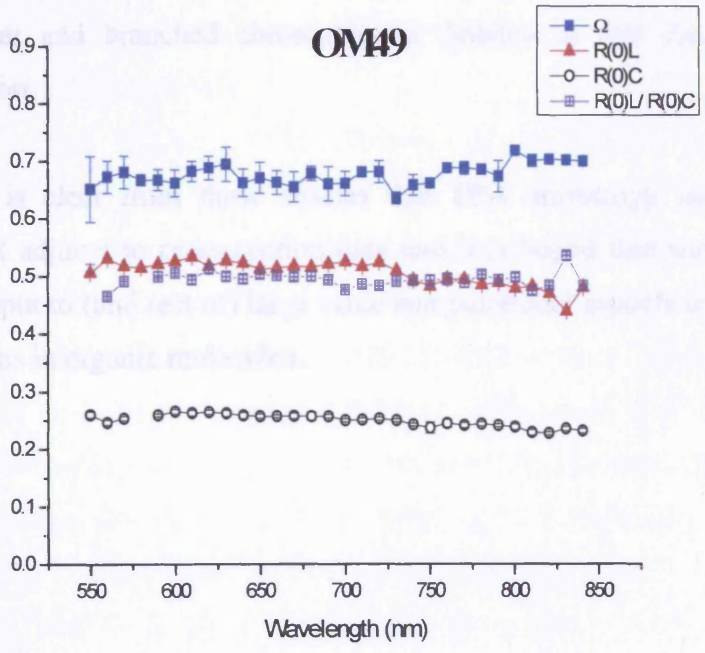

Figure 4.16: The two-photon initial anisotropies and Ω ratios for OM49 shown alongside the ratio of the two anisotropies. The invariance of this ratio with wavelength suggest that tensor element changes may be due to a change in dipole moment direction.

4.10 Conclusion

The explosion of interest in molecular two-photon absorption has been stimulated by the myriad of applications it offers both in material science [22, 23, 24, 25] and biological imaging [26, 27, 28]. The search for two-photon absorbers optimised for use in low cost, mass production systems designed for two-photon excitation at low intensity and providing improved penetration depth coupled with a high degree of spatial selectivity in three dimensions, is currently the subject of intense research. It is for these reasons that the systematic study of the two-photon absorption properties for both quadrupolar and branched chromophores detailed in this chapter may be of significant interest.

Furthermore it is clear from these studies that TPA anisotropy measurements can provide a useful adjunct to cross-section data and it is hoped that such measurements will act as an input to (and test of) large scale computational models of two-and single-photon transitions in organic molecules.

References

[1] P Schwille, U Haupts and S Maiti, WW Webb, Biophys J., **77**, 2251 (1999)

[2] J D Bhawalker, N D Kumar, C F Zhao and N P Prasad, J. Clin. Laser Med. Surg., 15 (1997)

[3] W Denk and J H Strickler, W W Webb, Science., **248**, 73 (1990)

[4] O Mongin, L Porres, M Charlot, C Katan and M Blanchard-Desche. Chem. Eur. J., **13** (2007)

[5] B Larijani and A J Bain, *"Biological Applications of Single and Two-Photon Fluorescence"* in *"Biological Chemistry"*, Eds B Larijani, C A Rosser and R Woscholski, Wiley London (2006)

[6] P N Butcher and D Cotter *"The Elements of Nonlinear Optics"* Cambridge University Press (1990)

[7] F Terenziani, C Le Droumaguet, C Katan, O Mongin, M H V Werts, S Tretiak, M Blanchard-Desche. SPIE-Int. Soc. Opt. Eng., **5935** (2005)

[8] M Albota, D Beljonne, J-Luc Bredas, J E. Ehrlich, J-Ying Fu, A A. Heikal, S E. Hess, T Kogej, M D. Levin, S R. Marder, D McCord-Maughon, J W. Perry, H Rockel, M Rumi, G Subramaniam, W W Webb, X-Li Wu and C Xu, Science. **281**, 1653, (1998)

[9] J Fu, L A. Padilha, D J Hagan, E W Van Stryland, O V Przhonska, M V Bondar, Y L Slominsky and A D Kachkovski, J. Opt. Soc. Am. B. **24**, 1 (2007)

[10] D M Brink and G R Satchler *"Angular Momentum"* Third Edition, Oxford Publications (1994)

[11] W M McClain, J. Chem. Phys., **55**, 2789 (1971)

[12] C Z Wan and C K Johnson, Chem. Phys., **179** 513 (1994)

[13] P R Callis, J. Chem .Phys., **99,** 27 (1993)

[14] Bernard Valeur *"Molecular Fluorescence; Principles and Applications"* Second Reprint, Wiley-VCH (2005)

[15] S W Pauls, J F Hedstrom and C K Johnson, Chem. Phys. **237,** 205 (1998)

[16] *A J Bain to be published*

[17] M A Albota, C Xu and W W Webb, Applied Optics., **37**, 31 (1998)

[18] C Xu and W W Webb, J. Opt. Soc. Am. B., **13**, 3 (1996)

[19] F Terenziani, C Le Droumaguet, C Katan, O Mongin, M H V Werts, S Tretiak and M Blanchard-Desche. SPIE-Int. Soc. Opt. Eng., **5935** (2005)

[20] C. Katan, S. Tretiak,. M. H. V. Werts, A. J. Bain, R. J. Marsh, N. Leonczek, N. Nicolaou, E. Badaeva, O. Mongin and M. Blanchard-Desce, J. Phys. Chem. B., **111**; 9468 (2007)

[21] *The analysis takes the emission dipole moment direction to define X in the molecular frame ($\cos\theta$= 1 in equations 4.12 and 4.13)*

[22] A. S. Dvornikov and P. M. Rentzepis, Opt. Commun., **119**, 341 (1995)

[23] S M Kuebler, K L Braun, W Zhou, J K Cammack, T Yu, C K Ober, S R Marder and J W Perry, J. Photochem. Photobio. A: Chemistry, **158**, 163 (2003)

[24] C C Corredor, K D Belfield, M V Bondar, O V Przhonske, F E Hernandez and O D Kachkovsky, J J Photochem., **184**, 174 (2006)

[25] D A. Parthenopoulos and P. M. Rentzepis, Science., **245**, 843 (1989)

[26] J C Malone, A F Hood, T Conley, J Nurnberger, L A Baldridge, J L Clendenon, K W Dunn, C L Phillips and J. Cutan. Pathol., **29**, 453 (2002)

[27] M D Cahalan, I Parker, S H Wei and M J Miller, Nat. Rev. Immunol., **2**, 872 (2002)

[28] J M Squirrell, D L Wokosin, J G White and B D Bavister, Nat. Biotechnol., **17**, 763 (1999)

Chapter 5

Stimulated Emission Depletion Dynamics in a Branched Quadrupolar Chromophore

5.1 Introduction

In this chapter stimulated emission depletion dynamics are investigated in the branched fluorophore OM77. Stimulated emission depletion (STED) refers to the technique by which an excited state fluorescent population of molecules is partially depleted by stimulating transitions to the ground electronic state. STED was originally developed as a high resolution technique in molecular spectroscopy allowing access to highly vibrationally excited levels in the ground electronic states of molecules which are inaccessible to direct excitation [1]. The development of time resolved condensed phase STED techniques [2-4] enabled work to probe condensed phase relaxation dynamics in excited electronic states and high vibrational levels of ground electronic states [5-7]. Subsequently STED has attracted interest as an advanced tool in fluorescence microscopy permitting three dimensional imaging with sub-wavelength resolution [8, 9]. STED techniques were recently extended to two-photon excited states by the group where it was shown that time resolved STED techniques are sensitive to excited state properties (alignment) that are hidden from spontaneous emission (unperturbed fluorescence) [10] and in particular that it is possible to measure hexadecapole alignment relaxation $\langle \alpha_{40}^{ex}(t) \rangle$ from STED depolarization data [11] and polarization sensitive saturation measurements [12].

5.2 Two-Photon Excited Stimulated Emission Depletion

The principles of two-photon excited STED are depicted shown in figure 5.0. Initial excitation ('Pump') occurs from low lying vibrational levels in the S_0 ground state via the simultaneous absorption of two (non-resonant) near infra-red photons (c.a. 800nm).

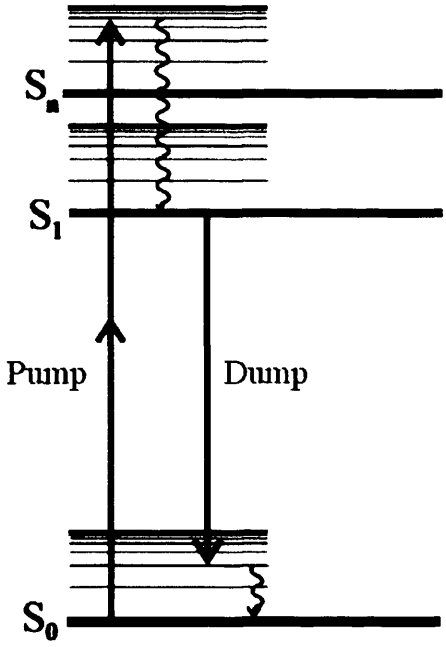

Figure 5.0: A Jablonski diagram describing the process of stimulated emission depletion of two-photon excited states.

This is followed by rapid internal conversion and solvent mediated relaxation yielding a vibrationally excited population in the S_1 electronic excited state. In the absence of external perturbations the excited state population in S_1 decays by the process of spontaneous emission to the upper vibrational levels in S_0 which is followed by rapid relaxation as a result of collisional deactivation and solvent relaxation. In STED a visible laser ('Dump') pulse resonant with the $S_1 \rightarrow S_0$ emission is applied to induce transitions to the upper vibrational levels of S_0. The net result of this process is twofold; firstly, a sudden reduction in the excited state population manifest by a loss in the fluorescence intensity (figure 5.1a) and, depending on the relative polarisations of the two laser beams, a change in molecular alignment (fluorescence anisotropy) (figure 5.1b).

For optimum two-photon STED efficiency several factors must be taken into account. Firstly the Dump wavelength, whilst resonant with the emission, must be sufficiently red- shifted from any single-photon absorption as to avoid single-photon excitation of those molecules which remain unexcited within the interaction volume.

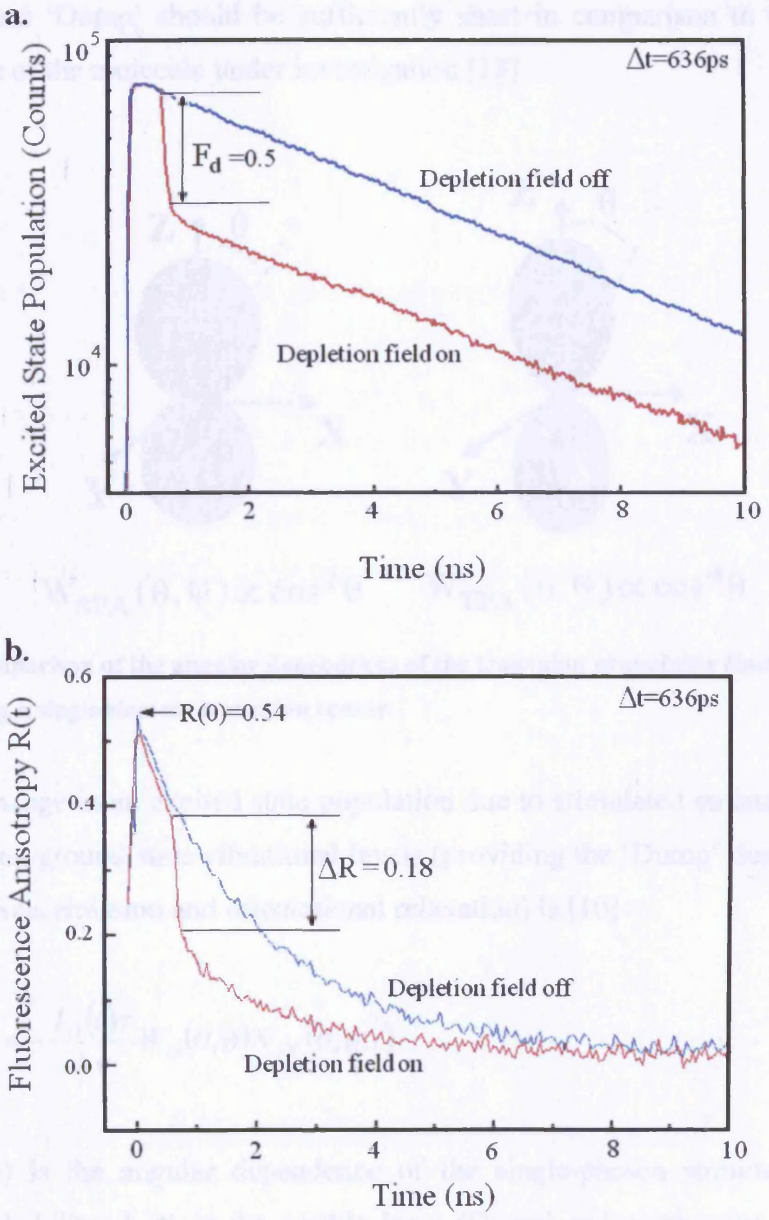

Figure 5.1: Diagram showing the effect of depletion - 'Dumping' of the excited state population following two-photon excitation 'Pumping' for fluorescein in ethylene glycol [10]. (a) For a Pump-Dump delay set at 636ps, the fraction remaining in the excited state population is reduced by a factor of two. (b) The selective removal of molecules which are oriented parallel to the Dump pulse polarisation causes an abrupt change in fluorescence anisotropy R(t).

Secondly, for two-photon excitation in an isotropic medium (given a favourable transition tensor as discussed in Chapter 4) the angular distribution of molecular transition dipole moment directions in the laboratory frame is more sharply peaked than for single photon excitation (figure 5.2). Depletion of the excited state is maximised for parallel 'Pump' and 'Dump' polarisations [10, 11]. Finally, the time separation between

the 'Pump' and 'Dump' should be sufficiently short in comparison to the rotational diffusion time of the molecule under investigation [13].

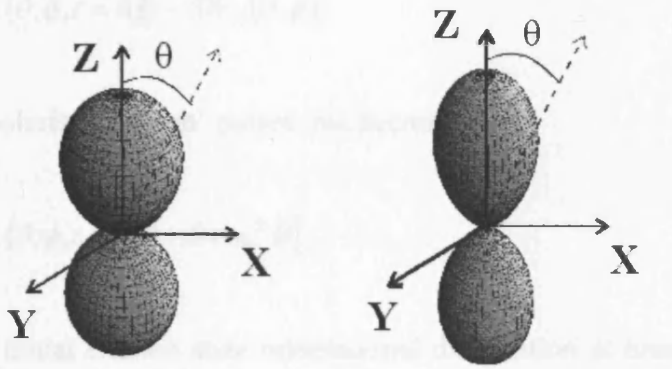

Figure 5.2: Comparison of the angular dependence of the transition probability (initial excited state order) assuming a single element transition tensor.

The rate of change in an excited state population due to stimulated emission to a set of rapidly relaxing ground state vibrational levels (providing the 'Dump' duration is faster than spontaneous emission and orientational relaxation) is [10]

$$\frac{dN_{EX}(\theta,\phi,t)}{dt} = -\frac{I_D(t)\sigma}{h\nu} W_D(\theta,\phi) N_{EX}(\theta,\phi,t) \qquad [5.0]$$

Here $W_D(\theta,\varphi)$ is the angular dependence of the single-photon stimulated emission transition probability, $I_D(t)$ is the visible laser (Dump) pulse intensity and σ is the stimulated emission cross-section (cm^2).

Integrating over the pulse duration yields

$$N_{EX}(\theta,\phi,t_D) = N_{EX}(\theta,\phi,t=0)\exp[-SW_D(\theta,\phi)] \qquad [5.1]$$

where

$$S = \frac{E_D\sigma}{h\nu A} \qquad [5.2]$$

in this case E_D is the pulse energy, and A is the pulse area. In the limit of weak stimulated emission depletion (S<<1) equation 5.1 becomes

$$N_{EX}(\theta,\phi,t_D) = N_{EX}(\theta,\phi,t=0)\left[1 - SW_D(\theta,\phi)\right] \quad [5.3]$$

For Z (Vertically) polarised 'Dump' pulses this becomes

$$N_{EX}(\theta,\phi,t_D) = N_{EX}(\theta,\phi,t=0)\left[1 - S\cos^2\theta\right] \quad [5.4]$$

Prior to STED the initial excited state orientational distribution at time *t* for isotropic rotational diffusion following two-photon excitation is given by

$$N_{EX}(\theta,\phi,t_D) = N_{EX}\exp\left(\frac{-t}{\tau_f}\right)\frac{1}{\sqrt{4\pi}}\left[Y_{00} + \frac{20}{7\sqrt{5}}Y_{20}\exp\left(\frac{-t}{\tau_{20}}\right) + \frac{8}{21}Y_{40}\exp\left(\frac{-10t}{3\tau_{20}}\right)\right] \quad [5.5]$$

and for single-photon excitation is given by

$$N_{EX}(\theta,\phi,t_D) = N_{EX}\exp\left(\frac{-t}{\tau_f}\right)\frac{1}{\sqrt{4\pi}}\left[Y_{00} + \frac{2}{\sqrt{5}}Y_{20}\exp\left(\frac{-t}{\tau_{20}}\right)\right] \quad [5.6]$$

After the onset of stimulated emission depletion the altered excited state population is given by [10]

$$N_D(\theta,\phi) = N^0_{EX}(\theta,\varphi,t)\left(1 - S\cos^2\theta\right) = N^0_{EX}(\theta,\varphi,t)\left[1 - \frac{S}{3}\sqrt{4\pi}\left(Y_{00} + \frac{2}{\sqrt{5}}Y_{20}\right)\right] \quad [5.7]$$

Integrating over the orientational distribution and rearranging equation 5.7 gives the fraction of the population remaining (F_R) in terms of the anisotropy prior to 'Dumping' (R_U):

$$F_R = 1 - \frac{(1+2R_U)S}{3} \quad [5.8]$$

The 'Dumped' anisotropy R_D is given by [10]

$$R_D = \frac{\left[\left(3-\frac{11}{7}S\right)R_U - \frac{2}{5}S - \frac{12}{35}\left\langle\alpha_{40}^{EX}(0)\right\rangle S\right]}{\left(3-(1+2R_U)S\right)} \qquad [5.9]$$

From equation 5.9 it can be seen that the Dumped anisotropy is dependent on $\left\langle\alpha_{40}^{EX}\right\rangle$ which is not observed in unperturbed conventional experiments.

In the limit of fast ground state relaxation and in the regime of weak depletion of the excited state population, STED dynamics can be modelled analytically. Analytic solutions to the coupled rate equations, (equations which describe the evolution of the excited (N_{EX}) and upper vibrational (N_{GS}) states) are possible providing there is strong saturation of the 'Dump' transition [10, 11, 12]. Given these conditions and providing the 'Dump' pulse is significantly shorter than any spontaneous emission or molecular reorientation, the rate equations for STED are given by [10]

$$\frac{dN_{EX}(\theta,t)}{dt} = -\frac{I_D(t)\sigma W_D(\theta)}{h\nu}\left(N_{EX}(\theta,t) - N_{GS}(\theta,t)\right) \qquad [5.10]$$

$$\frac{dN_{GS}(\theta,t)}{dt} = \frac{I_D(t)\sigma W_D(\theta)}{h\nu}\left(N_{EX}(\theta,t) - N_{GS}(\theta,t)\right) - \frac{N_{GS}(\theta,t)}{\tau_R} \qquad [5.11]$$

where N_{EX} (θ,t) and N_{GS} (θ,t) are the ground and excited state populations and τ_R is the ground state vibrational relaxation time. By assuming a square 'Dump' pulse, (constant Dump intensity over a time duration τ_P), it is possible to obtain analytic solutions to the rate equations which yield the fractional population remaining (F_R) after depletion of the excited state as a function of the saturation parameter S for given ratios of τ_P/τ_R [10]. Given that in the upper ground state vibrational levels the initial population distribution is negligible, then the excited state population evaluated at $t=\tau_P$ is given by [10]

$$N_{EX}(\theta,\tau_P) = \frac{N_{EX}(\theta,0)}{2d}\left[\exp\left(-\frac{1}{2}\left\{\frac{\tau_P}{\tau_R} + 2S\cos^2\theta + d\right\}\right)\right]\left\{\frac{\tau_P}{\tau_R}\left(e^d - 1\right) + d\left(e^d + 1\right)\right\} \qquad [5.12]$$

where the parameter d is given by

$$d = \sqrt{(\tau_P/\tau_R)^2 + 4S^2\cos^4\theta} \qquad [5.13]$$

The fractional depletion of the excited state population can be calculated from [10]

$$F_D = (1 - F_R) = \frac{\int_0^{2\pi}\int_0^{\pi}[N_{EX}(\theta,\tau_P) - N_{EX}(\theta,0)]\sin\theta d\theta d\varphi}{\int_0^{2\pi}\int_0^{\pi} N_{EX}(\theta,0)\sin\theta d\theta d\varphi} \qquad [5.14]$$

where $N_{EX}(\theta,0)$ is the excited state population immediately prior to STED. The fluorescence anisotropy of the remaining excited state molecules is similarly given by

$$R_D = \frac{\int_0^{2\pi}\int_0^{\pi} N_{EX}(\theta,t_p)\cos^2\theta\sin\theta d\theta d\varphi - \int_0^{2\pi}\int_0^{\pi} N_{EX}(\theta,t_p)\sin^2\theta\sin\theta d\theta d\varphi}{\int_0^{2\pi}\int_0^{\pi} N_{EX}(\theta,t_p)\cos^2\theta\sin\theta d\theta d\varphi + 2\int_0^{2\pi}\int_0^{\pi} N_{EX}(\theta,t_p)\sin^2\theta\sin\theta d\theta d\varphi} \qquad [5.15]$$

Numerical integration of equations 5.14 and 5.15 is achieved using a Mathematica program [10]. This yields (for a given $N_{EX}(\theta,0)$) numerical solutions for the population removal and anisotropy immediately following STED for varying S and ratios of 'Dump' pulse width (τ_P) to ground state vibrational relaxation time (τ_R). A typical set of numerical solutions for F_R with S for different values of τ_P/τ_R is shown in figure 5.3.

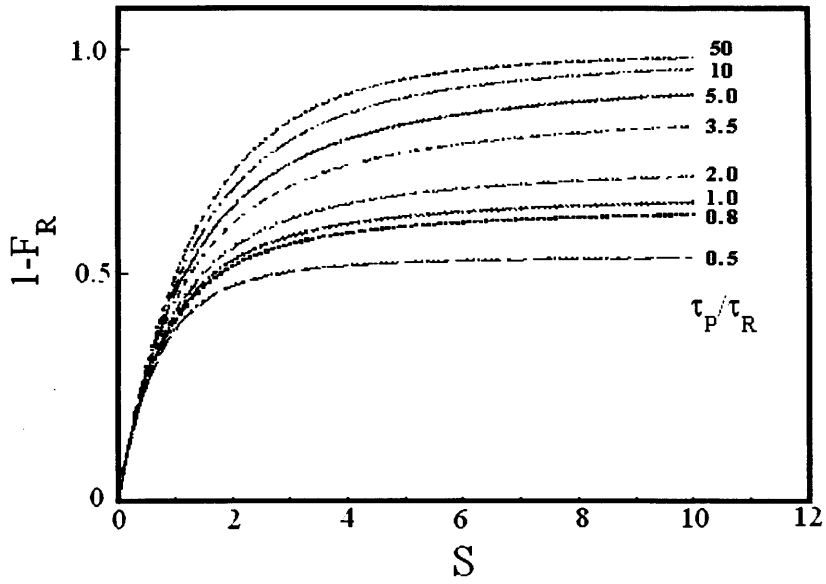

Figure 5.3: Diagram showing numerical solutions to the rate equations generating a family of saturation curves for population removal by stimulated emission depletion for different values of τ_P/τ_R . Fitting numerical solutions this way yields values for the stimulated emission cross-section and ground state vibrational relaxation times [10, 11].

5.3 Experimental Procedure

The experimental apparatus used to measure STED dynamics for OM77 in toluene is illustrated in figure 5.4. The sample, a 5 x 10^{-4} solution of OM77 in toluene was contained in a quartz cuvette (Hellma: 45µl) with three optical windows. Two-photon excitation of the sample was achieved using the partial output of a regeneratively amplified Ti:Sapphire laser (Coherent Mira 900F, Coherent RegA 9000) which provided 800nm laser pulses with c.a. 55nJ energy and 140fs FWHM pulse width at a repetition rate of 250kHz (as described in Chapter 2), the majority of the 800nm output was used to Pump an optical parametric amplifier from which a Dump wavelength of 551nm was chosen with strong emission from OM77 at this wavelength as shown in figure 5.5.

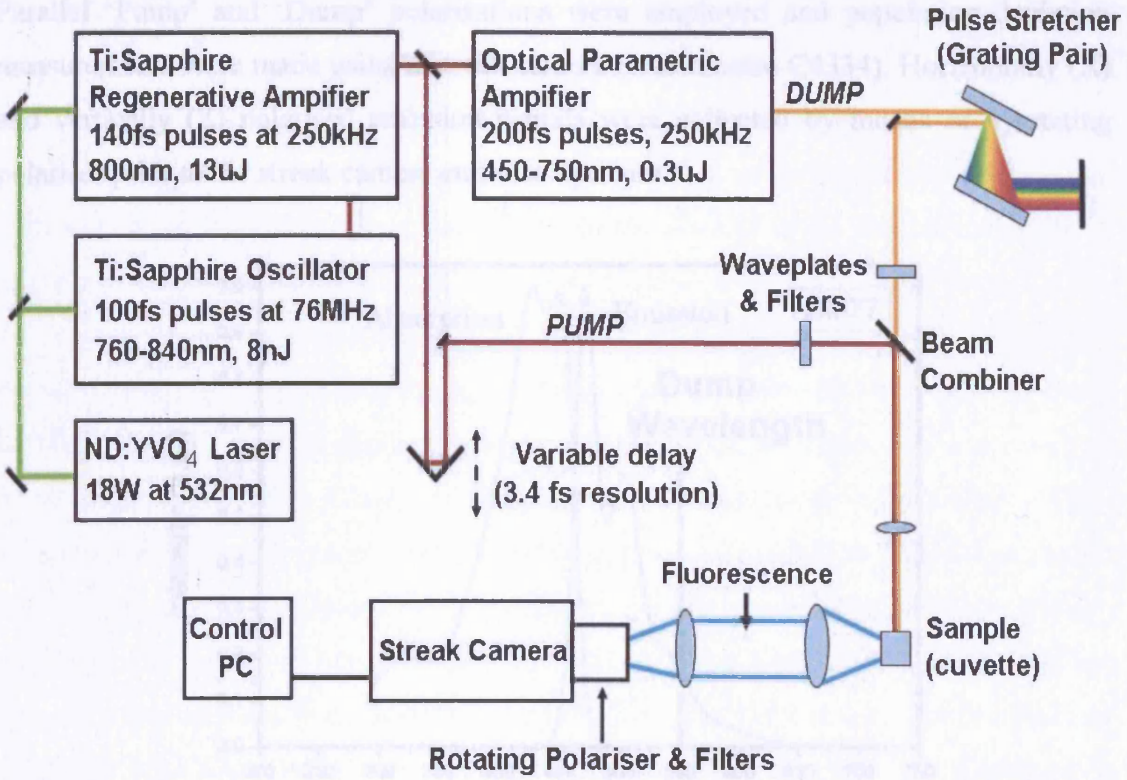

Figure 5.4: Schematic diagram of the experimental apparatus used for STED. Collection of fluorescence is made using 90° excitation-detection geometry.

The OPA pulses were temporally stretched using a grating pair to prevent 'Dump' induced two-photon fluorescence. The 'Pump' and 'Dump' wavelengths were monitored using a laser spectrum analyser (IST-Rees) and the pulse widths measured using a scanning autocorrelator (APE Pulse Check). Broadband half waveplates (Melles-Griot) were used to control the 'Pump' and 'Dump' beam polarisations. A variable optical delay line (Time and Precision) allowed scanning of the Pump-Dump separation which was set at 200ps. Adjustment of the 'Pump' and 'Dump' powers were made using neutral density wheels and measured by a precision power meter (Anritsu). To ensure that both 'Pump' and 'Dump' beams were incident on the same spot in the sample, both beams were spatially overlapped prior to the sample using a broadband dichroic beam combiner (CVI Optics). The beams were passed through an aperture of fixed diameter (2.2mm) and focused into the sample using a 2.54 achromatic lens (Melles-Griot). Any scattered laser light was blocked using appropriate short-pass filters (Corion LS550) and glass infra-red cut-off filters (Schott BG39). A long-pass glass cut-off filter (OG530) was placed before the sample to ensure the 'Dump' pulse was not contaminated by remnants of white light from the continuum generated in the OPA.

Parallel 'Pump' and 'Dump' polarisations were employed and population depletion measurements were made using a streak camera (Hamamatsu C4334). Horizontally (X) and vertically (Z) polarised emission signals were collected by means of a rotating polariser prior to the streak camera entrance aperture.

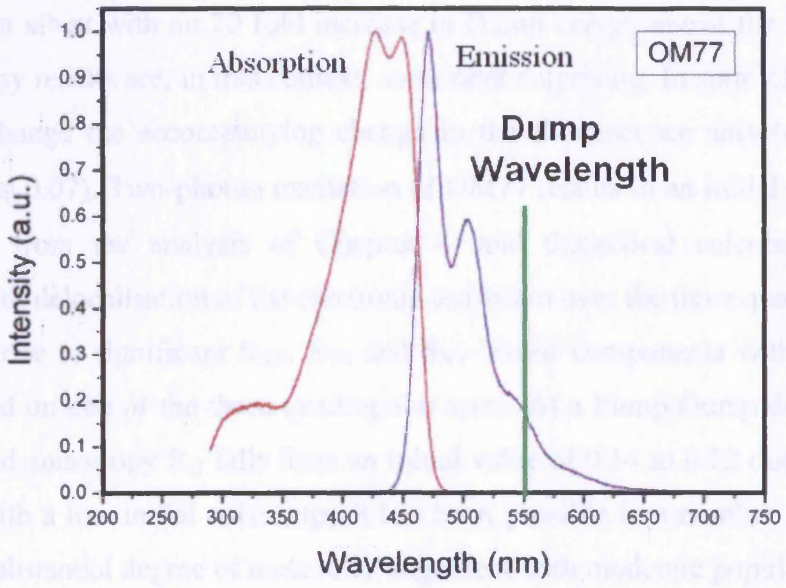

Figure 5.5: Single photon absorption and emission spectra for OM77 in toluene. Single photon emission intensity is c.a. 18% of the peak (455nm) at the chosen 'Dump' wavelength of 551nm.

5.4 Results

The choice of Dump wavelength is restricted to regions where the spectral overlap with the absorption is negligible; to induce significant population depletion the saturation parameter S is significantly greater than unity, and under these circumstances the Dump excitation of ground state molecules will be significant unless the absorption cross section is vanishingly small or zero. From figure 5.5 a reasonable compromise between fluorescence intensity (stimulated emission cross-section) and single photon transparency is around 550nm. As shown in Chapter 4, OM77 possesses a very substantial two-photon cross section (ca. 11.000GM) in this wavelength region. However as the effective two-photon transition rate is inversely proportional to the laser pulse width (see equation 4.2) stretching the Dump pulse by means of a grating pair as detailed in section 5.3 to a width greater than 10ps (the maximum range of the scanning autocorrelator) gives rise to a negligible Dump induced fluorescence background.

Population depletion and anisotropy changes induced by the stretched Dump pulses are shown in figure 5.6. Dump energies were varied between 0.2nJ (15% depletion) and 29nJ (97% depletion). Population depletion is approximately linear with energy up to a Dump energy of 1.3nJ (56% depletion) with increasing saturation of the transition at higher energies; nonetheless it is possible to obtain close to 100% population depletion in this system albeit with an 20 fold increase in Dump energy above the linear region. The anisotropy results are, in this context, somewhat surprising. In spite of a substantial population change the accompanying change in the fluorescence anisotropy is much smaller ($\Delta R \cong 0.07$). Two-photon excitation of OM77 results in an initial anisotropy of 0.14 which, from the analysis of Chapter 4, and theoretical calculations [14] is consistent with delocalisation of the electronic transition over the three quadrupolar sub-units giving rise to significant S_{XX}, S_{YY} and S_{XY} tensor components with an emission dipole located on one of the three quadrupolar arms. At a Pump-Dump delay of 200ps the undumped anisotropy R_U falls from an initial value of 0.14 to 0.12 due to rotational diffusion. With a low initial anisotropy it has been possible in a number of systems to 'burn in' a substantial degree of molecular alignment with moderate population changes [13].

Removal of 90% of the excited state population with a Z-polarised Dump pulse in non-branched systems such as EGFP (possessing a near single element transition tensor) gives substantially different anisotropy behaviour [9].

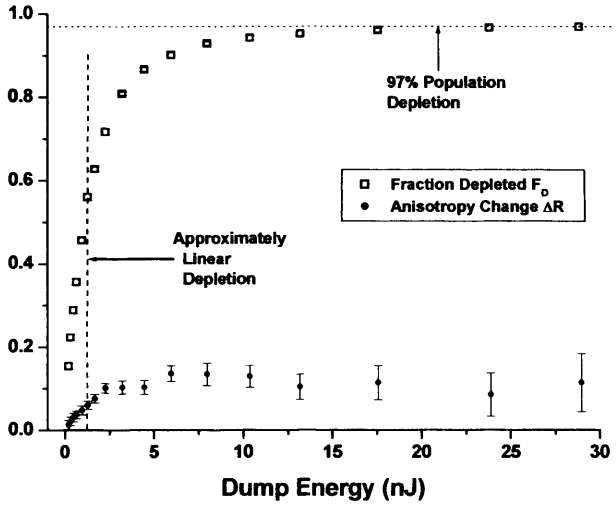

Figure 5.6 Variation in the population and anisotropy in the excited state of OM77 as a function of Dump pulse energy, R_U=0.12, Dump pulsewidth >10ps.

5.5 Discussion

Analysis of the population depletion data as described in the previous section is shown in figure 5.8.

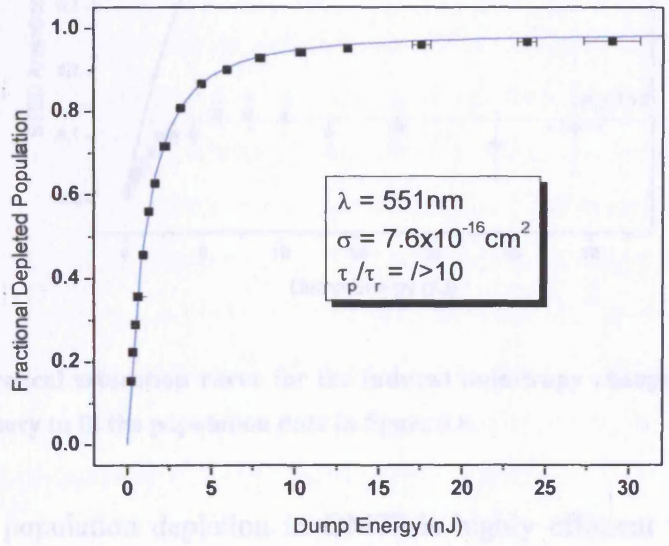

Figure 5.7: Theoretical saturation curve for population depletion in OM77, to follow the saturation behaviour observed R_U=0.476, $\langle\alpha_{40}\rangle$ = 0.318, these are significantly larger than those measured/predicted for OM77. The fit yields an apparent cross-section for stimulated emission of $7.6\times10^{-16}cm^2$.

The population depletion can be described by equation 5.14 with R_U =0.476 and a quadrupolar alignment of 0.318 (values corresponding to a single element transition tensor modified by rotational diffusion over the Pump-Dump time delay). The degree of initial alignment needed to generate the observed behaviour is clearly far greater than that measured. Furthermore with these inputs it is not possible to reproduce the anisotropy data as can be seen in figure 5.9

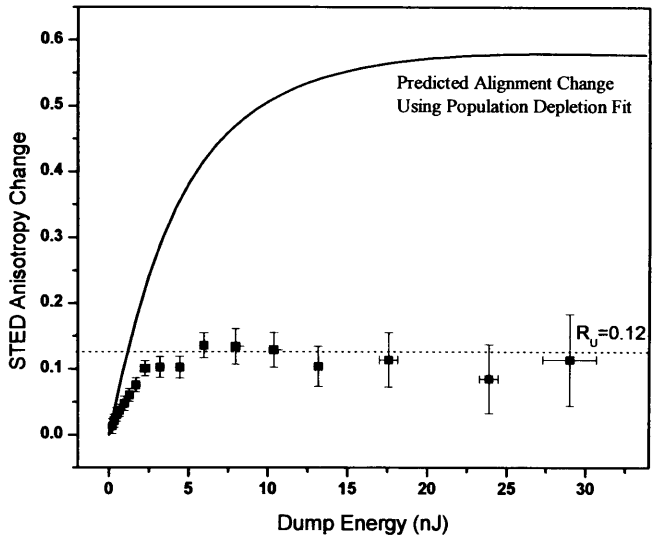

Figure 5.8: Theoretical saturation curve for the induced anisotropy changes in OM77, using the parameters necessary to fit the population data in figure 5.8.

It is clear that population depletion in OM77 is highly efficient with the molecular population behaving (in this instance) as if it were an array of dipoles with a degree of ordering close to the maximum allowed by two-photon absorption. For the fluorescence anisotropy the Dumped anisotropy approaches zero in an approximately linear fashion but after a Dump energy of approximately 2.5nJ (c.a. 71% population depletion) this appears to be the minimum value (to within experimental uncertainties) that can be obtained even with an order of magnitude increase in the photon flux. With a $\cos^2\theta$ transition probability in the laboratory frame and an array of well defined molecular axes and emission dipole orientations it has been possible to engineer populations with negative fluorescence anisotropies [11]. OM77 differs considerably from 'conventional' fluorophores in that the spontaneous emission, whilst localised on one of the branches [15], is not restricted to any particular branch. The low fluorescence anisotropy in both single and two photon excited fluorescence presumably reflects this averaging. For single-photon excitation the average angle between absorption and emission transition dipole moments is estimated to be ca. 43°†.

†*This is based on the deviation of the measured initial anisotropy R(0) from 0.4 via* $R(0) = 0.4 \times \left(3\cos^2\gamma - 1\right)/2$ *where* γ *is the angle between the absorption and emission transition dipole moment directions.*

If for any given excited molecule the location of the transition dipole moment along a particular branch is not determined until the moment of (spontaneous) emission then stimulated emission would be expected to 'force' emission along the branch with the most favourable angular orientation to the Dump polarisation. In non-degenerate transitions i.e. with a 'unique' direction in the molecular frame the molecular alignment dependence of STED and the fluorescence anisotropy are the same. The clear evidence we have for OM77 is that this is not the case. The effective molecular alignment is apparently enhanced by selection of the most appropriately aligned quadrupolar branch - an 'option' not available to single chromophore systems. Now considering the small anisotropy changes that are observed, efficient internal photoselection (which as argued above, is insensitive to the low degree of apparent molecular alignment) will, unless the molecular orientation (i.e. the plane of OM77) of the removed molecules were such that they would have made a significant contribution to Z-polarised emission in the laboratory frame (e.g. with an end on orientation to the emission collection direction for instance) the fluorescence anisotropy will see little change.

5.6 Conclusions

In addition to possessing a substantial two photon cross section OM77 appears to be well suited to photo-engineering STED. The effective alignment of the molecules for stimulated depletion appears to be significantly larger than that predicted by the spontaneous emission anisotropy which involves the averaging of the emission probability over the three branches of the fluorophore. The fluorescence anisotropy of the depleted distribution is however resilient to strong depletion which gives rise to significant change in systems where the transition dipole moment direction is well defined in the molecular frame. It is clear that STED depletion dynamics in branched systems cannot be described by the conventional models that have worked well for non-degenerate fluorophores. It will be particularly interesting to study population and anisotropy dynamics in branched systems such as OM77 at Pump-Dump delays where significant orientational relaxation has taken place and the excited state more closely approximates an isotropic ensemble. The creation of fluorescence anisotropy from an isotropic ensemble of branched chromophores may prove challenging! In this light a

combination of two and single-photon STED experiments would also be useful as higher degrees of molecular alignment are not initially present in the latter.

References

[1] D E Reisner, R W Field, J L Kinsey and H-L Dai, J. Chem. Phys., **80**, 5968 (1984)

[2] I Gryczynski, J Kusba and J R Lackowicz, J. Chem. Phys., **98,** 8886 (1994)

[3] J Kuśba, V Bogdanov, I Gryczynski and J R Lakowicz, Biophys. J., **67**, 2024 (1994)

[4] J R Lakowicz, "*Principles of Fluorescence Spectroscopy*" Second Edition, Kluwer Academic (1999)

[5] G Haran, E A Morlino, J Mathes, R Callendar and R M Hochstrasser, J. Phys. Chem. A., **103**, 2202 (1999)

[6] P Changenety-Barret, C T Choma, E F Gooding, W F DeGrado and R M Hochstrasser J. Phys. Chem. B., **104**, 9322 (2000)

[7] S. A. Hambir, Y. Jiang and G. J. Blanchard, J. Chem. Phys., **98**, 6075 (1993).

[8] T A Klar, S Jakobs, M Byba, A Egner and S W Hell, Proc. Nat. Acad. Sci. (USA) **97**, 8206 (2000)

[9] S W Hell and J Wichmann, Opt. Lett., **19**, 780 (1994)

[10] R J Marsh, D A. Armoogum and A J Bain, Chem. Phys. Lett., **366**, 398 (2002)

[11] A J Bain, R J Marsh, D A Armoogum, L Porres O Mongin and Mireille Blanchard-Desce, BioChem. Soc. Trans., **31**, 1047 (2003)

[12] T Masters, D A Armoogum R J Marsh and A J Bain, *to be published*

[13] D A Armoogum, PhD thesis, University College London, (2004)

[14] C Katan, S Tretiak, M H V Werts, A J Bain, R J Marsh, N Leonczek, N Nicolaou, E Badaeva, O Mongin and M Blanchard-Desce, *to be published*

[15] C Katan, S Tretiak, M H V Werts, A J Bain, R J Marsh, N Leonczek, N Nicolaou, E Badaeva, O Mongin and M Blanchard-Desce, J. Phys.Chem. B., **111**, 9468 (2007)

Appendix I.I

The Orientational Distribution Function

By defining the order parameter using a polar coordinate system the orientational distribution function $P(\theta,\varphi)$ represents the probability of finding the molecule oriented between θ and dθ and φ and dφ (figure I.0).

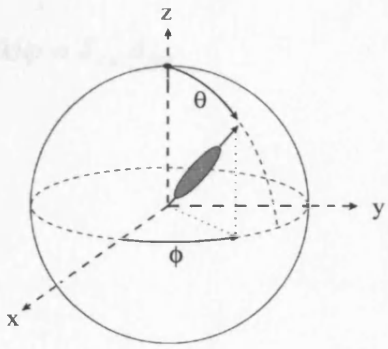

Figure I.0: The spherical polar coordinate system used to define the orientational distribution function P(θ,φ).

The orientational distribution function can be expanded in terms of a complete set of orthonormal basis functions. An expansion of the orientational distribution function in terms of spherical harmonics is most convenient in describing the molecular order created by the interactions between the light and molecule. The function also best defines the restricted environment of the experimental observables.

The orientational distribution function $P(\theta,\varphi)$ in terms of a spherical harmonic expansion is given by

$$P(\theta,\varphi) = \Sigma_{KQ} \langle C_{KQ} \rangle Y_{KQ}(\theta,\varphi) \qquad [I.1]$$

Where the expansion coefficients $\langle C_{KQ} \rangle$ define the moments of the distribution and their magnitude and sign determine the form of $P(\theta,\varphi)$. $Y_{KQ}(\theta,\varphi)$ is a spherical harmonic of rank K and projection Q where Q takes $2K+1$ values in integer steps

from $+K$ to $-K$. Spherical harmonics are constructed from Legendre Polynomials $P_{K0}(\cos\theta)$) as:

$$Y_{KQ}(\theta,\varphi)=\sqrt{\frac{(2K+1)(K-Q)!}{4\pi(K+Q)!}}P_{KQ}(\cos\theta)e^{iQ\varphi} \qquad [I.2]$$

The orientational distribution function can be written in terms of spherical harmonics as

$$\int_0^{2\pi}\int_0^{\pi} Y^*_{KQ}(\theta,\varphi)Y_{KQ}(\theta,\varphi)\sin\theta d\theta d\varphi = \delta_{KK'}\delta_{QQ'} \qquad [I.3]$$

where

$$Y^*_{KQ}(\theta,\varphi)=(-1)^Q Y_{K-Q'}(\theta,\varphi) \qquad [I.4]$$

the moments of the expansion can then be found from [1]

$$\langle C_{KQ}\rangle = \int_0^{2\pi}\int_0^{\pi} Y^*_{KQ}(\theta,\varphi)P(\theta,\varphi)\sin\theta d\theta d\varphi \qquad [I.5]$$

The graphical representations of several spherical harmonics together with their functional forms are shown in table I.0:

$Y_{00} = \left(\frac{1}{4\pi}\right)^{1/2}$	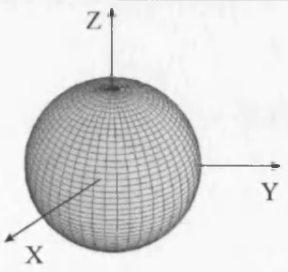
$Y_{20} = \left(\frac{5}{4\pi}\right)^{1/2} \frac{1}{2}\left(3\cos^2\theta - 1\right)$	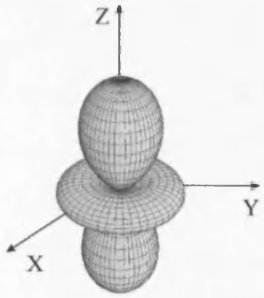
$Y_{2\pm2} = \left(\frac{15}{32\pi}\right)^{1/2} \sin^2\theta e^{\pm 2i\varphi}$	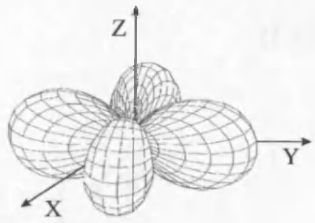
$Y_{40} = \left(\frac{1}{4\pi}\right)^{1/2} \frac{3}{8}\left(35\cos^4\theta - 30\cos^2\theta + 3\right)$	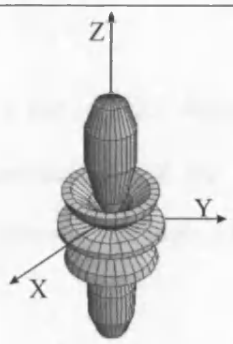
$Y_{60} = \left(\frac{13}{4\pi}\right)^{1/2} \frac{1}{16}\left(\begin{matrix}231\cos^6\theta - 315\cos^4\theta \\ +105\cos^2\theta - 5\end{matrix}\right)$	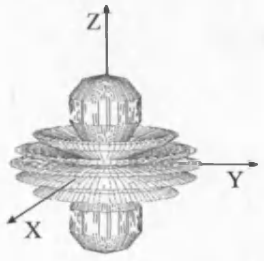

Table I.0: Graphical representations of the axially symmetric and axially asymmetric spherical harmonics. The moments of Y_{00}, Y_{20} and $Y_{2\pm2}$ are fluorescence observables and directly measurable in polarised fluorescence experiments. Moments of higher order moments of even rank and zero projection (i.e. $K_{EVEN}>2$, $Q=0$) are employed to describe fully the ground state distribution function of dye probes in aligned nematic liquid crystals.

The probability of finding a molecule on the unit sphere is necessarily unity:

$$\int_0^{2\pi}\int_0^{\pi} P(\theta,\varphi)\sin\theta d\theta d\varphi = 1 \qquad \text{[I.6]}$$

Substitution of equation I.5 into equation I.6 yields

$$\sum_{KQ}\langle C_{KQ}\rangle \int_0^{2\pi}\int_0^{\pi} Y_{KQ}(\theta,\varphi)\sin\theta d\theta d\varphi = 1 \qquad \text{[I.7]}$$

This can be written as [1]

$$\sum_{KQ}\langle C_{KQ}\rangle (4\pi)^{1/2} \int_0^{2\pi}\int_0^{\pi} Y_{00}^{*}(\theta,\varphi) Y_{KQ}(\theta,\varphi)\sin\theta d\theta d\varphi = 1 \qquad \text{[I.8]}$$

From equation I.8 the only non-zero contribution is $\langle C_{00}\rangle = \left(\frac{1}{4\pi}\right)^{1/2}$.

The $\langle C_{00}\rangle$ (population) term is ever present irrespective of the angular distribution. It is convenient to normalise the higher order expansion coefficients of the distribution function to $\langle C_{00}\rangle$, as these often correspond to directly measurable physical properties of the system giving:

$$P(\theta,\varphi) = \langle C_{00}\rangle \sum_{KQ}\langle \alpha_{KQ}\rangle Y_{KQ}(\theta,\varphi) \qquad \text{[I.9]}$$

where $\langle \alpha_{KQ}\rangle = \langle C_{KQ}\rangle / \langle C_{00}\rangle$.

Appendix I.II

Orientational Distribution Function for Nematic Liquid Crystals: Order Parameters

As a molecule undergoes diffusion in the nematic phase of a liquid crystal there is a tendency for one of the molecular axes to point along a preferred direction. This preferential orientation is denoted by the unit vector **n**. The tendency for the molecules to align along a preferred direction **n** gives rise to an orientational distribution function that is not uniform over the unit sphere. The nematic phase is more ordered than the isotropic phase and to describe the degree of order quantitavely an order parameter must be defined such that it is non-zero in the nematic phase and vanishes in the isotropic phase.

To fully describe P(θ,φ) the number of order parameters $\langle \alpha_{KQ} \rangle$ must be reduced. This is achieved by examining the inherent symmetry of the system under consideration. In the nematic phase of liquid crystals, there exists axial symmetry with respect to the orientation of the nematic director **n**, which defines the laboratory fixed Z-axis. Spherical harmonics with Q=0 are φ independent and so are invariant to rotation about Z. For a nematic liquid crystal, P(θ,φ) will only have non-zero moments for Q=0. As nematic liquid crystals are invariant to inversion of the nematic director i.e. P(θ,φ) = P(Π-θ,φ), moments where K is even will be present in the expansion of P(θ,φ). Applying the symmetry conditions the orientational distribution function becomes

$$P(\theta,\varphi) = \langle C_{00} \rangle \left[Y_{00}(\theta,\varphi) + \langle \alpha_{20} \rangle Y_{20}(\theta,\varphi) + \langle \alpha_{40} \rangle Y_{40}(\theta,\varphi) + \langle \alpha_{60} \rangle Y_{60}(\theta,\varphi) + \ldots \right] \qquad [I.10]$$

$$P(\theta,\varphi) = \frac{1}{4\Pi} \left[1 + \sum_{K>0(EVEN)} (4\Pi)^{\frac{1}{2}} \langle \alpha_{k0} \rangle Y_{K0}(\theta,\varphi) \right] \qquad [I.11]$$

Which in terms of Legendre polynomials $P_K(\theta)$ becomes [2]

$$P(\theta,\varphi)=\frac{1}{4\Pi}\left[1+\sum_{K\rangle 0(EVEN)}(4\Pi)^{\frac{1}{2}}\frac{\langle\alpha_{k0}\rangle}{(2K+1)^{\frac{1}{2}}}P_K(\theta)\right] \qquad [I.12]$$

As Q=0 there is no φ dependence and we can therefore write

$$P(\theta,\varphi)=\frac{1}{2}\left[1+\sum_{K\rangle 0(EVEN)}(4\Pi)^{\frac{1}{2}}\frac{\langle\alpha_{k0}\rangle}{(2K+1)^{\frac{1}{2}}}P_K(\theta)\right] \qquad [I.13]$$

The $\langle\alpha_{KQ}\rangle/\langle 2K+1\rangle^{\frac{1}{2}}$ coefficients represent the order parameters of the system. For a fully aligned nematic system, all molecules are oriented along the nematic director **n,** yielding

$$\langle\alpha_{K0}\rangle=4\Pi^{\frac{1}{2}}Y_{K0}(\theta=0,\varphi) \qquad [I.14]$$

The degree of alignment $\langle\alpha_{20}\rangle$ of a fully ordered array is thus $\sqrt{5}$.

References

[1] A J Bain, P Chandna, and J Bryant, J. Chem. Phys. **112**, 10418 (2000)

[2] D M Brink and G R Satchler, "*Angular Momentum*" Second Edition, Clarendon Press, (1968)

Appendix II

Diffusion

The potential for diffusive flux J_x in an arbitrary direction x is proportional to the number density N(x,t) per unit distance dx [1]

$$J_x = -D\frac{dN(x,t)}{dx} \qquad \text{[II.1]}$$

where D is a proportionality constant known as the diffusion coefficient. The negative sign indicates the flow of matter in the direction of decreasing concentration. The conservation of mass applied to a restricted volume differential element formed by arbitrary area A and thickness dx can be expressed by

$$\frac{dN(x,t)}{dt} = -\frac{d(J_x)}{dx} \qquad \text{[II.2]}$$

Combining this expression with equation II.1 and assuming D to be independent of concentration yields an expression for the time evolution of concentration – the diffusion equation:

$$\frac{dN(x,t)}{dt} = D\frac{d^2N(x,t)}{dx^2} \qquad \text{[II.3]}$$

yielding solution [2]

$$N(x,t) = \frac{N}{(4\pi Dt)^{1/2}}\exp\left(-\frac{x^2}{4Dt}\right) \qquad \text{[II.4]}$$

This describes the spatial and temporal evolution of the particle concentration with initial conditions that all particles are concentrated in the YZ plane x=0 for t=0. Since

diffusion will occur in directions +x and –x, the mean displacement at any time is zero, so particle spread is measured via the mean square displacement:

$$\langle x^2 \rangle = \frac{1}{N} \int_{-\infty}^{\infty} x^2 N(x,t) dx \qquad \text{[II.5]}$$

yielding the Einstein-Smoluchowski equation [3]

$$\langle x^2 \rangle = \frac{1}{N} \frac{N}{(4\pi Dt)^{1/2}} \int_{-\infty}^{\infty} x^2 \exp\left(-\frac{x^2}{4Dt}\right) dx \qquad \text{[II.6]}$$

$$\langle x^2 \rangle = 2Dt \qquad \text{[II.7]}$$

Brownian motion [4] defines the random movements of a particle arising from a variable pressure difference caused by the continuous collisions on all sides of the particle by neighbouring particles. The application of Newtonian mechanics to a Brownian particle of mass M and velocity v experiencing a fluctuating force B(t) yields Langevin's equation:

$$M\frac{dv}{dt} = -M\xi v + B(t) \qquad \text{[II.8]}$$

where ξ is the microscopic friction constant [5]. Multiplication by x/M gives

$$x\ddot{x} = -\xi x\dot{x} + x\frac{B(t)}{M} \qquad \text{[II.9]}$$

Upon the substitutions $\dot{x}^2 = 2x\dot{x}$ and $\ddot{x}^2 = 2(\dot{x})^2 + 2x\dot{x}$ this becomes

$$\frac{1}{2}\ddot{x}^2 - (\dot{x})^2 = -\frac{\xi}{2}\dot{x}^2 + x\frac{B(t)}{M} \qquad \text{[II.10]}$$

Using the equipartition theorem the average kinetic energy can be written as [6]

$$\frac{1}{2}M\langle \dot{x}^2 \rangle = \frac{1}{2}k_B T \qquad \text{[II.11]}$$

where k_B is Boltzmanns' constant, T is the absolute temperature and $\langle\ \rangle$ denotes an average in time. If the average value of the fluctuating force is zero, the substitution of $\langle \dot{x}^2 \rangle$ into a time average form of equation II.10 gives

$$\frac{d^2}{dx^2}\langle x^2 \rangle - \left(\frac{2k_B T}{M}\right) = -\xi \frac{d}{dt}\langle x^2 \rangle \qquad \text{[II.12]}$$

Einstein's solution to this equation is written as [6]

$$\langle x^2 \rangle = \frac{2k_B T}{M\xi}\left\{t - (\xi)^{-1}\left(1 - e^{-\xi t}\right)\right\} \qquad \text{[II.13]}$$

In the very short time regime, $t<<\xi^{-1}$ and $\langle x^2 \rangle \approx (k_B T/M)t^2$ so the particles move with thermal velocity $\sqrt{2k_B T/M}$. At longer times the dominant process is Brownian motion and

$$\langle x^2 \rangle \approx (2k_B T/M\xi)t \qquad \text{[II.14]}$$

Combining this equation with equation II.7 allows the macroscopic diffusion coefficient D to be written in terms of the microscopic frictional force constant:

$$D = \frac{k_B T}{\xi} \qquad \text{[II.15]}$$

For a spherical molecule of radius R in a medium with viscosity η, the frictional coefficient can be expressed by applying Stokes' law [7]:

$$\xi = 6\pi\eta R \qquad \text{[II.16]}$$

and the diffusion coefficient becomes

$$D = \frac{k_B T}{6\pi\eta R} \qquad \text{[II.17]}$$

In the Brownian motion description, diffusion can be separated into independent translational and rotational motion. Equation II.7 expressed the translational diffusion coefficient in terms of the mean square displacement in time along one spatial (x) dimension. Extending this to three dimensional space yields

$$\left\langle r^2 \right\rangle_{XYZ} = 6D_{trans}t \qquad \text{[II.18]}$$

Similarly, the rotational diffusion coefficient can be expressed in terms of the mean square angular displacement $\left\langle \theta^2 \right\rangle$ with time by

$$\left\langle \theta^2 \right\rangle = 4D_{rot}t \qquad \text{[II.19]}$$

Furthermore, in the same way that the translational frictional coefficient for a particle with diffusion velocity v can be described by a force $f=-\xi_{trans}v$, so too can the rotational frictional coefficient be described in terms of a torque T acting on a particle with rotational velocity Ω, such that

$$T = -\xi_{rot}\Omega \qquad \text{[II.20]}$$

Applying the Langevin equation to rotational Brownian motion yields [2]

$$D_{rot} = \frac{k_B T}{\xi_{rot}} \qquad \text{[II.21]}$$

Up to this point it has been assumed that diffusing molecules can be described by an isotropic diffusion coefficient. In reality this is not the case; for non-spherical molecules, the diffusion coefficient is not a scalar quantity but a second rank tensor [8] with up to three independent components Dx, Dy, and Dz. For uniaxial molecules such as nematic liquid crystals two of the three principle axes are equivalent, resulting in two independent diffusion coefficients $D_\perp$ and $D_\parallel$ which correspond to θ and φ diffusion respectively:

$$D_\perp = D_x = D_y \qquad (\theta \text{ diffusion}) \qquad [II.22]$$

$$D_\parallel = D_z \qquad (\varphi \text{ diffusion}) \qquad [II.23]$$

The temporal evolution of the excited state distribution function moments with rank K and projection Q in an isotropic system is given by:

$$\left\langle C_{KQ}^{ex}(t)\right\rangle_{isotropic} = \left\langle C_{KQ}^{ex}(0)\right\rangle \exp[-DK(K+1)t] \qquad [II.24]$$

where D is the diffusion coefficient. The time dependent diffusion dynamics can be written as:

$$\left\langle C_{KQ}^{ex}(t)\right\rangle - \left\langle C_{KQ}^{ex}(ss)\right\rangle = \left\{\left\langle C_{KQ}^{ex}(0)\right\rangle - \left\langle C_{KQ}^{ex}(ss)\right\rangle\right\}\exp(-\gamma_{KQ}t) \qquad [II.25]$$

where

$$\gamma_{KQ} = D\langle KQ|\nabla^2|KQ\rangle \qquad [II.26]$$

Expressing ∇^2 in terms of normalised angular momentum operators (in units of ħ) yields

$$\nabla^2 = -\left(\hat{J}_X^2 + \hat{J}_Y^2 + \hat{J}_Z^2\right) = -\hat{J}^2 \qquad [II.27]$$

where $\hat{J}_X$, $\hat{J}_Y$ and $\hat{J}_Z$ are the generators of infinitesimal rotation about the x, y and z laboratory axes respectively. In terms of polar co-ordinates $\hat{J}_X^2 + \hat{J}_Y^2$ corresponds to θ diffusion and $\hat{J}_Z^2$ corresponds to φ diffusion. Expressing $\hat{J}_X^2 + J_Y^2$ in terms of angular momentum raising and lowering operators yields

$$\hat{J}_X^2 + J_Y^2 = \frac{1}{2}\{J_+ J_- + J_- J_+\} \qquad \text{[II.28]}$$

$D\nabla^2$ contains both θ and φ diffusion operators, which can be expressed as follows:

$$\gamma_{KQ}(\theta) = D(\theta)\langle KQ|\frac{1}{2}\{J_+ J_- + J_- J_+\}|KQ\rangle = D_\perp\left[K(K+1) - Q^2\right] \qquad \text{[II.29]}$$

$$\gamma_{KQ}(\varphi) = D(\varphi)\langle KQ|\hat{J}_Z^2|KQ\rangle = D_\parallel Q^2 \qquad \text{[II.30]}$$

Applying equations II.29 and II.30 to equation II.24 yields the following diffusion rates for the fluorescence observable moments $\langle C_{20}^{ex}(t)\rangle$ and $\langle C_{2+2}^{ex}(t)\rangle + \langle C_{2-2}^{ex}(t)\rangle$ in terms of θ and φ diffusion:

$$\gamma_{20} = 2(3)D_\perp + 0D_\parallel = 6D_\perp \qquad (\theta \text{ diffusion only}) \qquad \text{[II.31]}$$

$$\gamma_{22} = \gamma_{2-2} = 2D_\perp + 4D_\parallel \qquad (\theta \text{ and } \varphi \text{ diffusion}) \qquad \text{[II.32]}$$

References

[1] A Fick, Pogg. Annin., **94**, 59 (1855)

[2] D A Armoogum, Ph.D. Thesis, University College London (2004)

[3] A Einstein, Ann. D. Physik. **17**, 549 (1905)

[4] R Brown, Philos. Mag. **4**, 161 (1828)

[5] N V Brilliantov, V P Denisoc and P L Krapivsky, Physica A, **175**, 293 (1991)

[6] C E Hecht, "*Statistical Thermodynamics & Kinetic Theory*" Freeman, New York, (1990)

[7] W P Crummett and A B Western, "*University Physics*", WCB (1994)

[8] A J Bain, P Chandna, and J Bryant, J. Chem. Phys. **112**, 10418 (2000)

Appendix III

Mathematica Program to Determine value of The Peak Angle (θ_{MAX}) and Full Width Half Maximum ($\Delta\theta_{FWHM}$) of the Distribution Function in the Nematic Phase of 5CB

```
ac20 = 0.630457
ac40 = -0.212244
them = 0.615
hw = 0.63
(Integrate[SphericalHarmonicY[2, 0, the, phi] * Sqrt[4 Pi] * Sin[the], {the, them - hw, them + hw}, {phi, 0, 2 Pi}] /
   Integrate[Sin[the], {the, them - hw, them + hw}, {phi, 0, 2 Pi}]) - ac20
(Integrate[SphericalHarmonicY[4, 0, the, phi] * Sqrt[4 Pi] * Sin[the], {the, them - hw, them + hw}, {phi, 0, 2 Pi}] /
   Integrate[Sin[the], {the, them - hw, them + hw}, {phi, 0, 2 Pi}]) - ac40


g = NIntegrate[Sin[the], {the, them - hw, them + hw}, {phi, 0, 2 Pi}]
Plot[{1 / (g^2),
  (1 / (4 Pi)) * (1 +
     (ac20 * SphericalHarmonicY[2, 0, the, phi] / SphericalHarmonicY[0, 0, the, phi]) +
     (ac40 * SphericalHarmonicY[4, 0, the, phi] / SphericalHarmonicY[0, 0, the, phi]))},
 {the, them - hw, them + hw}, PlotRange → All, PlotStyle → {RGBColor[0, 0, 0], RGBColor[1, 0, 0]}]


ac60 = Integrate[SphericalHarmonicY[6, 0, the, phi] * Sqrt[4 Pi] * Sin[the], {the, them - hw, them + hw}, {phi, 0, 2 Pi}] /
  Integrate[Sin[the], {the, them - hw, them + hw}, {phi, 0, 2 Pi}]
ac80 = Integrate[SphericalHarmonicY[8, 0, the, phi] * Sqrt[4 Pi] * Sin[the], {the, them - hw, them + hw}, {phi, 0, 2 Pi}] /
  Integrate[Sin[the], {the, them - hw, them + hw}, {phi, 0, 2 Pi}]
ac100 = Integrate[SphericalHarmonicY[10, 0, the, phi] * Sqrt[4 Pi] * Sin[the], {the, them - hw, them + hw}, {phi, 0, 2 Pi}] /
  Integrate[Sin[the], {the, them - hw, them + hw}, {phi, 0, 2 Pi}]
ac120 = Integrate[SphericalHarmonicY[12, 0, the, phi] * Sqrt[4 Pi] * Sin[the], {the, them - hw, them + hw}, {phi, 0, 2 Pi}] /
  Integrate[Sin[the], {the, them - hw, them + hw}, {phi, 0, 2 Pi}]
ac140 = Integrate[SphericalHarmonicY[14, 0, the, phi] * Sqrt[4 Pi] * Sin[the], {the, them - hw, them + hw}, {phi, 0, 2 Pi}] /
  Integrate[Sin[the], {the, them - hw, them + hw}, {phi, 0, 2 Pi}]
ac160 = Integrate[SphericalHarmonicY[16, 0, the, phi] * Sqrt[4 Pi] * Sin[the], {the, them - hw, them + hw}, {phi, 0, 2 Pi}] /
  Integrate[Sin[the], {the, them - hw, them + hw}, {phi, 0, 2 Pi}]
```

Appendix IV

Instrument Response Function

An instrument response function (IRF) is recorded to check the response of the MCP and to confirm that unwanted reflections (identifiable by spikes on the logarithmic plot) have been eliminated. For the purposes of experiments carried out in this thesis an IRF with a full width half maximum of less than 100ps was deemed acceptable. A scattering sample ($\tau_{lifetime}$=0) is used to measure the IRF. Prior to recording an instrument response function all optical elements must be aligned such that the laser beam is back reflected along the optical path thus preventing detection of unwanted artifacts such as stray optical reflections. Calibration of the system is achieved by measuring two instrument response pulses separated by some known delay, typically 8ns. The resulting function is represented by two peaks separated by some channel number. A typical calibration is shown in (figure IV.1).

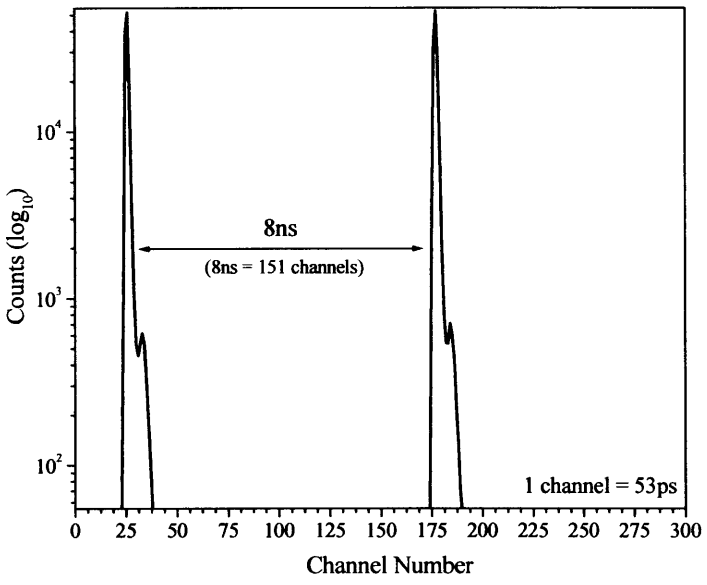

Figure IV.1: Logarithmic plot of an instrument response function and detection electronics calibration using a zero lifetime scattering sample (milk and water). The IRF measured for experiments carried out in this thesis is c.a. 83ps

Appendix V

Model for Triple Exponential Fits and Application to Polarised Intensity Decays

(i) Blue Edge Emission

$$\left[\left(A+B\exp^{-t/\tau_{fast}}\right)\left(1+2\Delta \mathrm{Re}\, xp^{-t/\tau_{20}}\right)\right]\exp^{-t/\tau_{fluor}} \qquad [V.1]$$

where A is the fraction of the population remaining in the visible spectrum and B is the fraction of the population shifted by solvent relaxation. ΔR represents the difference between the initial anisotropy R(0) and the steady state anisotropy R_{SS}. Multiplying out equation [V.1] gives equation [V.2] and [V.3]

$$A\left(1+2\Delta \mathrm{Re}\, xp^{-t/\tau_{20}}\right)\exp^{-t/\tau_{fluor}}+\left(B\exp^{-t/\tau_{fast}}\exp^{-t/\tau_{fluor}}\right)\left(1+2\Delta \mathrm{Re}\, xp^{-t/\tau_{20}}\right) \qquad [V.2]$$

$$A\exp^{t/\tau_{fluor}}+2\Delta \mathrm{Re}\, xp^{-t/\tau_{20}}\exp^{-t/\tau_{fluor}}+B\exp^{-t/\tau_{fast}}\exp^{-t/\tau_{fluor}}\left(1+2\Delta \mathrm{Re}\, xp^{-t/\tau_{20}}\right)[V.3]$$

By fitting the polarized intensity decays to a triple exponential function described by equation [V.3] it is possible extract three times as shown in table V.I

Component of Equation [V.3]	Fitting Triple Exponential Decay Extracts	
$A\exp^{t/\tau_{fluor}}$	$1/\tau_{fluor}$	fluorescence lifetime
$2\Delta \mathrm{Re}\, xp^{-t/\tau_{20}}\exp^{-t/\tau_{fluor}}$	$1/\tau_{fluor}+1/\tau_{20}$	rotational time modulated by the fluorescence lifetime
$B\exp^{-t/\tau_{fast}}\exp^{-t/\tau_{fluor}}\left(1+2\Delta \mathrm{Re}\, xp^{-t/\tau_{20}}\right)$	$1/\tau_{fast}+1/\tau_{fluor}\approx 1/\tau_{fast}$	solvent relaxation

Table V.I: Components of equation V.3 with times modulated or otherwise, extracted from fit to triple exponential function for blue edge emission.

It is evident from table V.I that τ_{20} is convoluted with the fluorescence lifetime τ_{fluor}. Application of equation [V.4] gives the deconvoluted τ_{20} time

$$\tau_{20} = \frac{1}{\left(\frac{1}{\tau_{20}} - \frac{1}{\tau_{fluor}}\right)} \qquad [V.4]$$

(ii) Red Edge Emission

For red edge emission there is no pre-exponential factor A for the fraction of the population remaining in the visible spectrum

$$B\left(1-\exp^{-t/\tau_{fast}}\right)\left(1+2\Delta \mathrm{Re}\, xp^{-t/\tau_{20}}\right)\exp^{-t/\tau_{fluor}} \qquad [V.5]$$

multiplying out equation [V.5] gives

$$B\left(1+2\Delta \mathrm{Re}\, xp^{-t/\tau_{20}}\right)\exp^{-t/\tau_{fluor}} - B\left(1+2\Delta \mathrm{Re}\, xp^{-t/\tau_{20}}\right)\exp^{-t/\tau_{fast}}\exp^{-t/\tau_{fluor}} \qquad [V.6]$$

$$B\exp^{t/\tau_{fluor}} + 2\Delta \mathrm{Re}\, xp^{-t/\tau_{20}}\exp^{-t/\tau_{fluor}} - B\exp^{-t/\tau_{fast}}\exp^{-t/\tau_{fluor}}\left(1+2\Delta \mathrm{Re}\, xp^{-t/\tau_{20}}\right) \qquad [V.7]$$

By fitting the polarised intensity decays to a triple exponential function described by equation [V.7] it is possible extract three times as shown in table V.II. Application of equation [V.4] allows for the deconvoluted determination of τ_{20}.

Component of Equation [V.6]	Fitting Exponential Decay	Represents
$B\exp^{t/\tau_{fluor}}$	$1/\tau_{fluor}$	fluorescence lifetime
$2\Delta RB\exp^{-t/\tau_{20}}\exp^{-t/\tau_{fluor}}$	$1/\tau_{fluor} + 1/\tau_{20}$	rotational time modulated by the fluorescence lifetime
$-B\exp^{-t/\tau_{fast}}\exp^{-t/\tau_{fluor}}\left(1+2\Delta \mathrm{Re}\, xp^{-t/\tau_{20}}\right)$	$1/\tau_{fast} + 1/\tau_{fluor} \approx 1/\tau_{fast}$	solvent relaxation

Table V.II: Components of equation V.6 and times, modulated or otherwise, extracted from fit to triple exponential function for red edge emission.

Triple exponential functions are fitted to the vertically and horizontally polarised intensity decays for excitation polarisation angles of $\beta=0^o$, $\beta=90^o$ and $\beta=54.7^o$ allowing for determination of τ_{20}, τ_{fluor} and τ_{fast}. Convoluted times are shown in table V.III.

Phase-Nematic		Intensity (Vertical)								
Lambda (nm)		β=0°			β=54.7°			β=90°		
Excitation	Emission	τ_1	τ_2	τ_3	τ_1	τ_2	τ_3	τ_1	τ_2	τ_3
440	455-500	0.5854	1.9051	5.7355	0.6287	2.0052	5.7567	0.5512	1.8393	5.7525
440	>530	0.3046	2.5392	5.8347	0.3476	Part*	5.7895	0.5117	1.9583	5.8234
440	>570	0.4891	2.3639	5.8111	0.5118	N/A	5.7992	0.5276	1.6942	5.8307
		Intensity (Horizontal)								
Lambda (nm)		β=0°			β=54.7°			β=90°		
Excitation	Emission	τ_1	τ_2	τ_3	τ_1	τ_2	τ_3	τ_1	τ_2	τ_3
440	455-500	0.5547	1.9148	5.7438	0.6170	1.9820	5.7287	0.5419	1.8122	5.7248
440	>530	0.5851	N/A	5.7946	0.4091	2.9587	5.8485	0.3015	2.1887	5.7968
440	>570	0.6435	N/A	5.8360	0.5031	3.0206	5.8481	0.3625	2.6447	5.8200

Table V.III: Convoluted times for $\tau_{fast}(\tau_1)$, $\tau_{20}(\tau_2)$, and $\tau_{fluor}(\tau_3)$ from triple exponential fits to vertically and horizontally polarised intensity decays at excitation polarization angles of $\beta=0^o$, $\beta=90^o$ and $\beta=54.7$. It is evident that for vertically polarised intensity decays at excitation polarisation angle $\beta=54.7^o$ and horizontally polarised intensity decays at excitation polarization angle $\beta=0^o$ it is not possible to fit a triple exponential function to the intensity decays. Instead a double exponential fit is made.

Appendix VI

Values of the Pre-Exponential Factors for Blue and Red Edge Emission of Coumarin 153 in the Nematic and Isotropic Phase of 5CB

NEMATIC		Blue Edge			Red Edge	
Temperature	**$T-T_{NI}$**	**Rapid**	**Fast**	**Slow**	**Fast**	**Slow**
27.0	-6.2	80623	46788	133582	-52821	203104
30.0	-3.2	76567	46731	135487	-53965	206380
32.0	-1.2	No Data	No Data	No Data	-39890	164192
32.5	-0.7	78324	43788	131326	-44113	171330
32.9	-0.3	85684	52553	146941	-29479	123237
33.1	-0.1	79461	42702	128935	-34406	144728
ISOTROPIC		Blue Edge			Red Edge	
Temperature	**$T-T_{NI}$**	**Rapid**	**Fast**	**Slow**	**Fast**	**Slow**
32.6	-0.6	101809	57328	173734	-53213	193295
32.9	-0.3	71005	42269	127707	-65187	248103
33.1	-0.1	84219	49287	140095	-43158	169470
33.2	0	103782	63852	177907	-43073	173220
33.3	0.1	111474	74778	211033	-51012	208687
33.4	0.2	79808	44625	145181	-68995	253295
33.5	0.3	83765	38813	136447	-44361	168002
33.7	0.5	71321	48290	146298	-43865	166005
34.0	0.8	84009	44970	146870	-49072	184343
34.5	1.3	76896	41469	140109	-42084	165163
35.0	1.8	79042	41134	138960	-41593	162325
36.0	2.8	82102	39477	146277	-43057	165251
38.0	4.8	78870	36370	148679	-44426	178783
40.0	6.8	78526	36047	156040	-44755	180023
45.0	11.8	73199	34061	161663	-41511	179097
50.0	16.8	65415	29474	160767	-48255	202722
60.0	26.8	68281	19960	169150	-41966	186922
70.0	36.8	71458	14163	205151	-42191	195819
80.0	46.8	53490	7792	191038	-23189	190571